

Theoretical and experimental investigation of membrane distillation

Jianhua Zhang

Bachelor of Chemical Engineering

Master of Inorganic Chemistry

**Institute for Sustainability and Innovation, School of Engineering & Science,
Victoria University**

Submitted in fulfilment of the requirements of the degree of Doctor of Philosophy

(2011)

Abstract

Invented in 1960s, membrane distillation is an emerging technology for water treatment attracting more attention since 1980s. There are four configurations of membrane distillation including air gap membrane distillation (AGMD), direct contact membrane distillation (DCMD), sweep gas membrane distillation (SGMD), and vacuum membrane distillation (VMD). DCMD and vacuum enhanced DCMD (VEDCMD), a variant of DCMD, were employed in this research. The objective of this study is to develop design tools for scale up of DCMD by analysing the characteristics of membrane suitable for DCMD, influences of membrane structure (hollow fibre membrane) and pressure (compressible PTFE membrane) on membrane performance, and modelling the energy efficiency of DCMD with varied process parameters.

There were four major stages in this project: a) selection of a suitable flat sheet membrane for membrane distillation based on criteria such as materials used for the active layer, active layer properties and support layer properties; b) study of a hollow fibre membrane in a tubular module, and analysis of the effect of the membrane's asymmetric structure on its performance; c) investigation of the relationship between applied pressure and membrane performance for compressible and incompressible membranes; and d) development of a simple relationship between membrane size, temperature and the MD flux based on experimentally determined global mass transfer coefficients, and theoretically modelling of the influence of process variables (flowrate, temperature, etc.), membrane properties (porosity, membrane thickness, etc.) and membrane geometric size on the membrane flux, energy efficiency and temperature polarisation of DCMD.

In the first stage, different types of membranes were tested with an Osmonics, flat sheet module. The membranes were classified by material of active layer, nominal pore size, and structure of the support layer. Each type of membrane was characterised by their contact angle, thickness and cross-sectional structure, porosity, and Liquid Entry Pressure (LEP). In the study, the global mass transfer coefficient was used to assess

membrane performance. A hydrophobic, micro-filtration, polyvinylidene fluoride (PVDF) membrane with nonwoven fabric support layer was considered, and compared to PTFE membranes with different support layers (nonwoven fabric and scrim) and different pore sizes (0.1-2 μm). The randomly structured nonwoven fabric support layer had torturous and tiny channels inside, which was apt to trap stagnant water inside so as to increase temperature polarisation. The scrim support layer had a regular structure with large, shallow, straight oval openings that reduced the chance of stagnant water being trapped inside the openings. For PTFE membranes with pore sizes of 1.5 and 2 μm , the membrane could not stop liquid water passing through the membrane even under a pressure less than 10 kPa; for PTFE membranes with pore size less than 1 μm , better salt rejection, higher flux, and higher energy efficiency were found in the MD application process, as compared to the PVDF membrane. Additionally it was shown that PTFE membranes with larger pore size and structured support layer (scrim) had a better performance in MD for desalination than that of a membrane with small pore size or supported with nonwoven fabric. However, the PTFE membranes were formed by the stretching the PTFE membranes, so that larger pore size membranes also had a reduced thickness (if made from the same raw material), causing loss of mechanic strength. Based on experimental experience, the membranes with a thickness ≥ 40 μm and pore size of 0.45-0.5 μm provided good flux and lasted longer in experiments. During this preliminary research, tests lasted for 2-6 days using reverse osmosis (RO) brines from wastewater treatment and groundwater treatment. The findings demonstrated that fouling and wetting were not a great issue in the membrane distillation when using PTFE membranes, especially for the test conducted at lower feed inlet temperature (40°C) in which the membrane performance was almost fully recovered by simply rinsing the scale off the membrane surface with de-ionised water.

In the second stage, a hollow fibre, tubular module specifically designed for membrane distillation was studied. The tubular module contains 95 hollow fibre membranes, which is made from a fluorinated polymer with a nominal pore size of 0.3 μm . To reduce the wetting risk caused by great pressure drop at high velocity, the designed hollow fibre membrane had an internal diameter of 1 mm. The hollow fibre membrane was characterised by SEM, BET pore size distribution, contact angle, and porosity. The membrane was found to be composed of a thin smooth skin layer located at the outer surface of the membrane and a thick porous principle layer. The influence of streams at

different velocities and temperatures on the global mass transfer coefficient and flux were studied. The membrane showed high flux ($18 \text{ Lm}^{-2}\text{h}^{-1}$, hot inlet temperature 80°C , cold inlet temperature 20°C) and good salt rejection ($>99\%$) under tested conditions. The asymmetric structure caused a large flux difference as the hot feed passing through the lumen compared to the shell side. This phenomenon was analysed by considering the heat and mass balance across each layer, from which it was found that the skin layer combining with the exponential relation between the interface temperature and vapour pressure lead to the difference. VEDCMD was also tested with this module. In the experiments, the cold stream was drawn through the module on the shell side, and the degree of vacuum was increased by increasing the stream velocity. It was found that the global mass transfer coefficient increased as negative pressure was applied on the cold side under the same hydrodynamic and thermal conditions. For a comparison test with positive pressure for the cold flow, a maximum global mass transfer coefficient was also found when only the cold stream velocity increased, due to the skin layer effect. In this case, the flux was reduced dramatically by swapping the feed stream from inside the fibre to outside the fibre, due to the change of heat conduction and mass transfer sequence. Therefore, based on this study, it is important to consider both the heat and mass transfers in fabrication of MD membranes.

The third stage focused on the influence of pressure on flux. From the theory of mass transfer through porous materials, it is clear that the pressure in the pore can affect mass diffusion. For compressible membranes in MD, as the air pressure in the pore increases, the rate of the water vapour diffusion slows. It is also expected that the membrane conductivity will increase due to reductions in thickness and porosity. Compressible PTFE membrane (pore size $0.5 \mu\text{m}$) and incompressible hollow fibre membrane (pore size $0.3 \mu\text{m}$) were used in these tests. Both the compressible and incompressible natures of the membranes were confirmed by deformation (volume change) experiments under different pressures. As the pressure increased from 3 to 63 kPa, there was negligible volume variation for the incompressible hollow fibre membrane, but there was a 1/3 reduction in volume for the compressible PTFE membrane. Curves and equations fitting the experimental data were used for the interpretation of PTFE membrane performance in MD. The PTFE membrane was subjected to measurements in volume, porosity, thickness, material density, and permeability (pore size), and was characterized using SEM. The experiments were performed at three different velocities at the same inlet

temperature and three different temperatures at the same velocity. The pressure in the experiment was increased in steps of 10 kPa over a total pressure increase of 40-50 kPa. There was a $\pm 5\%$ variation around the mean flux for the hollow fibre membrane as the pressure increased, which showed that the flux for the incompressible membrane was not related to the pressure applied on its surface. However, the flux for the PTFE membrane showed a decline with an increase in pressure. From the mass transfer theory and the thermal properties of the membrane, it can conclude that the flux reduction was directly related to the increased thermal conductivity and pressure in pores of the membrane. Based on the heat and mass balances, the mass transfer coefficient was also calculated for different pressures, and a maximum mass transfer coefficient was found. Therefore, the membrane mass coefficient increased initially in the lower pressure range and decreased in the higher pressure range, as the pressure rose.

The fourth stage considered the relationship between the geometric size of the membrane and flux, and a simple model for predicting the flux variation with length and temperature was developed based on the findings that the global mass transfer coefficient showed minor dependence ($\pm < 15\%$) on the temperatures and membrane length when the flow rate was set. A Perspex (Poly(methyl methacrylate)) module with symmetric flow channels was fabricated for this research. PTFE membranes with a nominal pore size of $0.5 \mu\text{m}$ and scrim support layer were used. The simple model predicted the flux at different temperatures and membrane lengths (5-13 cm) using the global mass transfer coefficient obtained at the same velocity. The modelling results were compared with the experimental results, and the errors varied in the range of $\pm < 15\%$ at different temperatures and in the range of $\pm < 15\%$ with different membrane lengths. Co-current and counter-current DCMD were both tested, and the counter-current DCMD showed higher flux than that of co-current DCMD under the same conditions. The study showed that shorter membrane modules had higher flux than that of longer membrane modules under the same conditions. Therefore, assessment of membrane performance by flux for membrane distillation can only be done for standard conditions and geometries, as the flux from the membrane distillation process is related to membrane size and temperature. A better parameter for assessing membrane performance is the global mass transfer coefficient, as it is independent of temperature and membrane module size. Although this simple model was able to predict MD flux, it was limited by the application of global mass transfer coefficient, which is confined to a

particular flowrate (ie. turbulence conditions in the module).

To overcome the limitations from the simple model (i.e. required experimentally determined mass transfer coefficients), a complex model was developed that required only the physical properties of the membrane as inputs. The modelling program was written in both Matlab and Visual Basic (implanted in an excel file) languages based on heat and mass balances. The model was used to predict flux for variations in the size and physical properties of membranes and process parameters. The assumptions included 1) no heat loss through the module wall, 2) the heat of vaporisation and condensation does not change with concentration, 3) with a given membrane, the properties of the membrane, such as thickness, porosity, pore size, and tortuosity are constant, 4) in balancing the heat transfer, the sensible heat carried by the water vapour can be neglected, 5) the stream has no temperature gradient in the direction perpendicular to the flow direction and parallel to the membrane, and 6) the mass balance neglects the mass flow difference due to vapour evaporation and condensation (ie. permeate flow is small compared to stream flows). The local convective heat transfer coefficient was calculated based on the spacer structure, channel depth and flow state, in which the Nusselt number was calculated based on the assumption of fully developed flow in a spacer filled channel. The model was also used for predicting flux for large module sizes ($0.75 \times 0.25 \text{ m}^2$). The error between the predicted results and experimental results was in range of $\pm < 15\%$. This compares to an experimental reproducibility of $\pm 5\%$. The model was also used to examine the energy efficiency of MD and the effect of applied pressure for compressible (PTFE) membranes. The properties varied with pressure, e.g. thermal conductivity, porosity, thickness and pore size, and were calculated from experimental data obtained during the fourth stage. The difference between this model and the simple model is that::

- The simple model was developed based on the experimentally obtained global mass transfer coefficient, which varied with the velocity and flow channel structure. Therefore, in the acceptable engineering error range, this model is only suitable for predicting flux at the same velocity or above the fully developed turbulent flow regime where the global mass transfer coefficient is available in the built database.
- This model was developed based on the measurable original membrane

permeability (ε/bt). Thus, the model can be used to predict flux from different velocities, temperatures, membrane lengths, and under different pressures

The findings in the study include: the scrim supported PTFE membrane has a better performance (both flux and energy efficiency) than that of the membrane supported by nonwoven fabric support layer; the flux of membrane distillation depends strongly on the membrane size along the flow direction; MD membrane performance is better characterised by membrane mass transfer coefficient or ε/bt ; for hollow fibre membranes with asymmetric structure, the selection of feed flow channel (hot flow through lumen or outside of the hollow fibre) has great influence on the flux; the pressure applied on the compressible membrane will affect flux and energy efficiency of membrane distillation; improvement of membrane properties based on current available membrane, such as porosity, thickness, pore size, etc., can not promote the flux or efficiency greatly, especially for membranes of large size. Additionally, the models have provided tools to scale up and design MD modules and processes.

Declaration

“I, Jianhua Zhang, declare that the PhD thesis entitled Theoretical and experimental investigation of membrane distillation is no more than 100,000 words in length including quotes and exclusive of tables, figures, appendices, bibliography, references and footnotes. This thesis contains no material that has been submitted previously, in whole or in part, for the award of any other academic degree or diploma. Except where otherwise indicated, this thesis is my own work”.

Signature:

Date:

Acknowledgement

I appreciate the great supervision of Professor Stephen, R. Gray, my principal supervisor, Director of Institute for Sustainability and Innovation, Victoria University. He always has been a source of knowledge and inspiration for providing clues and encouragement to solve the encountered problems in my research. Furthermore, he also gave me opportunities to undertake research in the broader filtration area, making me versatile in water treatment research.

I am also grateful to my associate supervisor, Associate Professor Jun-De Li, School of Engineering and Science, Victoria University. Under his guidance, I have obtained a comprehensive understanding of mass and heat transfers in my research area, and developed the skills of building mathematical models.

I acknowledge the CSIRO Cluster for Advanced Water Membrane Technologies for providing the financial support.

I acknowledge the help of Associate Professor Mikel Duke, Institute for Sustainability and Innovation, Victoria University. He provided constructive comments and suggestions during my paper writing.

I am thankful to our research officer, Noel Dow, Institute for Sustainability and Innovation, Victoria University. He helped me to start my research work smoothly and gave me many effective solutions for my laboratory work.

I appreciate the generosity of all my colleagues in the Institute for Sustainability and Innovation. Dr. Peter Sanciolo helped me obtain a preliminary understanding of Reverse Osmosis, Dr. Marlene Cran helped taught me to use of IR instrument, Dr. Bo Zhu gave me the training of BET machine, and Dr. Nicholas Milne gave the opportunity of Reverse Osmosis research.

I am thankful to the support from my family. Without their help, I could not have focused completely on my Ph.D study.

Jianhua Zhang

Werribee, Australia

Date: 22/12/2010

Research Papers

Published Journal Papers arising from research described in this thesis:

[1] J. Zhang, M. Duke, E. Ostarcevic, N. Dow, S. Gray, J.-d. Li, Performance of new generation membrane distillation membranes. *Water Science and Technology: Water Supply*. 9(2009) 8.

[2] J. Zhang, N. Dow, M. Duke, E. Ostarcevic, J.-D. Li, S. Gray, Identification of material and physical features of membrane distillation membranes for high performance desalination, *Journal of Membrane Science*. 349(2010) 295-303.

[3] J. Zhang, J.-D. Li, M. Duke, Z. Xie, S. Gray, Performance of asymmetric hollow fibre membranes in membrane distillation under various configurations and vacuum enhancement, *Journal of Membrane Science*. 362(2010) 517-528.

[4] J. Zhang, S. Gray, J.-D. Li, Effect of applied pressure on performance of PTFE membrane in DCMD, *Journal of Membrane Science*. (2010) (Accepted)

[5] J. Zhang, S. Gray, J.-D. Li, Modelling heat and mass transfer in membrane distillation process, *Chemical Engineering Journal*. (2010) (Submitted).

Published Conference Paper:

[1] J. Zhang, Jun-De Li, Stephen Gray. Researching and modelling the dependence of MD flux on membrane dimension for scale-up purpose. AWA, Specialty III, 2009

[2] J. Zhang, N. Dow, J. Li, M. Duke and S. Gray. High-flux Hollow Fibre Module for Membrane Distillation. IWA, Beijing, 2009

[3] J. Zhang, M. Duke, E. Ostarcevic, N. Dow, S. Gray, J.-d. Li, Performance of new generation membrane distillation membranes. Singapore international water week convention, 2008

Oral Presentations

Jianhua Zhang, Jun-De Li, Stephen Gray. Modelling for membrane distillation processes. Desalination for Clean Water and Energy, EuroMed, 3-7 October 2010, Tel Aviv, Israel

Jianhua Zhang, Jun-De Li, Stephen Gray. Researching and modelling the dependence of MD flux on membrane dimension for scale-up purpose. AWA Membrane Specialty III, 11-13 February 2009, Sydney, Australia

Poster presentations

J. Zhang, N. Dow, J. Li, M. Duke and S. Gray. High-flux Hollow Fibre Module for Membrane Distillation. IWA, Beijing, China, 2009

Jianhua Zhang, Noel Dow, Steven Mee, Jun-De Li, Mikel C. Duke and Stephen Gray. Progress on Membrane Distillation Scale-Up Using Polymer and Inorganic (Ceramic) Membranes. ICOM2008, Hawaii, USA, 12-18 July 2008

J. Zhang, J.-D. Li, and S. Gray. Effect of applied pressure on flux and membrane performance for DCMD. AMS6/IMSTEC10, 22-26 November 2010, Sydney, Australia

Table of Contents

Chapter 1 Introduction	1
Chapter 2 Literature review	5
2.1 Configurations of membrane distillation	5
2.2 Characteristics of membrane	7
2.3 Configurations of MD membranes	10
2.4 Configurations of MD modules	11
2.5 DCMD process diagram	13
2.6 Heat transfer and mass transfer in DCMD	15
2.6.1 Heat transfer	15
2.6.2 Mass transfer	19
2.7 Application of membrane distillation	23
2.8 Objective	25
Chapter 3 Identification of membrane characteristics for high performance in membrane desalination	26
3.1 Introduction	26
3.2 Experimental method	27
3.2.1 Membranes and their properties	27
3.2.1.1 Contact angle measurement	28
3.2.1.2 SEM characterisation	28
3.2.1.3 LEP measurement	28
3.2.1.4 Gas permeability measurement	30
3.2.1.5 Porosity measurement	31
3.2.2 DCMD Testing	32
3.3 Results and discussion	33
3.3.1 Membrane properties	33
3.3.2 Membrane fluxes and global mass transfer coefficients at different velocities	42
3.3.3 Membrane fluxes and global mass transfer coefficients at different temperatures	45
3.3.4 Temperature influence on membrane flux and energy efficiency	47
3.3.5 Key performance features of new generation membranes	52
3.4 Summary	53
Chapter 4 Performance of asymmetric hollow fibre membranes	55
4.1 Introduction	55
4.2 Theory	55
4.3 Experimental methods	57
4.3.1 Hollow fibre membrane and module	57
4.3.2 Characterisation of hollow fibre membrane	58
4.3.2.1 Measurement of hollow fibre membrane dimensions	58
4.3.2.2 Contact angle measurement	59
4.3.2.3 Porosity measurement	63
4.3.2.4 Pore distribution and pore size measurement	64
4.3.2.5 SEM characterisation	64
4.3.3 DCMD and Vacuum Enhanced DCMD (VEDCMD) Testing	64
4.4 Results	66

4.4.1 Membrane properties.....	66
4.4.2 Experimental results.....	71
4.4.2.1 Fluxes and global mass transfer coefficients at different Reynolds numbers	71
4.4.2.2 Temperature influence on membrane flux.....	73
4.4.2.3 Flux variation with enhanced vacuum on the cold side.....	75
4.4.2.4 Feed pressure and salt rejection	77
4.5 Discussion	77
4.5.1 Vacuum enhanced membrane distillation.....	79
4.5.2 Influence of asymmetric structure of hollow fibre membrane on flux	80
4.5.2.1 Mass transfer resistance analysis.....	80
4.5.2.2 Heat transfer resistance analysis	81
4.6 Summary	84
Chapter 5 Effect of applied total pressure on the performance of PTFE membranes in DCMD	86
5.1 Introduction.....	86
5.2 Force balance analysis at pore entrances	87
5.3 Experiment.....	88
5.3.1 Membrane characterisation	88
5.3.1.1 SEM characterisation.....	88
5.3.1.2 Air permeability measurement	89
5.3.1.3 Active layer porosity and thickness measurement.....	89
5.3.2 Membrane deformation measurement	92
5.3.3 DCMD experiments	94
5.4 Results and discussion.....	96
5.4.1 Analytical results and discussion.....	96
5.4.2 Deformation results and discussion.....	98
5.4.2.1 Thickness measurement of active layer under different pressures.....	98
5.4.2.2 Comparison of compressibility of PTFE and hollow fibre membrane	99
5.4.2.3 Calculation of pressure in the pores	100
5.4.2.4 Estimation of pressure influence on membrane properties.....	101
5.4.2.5 Estimation of mean membrane mass transfer coefficient ($C_{membrane}$).....	105
5.4.3 DCMD experimental results and discussion.....	106
5.4.3.1 Experimental results for incompressible hollow fibre membrane	106
5.4.3.2 Compressible PTFE membrane experimental results and discussion	109
5.4.3.2.1 Effect of applied pressure on compressible membrane at different velocities.....	109
5.4.3.2.2 Effect of applied pressure on compressible membranes at different temperatures	115
5.5 Summary	119
Chapter 6 Mathematical models for direct contact membrane distillation.....	120
6.1 Simple model developed based on the global mass transfer coefficient.....	120
6.1.1 Introduction.....	120
6.1.2 Simulation and experiment.....	121
6.1.2.1 Theoretical analysis of one-dimension model for DCMD.....	121
6.1.3 Experimental apparatus and procedure.....	126
6.1.4 Results and discussion.....	126
6.1.4.1 Verification of the modelling results.....	126
6.1.4.1.1 Validating the use of the mean global mass and heat transfer coefficients in flux prediction	126
6.1.4.1.2 Verification of the model at different temperatures	129
6.1.4.1.3 Verification the model with different membrane lengths.....	130

6.1.4.2 Mathematical modelling of temperature profile in direct contact membrane distillation	132
6.1.4.2.1 Prediction of temperature profile of co-and counter-current DCMD	132
6.1.4.2.2 Prediction of temperature difference at difference velocities based on fitting equations in Fig. 6.4b	133
6.1.4.2.3 Prediction of flux changes of co-and counter-current DCMD in flow direction at different feed velocities	135
6.2 Mathematic model of DCMD based on membrane properties and hydrodynamic and thermal conditions of streams	137
6.2.1 Introduction.....	137
6.2.2 Theoretical analyses of the heat transfer and mass transfer	137
6.2.3 Experiment and simulation.....	138
6.2.3.1 Membrane and module characterisation.....	138
6.2.3.1.1 Thermal conduction coefficient (λ/b) measurement.....	138
6.2.3.1.2 Spacer and module	139
6.2.3.2 Experimental process	141
6.2.3.3 Modelling heat and mass transfer.....	142
6.2.3.4 Numerical solution.....	143
6.2.4 Results and discussion.....	147
6.2.4.1 Analytical results and discussion	147
6.2.4.2 Modelling and experimental results	147
6.2.4.2.1 Verification of model.....	147
6.2.4.2.2 Application of model in analysis and discussion of co- and counter-current DCMD.....	155
6.2.4.2.3 Single-pass evaporation ratio variation with process parameters	167
6.3 Summaries for both models.....	172
Chapter 7 Conclusions and Recommendations.....	176
Chapter 8 Future research directions.....	183
Nomenclature.....	185
Reference.....	189
Appendix	195

List of Tables

Table 2.1 Reported surface energy and thermal conductivity of materials used in MD [41, 51]	9
Table 2.2 Mass transfer mechanism in membrane pore	20
Table 3.1 Properties of membranes as provided by the manufacturers	28
Table 3.2 Measured and calculated properties of membrane	40
Table 3.3 Sensible heat transfer and latent heat transfer at different temperatures	49
Table 3.4 Flux change with side in contact with feed	51
Table 4.1 Nominal specifications of hollow fibre membranes	57
Table 4.2 Diameter calculated based the measurement from image.....	59
Table 4.3 Measured height difference (h) between the top of the fibre and water surface	63
Table 4.4 Measured and calculated properties of membrane	66
Table 4.5 Estimated properties of the hollow fibre layers	70
Table 5.1 Calculated pore size and ε/bt from fitting equations in Fig. 5.2	89
Table 5.2 Data of the tubular hollow fibre module.....	95
Table 5.3 Properties of membrane.....	96
Table 6.1 Heat conduction measurement of the shim samples	139
Table 6.2 Dimension of module and spacer	140
Table 6.3 Thermal conductivity of the membrane and the plastic shim	147

List of Figures

Fig. 2.1 Membrane distillation configurations	6
Fig. 2.2 Schematics of hollow fibre and flat sheet membranes	11
Fig. 2.3 MD Modules	12
Fig. 2.4 DCMD process schematic	14
Fig. 2.5 Heat transfer and mass transfer through membrane	16
Fig. 2.6 Spacer structure	17
Fig. 2.7 Electrical circuit analogues for different transport mechanisms	21
Fig. 3.1 Schematic diagram of LEP test	30
Fig. 3.2 Air permeability testing instrument.....	31
Fig. 3.3 Schematic diagram of the experimental setup	33
Fig. 3.4 SEM images of support and active layers	37
Fig. 3.5 Relations between $J/\Delta P_{gas}$ and P_{pore} in nitrogen permeation test of different membranes	38
Fig. 3.6 Schematics of scrim embedded in the active layer	41
Fig. 3.7 Cross section of $M_{p0.30}$ active layer	41
Fig. 3.8 Relation between flux and velocity	42
Fig. 3.9 Mass transfer coefficients with respect to feed velocity.....	44
Fig. 3.10 Salt rejections related to feed velocity	45
Fig. 3.11 Relation between flux and temperature for the various membranes	46
Fig. 3.12 Mass transfer coefficients with respect to feed inlet temperature for the various membranes	46
Fig. 3.13 Salt rejection at different temperatures	47
Fig. 3.14 Variation of flux with hot side inlet temperature at a constant velocity	48
Fig. 3.15 Ratio of heat for water flux to the total feed heat loss, E , at different temperatures	52
Fig. 4.1 Schematic diagram of the force balance at the pore entrances	56
Fig. 4.2 Photo for inner and outer diameter measurement of hollow fibre membrane	58
Fig. 4.3 Contact angle measurement for outer surface	60
Fig. 4.4 Mass change against the time in contact angle measurement.....	61
Fig. 4.5 Contact angle measurement for the inner surface	62
Fig. 4.6 Schematic diagram of the experimental Setup III	66
Fig. 4.7 SEM images of the hollow fibre.....	69
Fig. 4.8 BJH membrane pore size distribution (pore size 0.0017-0.3 μm).....	70
Fig. 4.9 Influence of velocity on flux and global mass transfer coefficient	72
Fig. 4.10 Flux and global mass transfer coefficient affected by temperature	74
Fig. 4.11 Vacuum enhanced membrane distillation	76
Fig. 4.12 Relationship between inlet pressure and velocity (Setups I and II).....	77

Fig. 4.13 Schematic of the idealised membrane structure and temperature distribution	78
Fig. 4.14 Vapour pressure difference across skin layer at different temperatures ($\Delta T=0.31^{\circ}\text{C}$)	83
Fig. 5.1 Schematic of force balance in the pore	88
Fig. 5.2 Results of gas permeation test	90
Fig. 5.3 Schematic of membrane deformation measure measurement	93
Fig. 5.4 Volume change under different pressures in blank experiment	94
Fig. 5.5 Schematic diagrams of the employed DCMD process	95
Fig. 5.6 Images for membrane structures	97
Fig. 5.7 Thickness change under different pressures for the PTFE membranes	98
Fig. 5.8 Ratio of volume change to total active layer volume under pressure	99
Fig. 5.9 Applied pressure vs calculated pressure in the pore of PTFE membrane	100
Fig. 5.10 $\epsilon_p^{1.5}(1-\epsilon_p)$ vs porosity variation	102
Fig. 5.11 Thermal properties changes under pressure	105
Fig. 5.12 Hollow fibre flux vs applied pressure at different velocities.....	107
Fig. 5.13 Hollow fibre flux vs applied pressure at different feed inlet temperatures	108
Fig. 5.14 Flat sheet PTFE flux vs applied pressure	111
Fig. 5.15 Changes of thermal conditions under different pressures ($T_{fi}=60^{\circ}\text{C}$, $T_{pi}=20^{\circ}\text{C}$)	113
Fig. 5.16 Mean membrane mass transfer coefficient under different pressures	114
Fig. 5.17 Flux changed with varied pressures at different temperatures	116
Fig. 5.18 Changes of thermal conditions under different pressures	118
Fig. 5.19 Mean membrane mass transfer coefficient under different pressures (Velocity=0.097 m/s)	119
Fig. 6.1 Heat and mass transfer element of a co-current DCMD.....	123
Fig. 6.2 Schematic diagram for numerical flux calculation of co-current flow	124
Fig. 6.3 Schematic diagram for numerical flux calculation of counter-current flow	125
Fig. 6.4 Validation of mean global mass and heat transfer coefficients with velocity	128
Fig. 6.5 Comparison between experimental and modelling results at different temperatures for counter-current setup	129
Fig. 6.6 Comparison between experimental and modelling results for different membrane lengths in counter-current setup	131
Fig. 6.7 Comparison between experimental and modelling results for different membrane lengths in co-current setup	131
Fig. 6.8 Temperature distributions along the membrane for co-current flow	132
Fig. 6.9 Temperature profile along the membrane for counter-current flow	133
Fig. 6.10 Average temperature difference across the membranes at different velocities	134
Fig. 6.11 Flux at different velocities.....	135
Fig. 6.12 Flux changes of co-current DCMD in flow direction at different velocities	136
Fig. 6.13 Flux changes of counter-current DCMD in flow direction at different velocities.....	136
Fig. 6.14 Dimensions of the module and spacer.....	141
Fig. 6.15 Flow chart for co-current DCMD modelling.....	145
Fig. 6.16 Flow chart for counter-current DCMD modelling	146

Fig. 6.17 Model verified at different velocities	148
Fig. 6.18 Model verified at different temperatures	150
Fig. 6.19 Relationship between the recovery and temperatures and velocity	151
Fig. 6.20 Relationship between single pass recovery and modelling error.....	151
Fig. 6.21 Pressure analysis in counter- and co-current DCMD	152
Fig. 6.22 Accuracy assessment with varied membrane lengths.....	154
Fig. 6.23 Modelled temperature distribution in counter- and co-current DCMD	156
Fig. 6.24 Percentage flux difference between counter current and co-current modes	158
Fig. 6.25 Temperature polarisation coefficient vs feed velocity	160
Fig. 6.26 Local flux distribution vs membrane length.....	162
Fig. 6.27 Local temperature polarisation coefficient distribution vs membrane length	163
Fig. 6.28 Flux and temperature polarisation affected by temperature	165
Fig. 6.29 Influence of membrane characteristics on flux.....	166
Fig. 6.30 Evaporation ratio and flux at different process conditions	170
Fig. 6.31 Evaporation ratio and flux varied with membrane length	172

Chapter 1 Introduction

Membrane distillation (MD) is one of the membrane-based separation processes. The driving force for MD processes is quite different from other membrane processes. It is the vapour pressure difference across the membrane, rather than a pressure or concentration gradient or an electrical potential gradient, which drives mass transfer through a membrane.

Membrane distillation was introduced in the late 1960s [1, 2]. However, it was not commercialised at that time for desalination purposes. There were two major factors hindering its development [3]: 1) membranes with adequate characteristics and reasonable cost were not available, and 2) there were some negative opinions obtained long ago about the economics of the process [4]. The opinion was based on typical data from those membranes and systems which are far-from optimal, and showed that the temperature polarization coefficient was roughly estimated by Schofield et al. [5] to be 0.32. Hence, for this system, when the temperature difference between the bulk temperature of hot and cold channels is 10°C, the actual temperature difference across the membrane is only 3.2°C. In the 1980s, with the availability of new membranes, more research focused on membrane distillation and many novel MD modules were designed based on improved understanding of the mass and heat transfer principles of MD [6-8]. Furthermore, new applications for membrane distillation [9, 10] were considered in environmental protection and wastewater treatment.

The membrane distillation process was defined in the “Round Table” at the “Workshop on Membrane Distillation” in Rome on May 5, 1986. According to the Terminology for Membrane Distillation [11], the MD process should have the following characteristics:

- the membrane should be porous,
- the membrane should not be wetted by process liquids,
- no capillary condensation should take place inside the pores of the membranes,
- only vapour should be transported through the pores of the membrane,
- the membrane must not alter the vapour equilibrium of the different components in the process liquids,
- at least one side of the membrane should be in direct contact with the process

liquid, and

- for each component, the driving force of the membrane operation is a partial pressure gradient in the vapour phase.

Therefore, in MD systems, the micro-porous hydrophobic membranes only allow water in the vapour state, but not in the liquid state, to pass through, and the driving force is the effective vapour pressure difference produced by temperature difference and/or reduced pressure across the membrane. Since its driving force is thermal, membrane distillation is not very sensitive to the feed concentration. In comparison with other pressure/potential-driven membrane separation processes and technologies for desalination, MD has some distinctive advantages, such as a theoretically complete rejection of non-volatile components, low operating pressure, large membrane pore size, reduced vapour space compared to conventional distillation (Multi-Stage Flash Distillation), and low operating temperature (40-80°C) of the feed [10]. Thus, theoretically MD is not nearly as sensitive to feed concentration as that of RO, has relative smaller footprint than Multi-Stage Flash Distillation (MSF), and is able to utilise low-grade heat energy.

According to the characteristics of membrane distillation, many technologies have been developed. Because of its capability of utilising low grade heat, membrane distillation has been coupled with solar energy systems [12] to develop zero liquid discharge desalination systems. Membrane distillation can also be used to provide potable water in remote areas with low infrastructure and without connection to a grid [9, 13], due to its simple structure and low maintenance requirement.

The cost of desalination or separation processes varies from location to location as the conditions of the processed water and the nature and the size of the plant are different. Many leading cost components of MD are not yet known because the process has not been applied in commercial size to have the cost benefits of mass production; neither are factors such as permeate flux, pretreatment, fouling and membrane life known adequately yet. In an economic evaluation to assess the feasibility of direct contact membrane distillation (DCMD), the estimated cost for DCMD with heat recovery was \$1.17-4.04 m⁻³ [3, 9, 14, 15], which was comparable to the cost of water produced by conventional thermal processes: i.e. around \$1.00 m⁻³ for multiple effect distillation (MED) and \$1.40 m⁻³ for MSF. As a term of comparison, Memstill® research group

claimed to be able to obtain very competitive water cost ($\text{€}26 \text{ m}^{-3}$) when they operated MD using cheap industrial waste steam [16, 17]. The cost estimated by [18] based on a fully developed MD technology was $\$0.782 \text{ m}^{-3}$ with a purified water production rate of $3,800 \text{ m}^3/\text{day}$ and heat recovery of 30%. In recent years, some pilot plants have been established or designed. One of the layouts to be implemented in Almeria (Spain) using solar energy involves the concept of multi-step MD [9], which will minimise the cost of specific energy and membrane area required.

A $2 \text{ m}^3/\text{day}$ pilot plant using MEMSTILL® was tested at Senoko Refuse Incineration Plant from February 2006 to June 2007, from which the principle of MEMSTILL® and sustainable operation of the M26 type MEMSTILL® module were demonstrated on a pilot scale [16, 19]. The scaling-up of 3 m^2 (membrane area) bench scale to 600 m^2 proved that the integrity of membrane modules and no severe leakage was observed. The distillate quality was very high throughout the pilot plant study period. Future study will address some issues discovered during this pilot study regarding pre-treatment, heat recovery, etc. The MEMSTILL® Singapore pilot also pointed out certain areas for improvement to meet commercialization requirements.

According to previous research [20], there are two major criteria hindering the application of membrane distillation: one is the kind of membrane suitable for membrane distillation and the other is energy efficiency improvement by controlling the process parameters or membrane properties. Accordingly, this study has been divided into four stages:

1. selection of a suitable membrane for membrane distillation based on the criteria, such as materials used for the active layers, active layer properties and support layers,
2. study of hollow fibre membranes in a tubular module, and analysis of the effect of the membrane asymmetric structure on the membrane performance,
3. experimentally investigating the relationship between pressure applied on the membrane surface and membrane performance, and
4. mathematical modelling including two parts:
 - experimentally researching on relationship between membrane geometric size and the MD flux, and programming a simple model to predict flux at different temperatures and with different membrane lengths, and

- theoretically modelling the influences of process parameters (flowrate, temperature, etc.), membrane properties (porosity, membrane thickness, etc.) and membrane geometric size on the membrane flux and temperature polarisation, and researching the influences of process parameters (flowrate, temperature, etc.), membrane properties (porosity, membrane thickness) and membrane geometric size on energy efficiency of DCMD.

Through the four stages of study, it is concluded to optimise the membrane and the process parameters to improve both the energy efficiency and the flux, so as to increase the commercial applicability of DCMD.

Chapter 2 Literature review

2.1 Configurations of membrane distillation

Membrane distillation is a thermally driven process. Mass transfer in gas phase is driven by a vapour pressure difference, arising from a temperature difference or reduced pressure, across the membrane, and from the feed side to the permeate side.

Fig. 2.1 illustrates four configurations of the MD system, which differ based on the nature of the cold side processing of the permeate [3, 11]:

- Direct Contact Membrane Distillation (DCMD), in which the membrane is only in direct contact with liquid phases. This is the simplest configuration capable of producing considerable flux. It is best suited for applications such as desalination and concentration of aqueous solutions (e.g., juice concentrates) [21-26].
- Air Gap Membrane Distillation (AGMD), in which an air gap is interposed between the membrane and a condensation surface. The configuration has the highest energy efficiency, but the flux obtained is in general low. The air gap configuration can be widely employed for most membrane distillation applications [27].
- Vacuum Membrane Distillation (VMD), in which the permeate side is vapour or air under reduced pressure, and if needed, permeate is condensed in a separate device. This configuration is useful when volatiles are being removed from an aqueous solution. [28, 29].
- Sweep Gas Membrane Distillation (SGMD), in which stripping gas is used as a carrier for the produced vapour. It is used when volatiles are removed from an aqueous solution [30-34].

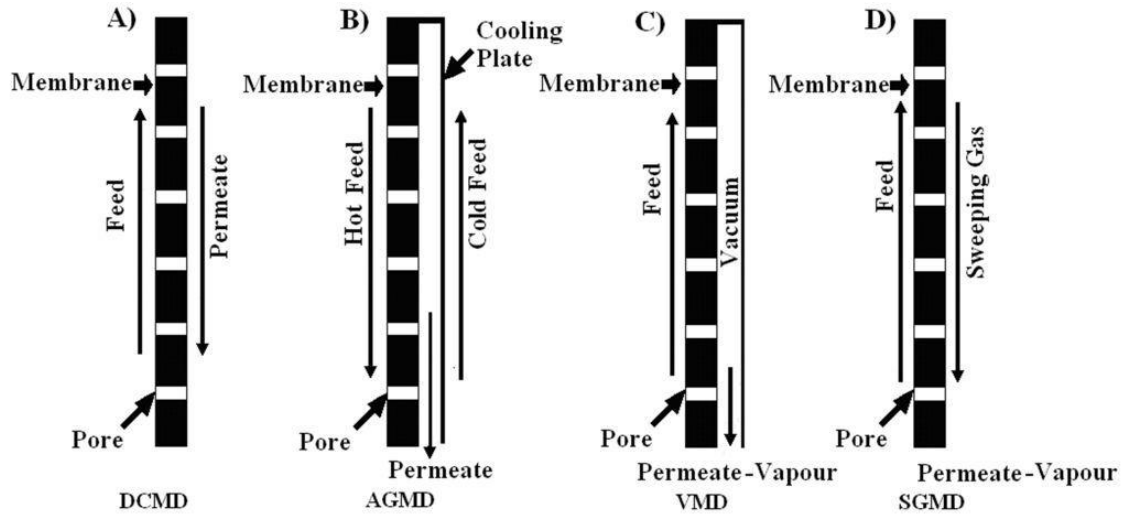


Fig. 2.1 Membrane distillation configurations

Due to its simple structure and high flux relative to AGMD and SGMD, laboratory-scale DCMD has been widely studied [35]. The main disadvantage for DCMD in commercial applications is its low energy efficiency. Although the polymeric membrane generally has low thermal conductivity, the driving force (temperature difference between the feed and permeate sides) for mass transfer will also lead to a great conductive heat transfer through the membrane due to the small membrane thickness, so only part of the supplied heat energy is used for production. Of the four configurations, DCMD has the highest heat conduction loss, which results in relatively low thermal efficiency (defined as the fraction of heat energy used for evaporation) [36, 37].

In AGMD, the air gap is usually the controlling factor for the mass and heat transfers [38] because of its greater thermal and mass transfer resistances. In comparison with the thickness (40-250 μm) and conductivity of the membrane, the air gap is much thicker (general 2,000-10,000 μm) [39, 40] and has lower thermal conductivity. Therefore, more heat energy in AGMD will be used for water evaporation than that of DCMD. Additionally, if a low temperature feed is used as the cooling stream in this configuration, the latent heat can be recovered through the condensation of the vapour on the cooling plate. However, the AGMD has a typical low flux with the same temperature difference between the feed and permeate streams as that of DCMD, due to the high mass transfer resistance across the air gap [3, 27, 40].

In SGMD, the vapour is stripped from the hot feed by a gas stream, and then condensed in an external condenser. It has higher mass transfer rates than AGMD, due to the

greater driving force originating from the reduced vapour pressure on the permeate side of the membrane, and has less heat loss through the membrane. However, an external condenser and an air blower or compressed air are needed to maintain the running of this configuration, which will cause an increase in investment [32] and running costs.

In VMD, the vapour permeate is removed continuously from the vacuum chamber to form a vapour pressure difference across the membrane. Theoretically, this configuration can provide the greatest driving force at the same feed temperature, because the vapour pressure at the cold side can be reduced to almost zero. An external condenser is required as for AGMD, if the liquid permeate is the product.

Of the four configurations, DCMD is the most popular for MD laboratory research, with more than half of the published references for membrane distillation based on DCMD [3, 22, 35, 41]. However, AGMD is more popular in commercial applications, because of its high energy efficiency and capability for latent heat recovery [16, 19].

2.2 Characteristics of membrane

In membrane distillation, membranes on the basis of their selective properties are not involved in the mass transport phenomena, but are involved in heat transport from the hot side to the cold side. Therefore, compounds transferred across the membrane in gas phase are driven by vapour pressure differences based on vapour-liquid equilibrium, and the microporous polymeric or inorganic membrane employed between the permeate and feed sides acts as a physical barrier providing the interfaces where heat and mass are simultaneously exchanged. Thus, the properties of membranes suitable for membrane distillation should include [11, 42-46]:

- an adequate thickness, based on a compromise between increased membrane permeability (tend to increase flux) and decreased thermal resistance (tend to reduce heat efficiency or interface temperature difference) as the membrane becomes thinner,
- reasonably large pore size and narrow distribution of pore size, limited by the minimum Liquid Entry Pressure (LEP) required of the membrane. In membrane distillations, the hydrostatic pressure must be lower than LEP to avoid membrane wetting. This can be quantified by the Laplace (Cantor) equation [3]

$$LEP = \frac{-2B\gamma_l}{r_{max}} \cos\theta < P_{process} - P_{pore} \quad (2.1)$$

where B is a geometric factor, γ_l is the surface tension of the solution, θ is the contact angle between the solution and the membrane surface which depends on the hydrophobicity of the membrane, r_{max} is the largest pore size, $P_{process}$ is the liquid pressure on either side of the membrane, and P_{pore} is the air pressure in the membrane pore.

- low surface energy, equivalent to high hydrophobicity. Based on Eq. (2.1), material with higher hydrophobicity can be made into membranes with larger pore sizes, or membranes made from more hydrophobic material will be applicable under higher pressures for a given pore size,
- low thermal conductivity. High thermal conductivities increases sensible heat transfer and reduce vapour flux due to lowered interface temperature difference, and
- high porosity. High porosity increases both the thermal resistance and the permeability of MD membranes, so both the heat efficiency and flux are increased. However, high porosity membranes have low mechanical strength and tend to crack or compress under pressure, which results in the loss of membrane performance.

The most common materials used for MD membranes are polytetrafluoroethylene (PTFE), polypropylene (PP) and polyvinylidene fluoride (PVDF) [47]. The porosity of the membranes used is in the range of 0.06 to 0.95, the pore size is in the range of 0.2 to 1.0 μm , and the thickness is in the range of 0.04 to 0.25 mm [3, 48]. The surface energies and thermal conductivities of these materials are listed in Table 2.1.

Of these materials, PTFE has the best hydrophobicity (largest contact angle with water), good chemical and thermal stability and oxidation resistance, but it has the highest conductivity which will cause greater heat loss through PTFE membranes; PVDF has good hydrophobicity, thermal resistance and mechanical strength and can be easily prepared into membranes with versatile pore structures by different methods; PP also exhibits good thermal and chemical resistance [41]. Recently, new membrane materials, such as carbon nanotubes [49] and fluorinated copolymer materials [50], have been developed to make MD membranes with good mechanical strength and high

hydrophobicity and porosity.

Table 2.1 Reported surface energy and thermal conductivity of materials used in MD [41, 51]

Membrane Material	Surface Energy ($\times 10^{-3}$ N/m)	Thermal Conductivity ($\text{W}\cdot\text{m}^{-1}\text{K}^{-1}$)
PTFE	9.1	~0.25
PP	30.0	~0.17
PVDF	30.3	~0.19

Sintering, stretching, and phase inversion are some of the methods to fabricate MD membranes from these materials [51-53].

The sintering method can be used to prepare PTFE membranes [54, 55]. In the sintering process, polymeric powder is pressed into a film or plate and sintered just below the melting point. The porosity of the membranes made in this manner is in the range of 10–40% and typical pore sizes are in the range of 0.2 to 20 μm .

Stretching technology can be used to make PP and PTFE membranes. In this process, films are formed by extrusion from a polymeric powder at temperatures close to the melting point coupled with a rapid draw-down. The membranes made have pore sizes in the range of 0.2–20 μm and porosity of about 90% [41, 48, 56].

Phase inversion can be used to produce PVDF membranes. In this process, the polymer is dissolved in an appropriate solvent [57] and spread as a 20–200 μm thick film on proper supports, such as nonwoven polyester, PP backing material or PP scrim backing [48, 58], and an appropriate precipitant (typically water) is added to split the homogeneous solution film into two phases (a solid polymer rich phase and a liquid rich phase). The prepared membrane has a pore size in the range of 0.2 to 20 μm , and porosity of approximately 80% [59].

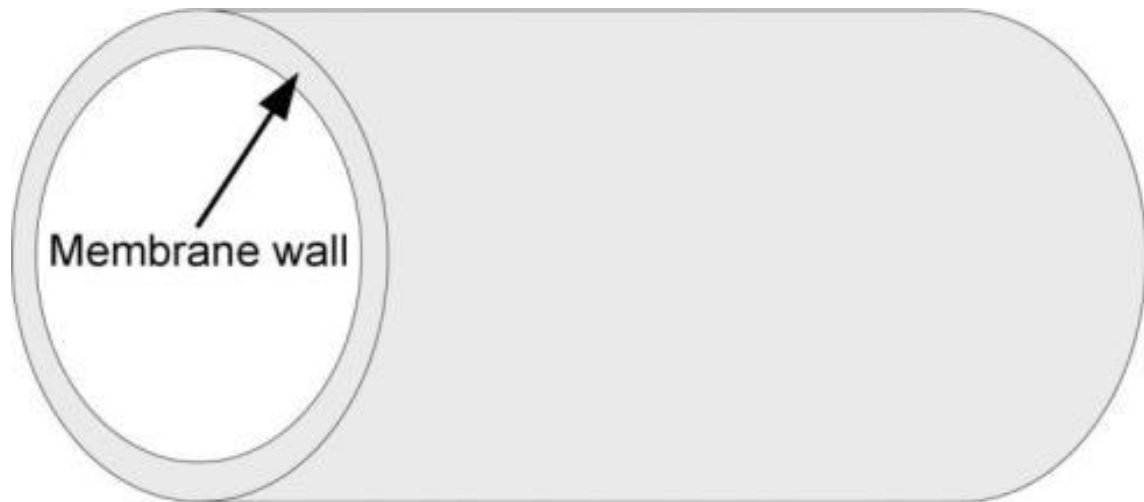
Compared to other membrane separation processes such as pervaporation, reverse osmosis, and gas separation, only a few authors have considered the possibility of designing and manufacturing new membranes for MD processes [43, 60]. Identification of suitable membranes is an important research step for commercial application of membrane distillation.

2.3 Configurations of MD membranes

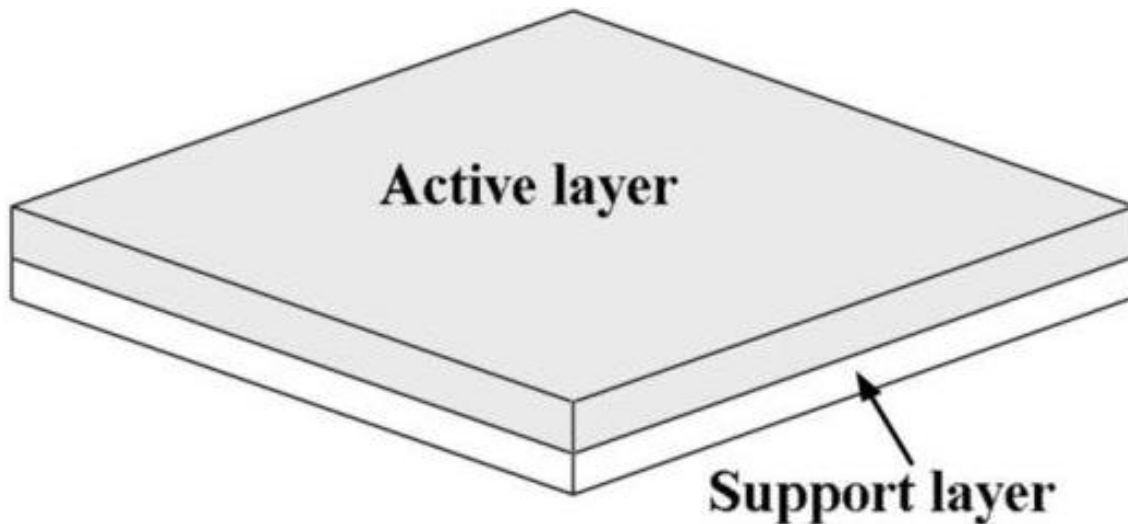
There are two common types of membrane configurations shown in Fig. 2.2:

- hollow fibre membrane mainly prepared from PP, PVDF, and PVDF-PTFE composite material [59, 61], and
- flat sheet membrane mainly prepared from PP, PTFE, and PVDF.

Compared with flat sheet membranes, hollow fibre membranes have relatively large specific surface areas [62], but the main impediment of the hollow fibre module was its typically low flux (generally $1-4 \text{ L}\cdot\text{m}^{-2}\cdot\text{h}^{-1}$ at $40-60^\circ\text{C}$) [63-65]. However, high-flux hollow fibre membranes with different features suitable for membrane distillation have been developed recently, such as dual-layer hydrophilic-hydrophobic fibres with a very thin effective hydrophobic PVDF layer ($50 \mu\text{m}$), and hollow fibre membranes with a sponge-like structure and thin walls [59, 63, 66, 67], which have flux of about $50-70 \text{ kgm}^{-2}\cdot\text{h}^{-1}$ at about $80-90^\circ\text{C}$. This flux is as high as that from flat sheet membrane.



a. Hollow fibre membrane



b. Flat sheet membrane

Fig. 2.2 Schematics of hollow fibre and flat sheet membranes

The reported flux from flat sheet membranes is typically $20\text{-}30 \text{ Lm}^{-2}\text{h}^{-1}$ [3] at inlet temperatures of hot 60°C and cold 20°C . In general, the polymeric membrane shown in Fig. 2.2b is composed of a thin active layer and a porous support layer. This structure is able to provide enough mechanic strength for the membrane, so it enables the active layer to be manufactured as thin as possible, which reduces the mass transfer resistance.

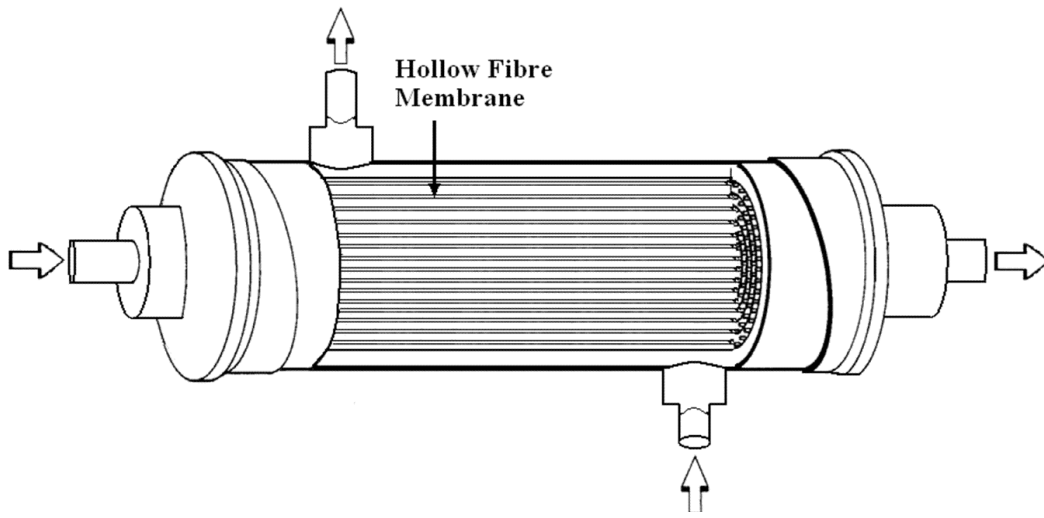
As the flux from membrane distillation is related to the membrane size (in the flow direction), it is more appropriate to compare membrane performance with the mass transfer coefficient rather than the flux from different research works. However, it is difficult to calculate the mass transfer coefficients from the different works, because of the insufficient provision of data. Therefore, the flux provided here is only used as an approximate indication of performance.

2.4 Configurations of MD modules

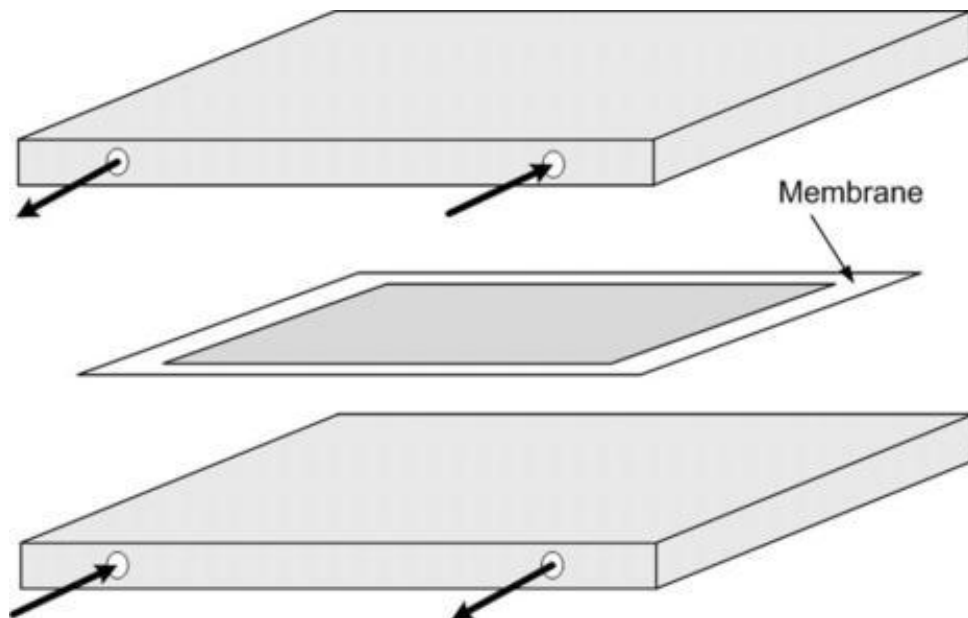
There are three major MD module configurations [35], which are the spiral wound (flat sheet), hollow fibre and the plate & frame modules. All of these modules have been used in pilot plant trials [19, 68, 69].

Fig. 2.3a shows a schematic diagram of a hollow fibre tubular module, in which hollow fibre membranes were glued together and encased in the housing. This configuration

can have a very high packing density ($3,000 \text{ m}^2/\text{m}^3$) [41, 70]. The feed is introduced into the shell side or into lumen side of the hollow fibres, and cooling fluid, sweeping gas, or negative pressure can be applied on the other side to form VMD, SGMD, or DCMD. Because of its large active area combined with a small footprint, hollow fibre tubular module has great potential in commercial applications [41]. Although broken hollow fibres can not be replaced, it can be detected by the liquid decay test (LDT) [71, 72] and pinned afterward.



a. Tubular module for hollow fibre



b. Plate & frame module for flat sheet membrane

Fig. 2.3 MD Modules

Fig. 2.3b shows the structure of the plate & frame module. This module is suitable for flat sheet membranes and can be used for DCMD, AGMD, VMD, and SGMD. In this configuration, the packing density is about 100–400 m²/m³ [41, 69]. Although this configuration has a relatively smaller effective area for the same volume when compared to the tubular modules, it is easy to construct and multiple layers of flat sheet MD membranes can be used to increase the effective area. As shown in Fig. 2.3b, it is easy to change damaged membranes from this configuration. Thus, this module is widely employed in laboratory experiments for testing the influence of membrane properties and process parameters on the flux or energy efficiency of membrane distillation [41].

2.5 DCMD process diagram

Fig. 2.4 is a schematic of DCMD process capable of utilising low grade or waste heat. There are two streams circulating. On the hot side, the feed stream is pumped through a heat exchanger which is able to utilise waste heat or low grade heat to heat the feed to a set temperature. The feed flows into the module where heat and mass exchanges were carried out through the membrane, and then flows back to the feed reservoir. The cold stream is circulated in a similar manner to the feed side. The cold stream is warmed by the heat and mass exchange in the module and is cooled by an air cooled heat exchanger. The primary facilities needed are a heat source and a cooling source for temperature control, and two pumps for flow control. Therefore, the process and maintenance for MD are very simple [11, 60].

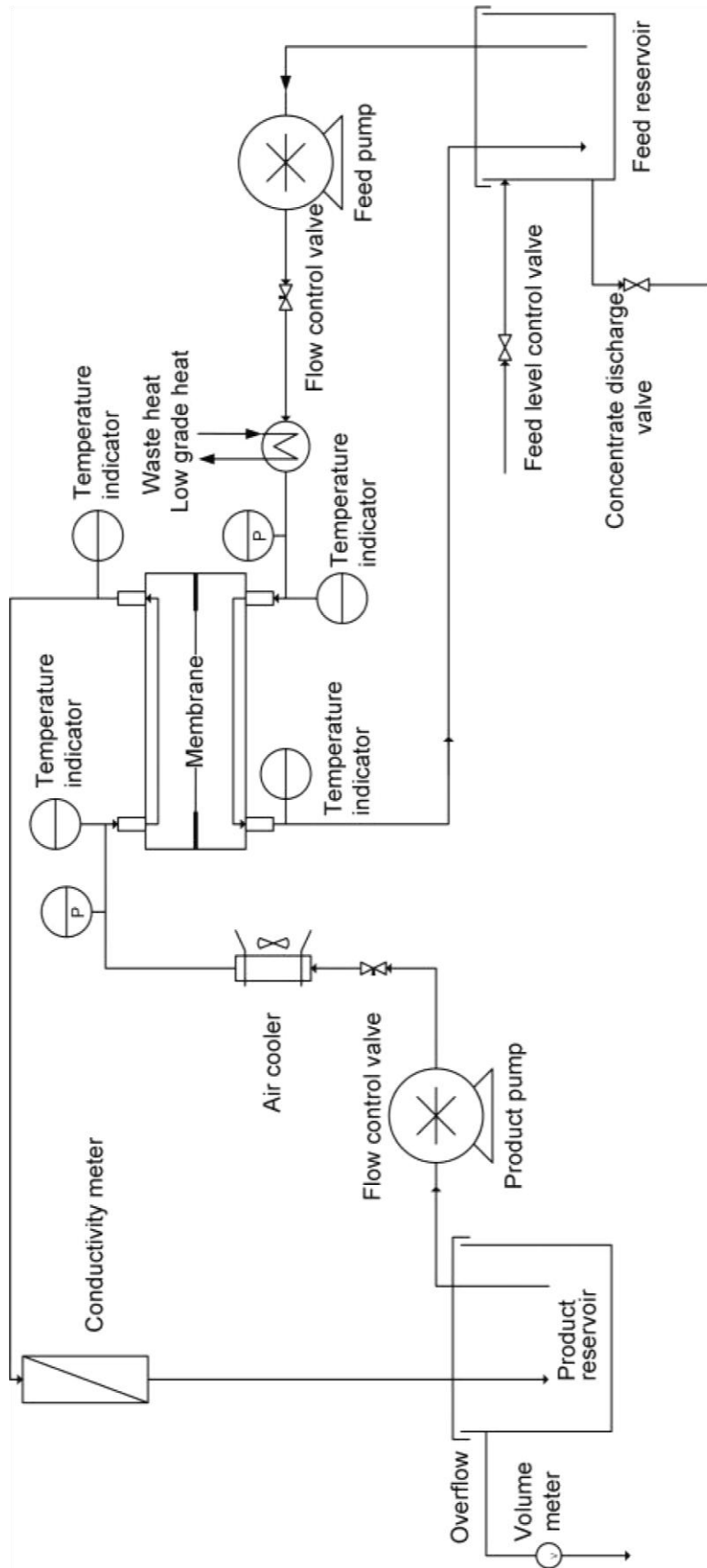


Fig. 2.4 DCMD process schematic

2.6 Heat transfer and mass transfer in DCMD

DCMD processes use a temperature difference as the driving force for mass transfer through the membrane. Thus, heat and mass transfers in MD are coupled together, and are in the same direction from the hot side to the cold side [73]. Fig. 2.5 illustrates these processes in DCMD. The feed temperature, T_f drops across the feed side boundary layer to T_1 at the membrane surface. Some water evaporates and is transported through the membrane. Simultaneously, heat is conducted through the membrane to the cold (permeate) side. The cold flow temperature T_p increases across the permeate boundary layer to T_2 at the membrane surface on the cold side as water vapour condenses into the fresh water stream and gains heat from the feed side. The driving force is therefore, the vapour pressure difference between T_1 and T_2 , which is less than the vapour pressure difference between T_f and T_p . This phenomenon is called temperature polarisation. The temperature polarization coefficient is defined by [5]

$$\tau = \frac{T_1 - T_2}{T_f - T_p} \quad (2.2)$$

2.6.1 Heat transfer

Heat transfer through the feed side to the permeate side includes two steps [35]: first, heat transfers from the hot side to the cold side across the membrane in the forms of sensible heat and latent heat, so as to form the temperature difference between boundary layer and bulk flow; second, the heat transfers from the bulk flow of the feed to the boundary layer via heat convection, due to the temperature difference arising from the first step. In the first step, as shown in Fig. 2.5, the sensible heat is conducted through the membrane to the cold side, and the latent heat is carried by the water vapour which is evaporated from the interface between the hot stream and membrane pores and condensed at the interface between the pores and cold stream [23]. The feed temperature (T_f) drops across the boundary layer on the feed side to T_1 . The permeate temperature T_p increases across the permeate boundary layer to T_2 . The vapour pressure difference across the membrane depends on the temperature T_1 and T_2 , and the driving force is therefore $P_{T1} - P_{T2}$ where P_{T1} and P_{T2} are the vapour pressures at T_1 and T_2 , respectively. The feed concentration C_f increases across the feed boundary layer to C_1 [73, 74].

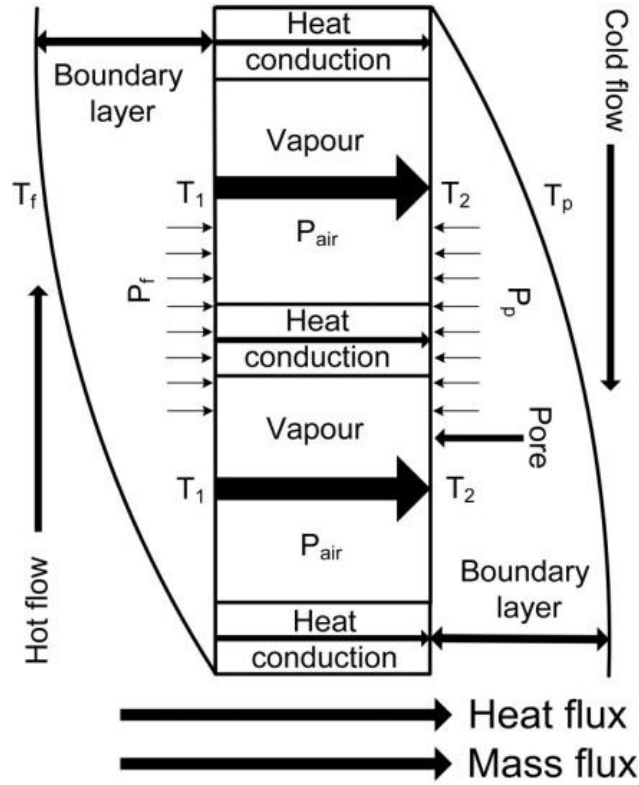


Fig. 2.5 Heat transfer and mass transfer through membrane

According to the two heat transfer processes, the heat balance of the feed stream can be described by [73, 75, 76].

$$Q_1 = \frac{\lambda}{b}A(T_1 - T_2) + JH_{latent} \quad (2.3)$$

$$\lambda = \lambda_{air}\varepsilon + \lambda_{solid}(1 - \varepsilon) \quad (2.4)$$

$$Q_2 = \alpha(T_f - T_1) \quad (2.5)$$

because $Q_1 = Q_2$,

$$Q = \alpha_f(T_f - T_1) = \frac{\lambda}{b}(T_1 - T_2) + JH_{latent} = \alpha_p(T_2 - T_p) = JH_{latent} + U(T_f - T_p) \quad (2.6)$$

where Q_1 or Q_2 are the total heat transferred from the hot side to the cold side, λ is the thermal conductivity of the membrane, b is the membrane thickness, ε is the membrane porosity, A is the membrane area, α_f is the convective heat transfer coefficient on the hot side, J is the permeate flux, and H_{latent} is the latent heat of vaporization. In Eq. (2.6), $(\lambda/b)A(T_1 - T_2)$ is the sensible heat loss through the membrane and JH_{latent} is the heat of evaporation. In the operation of membrane distillation, it is desirable to minimise the sensible heat loss or maximise the heat for evaporation. To minimize the sensible heat

loss, the heat transfer coefficient (λ/b) of the membrane needs to be reduced by lowering λ or increasing the membrane thickness. Since increasing the thickness of the membrane will also increase the mass transfer resistance, reducing the membrane thermal conductivity by making the membrane more porous (shown in Eq. (2.4)) is an effective method, since the thermal conductivity of the air is in general one order of magnitude less than that of the membrane material. Also, the more porous the membrane is, the lower the resistance of the membrane to the transport of the vapour across the membrane. In practice, the membrane thickness is limited by its mechanical strength. To maximise flux, it is necessary to increase the temperature difference between the hot and cold sides or to increase the temperature polarisation coefficient [77, 78]. Therefore, it is necessary to improve the convective heat transfer coefficient for purpose of producing more flux based on Eqs. (2.3), (2.5) and (2.6). The convective heat transfer coefficient can be expressed as [79],

$$\alpha_f = -\frac{\lambda_f}{T_f - T_1} \left(\frac{dT}{dy} \right)_{boundary} \quad (2.7)$$

where λ_f is thermal conductivity of the feed, and $\left(\frac{dT}{dy} \right)_{boundary}$ is the temperature gradient in the thermal boundary layer of the feed. From Eq. (2.7), it can be found that the convective heat transfer coefficient can be improved effectively by reducing the thickness of the thermal boundary layer.

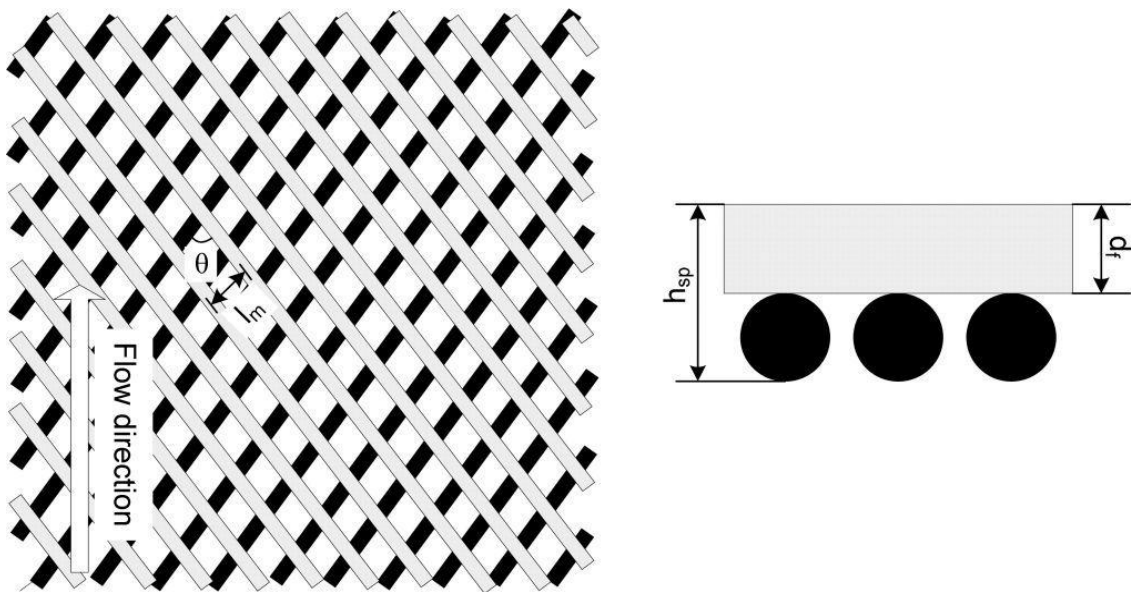


Fig. 2.6 Spacer structure

The presence of turbulence promoters, e.g. net-like spacers or zigzag spacers shown in Fig. 2.6 can effectively reduce the thickness of the thermal boundary layer and improve α_f [80-82], and it is also important that high heat transfer rates are achieved with a low pressure drop in the channels where the feed solution and cooling liquid are flowing [36, 77, 78, 80, 83]. From reported data [77], the temperature polarisation coefficient of spacer filled channels falls in the range of 0.9–0.97, in comparison with a temperature polarisation coefficient 0.57–0.76 in the flowing channel without spacer. Reynolds number for the spacer filled flat channel is expressed by [77, 80, 84]

$$Re = \frac{\rho v d_h}{\mu} \quad (2.8)$$

where v is the velocity in the spacer filled channel, ρ is the density of the liquid steam, d_h is the hydraulic diameter of the spacer filled channel, and μ is the liquid viscosity. The velocity v can be calculated by [80]

$$v = \frac{Q_{f/p}}{A_{cross} \varepsilon_{spacer}} \quad (2.9)$$

where $Q_{f/p}$ is the volumetric flow rate of feed/permeate, ε_{spacer} is the porosity of the spacer, and A_{cross} is the cross sectional area of empty channel. The hydraulic diameter d_h can be calculated by [81]

$$d_h = \frac{4 \varepsilon_{spacer}}{\left(\frac{2}{h_{sp}}\right) + (1 - \varepsilon_{spacer}) S_{spacer}} \quad (2.10)$$

where h_{sp} is the spacer thickness, and S_{spacer} is the specific surface of the spacer expressed by

$$S_{spacer} = \frac{4}{d_f} \quad (2.11)$$

where d_f is diameter of spacer filaments. The spacer porosity can be measured experimentally or calculated by

$$\varepsilon_{spacer} = 1 - \frac{\pi d_f^2}{2 l_m h_{sp} \sin \theta} \quad (2.12)$$

where l_m is mesh size.

Therefore, to increase the energy efficiency, it is important to use a membrane with high porosity, and provide enough turbulence to the feed stream.

2.6.2 Mass transfer

Mass transfer in the MD process includes three steps: firstly the hot feed vaporizes from the liquid/gas interface, secondly the vapour is driven by the vapour pressure difference and diffuses from the hot interface to the cold interface through the pores, and thirdly the vapour condenses into the cold side stream [48]. Therefore, there are two major factors controlling the mass transfer: one is the vapour pressure difference, and the other is the permeability of the membrane.

The influence of the membrane physical properties on membrane distillation includes:

- 1) the effective area for mass transfer is less than the total membrane area because the membrane is not 100% porous,
- 2) for most practical membranes, the membrane pores do not go straight through the membrane and the path for vapour transport is greater than the thickness of the membrane, and
- 3) the inside walls of the pores increase the resistance to diffusion by decreasing the momentum of the vapour molecules.

If the fluid dynamics conditions on both sides of the membrane could be considered good, mass transfer through the membrane may be the limiting step for mass transfer in MD [85].

The mass transport mechanism in the membrane pores is governed by three basic mechanisms known as Knudsen-diffusion (K), Poiseuille-flow (P) and Molecular-diffusion (M) or a combination between these known as the transition mechanism [35, 86]. The Knudsen number (Kn) is used to indicate the dominant mass transfer mechanism in the pores.

$$Kn=l/d \tag{2.13}$$

where d is the mean pore size of the membrane and l is the mean free path of the molecules defined by [87, 88]

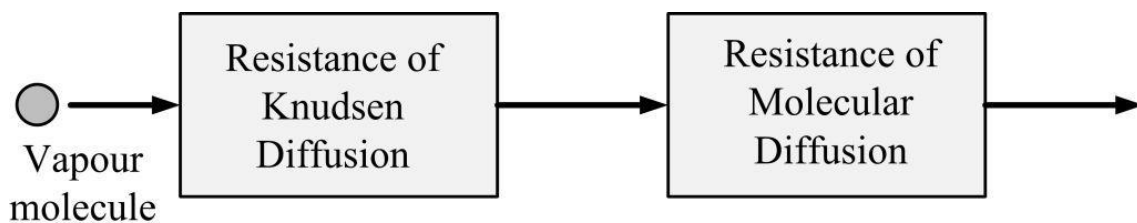
$$l = \frac{k_B T}{\pi((\sigma_w + \sigma_a)/2)^2 P_{pore}} \frac{1}{\sqrt{1+(m_w/m_a)}} \tag{2.14}$$

where k_B is the Boltzman constant ($1.381 \times 10^{-23} \text{ JK}^{-1}$), σ_w and σ_a the collision diameters for water vapour ($2.641 \times 10^{-10} \text{ m}$) and air ($3.711 \times 10^{-10} \text{ m}$) [89], T is the mean temperature in the pores, and m_w and m_a are the molecular weights of water and air. At a typical membrane temperature of 60°C , the mean free path of the water vapour in the membrane pores is $0.11 \text{ }\mu\text{m}$. Table 2.2 shows the dominating mass transfer mechanism based on the Kn in a gas mixture system without a total pressure difference [85]. Because the pore sizes of the membranes used for membrane distillation are in the range of 0.2 to $1.0 \text{ }\mu\text{m}$, Kn will be in the range of 0.5 to 0.1 . Thus, the dominant mass transfer mechanism is Knudsen-molecular diffusion transition mechanism in DCMD. Although the pore size distribution of the polymeric membrane will affect the mass transfer mechanism, the majority of the membrane area will be governed by the transition region as verified by Phattaranawik et al. [90], and as there is no total pressure difference existing in the pore, the Poiseuille flow can be ignored [35].

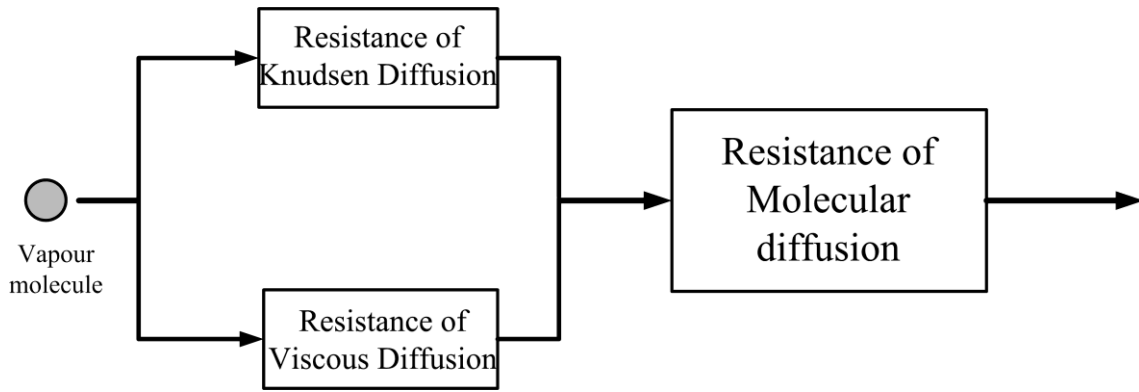
Table 2.2 Mass transfer mechanism in membrane pore

$Kn < 0.01$	$0.01 < Kn < 1$	$Kn > 1$
Molecular diffusion	Knudsen-molecular diffusion transition mechanism	Knudsen mechanism

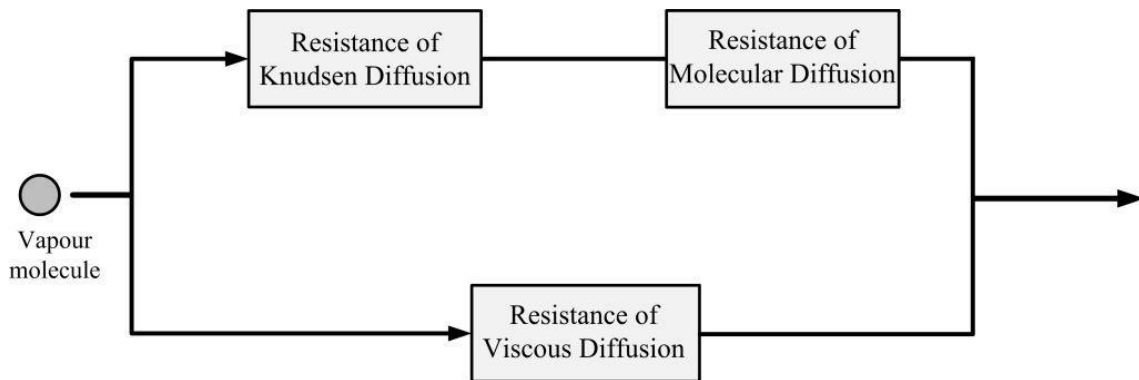
The molecular mass transport mechanisms through a membrane pores are shown as an electrical circuit analogue [3, 90] in Fig. 2.7a. There are also two other popular mass transfer models for membrane distillation, which are Schofield's model [75, 91] shown in Fig. 2.7b and the dusty-gas model shown in Fig. 2.7c for DCMD [92, 93].



a. Electrical circuit analogue for mass transfer mechanism in membrane pore



b. Electrical circuit analogue for Schofield's model



c. Electrical circuit analogue for the dusty-gas model

Fig. 2.7 Electrical circuit analogues for different transport mechanisms

According to the theory of the mass transfer shown in Fig. 2.7a, the mass transfer through the membrane pore can be expressed as [35, 90]

$$\frac{1}{J} = \frac{1}{J_m} + \frac{1}{J_k},$$

with

$$J_k = \frac{4}{3} d \frac{\varepsilon}{bt} \sqrt{\frac{M}{2\pi RT}} (P_{T1} - P_{T2}), \text{ and}$$

$$J_m = \frac{M}{1-x_A} \frac{\varepsilon D_{AB}}{btRT} (P_{T1} - P_{T2}) \quad (2.15)$$

where J_m and J_k are the vapour flux through the membrane arising from molecular and Knudsen diffusion, b is membrane thickness, t is the pore tortuosity, R ($=8314 \text{ Pa}\cdot\text{m}^3\cdot\text{mol}^{-1}\cdot\text{K}^{-1}$) is the universal gas constant, M is the molecular mass of the vapour, and P_{T1} and P_{T2} are the vapour pressures at temperature T_1 and T_2 , which can be

calculated by the Antoine equation [94]. According to [35, 82, 95], the diffusivity of water vapour (A) relative to air (B) D_{AB} (m²/s) in the temperature range of 273-373 K can be estimated from,

$$D_{AB} = \frac{1.895 \times 10^{-5} T^{2.072}}{P} \quad (2.16)$$

The Schofield's model shown in Fig. 2.7b is developed from kinetic theory and assuming that the sum of Knudsen permeability and viscous permeability equals the total permeability, in which the transition region between the Knudsen and viscous flows is described,

$$N = -M\bar{v}\left(A + B \frac{\sqrt{2}\sigma P_{pore}}{k_B T}\right) \frac{(P_{T1} - P_{T2})}{b}, \text{ in which}$$

$$A = \frac{d\varepsilon}{3tRT}, \text{ and } B = \frac{\pi r^2 \varepsilon}{128RT} \quad (2.17)$$

where \bar{v} the gas' mean molecular speed, and σ the collision cross-section.

In the ‘‘Dusty-Gas’’ model [92, 96], the porous membrane is assumed as an array of dust particles held stationary in space, and the dust particles in terms of the classical kinetic theory of gases are supposed to be giant molecules in the interactions between gas and surface. Based on this model, a general flux equation for a gas that permeates through a porous media in the Knudsen–viscous transition region can be described as:

$$J = -\frac{M}{RT} \left[K_0 \bar{v} + \frac{B_0 P_{pore}}{\mu} \right] \frac{(P_{T1} - P_{T2})}{b}, \text{ in which}$$

$$K_0 = \frac{d\varepsilon}{3t}, \text{ and } B_0 = \frac{\varepsilon d^2}{32t} \quad (2.18)$$

These equations of different mass transfer models can all be simplified as [48]

$$J = C_{membrane} (P_{T1} - P_{T2}), \text{ in which}$$

$$C_{membrane} \propto \frac{d^a \varepsilon}{tb} \quad (2.19)$$

where a is an exponent coefficient in range of 1-2. $C_{membrane}$ is an important parameter to assess the performance of a membrane as its value depends on the mass transfer characteristics of the membrane. However, it is difficult to accurately measure the temperature at the interface between the vapour phase and liquid phase experimentally.

Therefore, in our study, the performances of different membranes were compared under the same hydrodynamic and thermal conditions and subsequently under the same boundary layer conditions. A global mass transfer coefficient C_{global} , calculated from the bulk temperatures and which includes mass transfer phenomena in the boundary layer, was used to assess MD membranes.

From Eq. (2.19), the flux for MD can be increased by increasing pore sizes and porosity, and reducing the thickness of the membrane. However, from Eq. (2.4), reducing the thickness of the membrane also increases the sensible heat loss from the hot side to the cold side, which leads to a reduction of water flux due to decreased interfacial temperature differences (vapour pressure difference). Therefore, there is an optimum membrane thickness for membrane distillation efficiency.

In reviewed literature, there were many references to mass transfer relating to transmembrane phenomena. However, modelling focused on scale-up was not identified.

In analysis, it was found that the mass transfer coefficient will not be affected greatly by the temperature and flow rate, and the temperature changes (40-80°C) in MD will have little effect on the boundary layer. Therefore, a simple model can be developed to predict the flux from different feed temperatures and membrane sizes at given flow rates, based on an approximately constant global mass transfer coefficient [48] which is calculated from the bulk hot and cold temperatures at this flow rate and includes both the mass transfer phenomena across the membrane and boundary layer.

Furthermore, from the analysis of the channel and spacer conditions, a more general model can be developed based on the air permeability and thermal conductivity of the membrane, which can be used at different flow rates, temperatures and membrane sizes.

2.7 Application of membrane distillation

Although MD is currently used mostly at the laboratory scale, membrane distillation has potentially distinctive advantages in some particular areas [3, 41]. There are several pilot plants currently undergoing field trials: for treating wastewater from a power plant (in Singapore) [19], and wastewater in a chemical plant (The Netherlands) by Memstill®, and other wastewaters are currently being investigated at laboratory stage,

i.e., the RO concentrate treatment, ground water treatment and solar heat utilisation [97-99].

Producing high-purity water from salty water is one of the main MD applications. Since 1982, Gore [100] proposed MD membrane modules for desalting NaCl aqueous solutions. Papers related to MD research in desalination processes increased dramatically in the following years [4, 31, 69, 101]. Different types of hydrophobic membranes and configurations [102, 103] were studied for desalination purposes. Coupling membrane distillation with solar energy was studied and has demonstrated the feasibility of solar powered MD in which 60-80% of the energy was recovered [104-106]. Membrane distillation may also be integrated with reverse osmosis processes to increase the water recovery in the desalination plants [104, 107] by treating the brine. Lawson and Lloyd (1996) [84] stated that membrane distillation can be a viable process for desalination, while Schneider et al (1988) [85] have argued that small, portable desalination units utilising waste heat are more feasible for the applications of MD.

Membrane distillation also can be used for water treatment, such as removing heavy metal from wastewater [108], recovering HCl from cleaning solution in electroplating [109], concentrating sulphuric acid to recover lanthane compounds in apatite phosphogypsum extraction process [110], eliminating radioisotopes and reducing the waste volume from nuclear industry [111] and removing volatile organic components from dilute aqueous solutions [28, 29, 112, 113].

Due to the low feed temperature, MD can also be used for concentrating solutions in the food industry. It has been widely tested for the concentration of many juices including orange juice [25], apple juice [114] and sugarcane juice [115].

MD was also employed for selective extraction of volatile solutes and solvents for applications in the health and fermentation industries. Blood and plasma were treated by MD in order to promote a solute-free extraction of water from biomedical solutions without loss in quality [116, 117]. Membrane distillation has also been suggested as an innovative tool to ameliorate treatment of uraemia by allowing purification of the blood ultrafiltrate and the re-injection of the purified water to the patients [118]. MD was also combined with a bioreactor to promote the reaction rate of ethanol fermentation by selectively removing ethanol [119].

2.8 Objective

The objective of this study is to research the optimisation and applicability of MD in theoretical and experimental aspects by analysing the characteristics of membrane suitable for DCMD, influences of membrane structure (hollow fibre membrane) and pressure (compressible PTFE membrane) on membrane performance, and modelling the energy efficiency of DCMD with varied process parameters. The specific objectives to address this overall objective were:

1. Characterising the structure and material analysis of membranes suitable for membrane distillation, which is an important stage for commercial application of membrane distillation
2. Investigate how mass transfer is affected by the membrane structure of hollow fibre membranes, due to its significance in membrane structure design
3. Determining the influence of system pressure on flux of compressible membranes, which is rarely considered in the design of large modules, and
4. developing a simple model for scale-up of membrane distillation, and a general model to predict flux and energy efficiency under difference conditions, as this is important for process design and parameter optimisation.

Chapter 3 Identification of membrane characteristics for high performance in membrane desalination

3.1 Introduction

As stated previously, the membranes used in MD must be porous and hydrophobic. It can be a composite porous hydrophobic/hydrophilic bi-layer membrane, a hydrophobic single-layer membrane, or a composite hydrophilic hydrophobic/hydrophilic or hydrophobic/hydrophilic/hydrophobic porous tri-layer membrane [46, 120-122]. Both supported and unsupported membranes can be used in this process [60]. However, the membrane support layer selected should be strong enough to prevent deflection or rupture of the membrane, and not lead to a great increase of mass transfer resistance. Flat sheet commercial membranes made from different materials (PP, PVDF PTFE) primarily for microfiltration have also been used in MD experiments [35, 41, 60, 97]. Despite these works, there is still insufficient studies in the area of membrane design [60]. Hence, it is import to understand the influence of membrane material and physical structures, e.g., pore size, porosity, thickness and support layer, on mass transfer and heat efficiency.

From the above mass transfer and heat transfer equations in **Chapter 2**, membranes that are most suitable for membrane distillation processes should have the following properties [10]:

1. Small thickness and low tortuosity
2. Low thermal conductivity of membrane material, so that heat loss due to sensible heat transfer can be minimized
3. High porosity to lower conductive heat flux and increase the water vapour transport coefficient through the membrane
4. Reasonably large pore size, limited by membrane wetting that will occur when the interfacial pressure difference ΔP is greater than the minimum membrane Liquid Entry Pressure (LEP) [10]

$$\Delta P = P_{process} - P_{pore} \quad (3.1)$$

$$LEP = \frac{-2B\gamma_l}{r_{max}} \cos\theta \quad (3.2)$$

where B is the geometric factor of pore, γ_l is the surface tension of the liquid, r_{max} is maximum pore radius, and θ is the contact angle of the membrane.

5. Low surface energy or high hydrophobicity, so that the membrane is applicable under higher pressure or with larger pore size.

Early membranes had very poor performance when membrane distillation was invented in the late 1960s. Partly for this reason, membrane distillation was not commercially employed at that time [4]. In the 1980s, membranes with improved characteristics became available, and MD research rose again [123]. However, in recent years membranes with even much improved characteristics have become available. Hence, recently available MD membranes were investigated through their physical structures, and performance tests for flux, energy efficiency, and salt rejection under different operational conditions. Using the characteristics identified above, it will be shown how the membrane materials and physical features lead to the observed measures of flux and rejection. In turn guidance to further improve the performance of MD membranes will be provided.

3.2 Experimental method

3.2.1 Membranes and their properties

Table 3.1 lists the six membranes used in the experiments. The three supported by a non-woven fabric layer were microfiltration (MF) membranes, and the other three supported by a scrim were membranes designed for MD. The properties presented in Table 3.1 were provided by the manufacturers.

Table 3.1 Properties of membranes as provided by the manufacturers

Membrane	Material of active layers	Support layer	Nominal pore size (μm)	Provider	Location
$M_{\text{mt}0.45}$	PTFE	Nonwoven fabric	0.45	Membrane Solutions	China
$M_{\text{mt}1.00}$	PTFE	Nonwoven fabric	1.00	Membrane Solutions	China
$M_{\text{p}0.30}$	PVDF	Nonwoven fabric	0.30	GE Osmonics	USA
$M_{\text{gt}0.22}$	PTFE	Scrim	0.22	GE Osmonics	USA
$M_{\text{gt}0.45}$	PTFE	Scrim	0.45	GE Osmonics	USA
$M_{\text{gt}1.00}$	PTFE	Scrim	1.00	GE Osmonics	USA

3.2.1.1 Contact angle measurement

Contact angles of the membrane active layer were measured as an indicator of hydrophobicity. The contact angle of membrane samples were assessed by a contact angle meter (KSV, CAM200, USA) equipped with a video capturing system. Static contact angles were measured by the sessile drop method. An 8 μL drop was formed on the flat surface of the membrane using a syringe, and the contact angle of each membrane was measured for 2-3 times.

3.2.1.2 SEM characterisation

To observe their cross sections, the membranes were frozen in liquid nitrogen and then cut with a blade. Membrane active layer thicknesses were measured by a LEICA SEM (S440 W) via imaging of the cross section of the membrane. The thickness of each membrane was measured three times from different sections of the membrane contained in one image, and an average thickness was reported as the membrane thickness.

3.2.1.3 LEP measurement

LEP was measured by conductivity changes and Fig. 3.2 shows a schematic diagram of the apparatus. A salt solution was forced through the membrane as the pressure on the

salt solution side was gradually increased, and the LEP detected by an increase in conductivity on the permeate side. A Millipore filter holder (sx0002500, diameter=25 mm) was used to secure the membrane, and the holder cavity was filled with 20% NaCl solution. The holder was submerged in 200 mL deionised water in a beaker, and the deionised water was brought into contact with the membrane support layer. Having the membrane in contact with the deionised water and stirring the deionised water with a magnetic stirrer increased the diffusion rate of salt into the bulk water, so that an increase in conductivity could be detected when the LEP was exceeded. A HANNA HI 9032 conductivity meter was used to monitor changes in conductivity of the deionised water, and it was estimated from the sensitivity of this conductivity meter that 0.05 μL of 20% NaCl could be detected in the deionised water. The pressure of the salt solution was increased in increments of 5 kPa, and the pressure was maintained for one minute before the next 5 kPa pressure increase was implemented. The LEP was equal to the pressure at which a conductivity increase in the deionised water was detected.

Because very highly concentrated brine solution was used in the LEP test compared to the feed concentration, it was necessary to convert the measured LEP of 20% NaCl solution to that of 1% NaCl solution. Otherwise, a 10% error was expected. According to [124], the contact angle between the liquid and hydrophobic membrane changes only slightly with concentration variation, and the contact angle can be corrected for variations in salt concentration via changes in surface tension. The water surface tension varies with salt concentration and can be calculated by [125]:

$$\gamma_l = \gamma_0 + \frac{\Delta\gamma}{\Delta C_{solution}} C_{solution} \quad (3.3)$$

where γ_0 is the surface tension of pure water and equals 72.0 mN/m at 25°C, the value of $\Delta\gamma/\Delta C_{solution}$ is $1.46 \pm 0.05 \text{ mNm}^{-1}\text{Lmol}^{-1}$ for NaCl solutions [125], and $C_{solution}$ is the salt concentration. The measured LEP was converted to the LEP of the membrane under experimental condition (1% NaCl solution) via Eq. (3.3).

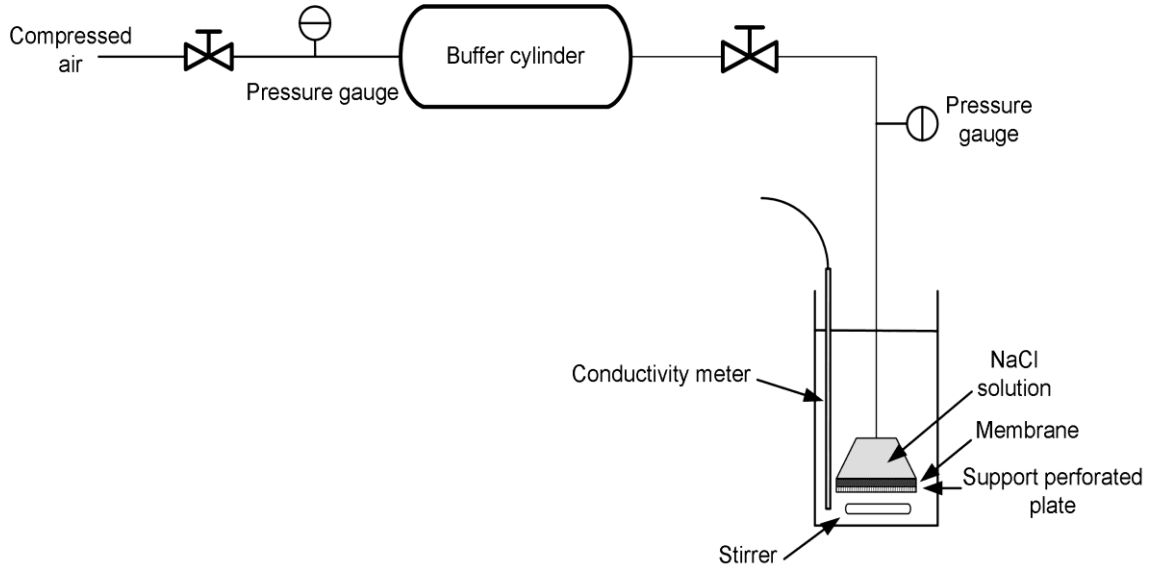


Fig. 3.1 Schematic diagram of LEP test

3.2.1.4 Gas permeability measurement

The porous membrane was characterised by the gas permeation method using compressed nitrogen and varying the pressure in the range of 5-80 kPa. A schematic drawing of the apparatus is shown in Fig. 3.3. The permeation of a single gas driven by a total pressure drop across a porous membrane will be regulated by Knudsen diffusion-Poiseuille flow mechanism [35, 86, 126]. Therefore,

$$J = \left(\frac{8r\varepsilon}{3tb} \sqrt{\frac{1}{2\pi RMT}} + \frac{r^2\varepsilon}{8RTb\eta} P_{pore} \right) \Delta P_{gas} \quad (3.4)$$

where ΔP_{gas} is the pressure difference across the membrane.

By keeping ΔP_{gas} constant, varying P_{pore} , and plotting the curve of $J/\Delta P_{gas}$ vs P_{pore} , the slope k is

$$k = \frac{r^2\varepsilon}{8RTb\eta} \quad (3.5)$$

and the intercept c is

$$c = \frac{8r\varepsilon}{3tb} \sqrt{\frac{1}{2\pi RMT}} \quad (3.6)$$

so

$$r = \frac{16k\eta}{3c} \sqrt{\frac{8RT}{\pi M}} \quad (3.7)$$

and

$$\frac{\varepsilon}{tb} = \frac{8RT\eta k}{r^2} \quad (3.8)$$

Therefore, by measuring the air permeation of the membrane, the mean pore size and ε/bt can be estimated. To avoid membrane deformation under pressure, the pressure difference across the membrane was set at 1.00 ± 0.01 kPa. A digital monometer (645, TPI) was used to measure the pressure and the pressure difference. The time of the soap bubble passing a soap meter (100 mL) was recorded at least four times under the same set of pressures by a stopwatch to estimate the gas flowrate.

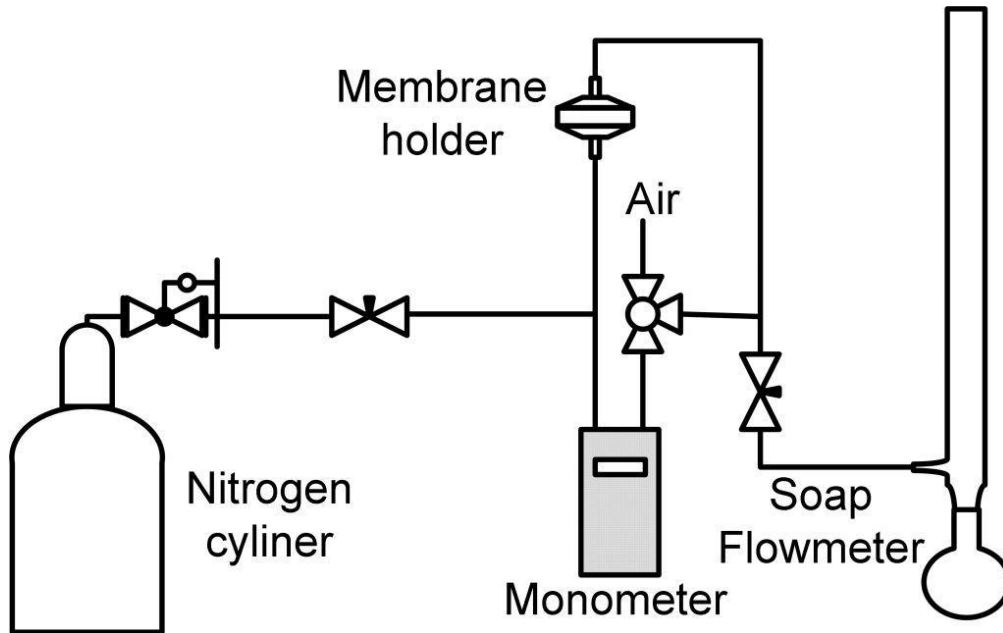


Fig. 3.2 Air permeability testing instrument

3.2.1.5 Porosity measurement

The porosity was determined by a mass difference method. The sizes of the prepared samples were in the range of $30\text{-}38 \times 45\text{-}63$ mm². The weight of each membrane (including active layer and support layer) and the weight of its support layer without the active layer were measured by an A&D balance (HR-200). Therefore, the porosity of the membrane active layer can be calculated by

$$\varepsilon = 1 - \frac{(m_{total} - m_{support})/\rho}{V_{PTFE}} \quad (3.9)$$

where ρ is the material density of the active layer, in which a midpoint in density range of the reported polymer density [127, 128] was used (an error less than 3%); m_{total} and $m_{support}$ are respectively the total mass of the membrane and the mass of the support layer only; V_{PTFE} is the volume of active layer, which was calculated by multiplying the area with the active layer thickness obtained from the SEM images. The porosity of the support layer was calculated similarly. The surface porosity of the active layer can be estimated by [129]

$$\varepsilon_{surface} = \frac{\varepsilon}{t} \quad (3.10)$$

where $\varepsilon_{surface}$ is the surface porosity, and t is the average tortuosity of the pore which can be calculated from value of ε/bt [126] and the measured membrane thickness.

3.2.2 DCMD Testing

Fig. 3.4 shows a schematic diagram of the counter-current DCMD experimental apparatus. A flat-sheet DCMD configuration with an area of 0.014 m² was used to evaluate the performance of the six membranes listed in Table 3.1. The velocities on both sides of the membrane were maintained equal and were controlled by two peristaltic pumps, one for the hot feed and the other for the cold stream. The speed was varied in the range of 0.17-0.36 m/s. The temperature of the feed water was controlled by a heater and was varied in the range of 45-70°C. A chiller was used to cool the cold stream so that it could be recycled and remained at a constant temperature. The cold stream temperature into the DCMD was set at 20°C. The brine feedwater was prepared by dissolving 100 g NaCl into 10 L water (10 g.L⁻¹). Water for the hot feed and the cooling stream were both deionised. The temperature and pressure of the feed and permeate were monitored at their respective inlets and outlets, and a conductivity indicator was used to measure the salt rejection. Spacers provided by GE Osmonics were used on both sides of the membrane to enhance the turbulence of the streams and to provide support to the membrane. The flux was determined by measuring the weight of the product reservoir over time. Our experimental results show that the flux of the new membranes was about 15-20% higher than that of the conditioned membranes under the same operating conditions. After the membrane was used for 5-8 hours, the flux became stable and its absolute variation was in the range of 5-10%. Membranes were conditioned by performing a DCMD test for 3 hours so as to allow any variation in

flux that might occur over short time frames to be removed from the experiments. The variation in flux between membranes was only 5% when this was done. All data were obtained from these conditioned membranes with stable flux, and the reported flux is the mean value measured every hour over a 4-6 h period. All the results presented for each type were measured from the same membrane piece, and the error in the flux was $\pm 5-10\%$. Error bars are not shown later in Figs. 3.9-3.15 for clarity.

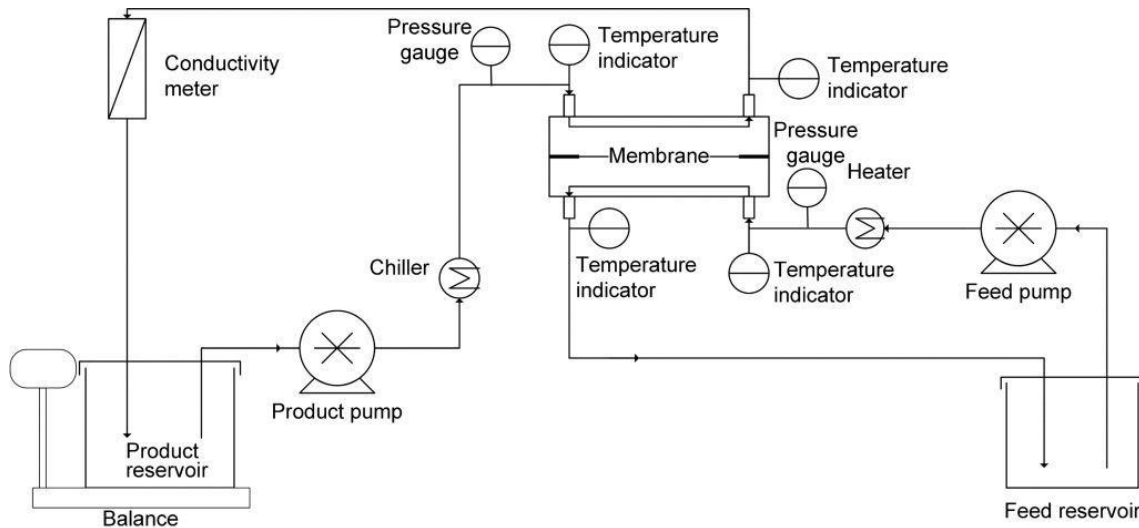
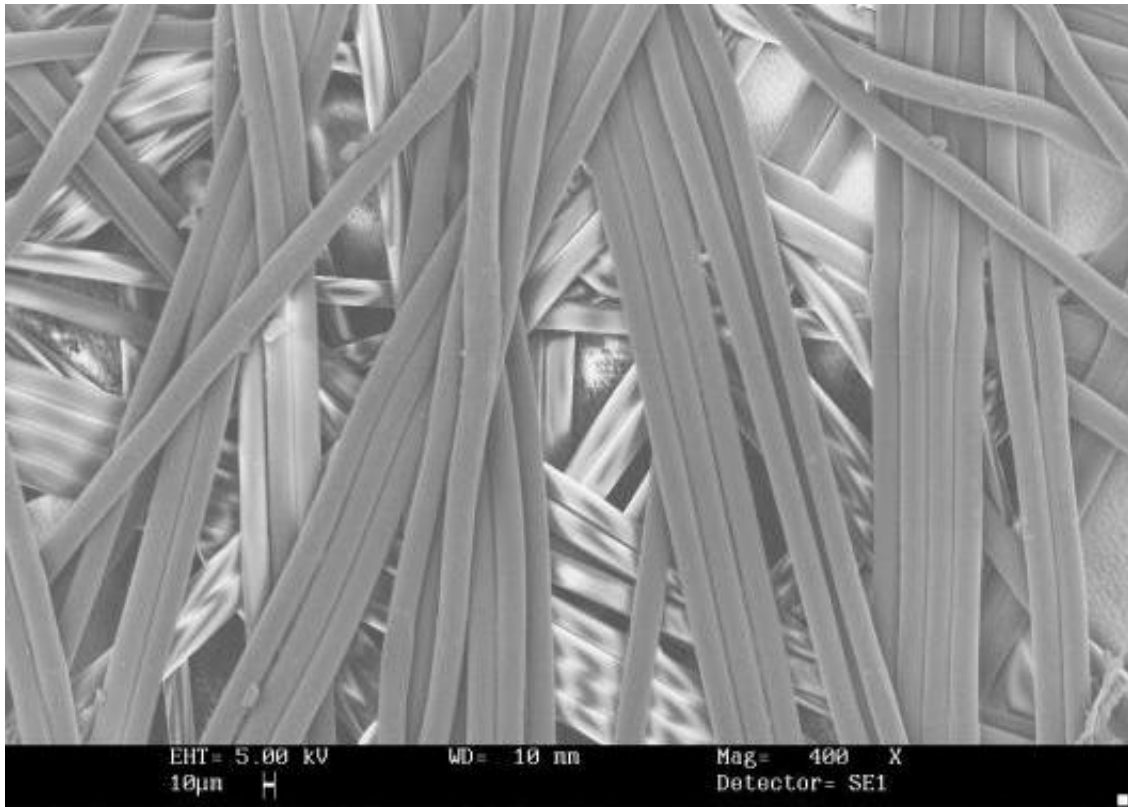


Fig. 3.3 Schematic diagram of the experimental setup

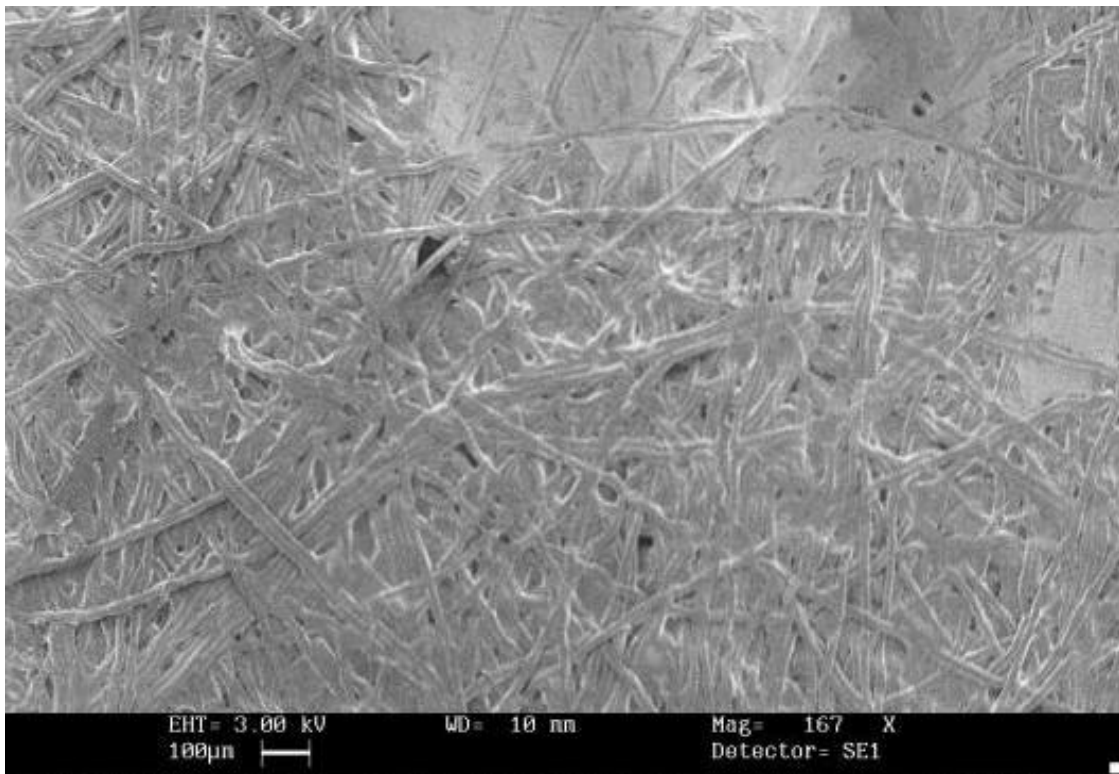
3.3 Results and discussion

3.3.1 Membrane properties

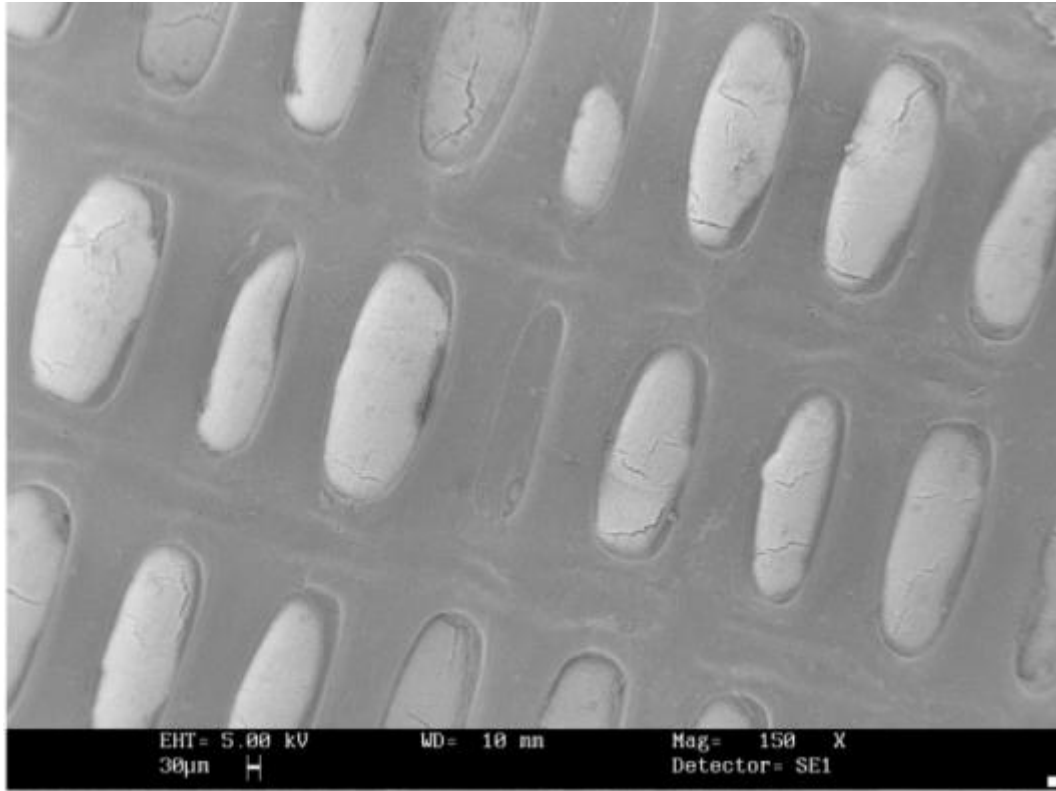
Fig. 3.5 shows the SEM images of the support layers and active layers. Images 3.5a and 3.5b are the structures of the non-woven fabric supports respectively for M_{mt} series membrane and $M_{p0.30}$, and image 3.5c shows the structure of the scrim support layer for M_{gt} series membrane. From those images, it was found that the tortuosities of the nonwoven fabric support layers were greater than 1, and the tortuosity of the scrim support layer was close to 1. From the surface structures of the PVDF and PTFE active layers shown in images 3.5d and 3.5e, it seemed that the knot-fibril net structured PTFE active layer have a higher surface porosity than that of the PVDF membrane. The cross sectional images (Figs. 3.5f and 3.5g) of the PVDF and PTFE membranes showed that the scrim support layer was also thinner than that of the nonwoven fabric support layer.



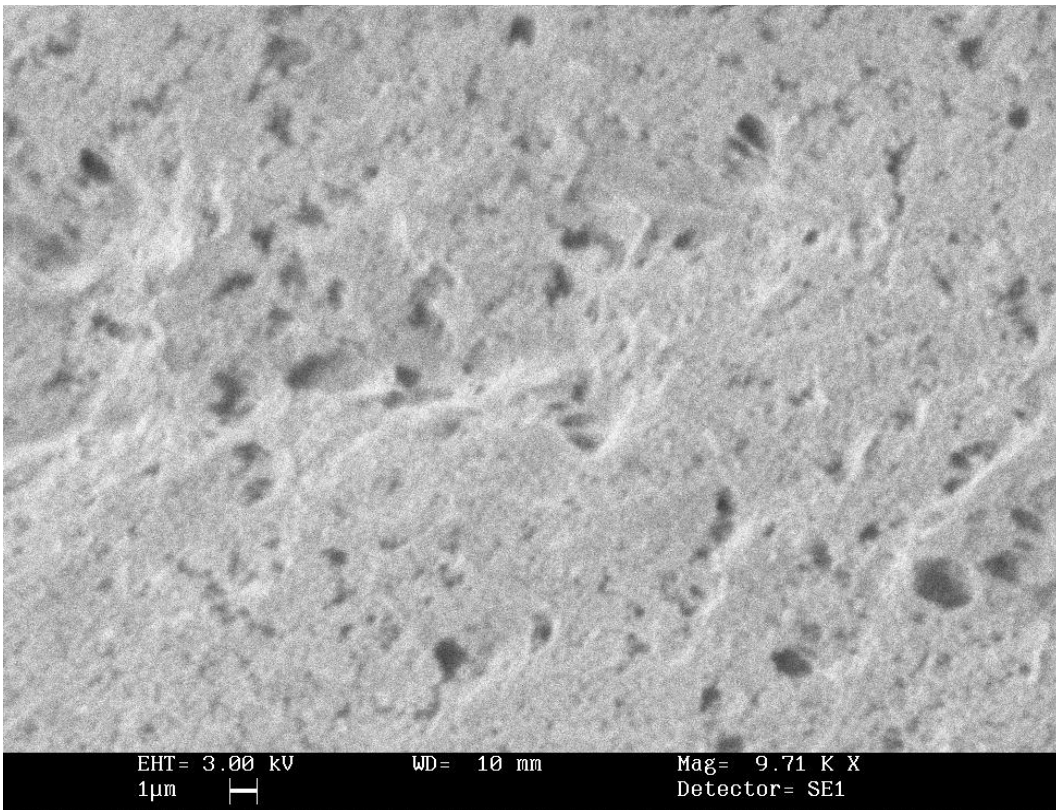
a. non-woven fabric support layer of $M_{mt1.00}$



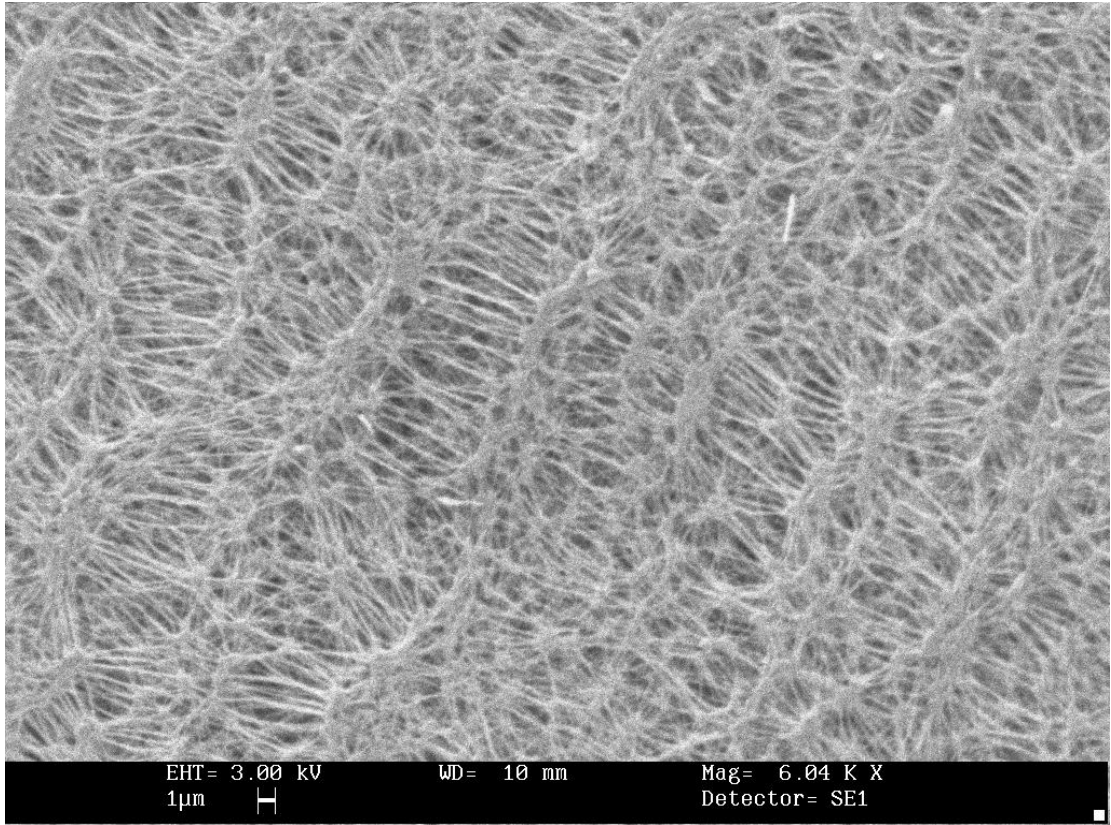
b. non-woven fabric support layer of $M_{p0.30}$



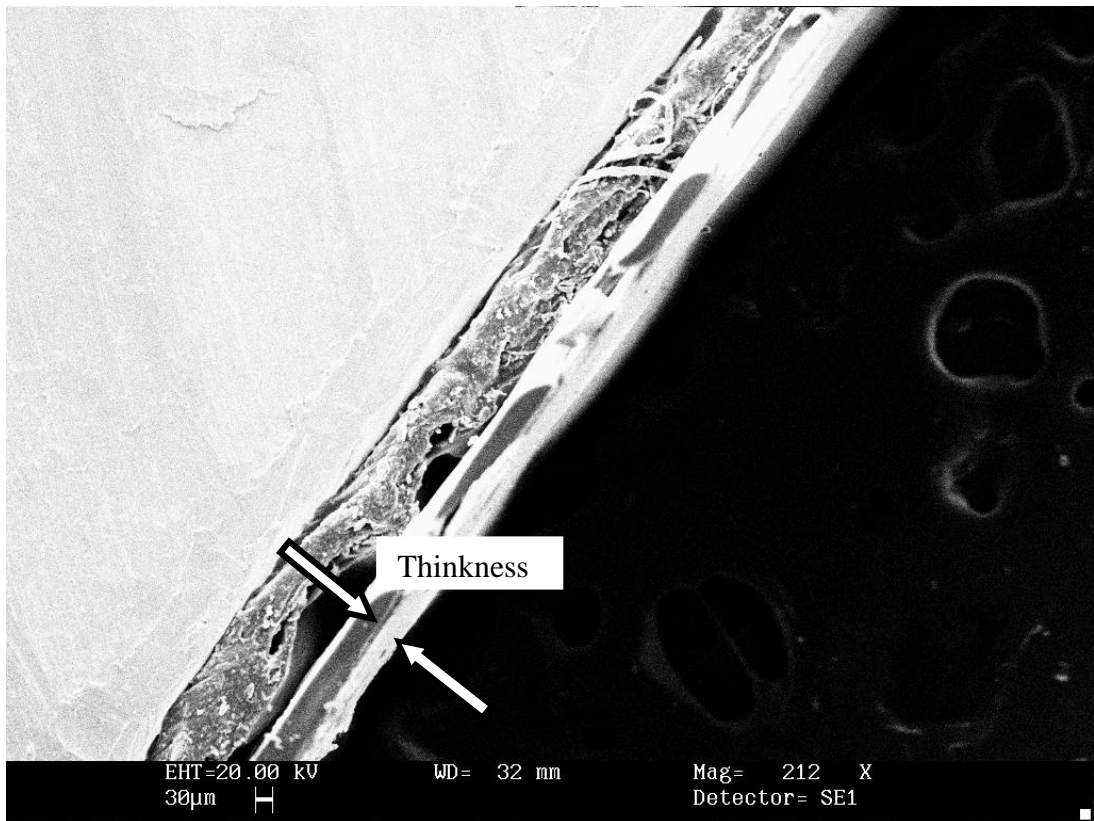
c. Scrim support layer of $M_{gt1.00}$



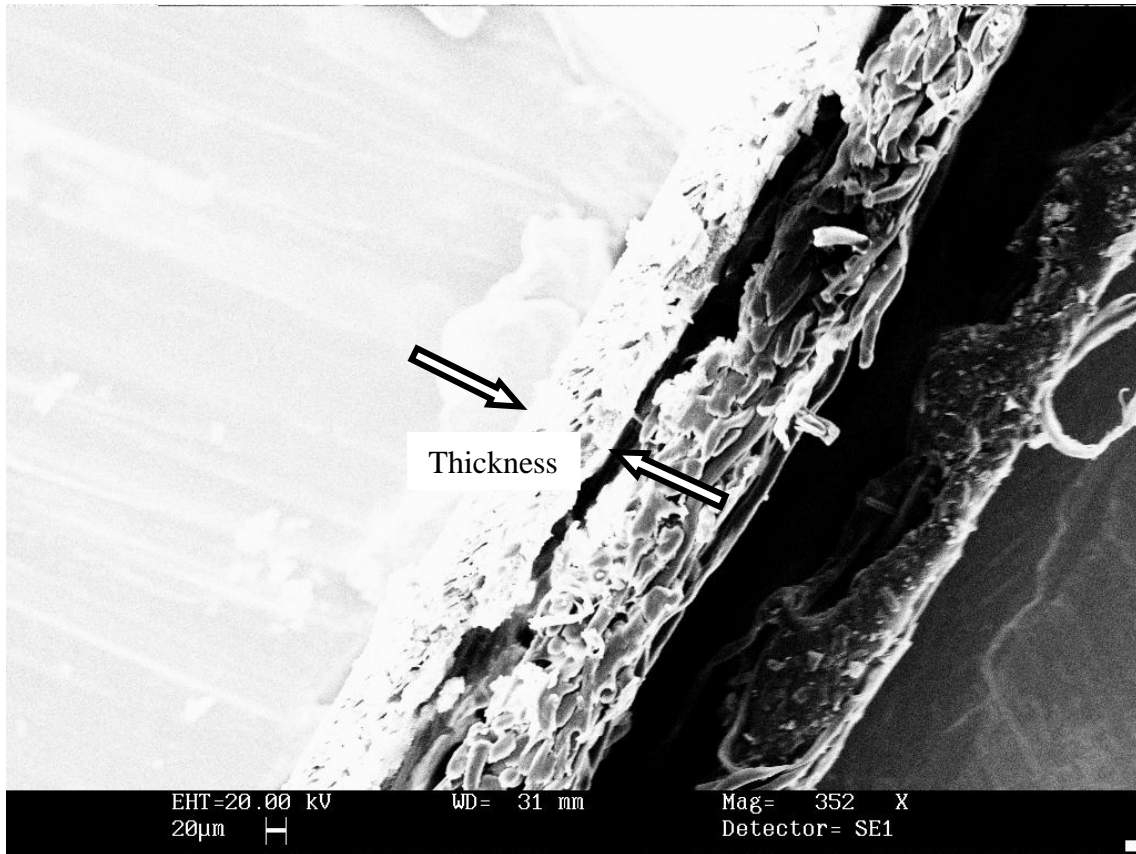
d. Active layer of $M_{p0.30}$



e. Active layer of $M_{gt0.22}$



f. Cross section of $M_{gt1.00}$



g. Cross section of $M_{p0.30}$

Fig. 3.4 SEM images of support and active layers

Based on Eq. (2.15), it can be found that the PTFE membranes seemed to be more suitable for membrane distillation, as they have a thinner active layer and support layer than that of the PVDF membrane. Furthermore, the more porous active layer of PTFE membrane reduced the mass transfer resistance and increased the heat transfer resistance compared to the PVDF membrane.

Fig. 3.6 shows the results from the gas permeation tests from different membranes. In this chart, the highest nitrogen flux under the same pressure difference across the membrane (1 kPa) was obtained for $M_{gt1.00}$, and the lowest flux was obtained from $M_{p0.30}$. In comparison with the membranes with the same pore size, the membranes with the scrim support layers ($M_{gt1.00}$ and $M_{gt0.45}$) have higher flux than that of membranes with the nonwoven fabric support layers ($M_{mt1.00}$ and $M_{mt0.45}$). The permeate flux from each membrane was linear curve fitted to obtain its slope and interception.

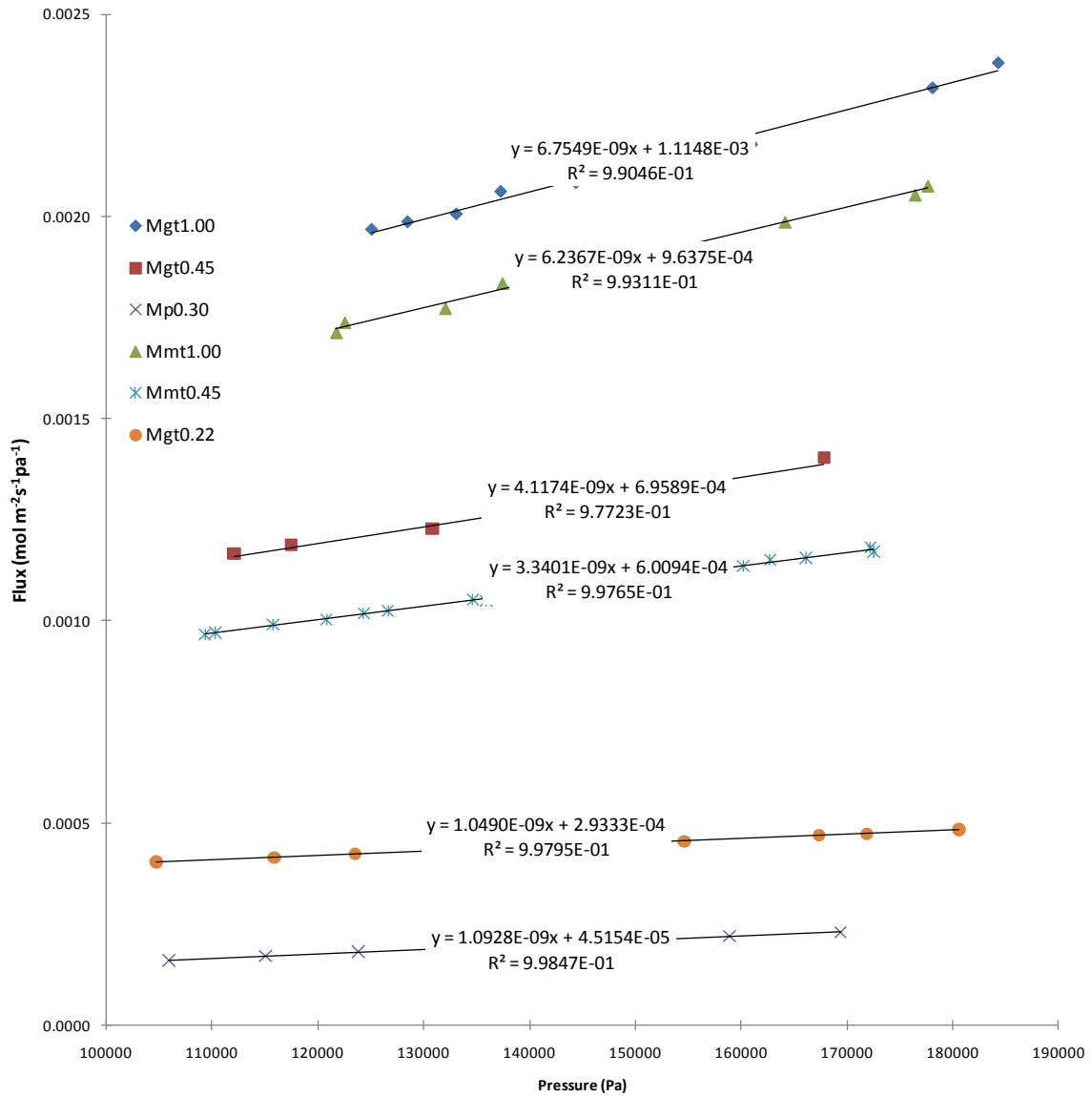


Fig. 3.5 Relations between $J/\Delta P_{gas}$ and P_{pore} in nitrogen permeation test of different membranes

In Table 3.2, the measured and calculated membrane properties are shown. According to this characterisation of the MD membranes and equations (2.19) and (3.1), the PVDF membrane ($M_{p0.30}$), which has the greatest overall and active layer thicknesses, and the smallest contact angle, porosities of active layer and support layer, ε/bt and LEP, will have the worst performance in membrane distillation. These results show the negative characteristics of the PVDF membrane for the membrane distillation in comparison with other membranes, while the scrim supported membrane $M_{gt1.00}$ has the best features for membrane distillation according to the equations describing DCMD heat and mass transfers.

As the calculated tortuosity of M_{gt} series membrane is less than one, which is caused by experimental error, the reported tortuosity of PTFE membrane was used in this table for the calculation of the surface porosity. As seen in Fig. 3.7, the scrim is partially embedded in the active layer. However, in the measurement, only the original thickness of the active layer (the part not being covered with the scrim) was considered, so the measured thickness has overestimated the actual mean membrane thickness. It also can be found from the data that the measured pore size of $M_{p0.30}$ ($2\ \mu\text{m}$) is much larger than the nominal pore size ($0.30\ \mu\text{m}$). Furthermore, from the magnified cross section image of $M_{p0.30}$ active layer (Fig. 3.8), pores of $5\ \mu\text{m}$ in size can also be found. The pore size difference may be caused by the definition of pore size and/or the pore size distribution (PSD) of the membrane. This PVDF membrane is used for micro-filtration, so its pore size will be determined by the cut-off of the solid particle size in the feed. Therefore, the pore size of the dense (surface) layer will be used as membrane pore size. However, in the gas permeation test, the mass transferring through the membrane will be affected by both the pore sizes of the dense layer and the loose layer, so the measured mean pore size will be the mean value of them.

From Fig. 3.5 and Table 3.2, it is seen that the PTFE active layers are more porous than the PVDF membrane and the scrim support layer can provide more open area for vapour transport than that of the non-woven fabric support layer. Furthermore, the M_{gt} membranes have larger contact angles, smaller overall thicknesses, and higher LEP. According to the characteristics listed in Table 3.2, and Eqs. (2.4), (2.19) and (3.2), M_{gt} membranes should have low thermal conductivity and mass transfer resistances, can be employed under relatively high pressure conditions, and are preferable for use in MD.

Table 3.2 Measured and calculated properties of membrane

Membrane		$M_{mt1.00}$	$M_{mt0.45}$	$M_{p0.30}$	$M_{gt0.22}$	$M_{gt0.45}$	$M_{gt1.00}$
Thickness (μm)	Overall	197	187	234	174	164	127
	Active layer	30 ± 2.5	40 ± 2.5	90 ± 2	77 ± 2	67 ± 2	30 ± 2
Contact angle		$126^\circ\pm 5$	$124^\circ\pm 5$	$113^\circ\pm 5$	$144^\circ\pm 5$	$144^\circ\pm 5$	$150^\circ\pm 5$
ε/bt (m^{-1})		26,369	19,146	330	14,511	20,412	30,722
Pore diameter (μm)		0.56	0.48	2.11	0.31	0.52	0.55
Tortuosity		1.17	1.19	27.06	1.1*	1.1*	1.1*
LEP (kPa)	Measured	24.0 ± 2.5	61.6 ± 2.5	21.3 ± 2.5	154.0 ± 2.5	90.8 ± 2.5	47.8 ± 2.5
	*Converted	21.8 ± 2.5	56.2 ± 2.5	19.4 ± 2.5	140 ± 2.5	82.5 ± 2.5	43.5 ± 2.5
Porosity of active layer (%)	Bulk	92.9	88.9	81.0	83.1	87.8	89.4
	Surface	79.4	74.7	3.0	75.5	79.8	81.3
Porosity of support layer (%)	Bulk	65.0	73.0	25.6	70.0	70.0	70.0
	Surface	<65.0	<73.0	<25.6	~70.0	~70.0	~70.0
Thermal conductivity ($\text{W}\cdot\text{m}^{-1}\text{K}^{-1}$)	Active layer	0.042	0.051	0.057	0.064	0.053	0.050

*Reported tortuosity data were used [75, 130],

* LEP using 20% NaCl solution was converted from measured values to the values of 1% feed solution by correcting for the change in surface tension at these concentrations.

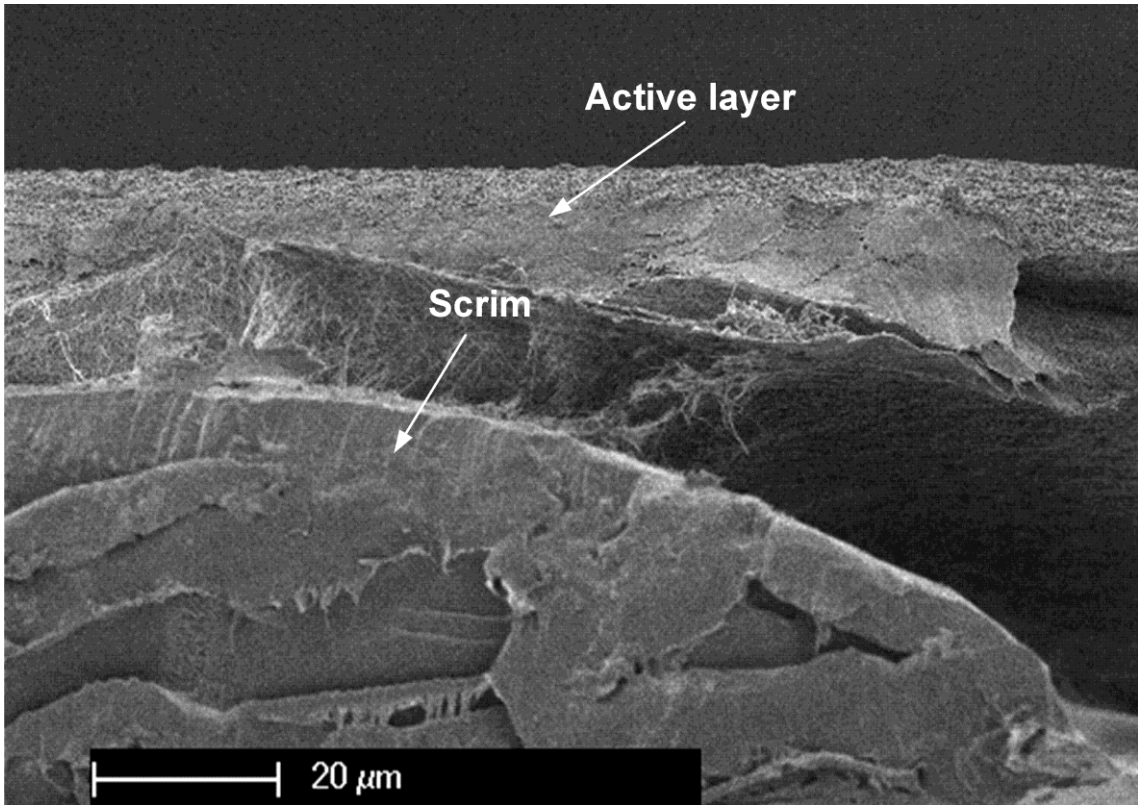


Fig. 3.6 Schematics of scrim embedded in the active layer

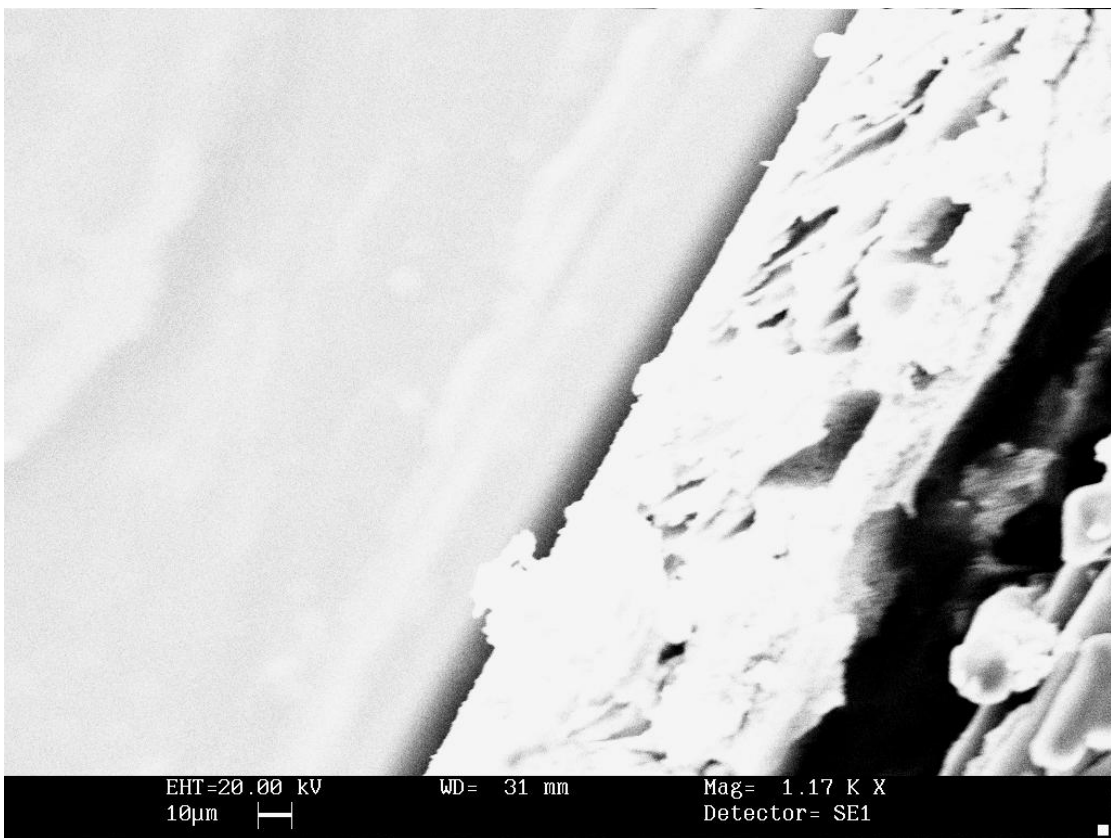


Fig. 3.7 Cross section of $M_{p0.30}$ active layer

3.3.2 Membrane fluxes and global mass transfer coefficients at different velocities

Fig. 3.8 shows the measured fluxes for hot side temperatures of 60°C and cold side temperatures of 20°C for the selected five membranes listed in Table 3.1. Permeate fluxes rose as the feed velocity increased for all the five membranes, because high velocity means high turbulence which will result in less temperature polarisation and increased driving force across the membrane. However, the rate of flux increase becomes slow at higher feed velocities (ie. the curves approach constant values). Similar asymptotic trends of permeate flux with increasing feed velocities were reported previously [34, 131].

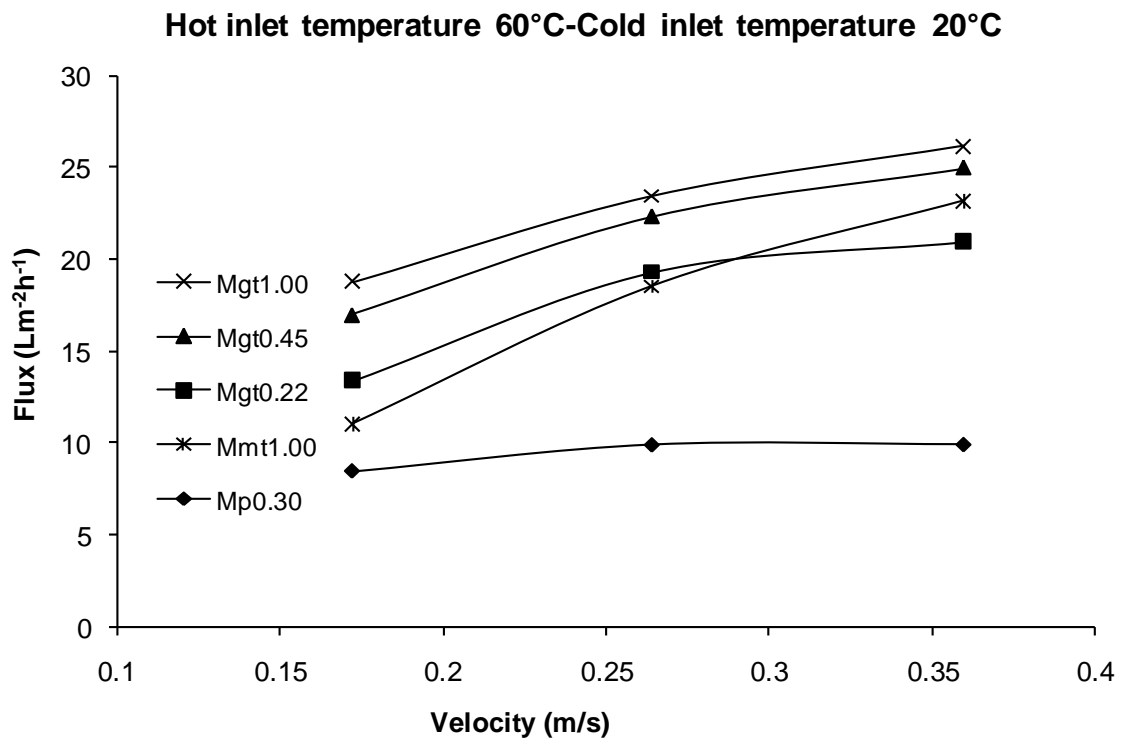


Fig. 3.8 Relation between flux and velocity

The $M_{gt1.00}$ membrane showed the best performance at all velocities, and achieved the highest flux of $26.2 \text{ Lm}^{-2}\text{h}^{-1}$ at the hot feed velocity of 0.36 m/s. The lowest flux was from $M_{p0.30}$, and its highest flux at the hot feed velocity of 0.36 m/s was only around half that of the lowest flux of the PTFE membrane $M_{gt1.00}$ at the hot feed velocity of 0.17 m/s. $M_{gt1.00}$ showed higher flux than $M_{gt0.45}$ at all hot feed velocities, and $M_{gt0.45}$ had higher fluxes than $M_{gt0.22}$ at all velocities, which corresponds to the findings of higher gas permeability for larger pore size membranes in the gas permeation test. However, in

Fig. 3.8, $M_{mt1.00}$ shows an average flux about 50% less than that of the $M_{gt0.45}$ in the tested flowrate range, although it has a higher nitrogen flux than that of $M_{gt0.45}$, and also has a higher active layer porosity, larger nominal pore size and thinner active layer than those of $M_{gt0.45}$. This suggests that the more porous and open support layer of the $M_{gt0.45}$ membrane leads to the higher flux relative to the nonwoven support layer of the $M_{mt1.00}$ membrane, and this is discussed later.

During the DCMD experiments, both the turbulence level and temperature differences across the membrane rose when the velocities were increased. To avoid the influence of higher temperature difference on flux in characterising the membrane properties, a global mass transfer coefficient C_{global} was calculated using Eq. (2.19). To do so, an average ΔP_{avg} for counter current flow was calculated from

$$\Delta P_{avg} = \frac{(P_{fi}-P_{po})-(P_{fo}-P_{pi})}{\ln[(P_{fi}-P_{po})/(P_{fo}-P_{pi})]} \quad (3.11)$$

where P_{fi} , P_{fo} , P_{pi} and P_{po} are the vapour pressures respectively at inlet and outlet temperatures of the hot side and cold side. The global mass transfer coefficient includes mass transfer in both the boundary layers and the membrane pores, which will vary with the turbulence state of the stream and is different from the local membrane mass transfer coefficient that is only determined by membrane properties shown in Eq. (2.19). Assuming that the mass transfer coefficients in the boundary layer are equal under the same hydraulic conditions in the experimental temperature range, the global mass transfer coefficient can be used to make a comparison in mass transfer performance among the different membranes. Based on this assumption, the global mass transfer coefficients were calculated from Eq. (2.19) and the results are shown in Fig. 3.9.

Fig. 3.9 shows that M_{gt} series membranes have significantly higher mass transfer coefficients than the other membranes. Although $M_{mt1.00}$ has the same nominal pore size as $M_{gt1.00}$, it only has a mass transfer coefficient similar to that of $M_{gt0.22}$ in the tested velocity range. The C_{global} of $M_{p0.30}$ is the lowest and is not sensitive to velocity changes, indicating that the mass transfer resistance in the membrane dominates that of the boundary layers. It also can be found from Fig. 3.6, air permeation of $M_{p0.30}$ was only half that of $M_{gt0.22}$ and 20% that of $M_{mt0.45}$, which shows that the mass transfer resistance of the $M_{p0.30}$ was much greater than that of other membranes. Furthermore, it can also be found from Fig. 3.9 that $M_{gt0.22}$, which has the second largest resistance, also

shows a flux not sensitive to velocity at a lower velocity than the membranes with low mass transfer resistance.

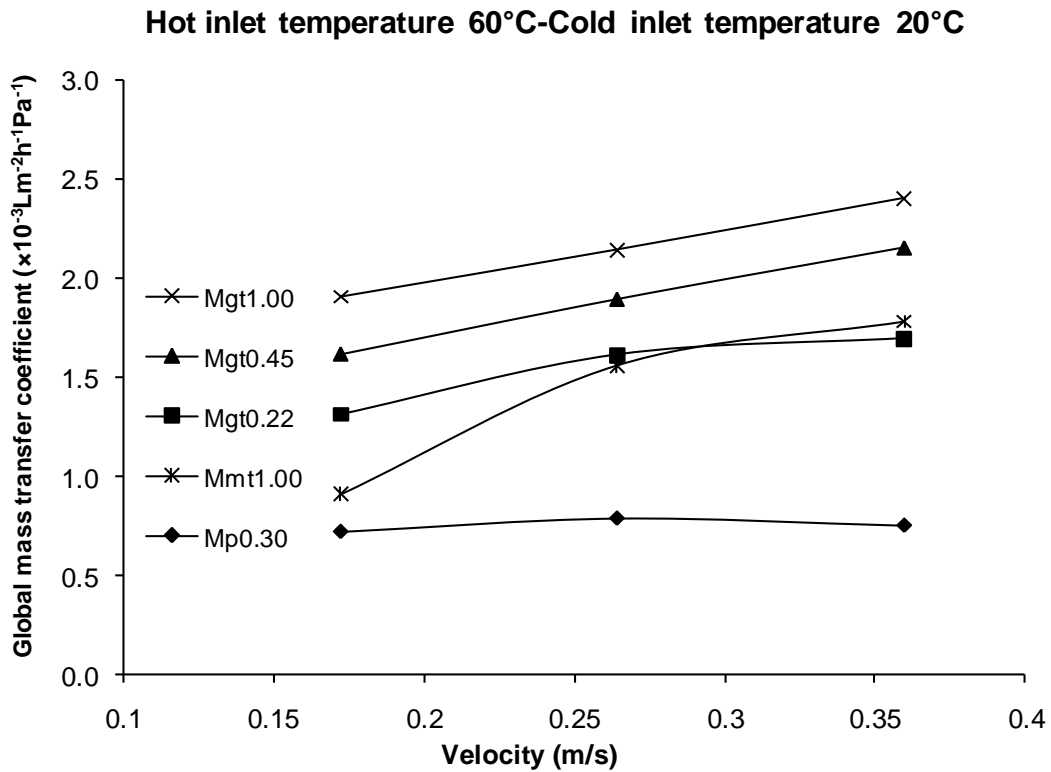


Fig. 3.9 Mass transfer coefficients with respect to feed velocity

In Figs. 3.8 and 3.9, the curves for the $M_{mt1.00}$ and $M_{gt0.22}$ intersect each other, which could be caused by the structure of their support layers. Figs. 3.4a and 3.4c and Table 3.2 show that the tortuosity and thickness of the nonwoven fabric support layer of $M_{mt1.00}$ are greater than those of the scrim support layer, so the non-woven fabric layer may trap more static water and cause a greater degree of temperature polarisation than the scrim support layer at lower flowrate. Therefore, the flux gained from membrane supported by nonwoven fabric may show stronger dependency on flowrate. At a low flowrate when the boundary layer or temperature polarisation has more influence on flux, $M_{mt1.00}$ showed lower flux than that of $M_{gt0.22}$, while at a high flowrate when turbulence reduces the temperature polarisation effect and flux is mainly controlled by the properties of the active layer, $M_{mt1.00}$ showed higher flux than that of $M_{gt0.22}$.

Fig. 3.10 shows the salt rejection rate with respect to velocity for the five membranes listed in Table 3.1. The pressure drop along the membrane was in the range of 8-20 kPa at these velocities. Salt rejection rates of all the PTFE membranes were more than 99%, regardless of the velocities. Although the salt rejection rate of the $M_{p0.30}$ was more than

99% at the low velocity, it reduced to 96% as the velocity increased to 0.36 m/s. This can be attributed to pressure variation in the range of 10-20 kPa at this flowrate, and from Table 3.2, it can be seen that the LEP of $M_{p0.30}$ was only 19.4 ± 2.5 kPa, which may have allowed wetting to occur under fluctuating pressures at high velocities. The PSD of the membrane was also a possible cause of the pore wetting, as any large pores that occur will wet more readily than the small pores.

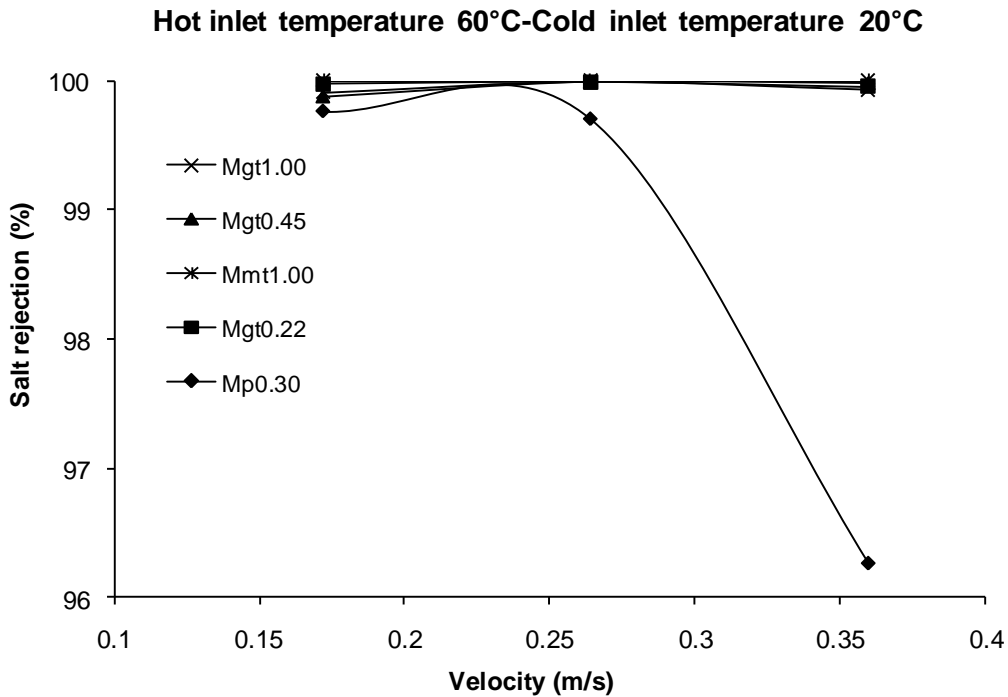


Fig. 3.10 Salt rejections related to feed velocity

3.3.3 Membrane fluxes and global mass transfer coefficients at different temperatures

Fig. 3.11 show the measured fluxes for the hot stream at a velocity of 0.36 m/s, different hot inlet temperatures and same cold inlet temperature for the five selected membranes listed in Table 3.1. Permeate fluxes increase as the temperature is increased for all the five membranes, because higher temperature will generate greater driving force for mass transfer through the membrane. Except for $M_{mt0.45}$, all membranes showed a similar flux trend to that of the gas permeation test. In Table 3.2, it can be seen that the $M_{mt0.45}$ has characteristics more suitable for membrane distillation than that of the $M_{gt0.22}$, other than the support layer, but the flux obtained from $M_{mt0.45}$ was less than that of the $M_{gt0.22}$. Thus, it was confirmed again that the support layer was one of the key factors for MD membrane structure.

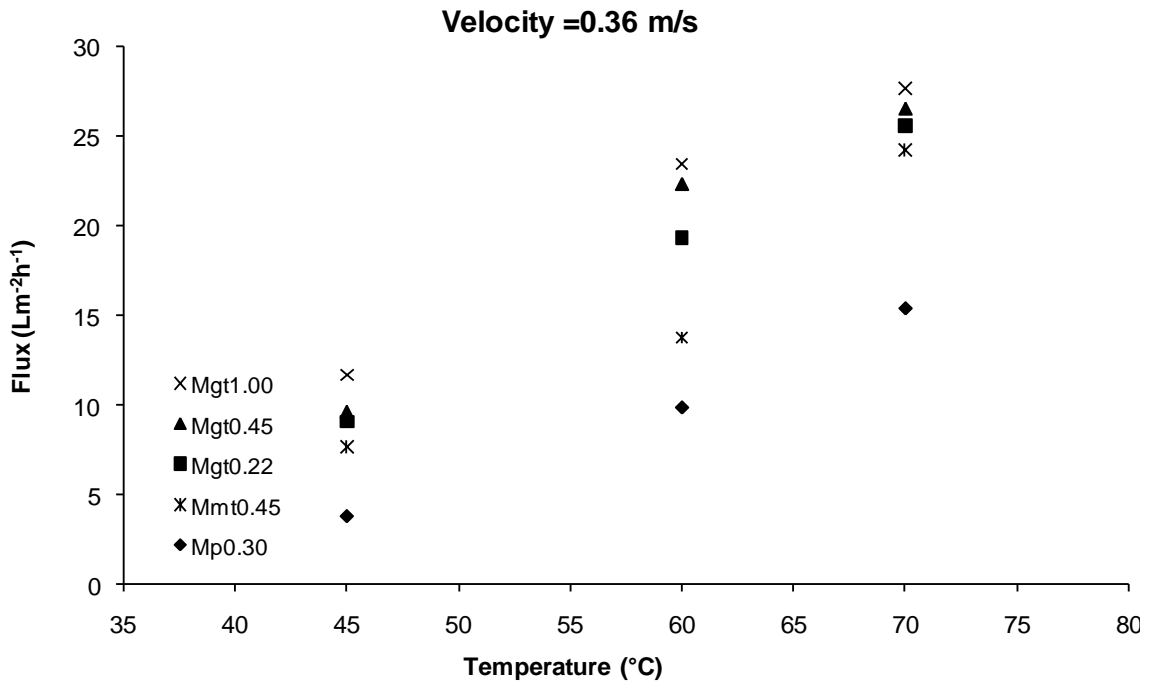


Fig. 3.11 Relation between flux and temperature for the various membranes

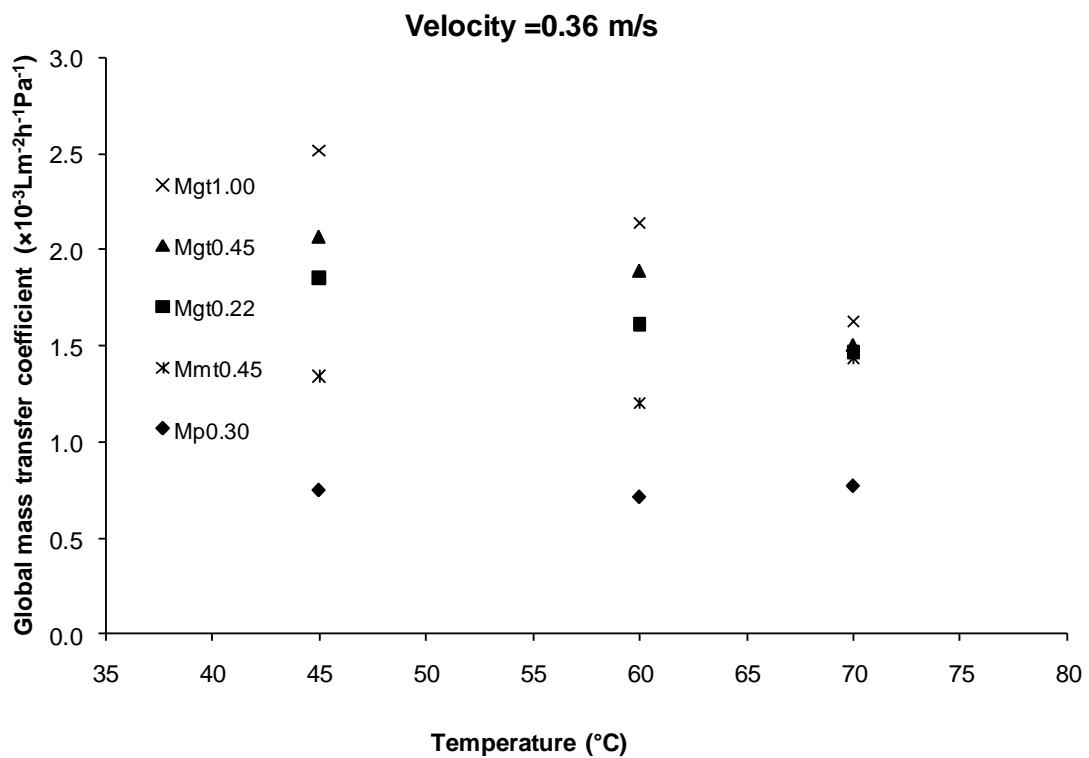


Fig. 3.12 Mass transfer coefficients with respect to feed inlet temperature for the various membranes

Fig. 3.12 shows the calculated global mass transfer coefficient at different temperatures. A declining trend of the global mass transfer coefficient was found as the temperature increased. Because more heat transfer was needed to support the higher flux at high temperature, a large temperature difference or temperature polarisation should be expected, assuming the heat transfer coefficient was constant at a given velocity. Besides the temperature polarisation becoming greater at higher temperature [132], based on Eqs. (2.17) and (2.18), a decrease of the membrane mass transfer coefficient also can be found when the temperature was increased.

The salt rejection at different temperatures is presented in Fig. 3.13, which showed a maximum difference of less than 1%. Therefore, the change in surface tension at different feed temperatures seemed to have little effect on the salt rejection under the experimental conditions.

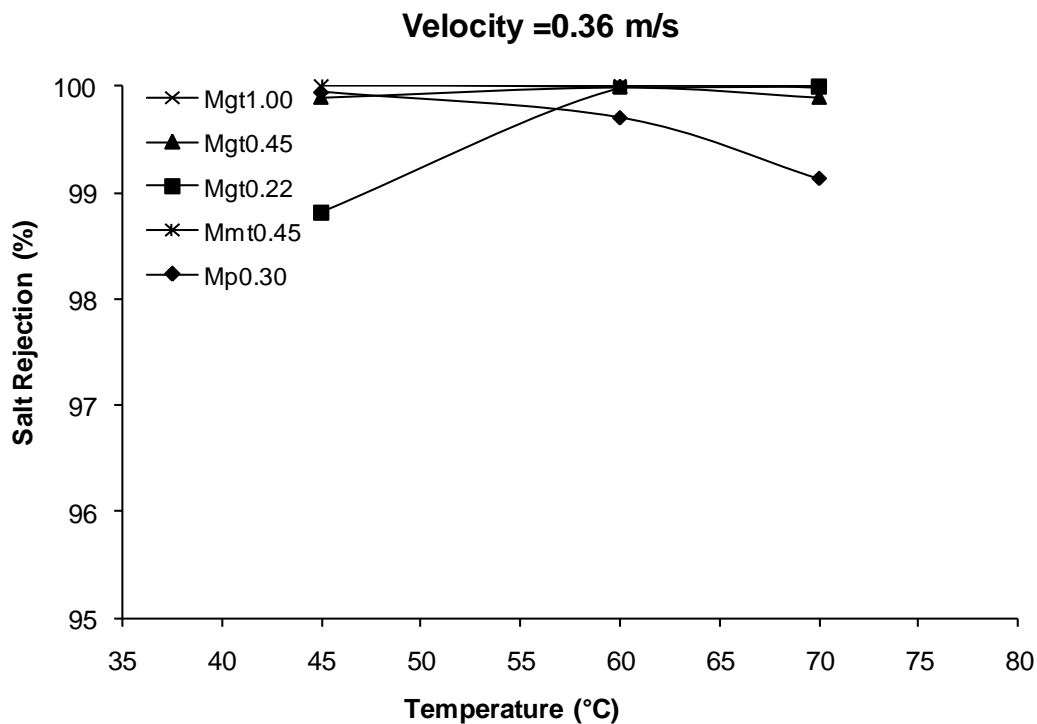


Fig. 3.13 Salt rejection at different temperatures

3.3.4 Temperature influence on membrane flux and energy efficiency

As $M_{mt1.00}$ and $M_{gt1.00}$ membranes showed the highest flux for a nonwoven backed and a scrim backed layers, they were selected for further testing over a wider temperature

range. The permeate fluxes of both membranes increased as the temperature rose. Fig. 3.14 shows the flux at different hot side inlet temperatures at a feed velocity of 0.36 m/s. Although the active layers of these two membranes were made from the same material, with the same nominal pore size measured by the gas permeation test (similar PSD), approximately same measured active layer thickness and having similar support layer porosities, $M_{gt1.00}$ showed consistently higher flux than that of $M_{mt1.00}$. The highest flux of $46.3 \text{ Lm}^{-2}\text{h}^{-1}$ was achieved from $M_{gt1.00}$ at 80°C . The difference in flux between these membranes was probably due to the difference in support layers used. From Table 3.2 and Fig. 3.4, it can be seen that the scrim support layer is thinner and more open (more surface porosity) than the nonwoven fabric support layer. Thus, the $M_{gt1.00}$ has a smaller overall thickness and a larger exposed effective area of the active layer than that of the $M_{mt1.00}$ membrane.

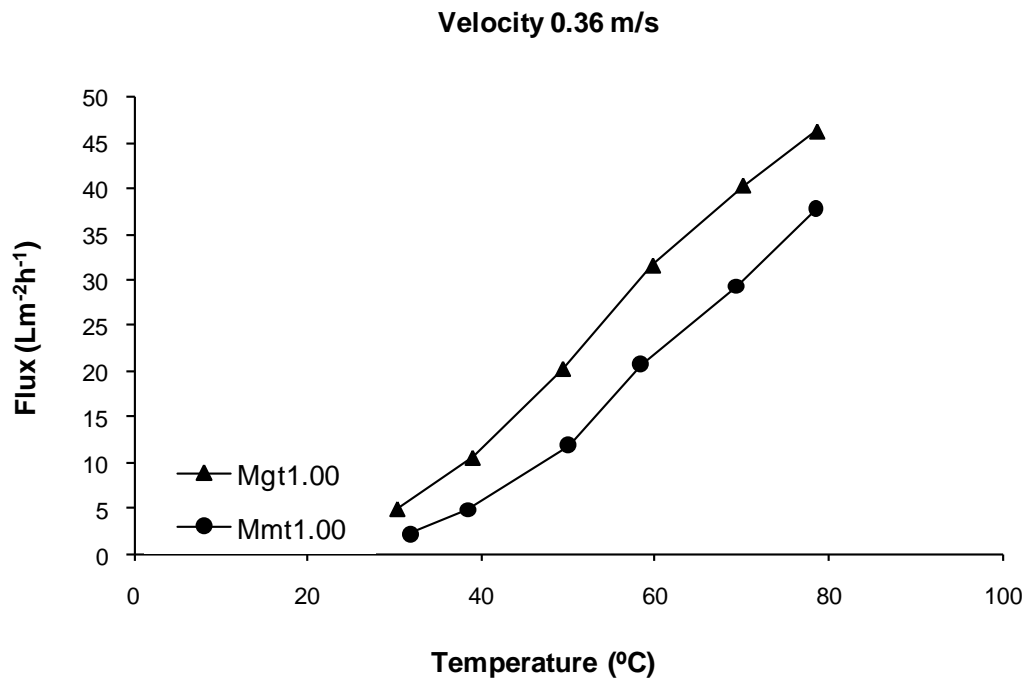


Fig. 3.14 Variation of flux with hot side inlet temperature at a constant velocity

The results listed in Table 3.3 were calculated using Eq. (2.6). From this table, it is found that the feed sensible heat transfer increases when the temperature is higher, and the heat loss due to the latent heat transfer increased faster than that of the sensible heat transfer, except for the $M_{gt1.00}$ when the temperature was increase from 70 to 80°C . Although $M_{mt1.00}$ is thicker than $M_{gt1.00}$, the global heat transfer coefficient (U) of $M_{mt1.00}$

is greater than that of $M_{gt1.00}$ under the same conditions. This means that more heat was wasted in the MD process when $M_{mt1.00}$ was used, and is consistent with the higher sensible heat transfer for $M_{mt1.00}$.

Table 3.3 Sensible heat transfer and latent heat transfer at different temperatures

Feed inlet temperature (°C)	30	40	50	60	70	80	
$M_{mt1.00}$	Q (kWm ⁻²)	12.9	19.2	31.1	39.8	56.6	69.3
	$H_{latent}J$ (kWm ⁻²)	1.1	3.1	7.5	10.4	18.3	23.7
	$\lambda/b(T_1-T_2)$ (kW·m ⁻²)	11.8	16.1	23.7	29.3	38.2	45.6
	U (kWm ⁻² K ⁻¹)	164.1	151.3	136.9	132.9	121.6	118.5
$M_{gt1.00}$	Q (kW·m ⁻²)	12.3	21.3	32.9	45.3	49.5	59.2
	$H_{latent}J$ (kWm ⁻²)	3.0	6.7	12.8	19.8	25.3	28.7
	$\lambda/b(T_1-T_2)$ (kWm ⁻²)	9.3	14.6	20.2	25.5	24.2	30.5
	U (kWm ⁻² K ⁻¹)	135.5	123.6	110.2	101.4	87.9	92.8

The degree of temperature polarisation incurred by their support layers was investigated based on two assumptions: the degree of temperature polarisation on the active layer side for both membranes was similar under similar operating conditions, and the support

layer could incur a higher degree of temperature polarisation than the active layer, because the turbulence of the bulk stream has less effect on the water in the scrim or nonwoven fabric support layer than the water on the surface of the active layer. In these experiments, the stream velocities were kept at 0.36 m/s and permeate and feed inlet temperatures were set at 20 and 60°C, respectively. The configuration of the membranes with respect to direct contact with the feed and permeate sides was varied, such that both the support layer and active layer of each membrane were contacted with feed in different experiments (ie. the membrane was turned over between experiments). From the experimental results listed in Table 3.4, it is seen that in comparison with the active layer in contact with the feed, the flux was reduced by 19% and by 3% for $M_{gt1.00}$ and $M_{mt1.00}$, respectively, when their support layers contacted the feed. From Eq. (2.19) and the exponential relationship between temperature and vapour pressure [133], it can be concluded that the flux shows more dependency on the feed side temperature polarisation than on permeate side temperature polarisation. This result maybe also due to the proportion of the mass transfer resistance of the boundary layer attributed to the total mass transfer resistance. At the experimental velocity, it is noted from Fig. 3.9 that the global mass transfer coefficient of membrane $M_{mt1.00}$ appeared constant, but the mass transfer coefficient of $M_{gt1.00}$ still seemed to be increasing linearly with velocity. Thus, at this flowrate, for membrane $M_{mt1.00}$, the mass transfer resistance of the boundary layer did not have great influence on the flux, while for membrane $M_{gt1.00}$, the boundary layer still contributed to a significant proportion of the resistance to mass transfer.

This indicates that the resistance of the whole membrane is not controlling the flux in the case of $M_{gt1.00}$ but it is for $M_{mt1.00}$. As shown in Table 3.2, both membranes have similar active layer characteristics, so it may be assumed that the resistance of both active layers are similar. From the Figs. 3.4a and 3.4c and the observed pressure drop in the module about 10-20 kPa at a stream velocity of 0.36 m/s, it was expected that both nonwoven and scrim support layers were fully wetted, because both support layers had much larger opening compared to the membrane pore size and were made from PP which has a lower contact angle than PTFE. However, $M_{gt1.00}$ produced more flux than that of $M_{mt1.00}$. Therefore, the lower flux of $M_{mt1.00}$ relative to $M_{gt1.00}$ is caused by the greater resistance of the nonwoven support layer compared to that of the scrim support layer. Furthermore, the lack of influence of having the feed on either of the active layer

side or support layer side in the $M_{mt1.00}$ experiment suggests that the support layer acts as an integral part of the membrane, and that the resistance of the membrane is composed of the resistance of the support layer and the resistance of the active layer in series. In contrast, the support layer of $M_{gt1.00}$ decreases the exposed active layer area on one side of the membrane, and also affects temperature polarisation via its effect on the hydrodynamics. Therefore, even greater flux through $M_{gt1.00}$ might be achieved via increasing the porosity (open area) of the scrim support layer.

Table 3.4 Flux change with side in contact with feed

Membrane	Feed contacting support layer		Feed contacting active layer	
	Flux ($\text{Lm}^{-2}\text{h}^{-1}$)	C_{global} ($\times 10^{-3} \text{Lm}^{-2}\text{h}^{-1}\text{Pa}^{-1}$)	Flux ($\text{Lm}^{-2}\text{h}^{-1}$)	C_{global} ($\times 10^{-3} \text{Lm}^{-2}\text{h}^{-1}\text{Pa}^{-1}$)
$M_{mt1.00}$	24.7	2.12	25.5	2.17
$M_{gt1.00}$	27.1	2.28	33.5	2.80

Fig. 3.15 shows the ratio between the heat transfer contributing to water flux (latent heat) and the total feed heat-loss in the module at different temperatures. The ratio is defined as

$$E = \frac{H_{\text{latent}}JA}{\dot{m}_f C_p (T_{fi} - T_{fo})} \quad (3.12)$$

where A is the membrane area, C_p is the specific heat of water, \dot{m}_f is the feed mass flowrate, and T_{fi} and T_{fo} are feed inlet and outlet temperatures respectively. E can be considered as the efficiency of energy used to produce condensate.

These ratios calculated using Eq. (3.12) represents the effective proportion of energy used for the production of permeate. This ratio is one of the key factors contributing to the operational cost of a MD system, as the more effectively heat can be used to drive mass transfer, the more energy efficient the process will be. Therefore, a higher E indicates more efficient energy use because more fresh water could be produced with the same energy.

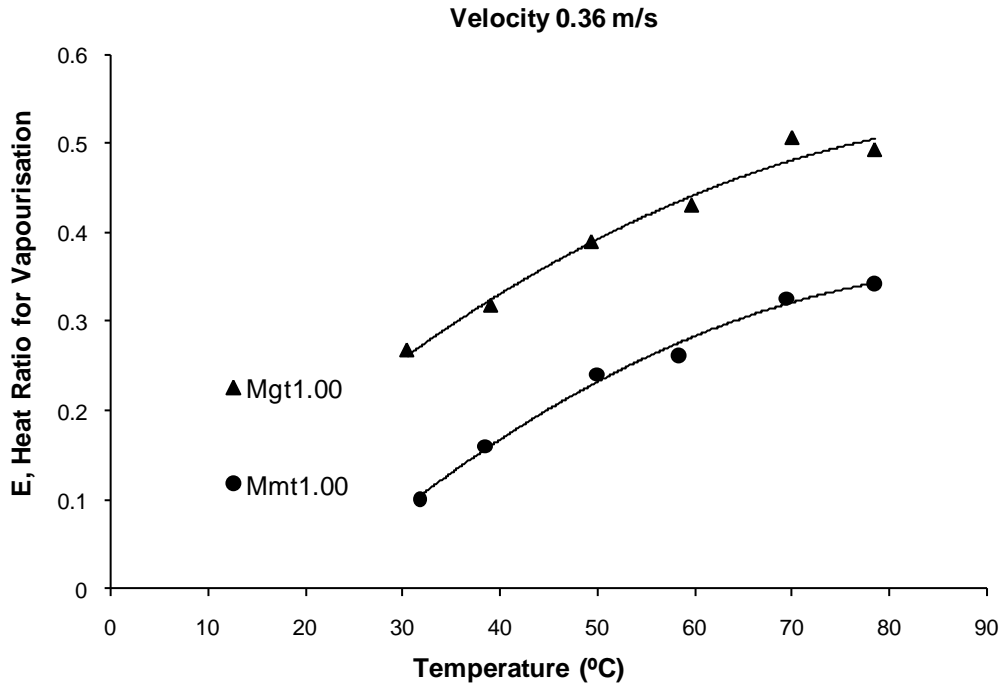


Fig. 3.15 Ratio of heat for water flux to the total feed heat loss, E , at different temperatures

The two curves in Fig. 3.15 are almost parallel to each other. Over the whole temperature range of 30-80°C, the average difference calculated at the same temperature was 0.16. For $M_{mt1.00}$, the ratio increased as the temperature rose across the entire temperature range, while for $M_{gt1.00}$, it increased initially, reached a maximum value of 0.50 at 70°C, and then plateaued between 70°C and 80°C. The heat ratio for evaporation of MD using $M_{gt1.00}$ was 1.4-2.8 times that of using $M_{mt1.00}$, which means that for the same heat loss in the hot brine stream, the fresh water produced from $M_{gt1.00}$ system was 1.4-2.8 times that of the $M_{mt1.00}$ membrane.

This is a consequence of the more open and smaller thickness of the $M_{gt1.00}$ support layer compared to that of $M_{mt1.00}$, which reduces the mass transfer resistance and enables more heat utilisable for evaporation. Therefore, there was less energy transfer associated with the sensible heat passing through the membrane.

3.3.5 Key performance features of new generation membranes

The membranes with the best flux and energy performance have been identified. More hydrophobic membranes appear to result in better salt rejection rate, particularly at

higher velocities where the feed pressure is higher. Although the scrim support layer seemed to incur more temperature polarisation than the nonwoven fabric support layer when the flowrate has less effect on the flux, the more open structure of the scrim backing was found to have less mass transfer resistance which is vital to enhance membrane performance as compared to the nonwoven fabric backing, as the scrim backing membranes consistently produced higher flux and greater conversion of heat to permeate flow.

For future membrane design, the following guidance is suggested to improve MD performance:

- Thin scrim support with wider accessible spaces to the membrane surface should yield further flux and energy efficiency improvements,
- Hydrophobicity is essential for MD operation, but was not found to link to flux as strongly as other physical features,
- Structures of the composite membrane, i.e, overall thickness, the openness of the support layer, are more important for flux improvement than pore sizes in the ranges tested (0.2–1 μm), and
- The geometric structure of the support layer seems to be more important for high flux than that of the porosity, as the flux of scrim backed 0.22 and 0.45 μm membranes were respectively greater than that of the nonwoven fabric supported $M_{\text{mt}0.45}$ and $M_{\text{mt}1.00}$ membrane at the tested conditions.

3.4 Summary

The performances of three new MD membranes supported with scrims were assessed based on flux and energy efficiency, and show greater potential for use in desalination processes than do the traditional microfiltration membranes. The new PTFE membranes achieved a significantly higher flux and had better energy efficiency than the MF membranes under the same conditions.

For the gas permeation tests, all PTFE membranes showed much higher gas permeability than that of the PVDF membrane. Additionally, for the same pore sizes, the scrim supported PTFE membrane showed higher gas permeability than that of the nonwoven fabric supported PTFE membranes.

The contact angles of the new membranes were in the range of 140-160°, which are 1.5 times that of $M_{p0.30}$ and 1.25 times that of $M_{mt1.00}$ and $M_{mt0.45}$. Similarly, the LEP of the new membranes were 2 times that of the MF membranes, so the new MD membranes can be used at higher operating pressures without the risk of wetting. The new membranes show good salt rejection even under critical conditions. In comparison with the 96% salt rejection rate of $M_{p0.30}$, all PTFE membranes achieved nearly 100% salt rejection rate at a feed velocity of 0.36 m/s and ≤ 20 kPa.

Global mass transfer coefficients were calculated to evaluate the mass transfer efficiency of the process under different conditions. All new PTFE membranes have mass transfer coefficients higher than or similar to that of MF membranes under the same conditions.

The more open support layers of the new membranes have less mass transfer resistance than the nonwoven fabric support layer, which incur great increase of flux and energy efficiency. Flux of up to $46 \text{ Lm}^{-2}\text{h}^{-1}$ was obtained at 80°C, which is comparable to the flux achieved in reverse osmosis systems. This suggests that membranes for a commercially viable MD process are available, and issues around module design and long term operation of the MD process (fouling, wetting) need to be resolved. All experimental results presented here were each measured for a period of four to six hours. Experiments over longer time periods are needed to investigate fouling and wetting issues.

Chapter 4 Performance of asymmetric hollow fibre membranes

4.1 Introduction

As mentioned in **Chapter 2**, the hollow fibre tubular module can have a very high packing capacity. Therefore, it is attractive in the commercial application of membrane distillation. However, most of the tubular hollow fibre modules used in MD are made commercially for other separation purpose [60], and its typically low flux is generally 1-4 $\text{Lm}^{-2}\text{h}^{-1}$ at 40-60°C [63-65] which is much lower than that of the flat sheet membranes with fluxes of 20-30 $\text{Lm}^{-2}\text{h}^{-1}$ [3].

The basic features of MD hollow fibre modules have been listed by Schneider and co-workers [70]:

- Housing and membranes should have good thermal and chemical resistances,
- Potted hollow fibres should be crack free and have good adhesion,
- The tubular module is dryable and fixable, if the hollow fibre membrane is wetted or broken, and
- The structure of the tubular module should ensure a uniform flow through the hollow fibre membrane to avoid dead corners or channel formation.

The recent renewed interest in membrane distillation has led to improved hollow fibre membranes and modules. In this chapter, the tubular module tested was fabricated for MD purposes and contained 94 asymmetric hollow fibre membranes specifically fabricated for membrane distillation. The performance of the membrane was explained based on mass transfer theory in microporous membrane materials.

4.2 Theory

Fig. 4.1 shows the force balance at the entrance of pore, in which P_f and P_p are the pressures applied respectively by the feed and permeate streams on the pore entrance, F is the force from surface tension, H is the water protrusion into the pore and θ' is the

angle between the water and membrane material. Additionally, θ' is greater than 90° and cannot be more than θ before wetting occurs, and the initial P_{pore} equals atmospheric pressure.

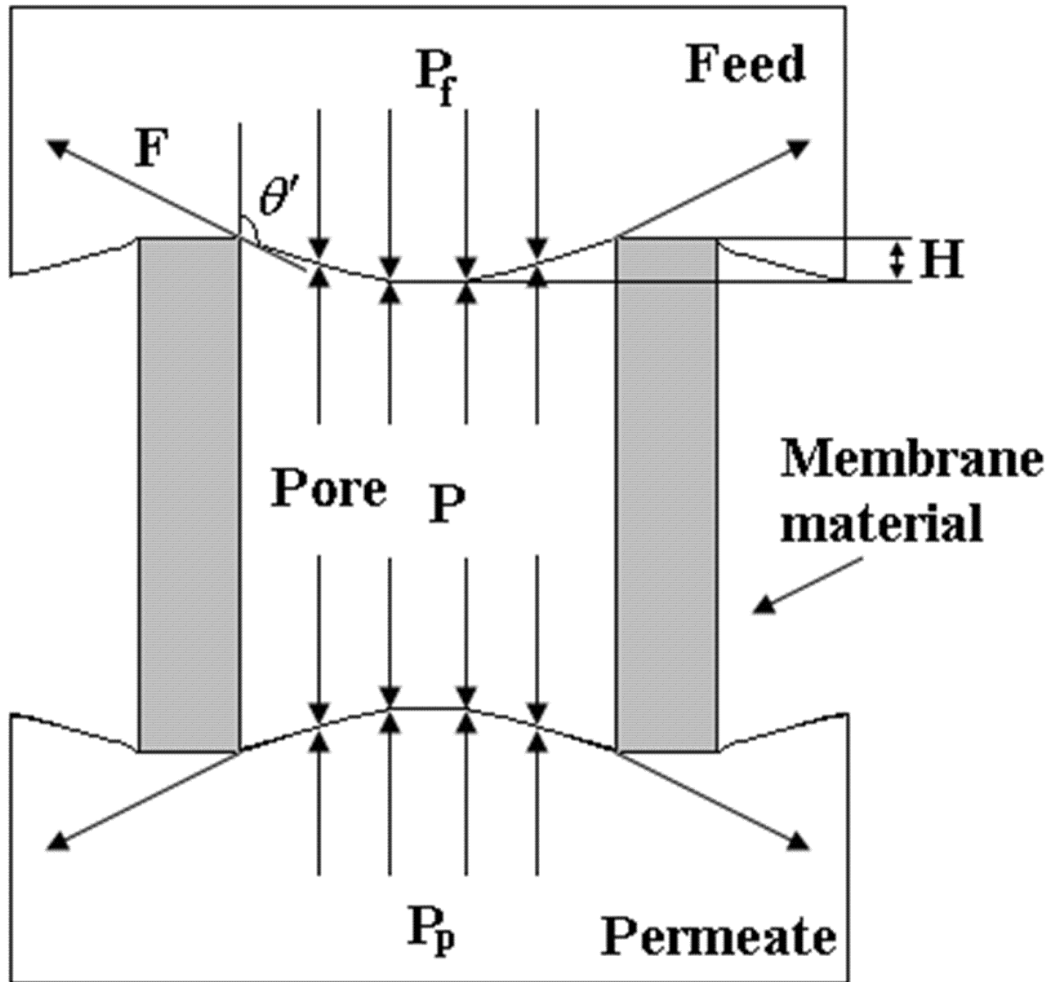


Fig. 4.1 Schematic diagram of the force balance at the pore entrances

The force generated from surface tension can be expressed by [134]

$$F = 2\pi r \gamma_l \quad (4.1)$$

In considering Fig. 4.1, when P_f is higher than P_{pore} , the force balance at the pore entrance can be expressed as

$$F \cos \theta' = -P_f \pi r^2 \quad (4.2)$$

As P_f increases in value relative to P_{pore} , θ' will become larger based on Eq. (4.2) before membrane wetting occurs. The protrusion depth can be calculated by

$$H = r(1 - \sin(180 - \theta')) \quad (4.3)$$

where r is radius of the pore.

Therefore, the protrusion depth will also increase as P_f is raised. According to these Eqs., the protrusion depth reaches its maximum value when the $\theta'=\theta$ for a given pore size. Furthermore, a larger pore and greater contact angle will lead to a greater protrusion. To assess the effect of protrusion depth on the air volume within the pore, a large pore size of $1 \mu\text{m}$ ($r=0.5 \mu\text{m}$) and a contact angle of 150° were assumed in the calculation of protrusion depth. Accordingly, the calculated maximum protrusion depth H was $0.25 \mu\text{m}$. When considering a typical membrane thickness of $10\text{-}50 \mu\text{m}$, this protrusion will have a negligible effect on the air volume within the pore. Therefore, if pressures applied on both pore entrances are higher than P_{pore} and the membrane material is not compressible, P_{pore} will be independent to the changes of pressures applied at the entrances based on the ideal gas law, because air volume within the pore will not change with the applied pressure at the entrances.

However, if either feed or permeate pressure is reduced to less than P_{pore} , the higher pressure air within the pore will bubble into the lower pressure stream, until the force balance is stabilised again (P_{pore} equals this lower pressure), although the air volume within the pore does not change.

4.3 Experimental methods

4.3.1 Hollow fibre membrane and module

Table 4.1 lists the characteristics of the membranes as specified by the supplier and the dimension of the module used in the experiments.

Table 4.1 Nominal specifications of hollow fibre membranes

Inner module diameter (mm)	Effective length (m)	Number of fibres	Nominal membrane pore size (μm)
25	0.51	94	0.3

4.3.2 Characterisation of hollow fibre membrane

4.3.2.1 Measurement of hollow fibre membrane dimensions

As shown in Fig. 4.2, the inner and outer diameters were measured directly from the cross section of the tubular module by taking photographs of the fibre cross sections alongside a millimetre scale reference. The printed photo is measured by a digital calliper. The magnification was 7.7 calculated based on the scale shown in the photo and measured by the digital calliper. The inner and outer diameters are calculated from the magnification and the measured dimension by the digital calliper. As shown in Table 4.3, measurements were taken for four fibre pieces and each fibre was measured three times. The mean value of the measured diameters was used to calculate the effective area.

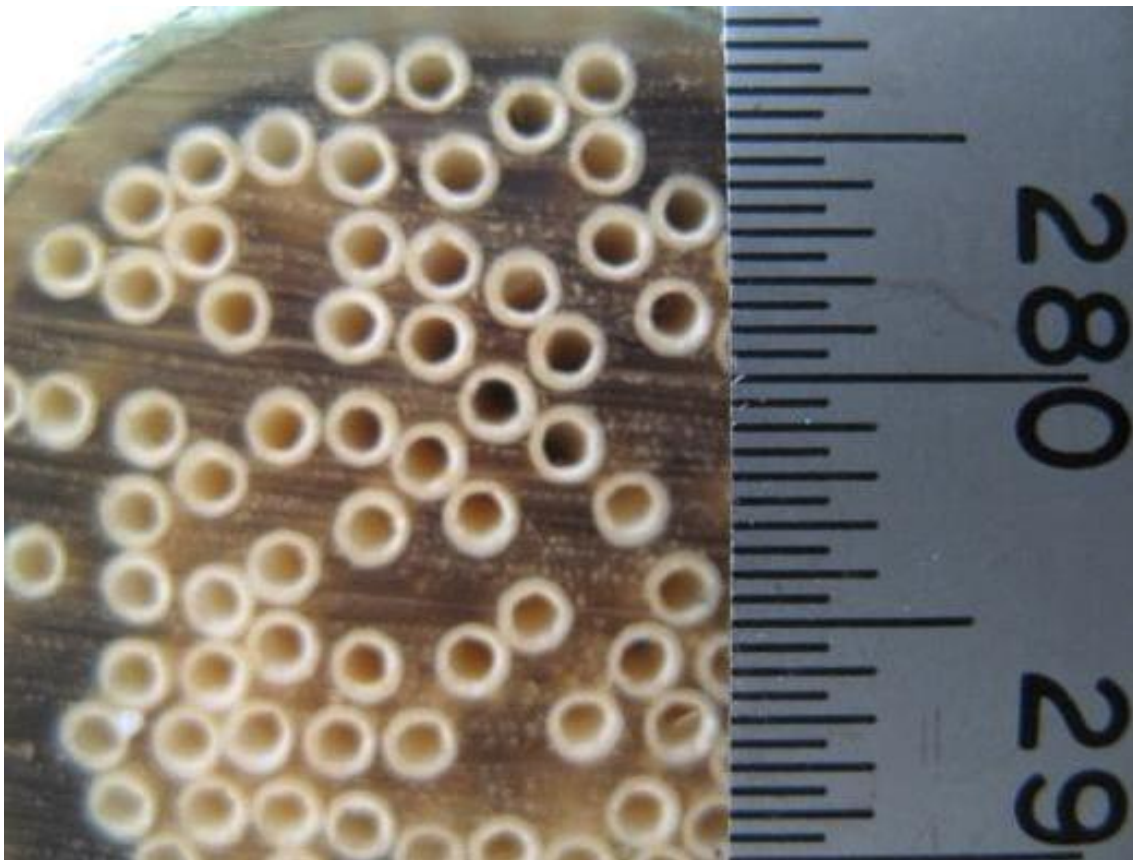


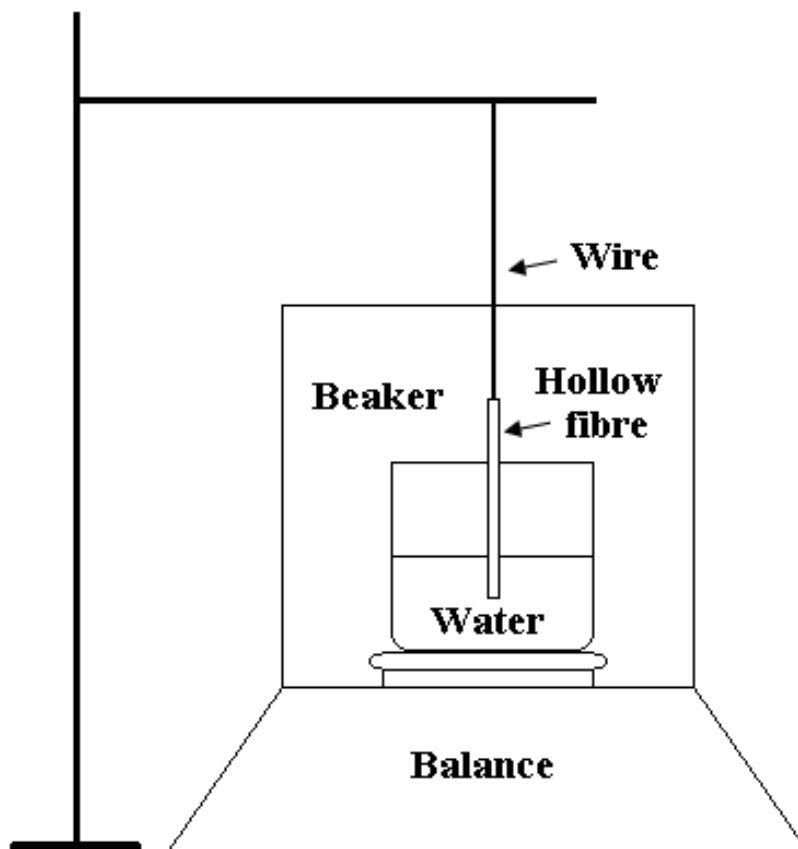
Fig. 4.2 Photo for inner and outer diameter measurement of hollow fibre membrane

Table 4.2 Diameter calculated based the measurement from image

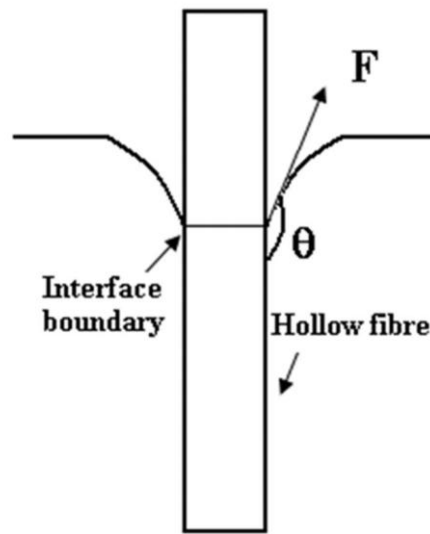
Sample	Inner diameter (d_i) (mm) n=3	Outer diameter (d_o) (mm) n=3
1	0.87	1.69
2	1.04	1.66
3	1.00	1.64
4	0.98	1.56
Average	0.97	1.64

4.3.2.2 Contact angle measurement

Contact angles of inner and outer surfaces were measured via surface tension effects based on [135]. A schematic diagram of the instrument for measuring the outer surface contact angle is shown in Fig. 4.3a.



a. Schematic diagram of the instrument for measuring the outer contact angle



b. Force balance at interface boundary

Fig. 4.3 Contact angle measurement for outer surface

During the measurement, a copper wire was inserted through the lumen side, part of the fibre was submerged in water, and silicon sealant was used to seal the submerged end of hollow fibre and fix the end of copper wire on the lumen side wall, so water could not penetrate the fibre lumen. Due to the surface tension effect, the mass weighed by an A&D balance (HR-200) will decrease. The mass reduction arises from the surface tension shown in Fig. 4.3b and can be described as:

$$\Delta m = F \cos \theta / g \quad (4.4)$$

Thus,

$$\theta = \cos^{-1} \left(\frac{\Delta m g}{F} \right) \quad (4.5)$$

in which F can be calculated with Eq. (4.1).

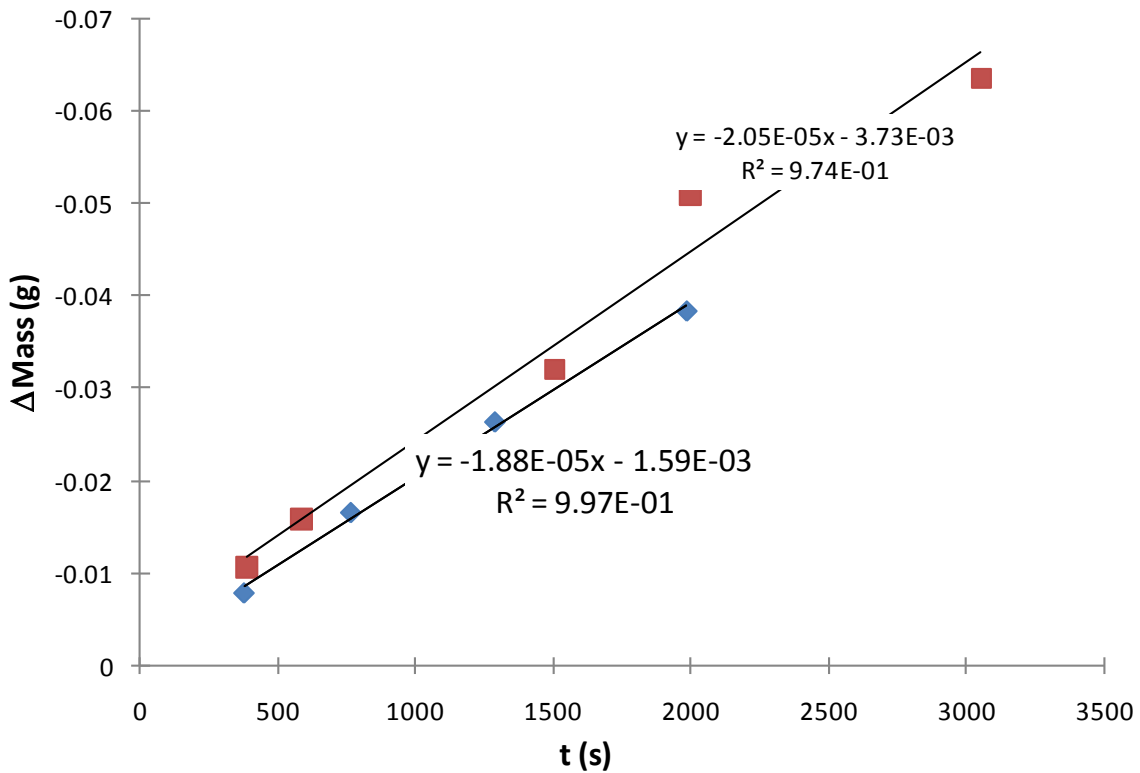
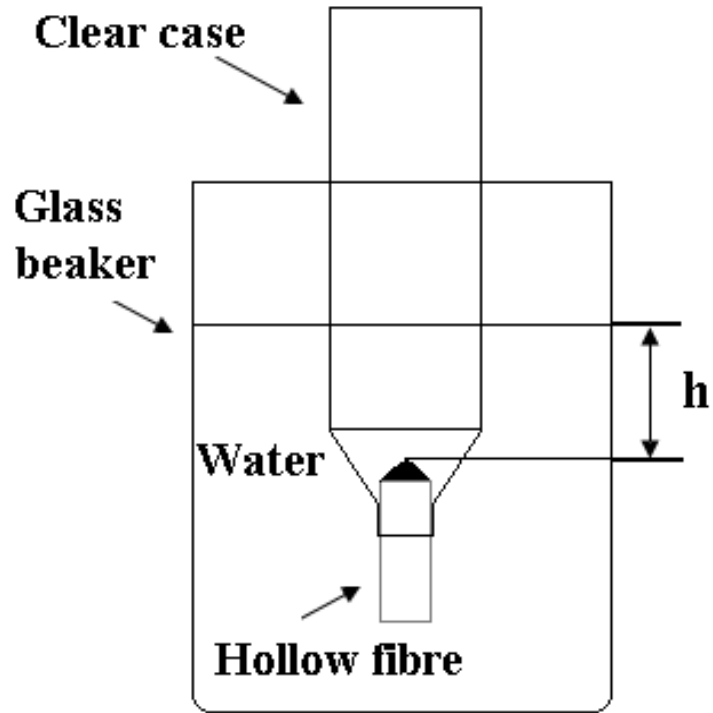


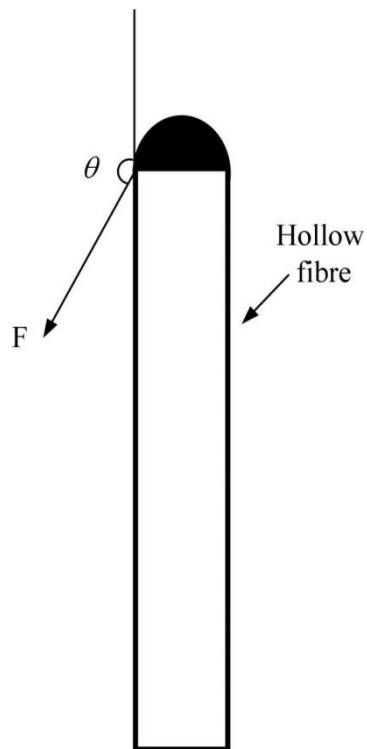
Fig. 4.4 Mass change against the time in contact angle measurement

However, the mass value shown on the balance decreased continuously throughout the measurement period, because the instrument is an open system and water evaporated. Hence, it was difficult to determine the mass reduction caused directly by the surface tension, and it is necessary to know the evaporation rate of the water. During the measurement, the recorded temperature in the laboratory only varied in the ranged of $20 \pm 1^\circ\text{C}$, so it is reasonable to assume the water evaporation rate was constant.

In Fig. 4.4, linear curves fitting the mass change against the time were drawn, from which linear fitting equations were obtained. Because the mass reduction caused by the surface tension will not change with the time, the results calculated as $t=0$ from the equations or the intercept of the curves are the mass reduction resulted from the surface tension. Two fibre pieces were tested and the average was used. Although the two curves showed different intercepts, which may be caused by the difference of fibre circumference, the calculated contact angles differed by less than 3° .



a. Schematic diagram of the instrument for measuring the internal contact angle



b. Force balance at interface boundary

Fig. 4.5 Contact angle measurement for the inner surface

The schematic of instrument for measuring contact angle of inner surface is shown in Fig. 4.5a. In the contact angle measurement for the inner surface, both sides of the fibre were open. One end of the hollow fibre was encased in a clear cylinder, and high vacuum grease was used to seal the clearance between the fibre and the cylinder nozzle. The other end of the fibre was slowly submerged into the water, and the height difference (h) between the top of the fibre and water surface recorded when water first protruded from the top of the fibre. The experiments were repeated four times. The data are shown in Table 4.4.

Table 4.3 Measured height difference (h) between the top of the fibre and water surface

Time	1	2	3	4	Mean
h (mm)	18.51	17.09	18.66	18.48	18.19

As that shown in Fig. 4.5b, the force balance can be expressed as

$$F \cos \theta = -\rho g h \pi (d_i/2)^2 \quad (4.6)$$

Based on Eq. (4.1),

$$h = -\frac{4\gamma_l \cos \theta}{\rho g d_i} \quad (4.7)$$

Therefore,

$$\theta = \cos^{-1} \left(\frac{h \rho g d_i}{4\gamma_l} \right) \quad (4.8)$$

where ρ is the water density, h is the height between the water protrusion and water surface in the beaker and g is acceleration due to gravity.

4.3.2.3 Porosity measurement

The porosity was measured by the wetting method [136]. To reduce measurement error, eight fibres with a total calculated volume of 4.2 ml (based on the mean ID and OD) were used. According to the wettability of the fibre material, the total unwetted fibre volume (including pore volume) and the total wetted fibre volume (mass volume) were measured by soaking the fibre in deionised water and ethanol. Four measurements were taken for the total volume, two measurements were taken for the mass volume, and

fibres were dried completely between each measurement. The porosity was calculated by

$$\varepsilon = 1 - \frac{V_{mass}}{V_{total}} \quad (4.9)$$

where the V_{mass} is the mass volume and V_{total} is the total fibre volume.

The measured mean volume was 4.17 mL which was about the same as the calculated volume, confirming the measurement of the inner and outer diameters.

4.3.2.4 Pore distribution and pore size measurement

Although it was not very popular to use BET to measure the pore size distribution of polymeric membrane, some studies had been conducted in this area [137, 138]. In this study, the pore size of the membrane skin layer was microspore (size less than 2 nm), so it was necessary to use BET for characterisation. Both pore size distribution and mean pore size were measured by a BET (Micromeritics TriStar 3000) instrument using nitrogen adsorption at 77K. Pore size and pore size distribution were calculated from the BJH absorption result. To avoid polymeric material degradation during degassing, the hollow fibre was degassed at a temperature of 70°C for 48 h.

4.3.2.5 SEM characterisation

Surface and cross sectional structures were observed by a Philips XL30 FEG Scanning Electron Microscope (SEM) to verify the results from BET. The investigated membrane was fractured following immersion in liquid nitrogen to form an intact cross section.

4.3.3 DCMD and Vacuum Enhanced DCMD (VEDCMD) Testing

Three experimental configurations were used in the experiments. In the three configurations, the feed temperature was controlled by a digitally controlled heater and was varied in the range of 30-90°C. A digitally controlled refrigerated water bath was used to control the temperature of the cold flow so that it could be recirculated at the set temperature (20°C) in all experiments. The brine feed was prepared by dissolving 100 g NaCl in 10 L water (10 g.L⁻¹). Four temperature sensors were used to measure the temperatures of the hot brine and cold flow sides at their respective inlets and outlets. Two pressures sensors were placed upstream of the hot feed and permeate entrances to

monitor the pressure of each side. A conductivity meter in the product reservoir was used to monitor changes which were used to calculate salt rejection. Flux was determined by measuring the weight of the product reservoir over time. All the flux results presented were calculated based on the outer surface area over a period of 3 to 8 hours and variation in flux over this time was $\pm 5\%$.

According to the lumen side of the hollow fibre or the shell side of the module (outside the hollow fibre) that the feed passed through, the configuration was classified into Setup I (feed on lumen side) and II (feed on shell side). The schematic diagrams of Setup I and II are similar to Fig. 3.4, except two centrifugal pumps and two flow control valves were used instead of the peristaltic pumps. The velocities of the hot and cold streams were controlled by changing the opening of the flow control valves and were varied in the range of 0.24-1.7 m/s (1-7 L/min) and 0.23-0.60 m/s (4-10.4 L/min) respectively in Setup I and II.

Fig. 4.6 shows a schematic diagram of Setup III. To reduce the pressure (P_{pore}) in the membrane pores, the cold stream in the cold cycle was drawn through the shell side of the hollow fibre by a positive displacement pump (Hydra-cell G-13), and the cold stream velocity was varied in the range of 0.1-0.35 m/s (2.1-6.1 L/min). The hot cycle of Setup III was identical to the Setup I.

Although no noticeable flux decay was found in these experiments, after every series of experiments, the membrane was cleaned by fully wetting with ethanol and soaking in 0.1 mol/L HCl solution for 3-10 min.

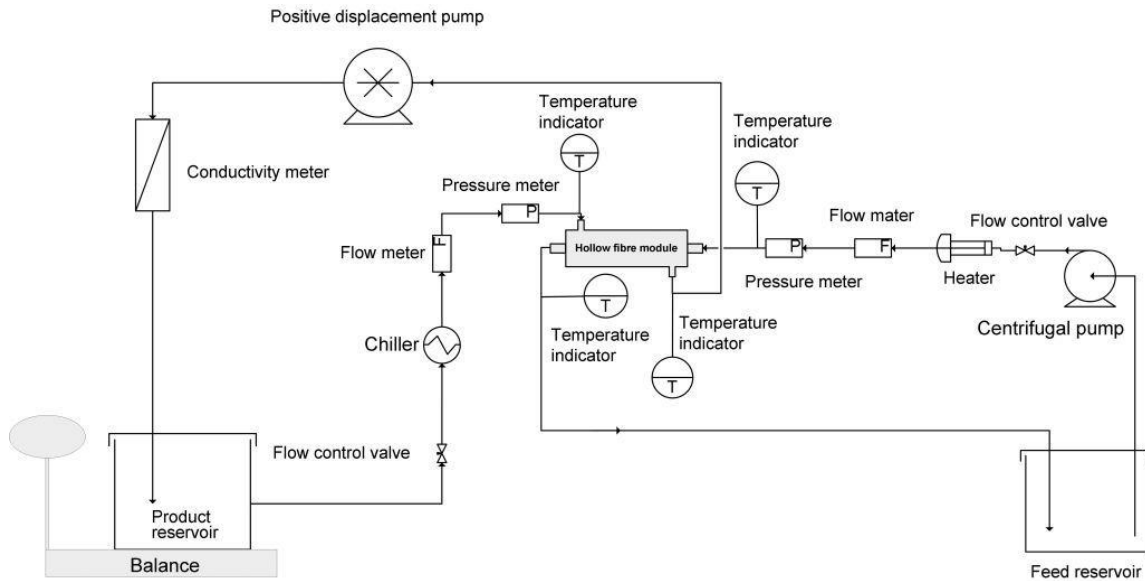


Fig. 4.6 Schematic diagram of the experimental Setup III

4.4 Results

4.4.1 Membrane properties

Table 4.4 lists the measured and calculated properties of the membrane.

Table 4.4 Measured and calculated properties of membrane

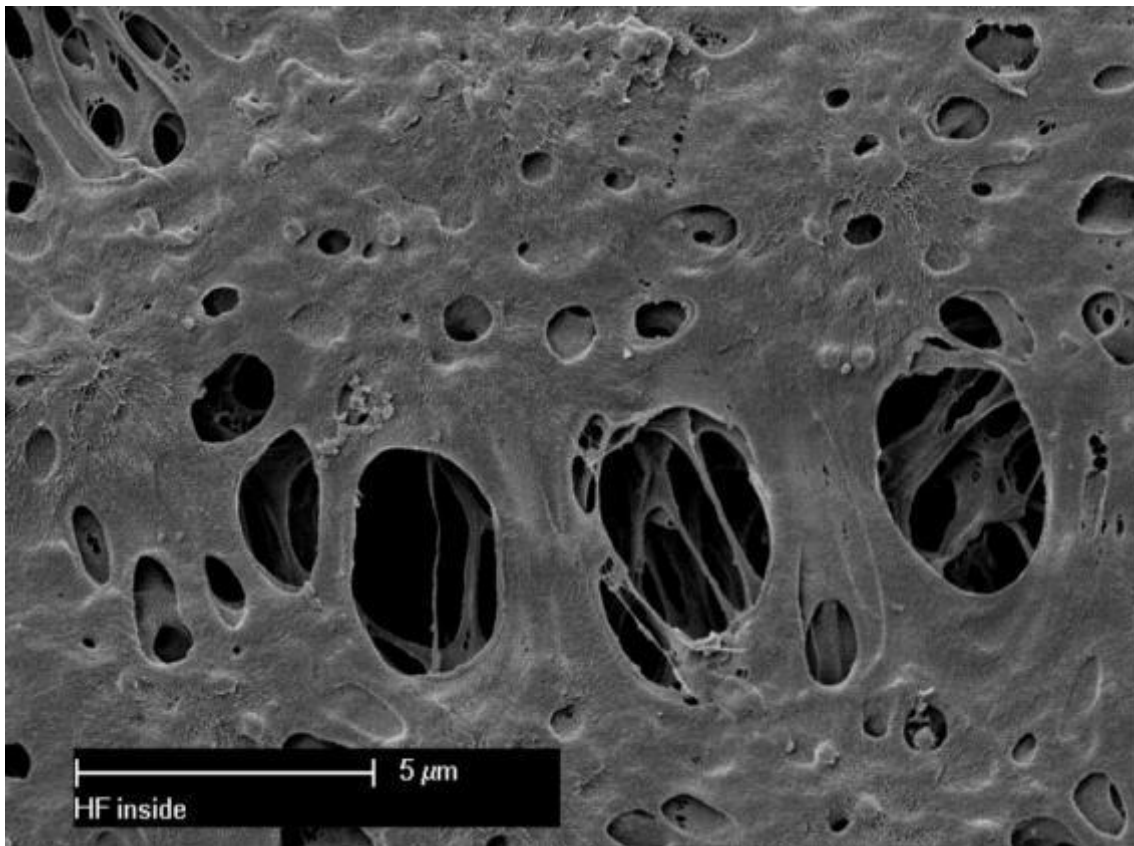
Mean fibre diameter		Membrane thickness	Mean effective area		Mean pore size	Surface contact angle		Mean porosity
(mm)	(mm)		(m ² /module)			(°)	(%)	
Inner	Outer	(mm)	Inner	Outer	(µm)	Inner	Outer	(%)
0.97	1.64	0.38	0.15	0.24	0.33	126±3°	94±2°	82.0

Based on the measured contact angle shown in the table, it can be concluded that the hollow fibre membrane was less hydrophobic than PTFE membranes [48], and its inner surface was more hydrophobic than the outer surface. The measured mean pore size acquired from BET was similar to the provider's data in Table 4.1.

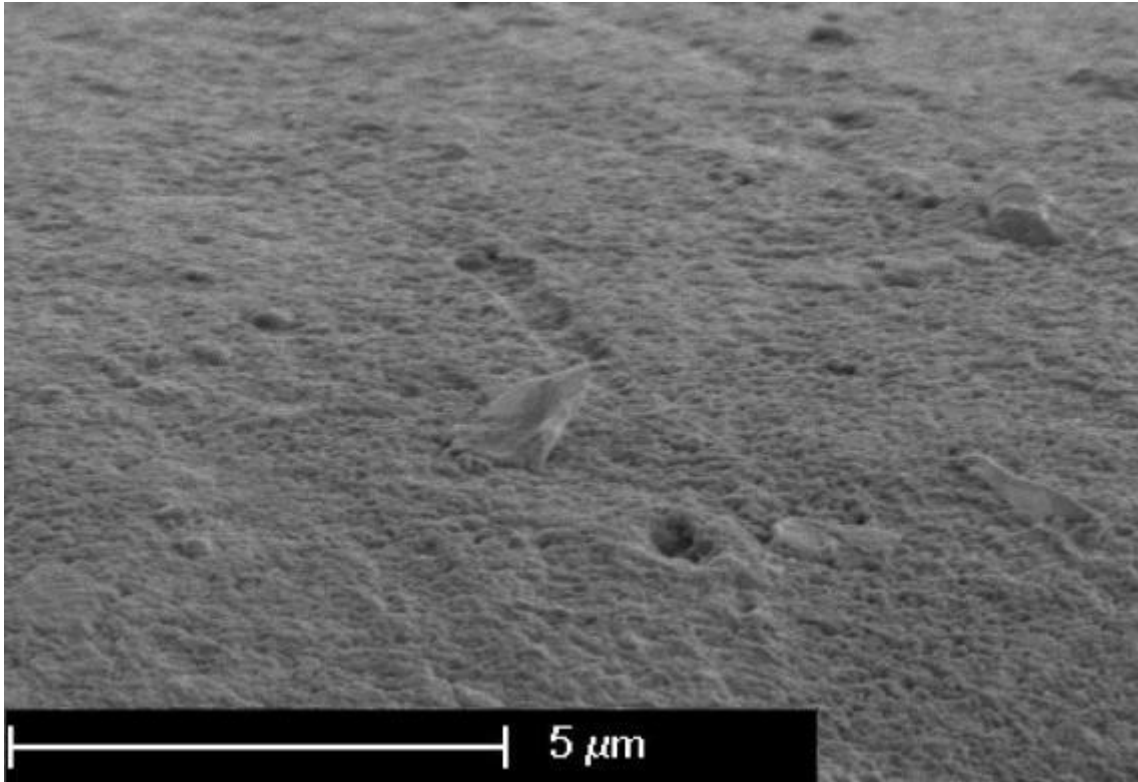
The porosity of the hollow fibre was higher than that of reported polypropylene hollow fibre membrane (~75% porosity) used for membrane distillation and other applications

[139, 140], lower than polyvinylidene fluoride (PVDF) MD membrane (~85% porosity) [59, 141], and similar to the reported (PVDF) MD membrane loaded with 30% polytetrafluoroethylene (PTFE) [59].

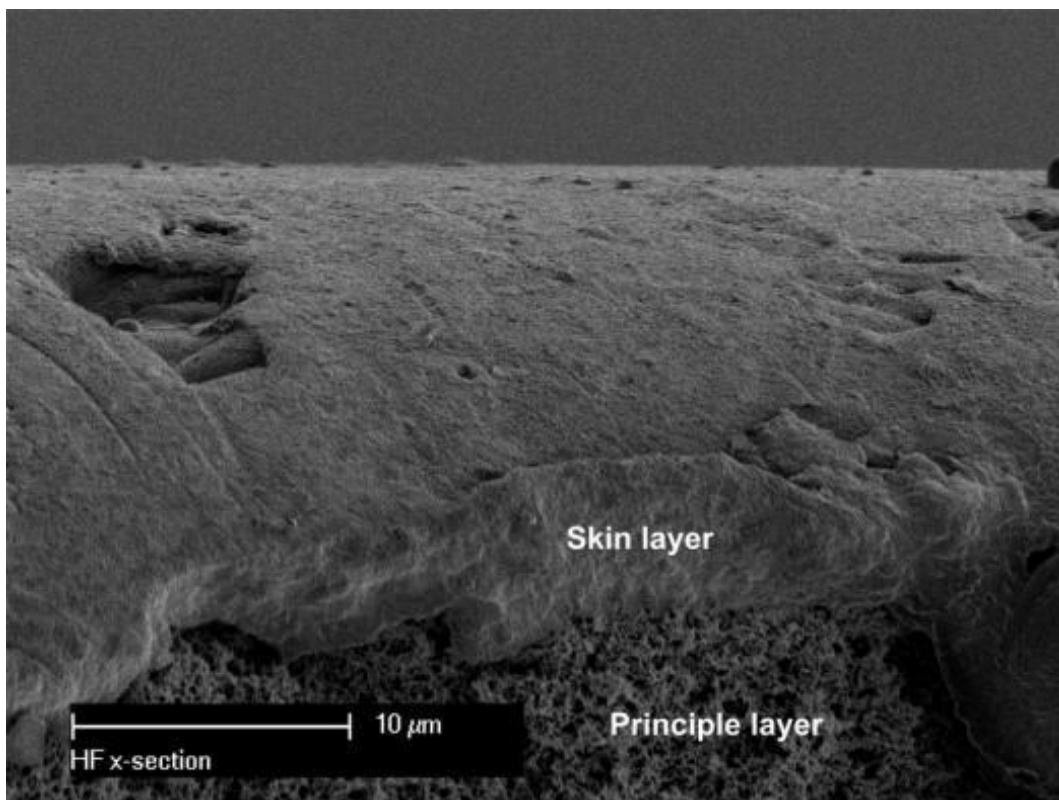
In Fig. 4.7, the SEM images show the structure of principal and skin layers of the hollow fibre membrane. The inner and outer surface (skin layer) structures are shown in images 7a and 7b, in which it can be seen that the outer surface is smoother and denser than the inner surface. Image 7c shows the structures of the cross section of the hollow fibre, which consists of a thick porous principal layer (7d) and a very thin skin layer with tiny pores (7b). From SEM image 7c, the skin layer was estimated to be 5 μm thick, which represents only 1.5% of the total membrane thickness (Table 4.4).



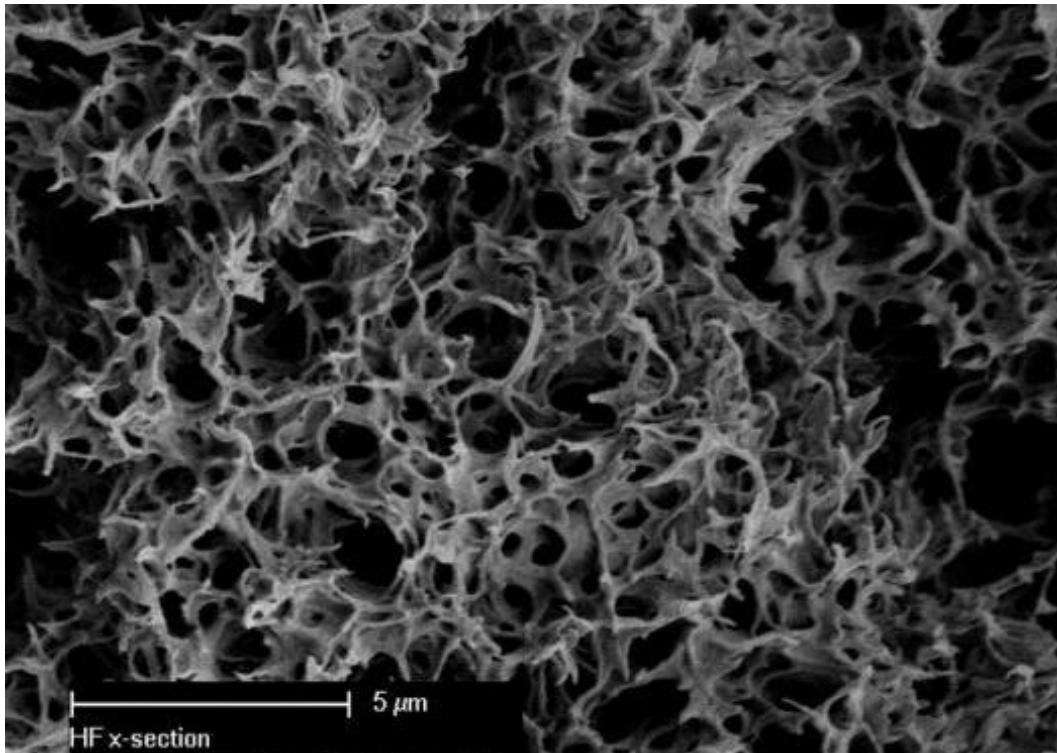
a. Inner surface of the hollow fibre membrane



b. Outer surface (skin layer) of the hollow fibre membrane



c. Cross section of the hollow fibre



d. Cross section of principal layer

Fig. 4.7 SEM images of the hollow fibre

In comparison with a symmetric membrane, this asymmetric structure (skin layer with a smooth surface and tiny pores) can reduce the risk of wetting, e. g. large molecule will not pass through the pores and cause the wetting of the membrane, and it also improves antifouling effects [19, 20] and thereby improves the performance [5]. For example, this kind of membrane can be employed for dewatering dairy product containing large protein molecules which may foul and wet conventional membranes quickly.

The BJH adsorption pore size distribution is presented in Fig. 4.8. There are two emerging peaks in the figure: one appears where the pore size is smaller than $0.002 \mu\text{m}$ and the other where the pore size is larger than $0.16 \mu\text{m}$, corresponding to results found in the SEM image 7c.

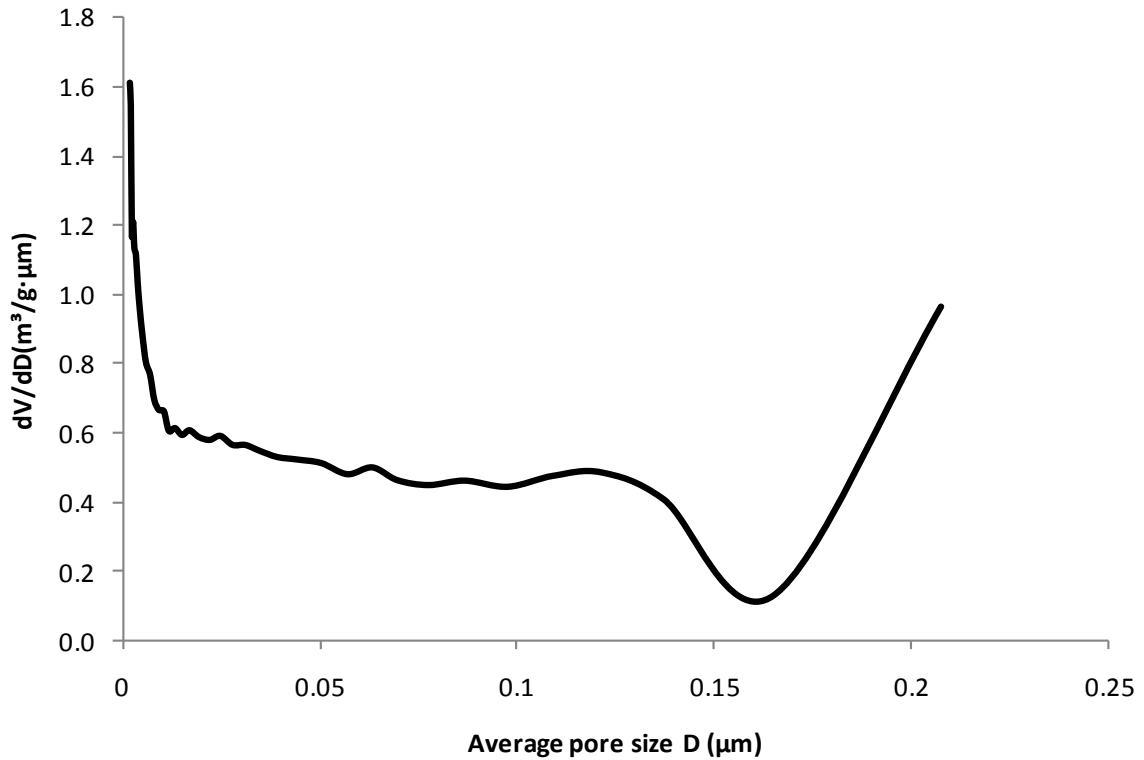


Fig. 4.8 BJH membrane pore size distribution (pore size 0.0017-0.3 μm)

For estimating purposes, Table 4.5 lists the estimated pore sizes of different layers and cumulative pore volumes of different pore size ranges based on the BJH analytical results, and the thicknesses of different layers based on Fig. 4.7 and over all membrane thickness (Table 4.4). For simplification, the pore tortuosities of both layers are assumed to be 1.

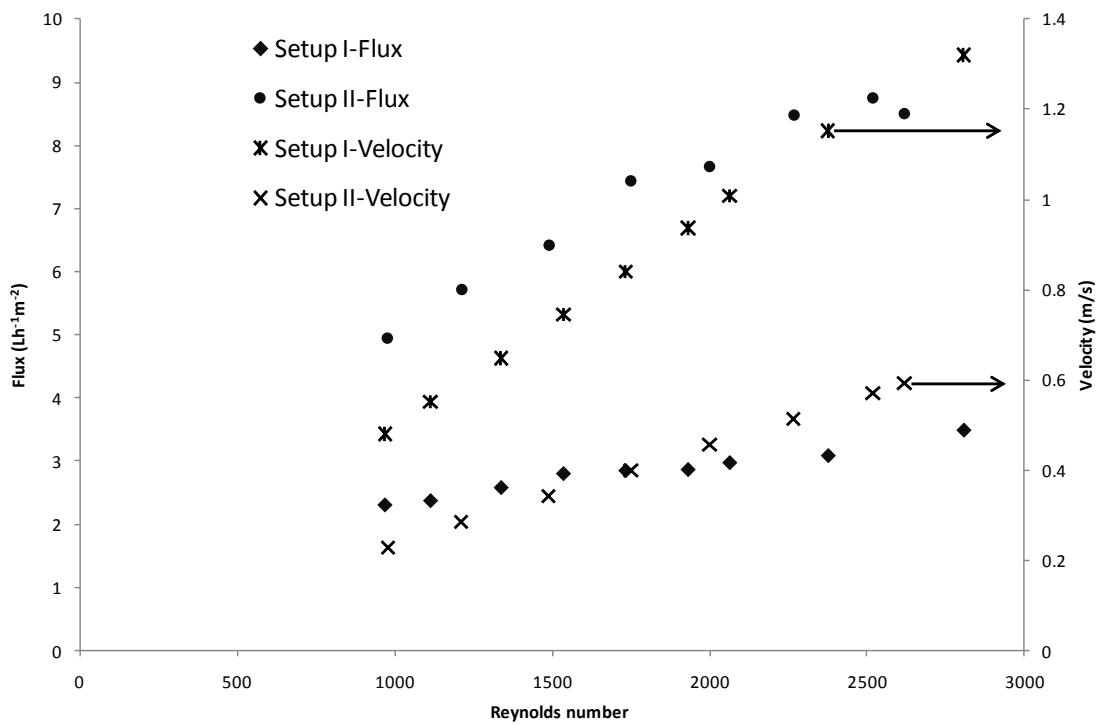
Table 4.5 Estimated properties of the hollow fibre layers

Pore tortuosity	Cumulative pore volumes (cm^3/g)		Pore size (μm)		Thickness (μm)	
	Skin layer ($1.7 \leq D \leq 1.9 \text{ nm}$)	Principle layer ($0.15 \leq D \leq 0.23 \mu\text{m}$)	Skin layer	Principle layer	Skin layer	Principle layer
1	0.0004	0.04	0.0018	0.33	5	665

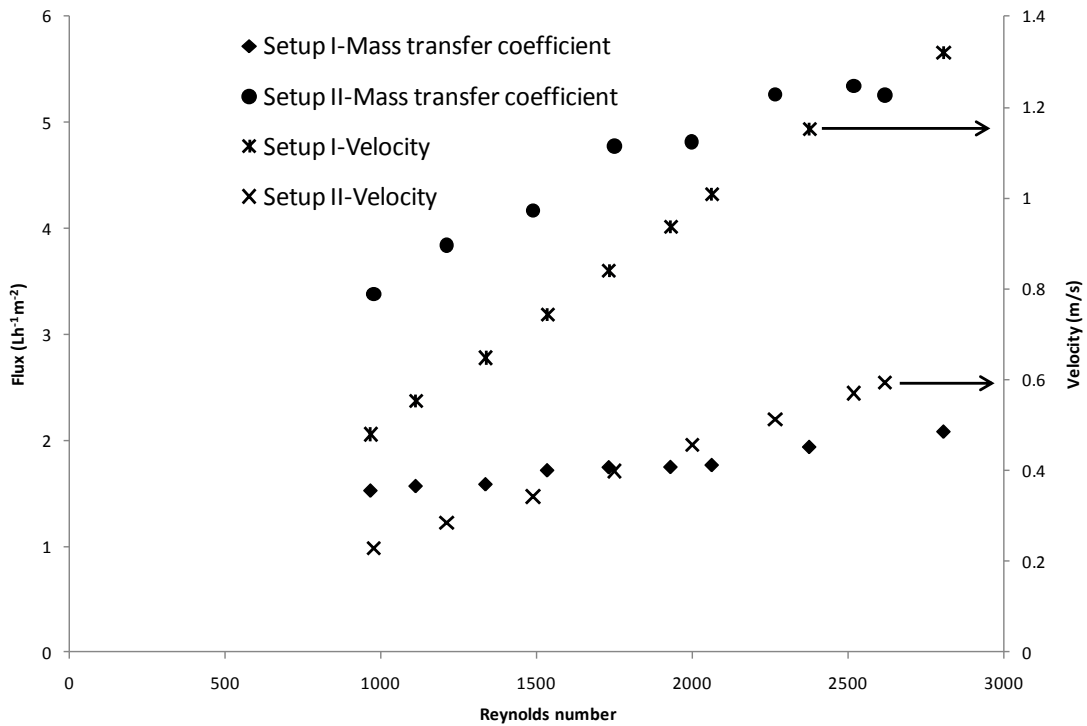
4.4.2 Experimental results

4.4.2.1 Fluxes and global mass transfer coefficients at different Reynolds numbers

In Fig. 4.9, both flux and global mass transfer coefficient curves show similar trends and become flatter at higher Reynolds number (velocities). A similar asymptotic trend of permeate flux with increasing flow rates was reported previously [34, 131].



a. Flux changes at different Reynolds number



b. Global mass transfer coefficients at Reynolds numbers

Fig. 4.9 Influence of velocity on flux and global mass transfer coefficient

(Feed temperature 60°C permeate temperature 20°C)

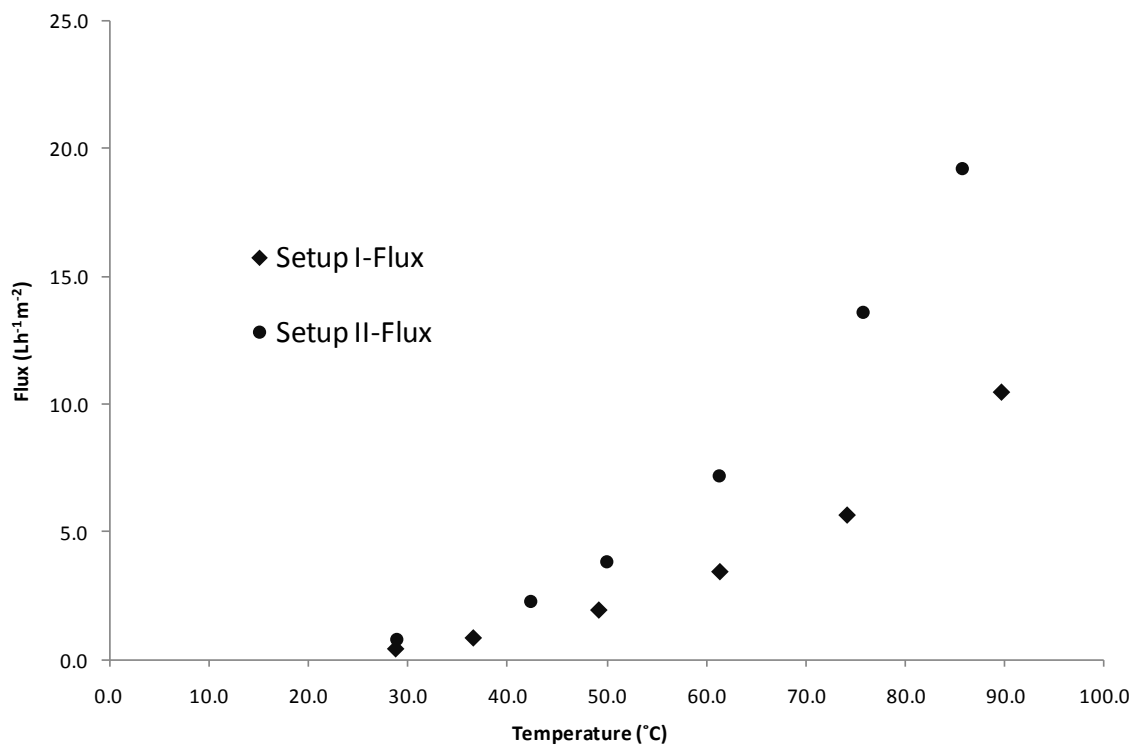
Variation of fluxes with Reynolds numbers for Setup I and II are shown in Fig. 4.9a. In the experiments, inlet temperatures of the cold and hot sides were kept constant and controlled at 20°C and 60°C respectively. The volumetric flowrate on the hot and cold sides were identical, and the feed flowrate was varied in the range of 2.0-5.5 L/min (velocity: 0.48-1.32 m/s, Reynolds number: 970-2,800) and 4-10.4 L/min (velocity: 0.23-0.60 m/s, Reynolds number: 980-2,600) in Setup I and II respectively. When the Reynolds number was increased, both the thermal and hydrodynamic boundary layers were thinned and temperature polarisation reduced because of greater turbulence [142]. As a result, the flux increased by 52% (from 2.3-3.5 L.m⁻².h⁻¹) for Setup I and 80% for Setup II (from 4.9 to 8.8 L.m⁻².h⁻¹).

However, the global mass transfer coefficient shown in Fig. 4.9b increased by 37% (Setup I) and 58% (Setup II) with increasing Reynolds number (velocity), which is less than the percentage increase of flux. Over the higher Reynolds number, e.g. when

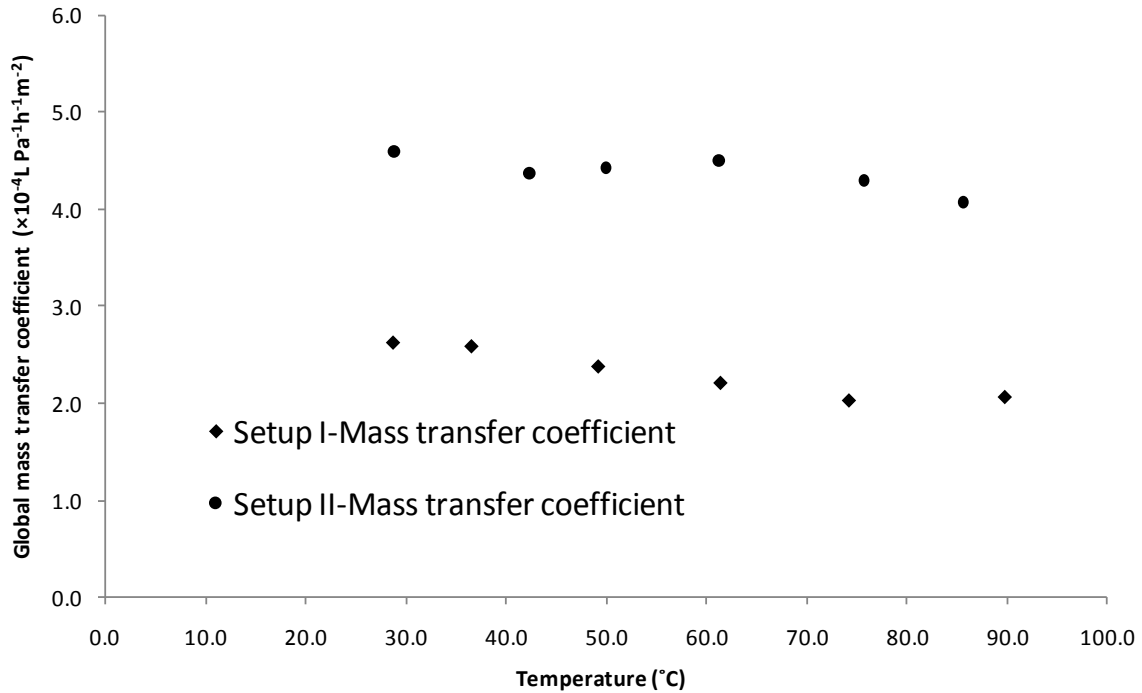
Reynolds number increased from 2,000 to 2,800, there were only 17% (Setup I) and 10% (Setup II) increases of global mass transfer coefficient, compared with 21% (Setup I) and 14% (Setup II) flux increases over the entire range of velocities. Therefore, at Reynolds number or high velocities (the flattened part of the flux vs Reynolds number curve), the increased flux resulted largely from the greater temperature difference across the membrane rather than that from greater turbulence, because the global mass transfer coefficient, which accounts for temperature changes in the bulk liquid, was close to constant at high velocity. This is consistent with the boundary layer thickness being less sensitive to flow velocity at high velocities [143].

4.4.2.2 Temperature influence on membrane flux

The fluxes as a function of hot side inlet temperatures (29-90°C) for Setup I and II are shown in Fig. 4.10a. The cold side inlet temperature was set at 20°C. The feed velocity was selected in the plateau part of the curves in Figs. 4.9a and 4.9b to reduce the effect of the boundary layer on flux and remained constant at 1.7 m/s (7 L/min) for Setup I and 0.4 m/s (7 L/min) for Setup II.



a. Flux at different temperatures



b. Global mass transfer coefficient at different temperatures

Fig. 4.10 Flux and global mass transfer coefficient affected by temperature

(Setup I - Feed velocity 1.7 m/s, Setup II - Feed velocity 0.4 m/s)

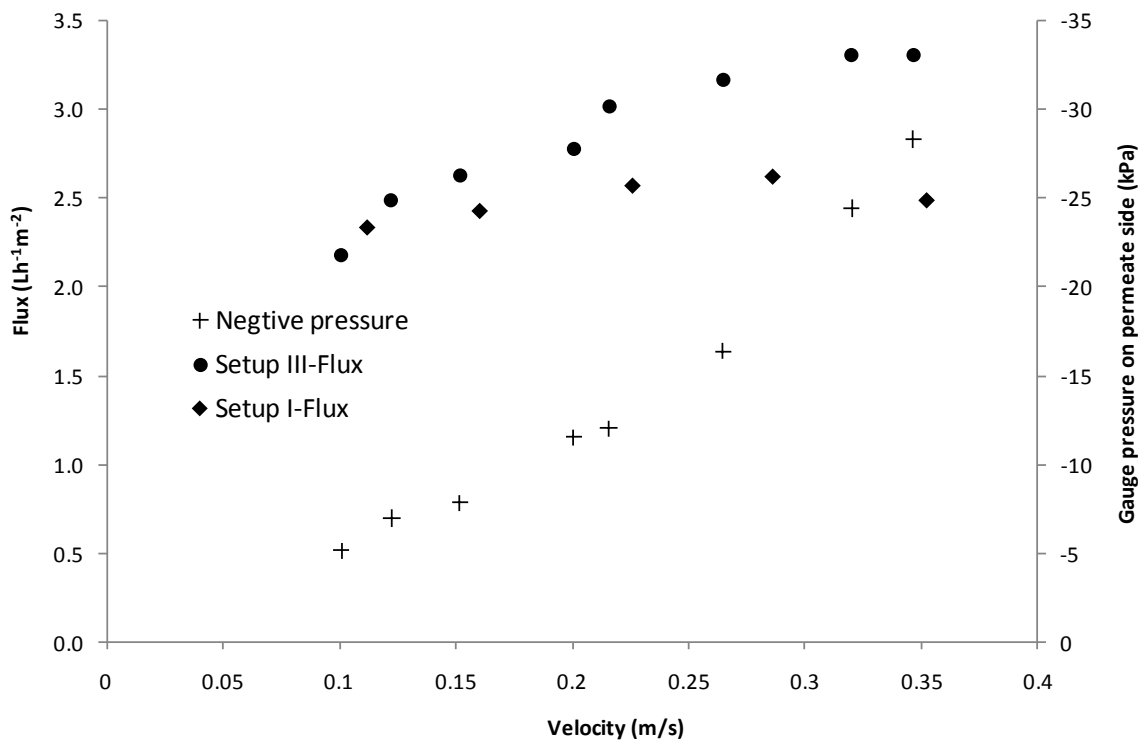
Fluxes for both setups showed an approximately exponential relationship with the temperature, consistent with the relationship between vapour pressure and water temperature. Setup II had higher flux than that of Setup I across the entire temperature range, and the highest flux of $19.2 \text{ L.m}^{-2}\text{h}^{-1}$ was observed at 86°C for Setup II. The global mass transfer coefficient shown in Fig. 4.10b decreased slightly when the temperature rose, suggesting increased polarisation at higher temperatures [24].

As it can be seen from Figs.4.9 and 4.10, the flux and global mass transfer coefficient showed different dependencies on Reynolds number and temperature. At different temperatures, the global mass transfer coefficient was varied by -12% to 11% around the average in Setup I and by -7% to 5% in Setup II, and the flux was varied by -90% to 178% around the average value in Setup I and by -90% to 146% in Setup II. However, at different velocities, the global mass transfer coefficient varied from -44% to 26% in Setup I and from -70% to 38% in Setup II, and the flux varied from -30% to 24% in Setup I and from -32% to 17% in Setup II. Therefore, it suggests that the global mass

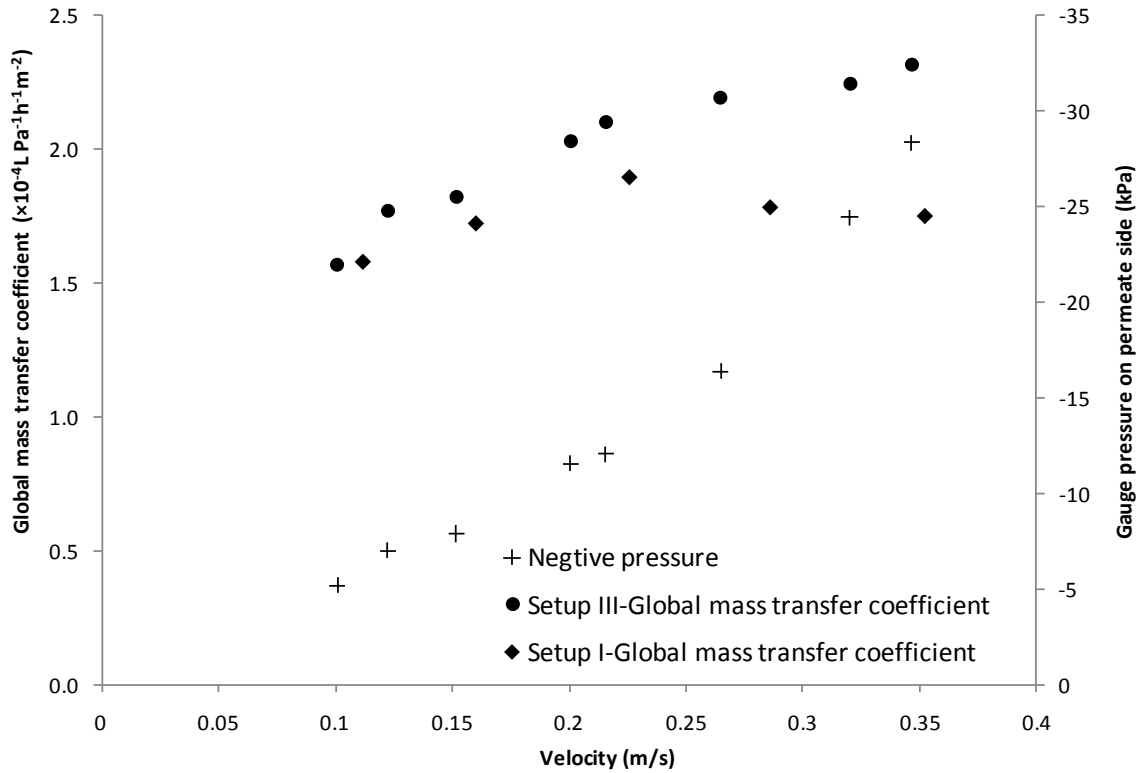
transfer coefficient is a strong function of Reynolds number but not temperature, and both the feed inlet temperature and stream Reynolds number have great influence on the flux, although flux variation over the temperature range was twice and triple that of the flux variation for the velocity range tested.

4.4.2.3 Flux variation with enhanced vacuum on the cold side

Setup III, Vacuum enhanced direct contact membrane distillation (VEDCMD) was used to test the effect of negative pressure in the pore on flux. Although no collapse of the fibre was observed, the large inner and outer diameters of the fibre made collapsing a possibility if the pressure on shell side is much higher than the pressure on lumen side. Because additional hollow fibre modules were not available, the cold flow was put under negative pressure from the shell side to avoid the risk of damaging the membrane.



a. Flux at different negative cold stream pressures



b. Global mass transfer coefficient at different negative cold stream pressures

Fig. 4.11 Vacuum enhanced membrane distillation

(Feed on lumen side, hot inlet temperature=60°C, cold inlet temperature=20°C)

In the experiment, the hot feed velocity was kept constant at 1.7 m/s (7 L/min), cold permeate velocity was varied in the range of 0.1-0.35 m/s (1.6-2.3 L/min), and inlet temperatures on the hot and cold sides were set at 60 and 20°C, respectively. The negative pressure was enhanced by increasing the cold stream velocity. For the purposes of comparison purposes, the experiment was also conducted in Setup I at the identical inlet temperatures and velocities.

Fig. 4.11a shows the relationship between velocity and pressure on cold side in Setup III, and the effect of the velocity (negative pressure) on flux in both Setups I and III. Fig. 4.11b shows the effect of cold side velocity (negative pressure) on the global mass transfer coefficient in both Setups I and III. With increasing cold stream velocity, the flux and global mass transfer coefficient from Setup I increased initially, reached a maximum value at a feed velocity of 0.23 m/s, and then decreased. However, the flux and global mass transfer coefficient obtained from Setup III increased with increasing

velocity (lowered negative pressure) over the entire test range, but the rate of flux increase reduced at higher vacuum pressures.

4.4.2.4 Feed pressure and salt rejection

Salt rejection in all experiments was higher than 99% and did not change appreciably with velocity and temperature, which may be attributed to the large inner diameter and the small pore size of the hollow fibre membrane.

In Fig. 4.12, the relationship between the inlet pressures on both sides of the membrane and the flow velocity is presented. Even when the linear velocity on the lumen side was as high as 2.5 m/s (10 L/min), the inlet pressure was only 90 kPa. This is still lower than the LEP (Eq. (3.2)) of a membrane with a maximum pore size of 1.7 μm , assuming B equals 1, γ_l is the surface tension at 60°C, and θ is the contact angle ($126^\circ \pm 3$) of the inside surface.

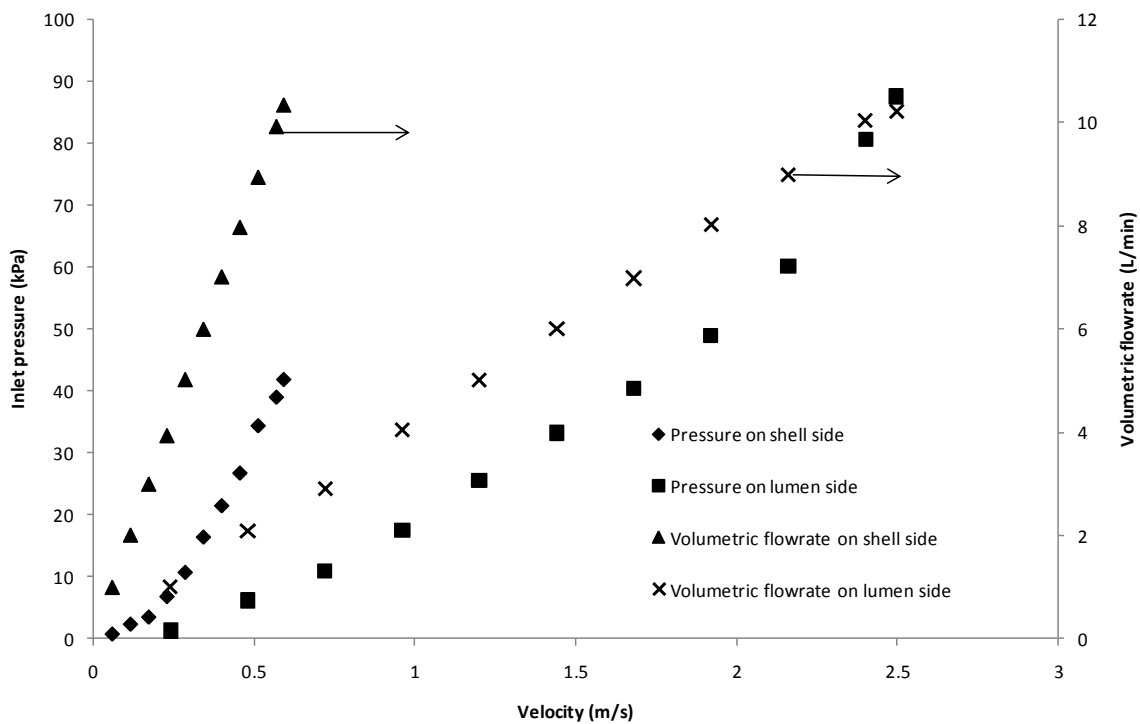


Fig. 4.12 Relationship between inlet pressure and velocity (Setups I and II)

4.5 Discussion

In Table 4.5, the pore size of the skin layer was calculated from

$$r_{skin} = \frac{4V_{skin}}{A_{skin}} \quad (4.10)$$

where A_{skin} is the cumulative pore surface area for pores in the size ranges of the skin layer.

The cumulative volume of the principle layer is only calculated from the pores with sizes in range of 0.15-0.23 μm , which is smaller than the measured membrane mean pore size so its real cumulative pore volume should be more than 0.04 cm^3/g .

Fig. 4.13 shows an idealised diagram of the membrane structure, which consists of a thin skin layer and a thick principle layer. Here, T_1' is the interface temperature between the skin layer and the stream it is contacted with, T' is the temperature between the skin layer and principle layer, and T_2' is the interface temperature between the principle layer and the stream it is contacted with.

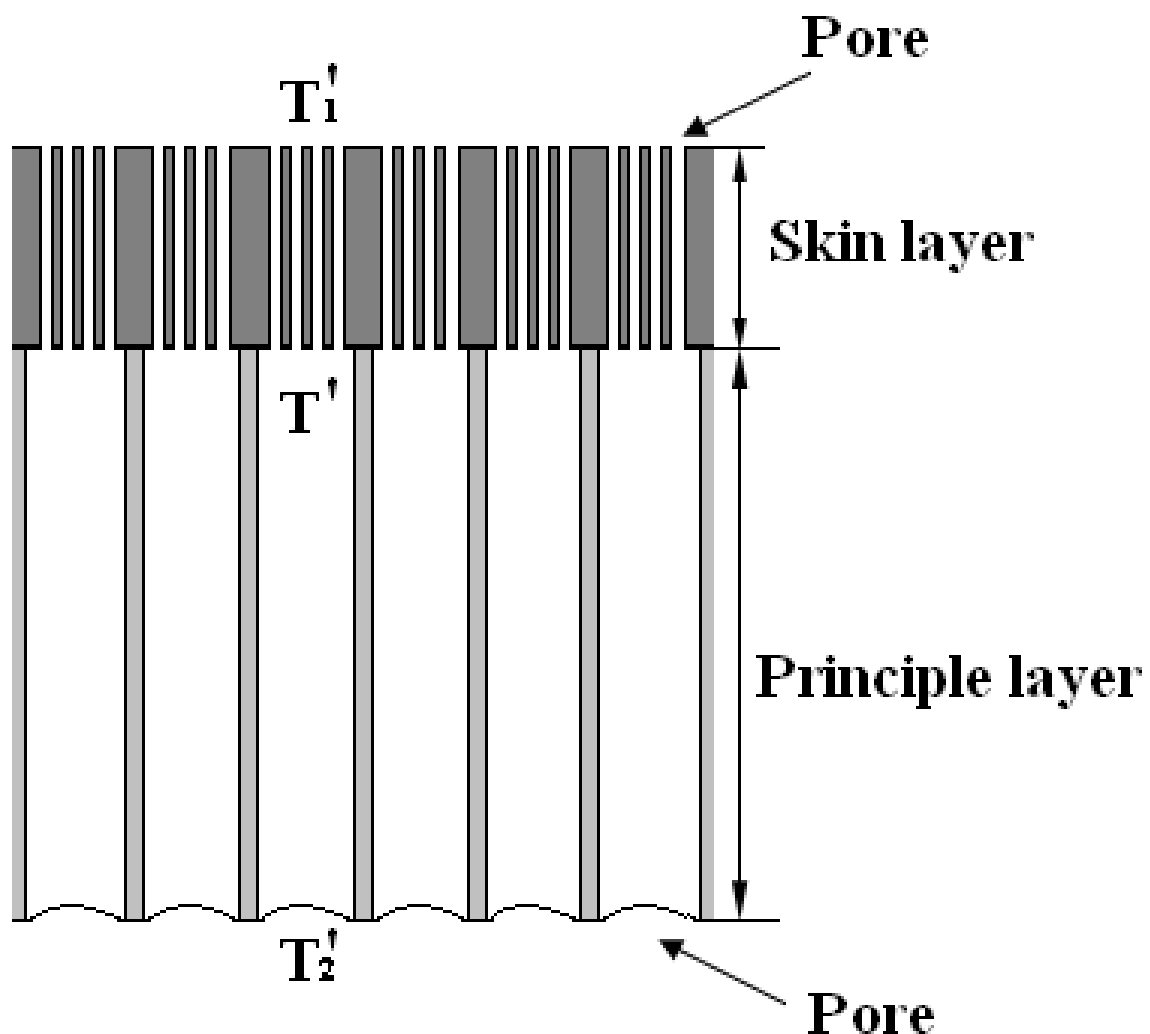


Fig. 4.13 Schematic of the idealised membrane structure and temperature distribution

4.5.1 Vacuum enhanced membrane distillation

The flux and global mass transfer coefficient increasing with the decreasing pressure on permeate side was first identified by Cath et al. [144]. Compared with DCMD, up to 15% increment of flux in the work of Cath et al. and 30% increment of flux in this study were obtained, when VEDCMD was employed. This observation can be explained by the diffusion theory. Under the experimental conditions, the pore sizes of the principle layer and skin layer are estimated as 0.33 and 0.0018 μm and the mean free path of water vapour is 0.11 μm at a feed temperature of 60°C [90], and Kn calculated from Eq. (2.13) is 0.33 in the principle layer and 61 in the skin layer. Thus, in this experiment, the transport of water vapour through the membrane can be interpreted by the Knudsen-molecular diffusion transition mechanism in principle layer and by the Knudsen mechanism in the skin layer [35, 90], and the flux can be described by:

In skin layer,

$$J_{skin} = J_k = \frac{8}{3} r_{skin} \frac{\varepsilon}{bt} \sqrt{\frac{1}{2\pi RMT}} \Delta P \quad (4.11)$$

In the principle layer,

$$\frac{1}{J_{principle}} = \frac{1}{J_k} + \frac{1}{J_m} = \frac{1}{\frac{8}{3} r_{principle} \frac{\varepsilon}{bt} \sqrt{\frac{1}{2\pi RMT}} \Delta P} + \frac{1}{\left(\frac{1}{1-x_A} \frac{\varepsilon}{bt} \frac{D_{AB}}{RT} \right) \Delta P} \quad (4.12)$$

Because in this case, the diffusivity in the pores can be described by:

$$D_{AB} = \frac{1.895 \times 10^{-5} T^{2.072}}{P} \quad (4.13)$$

and assuming it is an ideal gas mixture in the pore,

$$x_A = \frac{P_A}{P} \quad (4.14)$$

We derived:

$$J_m = \frac{1.895 \times 10^{-5} T^{1.072}}{(P_{pore} - P_A)R} \cdot \frac{\varepsilon}{bt} \Delta P \quad (4.15)$$

where ΔP is partial pressure difference across the membrane layer, and x_A and P_A are mole fraction and partial pressure of water vapour in the pore.

As depicted in Fig. 4.1 and discussed in force balance at the pore entrance in Section

4.2.1, when the stream pressure is lower than the total pressure in the pores, the air in the pores will bubble out until the pressures in the pore and the low pressure side are again balanced. Therefore, if the permeate pressure decreases, the total pressure in the pore will decrease. From Eqs. (4.11)-(4.15), it was found that J_k is a function of temperature and vapour pressure, and J_m is a function of temperature, vapour pressure and total pressure in the pores. Because the vapour pressure will only change with temperature under the experimental pressure range (shown in Fig. 4.12), J_k will not be affected by the pressure decrease on the permeate side. However, J_m as represented in Eq. (4.15) will increase as the total pressure in the pores reduce with decreasing permeate pressure. Thus, in VEDCMD, the increase of global mass transfer results from a faster molecular transfer mechanism under lower pore pressure.

4.5.2 Influence of asymmetric structure of hollow fibre membrane on flux

4.5.2.1 Mass transfer resistance analysis

The experimental results show that the flux of the hollow fibre module was not only affected by the temperature, velocity and negative pressure as generally accepted for membrane distillation [3], but also by the channel that the hot feed stream flowed through. This is seen in Fig. 4.9a, where flux from Setup II is nearly four times of that from Setup I under the same temperature and velocity conditions. In Fig. 4.10a, Setup II still produced more than twice the flux of that from Setup I at the same temperature, although the hot feed velocity in Setup I was more than four times of that in Setup II. The reason for this phenomenon can be explained by the asymmetrical structure of the hollow fibre. According to [145], the resistance of composite membranes to mass transfer can be represented by:

$$R_{membrane} = R_{skin} + R_{principle} = \frac{1}{C_{skin}} + \frac{1}{C_{principle}} \quad (4.16)$$

Combining with Eq. (2.19), as it is a hollow fibre membrane, the membrane thickness used is the logarithmic mean value. Therefore,

$$\frac{R_{principle}}{R_{skin}} = \frac{r_{skin}^a \varepsilon_{skin} \cdot d_{po} \ln(d_{po}/d_{pi}) t_{principle}}{d_{so} \ln(d_{so}/d_{si}) t_{skin} \cdot r_{principle}^a \varepsilon_{principle}} \quad (4.17)$$

The porosity can be calculated from the cumulative volumes of each layer as, for

example, the porosity of skin layer can be calculated as

$$\varepsilon_{skin} = \frac{V_{skin}}{\pi(d_{so}^2 - d_{si}^2)l_{fibre}} \quad (4.18)$$

Therefore,

$$\frac{R_{principle}}{R_{skin}} = \frac{r_{skin}^a}{r_{principle}^a} \frac{V_{skin}}{V_{principle}} \frac{\ln(d_{po}/d_{pi})}{\ln(d_{so}/d_{si})} \frac{d_{po}(d_{po}^2 - d_{pi}^2)}{d_{so}(d_{so}^2 - d_{si}^2)} \frac{t_{principle}}{t_{skin}} \quad (4.19)$$

where $R_{membrane}$, R_{skin} and $R_{principle}$ are the mass transfer resistance of membrane, skin layer and principle layer, C_{skin} and $C_{principle}$ are the mass transfer coefficients of skin layer and principle layer, d_{so} and d_{si} are the outer and inner diameters of the skin layer, d_{po} and d_{pi} are the outer and inner diameter of the principle layers, r_{skin} and $r_{principle}$ are the pore sizes of the skin layer and principle layer, and V_{skin} and $V_{principle}$ are cumulative pore volumes of pore size ranges respectively in skin layer and principle layer.

4.5.2.2 Heat transfer resistance analysis

Based on the data listed in Table 4.5 and using Eq. (4.19), it can be estimated that the mass transfer resistance of the skin layer is at least about 1-140 times that of principle layer, depending on the value of a .

According to Eq. (2.6) and Fig. 4.13, the heat balance of the two layers can be represented as,

$$\frac{\lambda_{skin}}{d_{so} \ln(d_{so}/d_{si})} (T'_1 - T') + J_{skin} H_{latent} = \frac{\lambda_{principle}}{d_{po} \ln(d_{po}/d_{pi})} (T' - T'_2) + J_{principle} H_{latent} \quad (4.20)$$

where d_{so} (1640 μm) \approx d_{po} (1635 μm) and flux is calculated based on the outer surface, so

$$J_{principle} = J_{skin} \quad (4.21)$$

Therefore,

$$\frac{T'_1 - T'}{T' - T'_2} = \frac{\lambda_{principle}}{\lambda_{skin}} \frac{d_{so} \ln(d_{so}/d_{si})}{d_{po} \ln(d_{po}/d_{pi})} \quad (4.22)$$

Assuming the skin layer and principle layer are prepared from the same material, based on Eq. (2.4) and the parameters of each layer:

$$\frac{T'_1 - T'}{T' - T'_2} = \frac{\lambda_{air} \varepsilon_{principle} + \lambda_{principle} (1 - \varepsilon_{principle})}{\lambda_{air} \varepsilon_{skin} + \lambda_{skin} (1 - \varepsilon_{skin})} \cdot \frac{d_{so} \ln(d_{so}/d_{si})}{d_{po} \ln(d_{po}/d_{pi})} \quad (4.23)$$

The conductivity of solid material is greater than that of air in general, and from Fig. 4.7, it can be found that the principle layer is more porous than the skin layer, so

$$\frac{\lambda_{air}\varepsilon_{principle}+\lambda_{principle}(1-\varepsilon_{principle})}{\lambda_{air}\varepsilon_{skin}+\lambda_{skin}(1-\varepsilon_{skin})} < 1 \quad (4.24)$$

Therefore, based on the inner and outer diameters of the skin layer and principle layer, it can be estimated:

$$\frac{T'_1-T_1}{T_1-T'_2} < \frac{1}{170} \quad (4.25)$$

Because

$$|T'_1 - T'_2| > |T_1 - T_2| \quad (4.26)$$

Derived

$$|T'_1 - T_1| < \frac{1}{170} |T'_1 - T'_2| \quad (4.27)$$

In this study, depending upon the velocities, the average bulk stream temperature difference between the hot side and cold side was 29-35°C at cold and hot inlet temperatures of 20 and 60°C respectively. The average bulk stream temperature difference was 52°C at cold and hot inlet temperatures of 20 and 86°C with a feed flow velocity of 0.4 m/s. Therefore, according to Eq. (4.27), the maximum theoretical temperature difference across the skin layer is less than 0.31°C, even when assuming the polarisation coefficient equals 1. Fig. 4.14 represents the vapour pressure difference across the skin at a temperature difference of 0.31°C ($T'_1 < T_1$), in which the vapour pressure is given by Antoine equation [9, 146]. From this figure, it was found that the vapour pressure difference across the skin layer at $T'_1=60^\circ\text{C}$ is 6.4 times of that at $T'_1=20^\circ\text{C}$. Thus, if the skin layer contacts the cold permeate, the vapour pressure across the skin layer will be much smaller than that when contacting the hot feed. Therefore, based on Eq. (2.19), the permeate flux across the skin layer will be much smaller, if the cold permeate rather than the hot permeate contacts the skin layer.

Based on this theory, the bow shaped flux and global mass transfer curves of Setup I in Figs. 4.11a and 4.11b can also be explained. In this experiment, increased cold stream velocities reduced both the boundary layer thickness and the surface temperature of the

skin layer. At lower velocities (<0.22 m/s), where the boundary layer on the cold side is still an important mass transfer barrier, the flux will increase with the thinning of the boundary layer. However, at higher velocities (>0.22 m/s), the resistance of the boundary layer to mass transfer will not change significantly with the increasing velocity, while lowering the temperature of the skin layer will reduce the vapour pressure driving force across the skin layer so as to cause a decrease in flux.

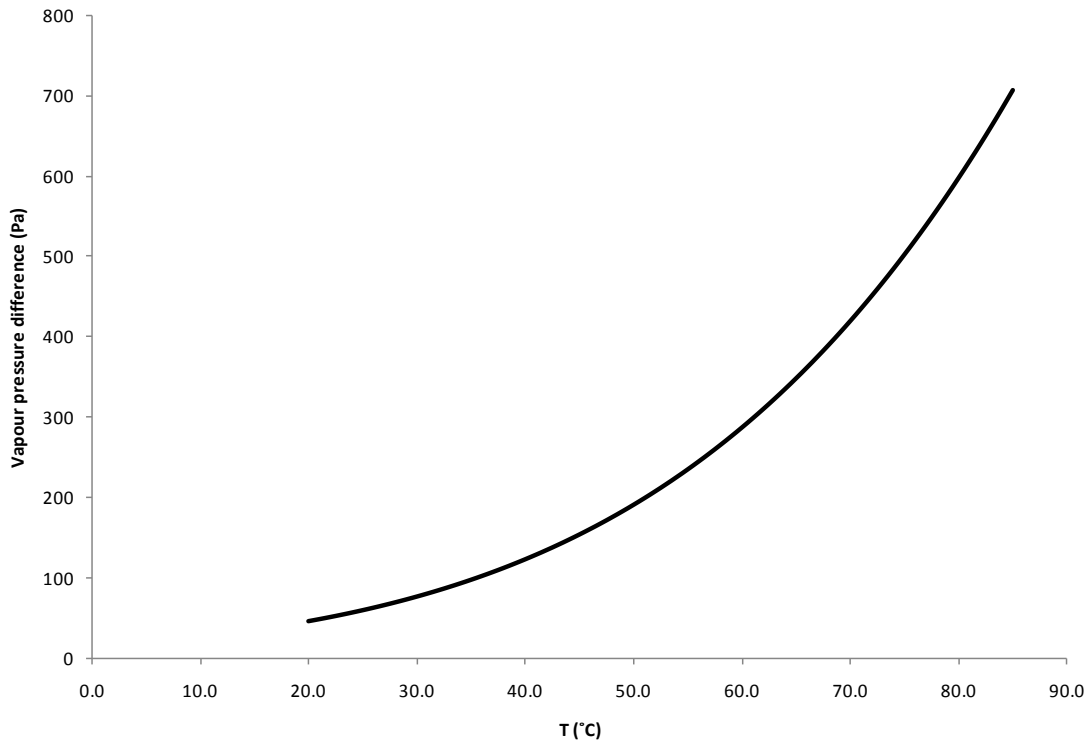


Fig. 4.14 Vapour pressure difference across skin layer at different temperatures ($\Delta T=0.31^{\circ}\text{C}$)

In comparison, it was also observed that the gradient of Setup III (Fig. 4.11b) started to stabilise at velocities higher than 0.22 m/s. In this region, the global mass transfer coefficient increased linearly with velocity in Setup III, while the global mass transfer coefficient for Setup I decreased at these velocities. The increase in the global mass transfer coefficient for Setup III is due to the effect of increasing negative pressure in the permeate stream overriding the lower skin temperature.

According to this finding, the greatest flux should be achieved when the hot feed is closest to the high mass transfer resistance skin layer and the permeate stream has negative pressure. For this particular membrane, this requires the hot feed to be placed

on the shell side and the cold flow under negative pressure on the lumen side. This condition may lead to collapse of the membrane used in this study, because the hollow fibre had a large diameter (force applied on the membrane is square ratio to the hollow fibre diameter) and was found to be fragile in the material property tests. Therefore, if a high resistance skin layer could be formed on the lumen side rather than the outer wall, the performance of the hollow fibre membrane will be improved in VEDCMD.

The analysis also showed the global mass transfer coefficient to be a better parameter than flux for comparison of MD membranes, as it was less sensitive to the effect of variations in operating temperatures and is therefore more dependent upon material properties.

4.6 Summary

The performance of asymmetric hollow fibre membranes in DCMD was assessed based on the variation of temperatures, Reynolds numbers, flow velocities, stream configuration, and the degree of cold side vacuum pressure in the hollow fibre module. Flux was calculated based on the outside surface area of the hollow fibre membrane, irrespective of the direction of permeate transport as the skin layer was the dominant mass transfer layer.

The membrane showed different performances when the hot feed passed through different sides (lumen and shell sides) of the membrane. In this study, the highest flux was $19.2 \text{ L.m}^{-2}\text{h}^{-1}$, when the feed flowed through the shell side with a velocity of 0.4 m/s and the inlet temperatures on the cold side and hot side were 20°C and 86°C respectively (without vacuum pressure on the permeate side). The variation in performance can be attributed to the asymmetric structure of the membrane, and the exponential relationship between vapour pressure and temperature.

Global mass transfer coefficients were calculated to evaluate the performance of the process under different conditions. The use of the global mass transfer coefficient removes the temperature dependence of the flux measurements, and so provides a means to study the polarisation effects. This was confirmed by the experimental results which showed that the global mass transfer coefficient at high velocities remained approximately constant as the hot feed temperature increased from 30 to 86°C .

Therefore, the global mass transfer coefficient is a better parameter than flux for the comparison of MD membranes, as it is less sensitive to the effect of variations in operating temperatures and is therefore more dependent upon material properties.

Negative gauge pressure on the cold side boosted the flux by reducing the pressure within the pores and thereby increasing the rate of mass transfer through the pores. However, the rate of increase in flux reduced at higher vacuum pressures indicating that there is a diminishing return for flux at higher negative pressures beyond -12 kPa (feed velocity > 0.22 m/s), due to the skin layer effect. A non-compressible hollow fibre would be advantageous for high flux hollow fibre MD, as it would enable a negative pressure to be employed in the permeate stream on the lumen side.

The results show that salt rejections higher than 99% can be achieved even at very high feed velocities, due to the large inner diameter of the hollow fibre membrane and the small pore sizes at the skin layer.

Chapter 5 Effect of applied total pressure on the performance of PTFE membranes in DCMD

5.1 Introduction

As was found in the theory section of **Chapter 4**, pressure change in membrane pores will theoretically affect the mass transfer mechanics across the membrane. In this **Chapter**, a series of experiments were designed to determine the influence of the total pressure on the flux. However, for an incompressible membrane, it was found that the positive pressure in the streams will not change the pore pressure from the force balance analysis of the pore entrance in **Chapter 4**, so the flux will not vary with positive stream pressure changes in this case.

For a compressible membrane, the membrane volume will be reduced as the pressure applied on the membrane surfaces is increased. As the membrane solid material is flexible but not compressible in the tested pressure range, the reduced membrane volume is identical to the pore volume reduction. Providing no air escapes, the pressure in the pores will increase based on the ideal gas law, so the flux will change with positive stream pressure applied on the membrane. Furthermore, the deformation of the membrane also leads to a change of porosity, thermal conductivity, pore size, and membrane permeability, which all also affect the membrane flux.

In this **Chapter**, compressible PTFE flat sheet membranes and incompressible hollow fibre membranes were tested in DCMD configuration. As mentioned in **Chapters 2 and 3**, PTFE is an ideal material for membrane distillation membranes. The PTFE membrane employed in this study is formed by dual-direction (longitudinal and transverse) stretching and lamination on a PP scrim support layer. It has a web-like structure composed of interconnected fibrils and is compressible under pressure. Hollow fibre membranes (used in **Chapter 4**) with an incompressible wall, were also selected for comparison and verification with the theoretical analysis in **Chapter 4** of stream pressure on flux for incompressible hollow fibre membranes.

5.2 Force balance analysis at pore entrances

Fig. 5.1 shows the force balance at the entrances of the pores. The force balance at the pore entrances can be expressed as,

$$P_{f(p)} = \frac{-4F\cos\theta'}{d} + P_{pore} \quad (5.1)$$

where P_f and P_p are respectively the positive gauge pressure of the feed and permeate streams and set to be approximately equal, in which the greater pressure is used in this equation, F is the force due to surface tension and can be calculated from Eq. (4.1), and θ' is the angle between the water protrusion and membrane material. Additionally, θ' cannot be more than the contact angle θ of the membrane material, and the initial P_{pore} equals zero gauge pressure (atmospheric pressure).

If the membrane is not compressible, in considering Fig. 5.1 and the analysis in **Chapter 4.2.1**, it can be assumed that the pressure in the pore will remain almost constant under varied positive P_f and P_p because the air volume will not change significantly [50]. Thus, for the incompressible membrane the force balance can also be expressed as,

$$P_{f(p)} = \frac{F_s}{A} \quad (5.2)$$

where F_s is the force from the membrane material.

For compressible membranes, the total volume of the membrane will reduce when P_f and/or P_p are applied to the membrane. Since the volume of the solid membrane material will not change as the pressure is increased (ie. incompressible material over the applied range), the membrane porosity (ε) or air volume (V_{air}) within the membrane is reduced. As shown in Fig. 5.1 and Eq. (5.1), if the air within the membrane cannot escape from the pores, the air pressure in the pore will increase. For the compressible PTFE membrane employed in this paper, the force balance can be described as;

$$P_{f(p)}A = F_s + P_{pore}A\varepsilon_{surface}, \text{ or}$$

$$P_{pore} = \frac{P_{f(p)} - F_s/A}{\varepsilon_{surface}} \quad (5.3)$$

Therefore, the pressure (P_{pore}) in the pores will change with maximum positive pressure

(P_f and/or P_p) applied on the compressible membrane.

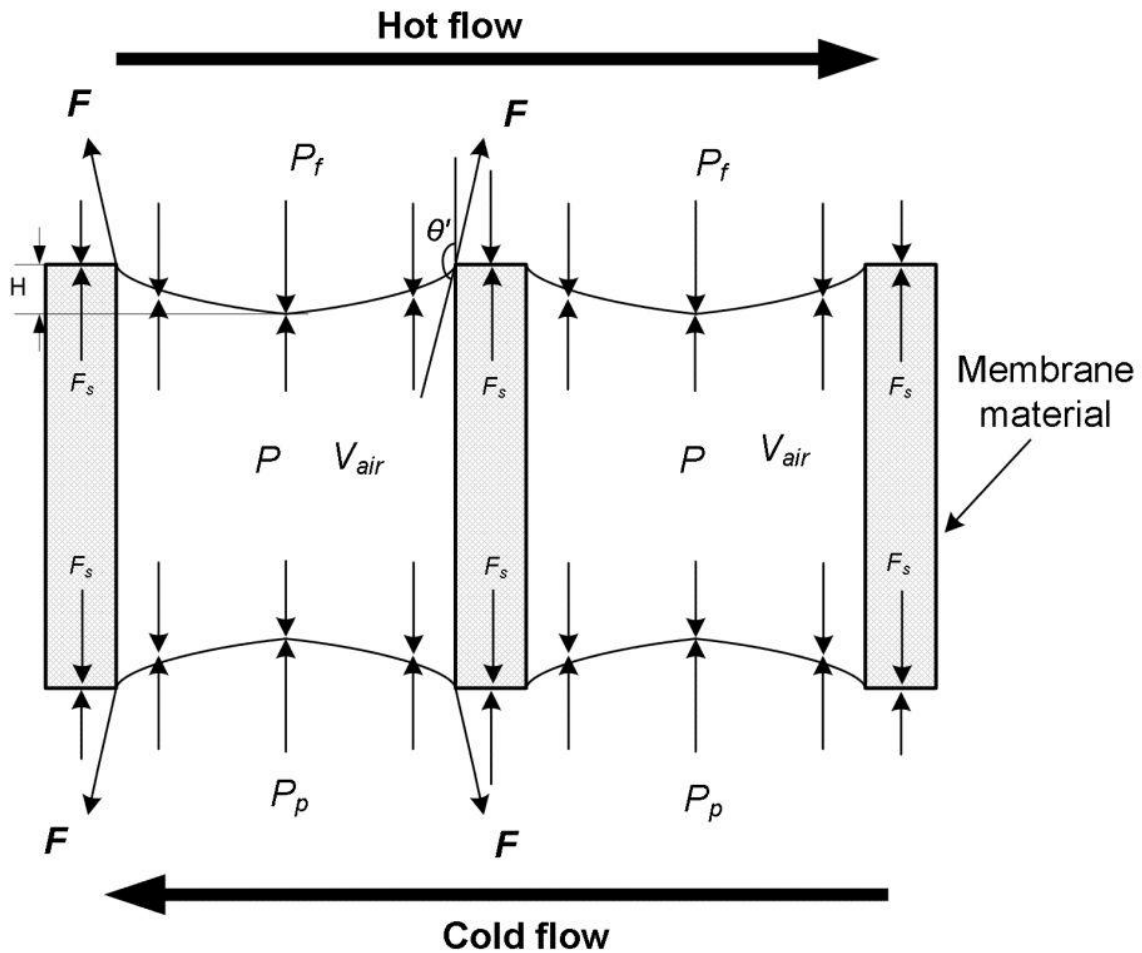


Fig. 5.1 Schematic of force balance in the pore

5.3 Experiment

5.3.1 Membrane characterisation

The PTFE membrane (Changqi Co. Ltd) consisted of a compressible PTFE active layer (nominal $d=0.5 \mu\text{m}$) and an incompressible polypropylene (PP) scrim support layer. The hollow fibre (ID=0.94 mm, OD=1.67 mm) was made of fluorinated polymer with a nominal pore size of $0.3 \mu\text{m}$.

5.3.1.1 SEM characterisation

Both the cross section and the surface of the active and support layers of the PTFE membrane and the cross section of the hollow fibre membrane were observed by a

Philips XL30 FEG Scanning Electron Microscope (SEM). Both membranes were fractured following immersion in liquid nitrogen to form an intact cross section [48] before it was scanned.

5.3.1.2 Air permeability measurement

The pore size (d) and ε/bt of the PTFE membrane were estimated by a gas permeability method [35] using compressed nitrogen mentioned in **Chapter 3.2.1.4**. The pressure was varied in the range of 5-80 kPa. Six samples (\varnothing 25 mm) from different parts of a large membrane sheet ($0.25 \times 40 \text{ m}^2$) were tested, and the average value was used to assess the performance of the PTFE membrane. The calculated results are listed in Table 5.1.

Table 5.1 Calculated pore size and ε/bt from fitting equations in Fig. 5.2

Sample	1	2	3	4	5	6
d (μm)	0.44	0.43	0.43	0.46	0.49	0.47
ε/bt ($\times 10^4$)	2.88	2.23	2.91	2.49	1.93	1.87

5.3.1.3 Active layer porosity and thickness measurement

The porosities of the membranes were measured by a wetting method. As discussed in **Chapter 3**, the density of a polymer varies across a certain range. If the mean density from the reference is used for the calculation of a single parameter, for example the membrane porosity as seen in **Chapter 3**, the error (<3%) caused by the variation is acceptable. However, if the mean referenced density is used as basic data for a series of calculations, the error will become unacceptable because of the accumulation of errors.

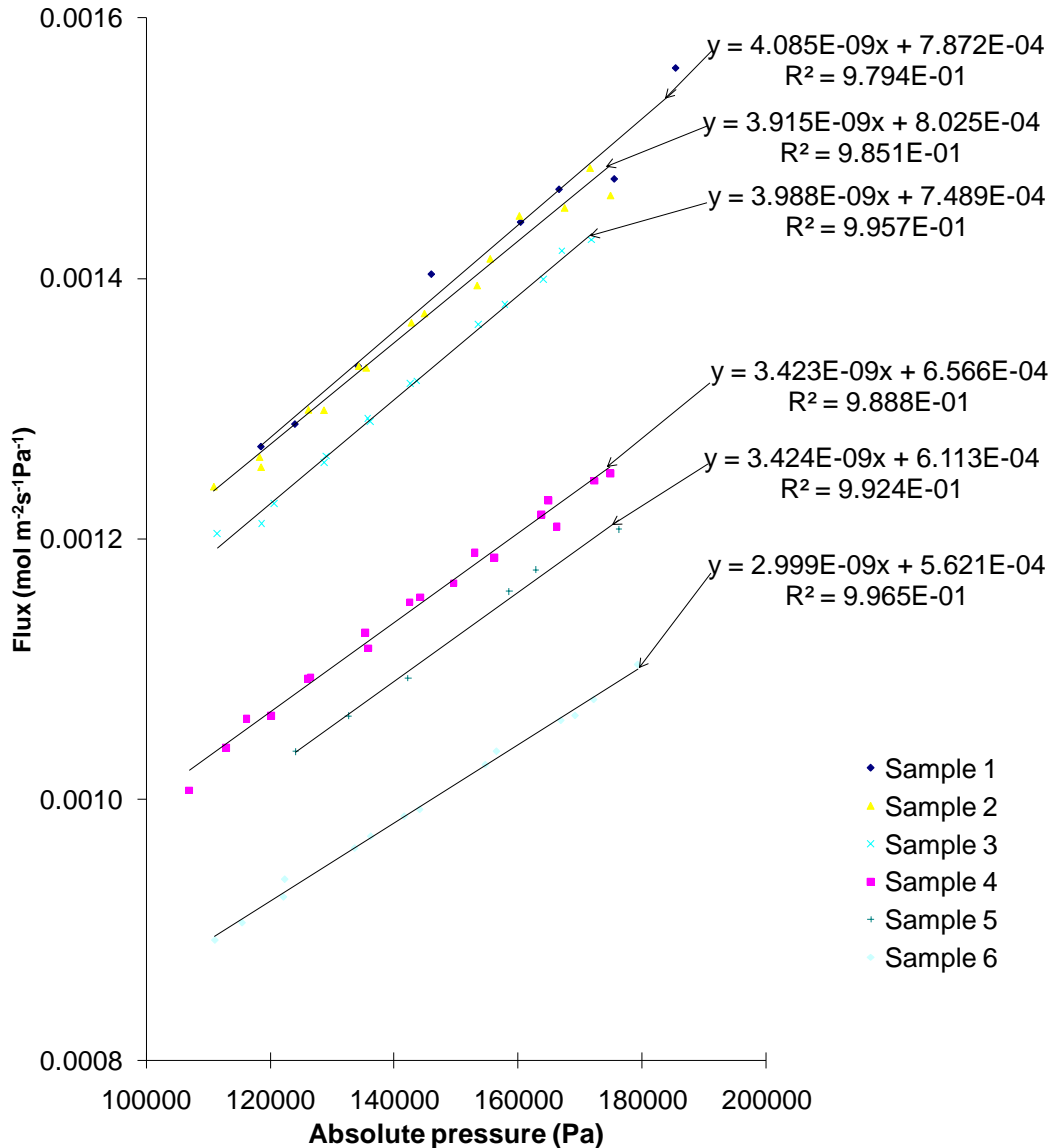


Fig. 5.2 Results of gas permeation test

To identify the PTFE density used for the active layer, the mass (1.8 g) of an active layer sample was first weighed. The volume of this sample was measured with a wetting method: the active layer sample was placed in a 25 mL volumetric flask (A), acetone was used as wetting agent and was filled up to the 25 mL mark; the flask was sealed and processed in an ultrasonic vibrator to enable the acetone to fully wet the active layer and remove air within the pores completely; the flask was allowed to cool to room temperature (23°C), and more acetone was filled up to the mark of the volumetric flask. To determine the density more accurately, another 25 mL volumetric flask (B) containing only 25 ml of acetone was subjected to the same process to measure the density of the acetone under the same condition. In this process, the masses of the flasks

and the membrane active layer were measured by an A&D balance (HR-200). The density of the active layer was calculated base on the mass balance,

$$m_{flask(A)} = \rho_{PTFE}V_{PTFE} + \rho_{acetone}V_{acetone}, \text{ and}$$

$$m_{flask(B)} = V_{flask} \times \rho_{acetone} \quad (5.4)$$

where $m_{flask(A)}$ and $m_{flask(B)}$ are the masses within the flasks (A) and (B), ρ_{PTFE} and $\rho_{acetone}$ are densities of PTFE and acetone, V_{PTFE} , $V_{acetone}$ and V_{flask} are volumes of PTFE active layer, acetone in flask (A) and flask.

so

$$\rho_{PTFE}V_{PTFE} = m_{flask(A)} - \frac{m_{flask(B)}}{V_{flask}}V_{acetone} \quad (5.5)$$

Because

$$m_{PTFE} = \rho_{PTFE}V_{PTFE} \text{ and } V_{flask} = V_{acetone} + V_{PTFE},$$

$$V_{PTFE} = V_{flask} - \frac{V_{flask}(m_{flask(A)} - m_{PTFE})}{m_{flask(B)}} \quad (5.6)$$

where m_{PTFE} is the mass of the PTFE active layer sample.

Therefore, the density of the PTFE can be calculated by:

$$\rho_{PTFE} = \frac{m_{PTFE}}{V_{PTFE}} \quad (5.7)$$

The density of the support (scrim) layer $\rho_{support}$ was also measured by a similar method, except that water was used as the wetting liquid instead of acetone.

As seen in Fig. 3.7, part of the scrim is embedded in the active layer, so it is necessary to find a method for calculating the mean thickness instead of using the SEM. To reduce the error of measurement, two large pieces of PTFE membranes including support layer ($m_{membrane}=0.35$ and 0.84 g) with areas $A=124.9$ and 297.7 cm² were used to determine the porosity and the mean thickness of the PTFE active layer, and the average value was used in this study. The sample was weighed first, and then was submerged in deionised water in a 100 mL volumetric flask (C), and flushed for 2 min to remove air trapped in the scrim opening. Another 100 mL volumetric flask (D) was also used to determine the density of the deionised water. The total membrane volume ($V_{membrane}$) was calculated

based on the Eq. (5.6). The weight ($m_{support}$) of the support (scrim) layer was also measured after the active layer was removed and the volume of the support layer was calculated by:

$$V_{support} = \frac{m_{support}}{\rho_{support}} \quad (5.8)$$

so,

$$V_{PTFE} = V_{membrane} - V_{support} \quad (5.9)$$

Therefore, the mean thickness of membrane can be calculated by

$$b = \frac{V_{PTFE}}{A} \quad (5.10)$$

and the porosity can be calculated as,

$$\varepsilon = 1 - \frac{m_{membrane} - m_{support}}{(V_{membrane} - V_{support})\rho_{PTFE}} \quad (5.11)$$

where $m_{membrane}$ and $V_{membrane}$ are total membrane weight and volume, and $m_{support}$ and $V_{support}$ are support layer weight and volume, respectively.

The porosity and density of a hollow fibre membrane sample (0.15 g) were also measured with the same methods as those used to determine the properties of the flat sheet membrane.

5.3.2 Membrane deformation measurement

Fig. 5.3 shows the apparatus for measuring volume change under different pressures. Two PTFE membrane samples ($V_{membrane} = 0.77$ and 1.91 mL) and one hollow fibre membrane sample ($V_{membrane}=0.50$ mL) were tested. The testing pressure was in the range of $0-60 \pm 5$ kPa. A pipette with an accuracy of 0.01 mL was used to measure the volume change (ΔV) under different pressures. The membrane was placed in a volumetric flask filled with deionised water, and was subjected to flushing for 2 min to remove air trapped in the scrim opening; a pipette with silicon tubing thereon was carefully inserted into the volumetric flask till the silicon tubing sealed the clearance between the flask and pipette completely; the seal was rechecked to confirm no air bubbles were left in the volumetric flask. The volume change was recorded after the membrane had stabilized under the testing pressure for 1.5 min. To reduce the

systematic error associated with the compression of the silicon tubing seal in these tests, two blank experiments (no membrane in the volumetric flask) were also run under different pressures on different days to form a blank calibration curve of the volume change (ΔV_{blank}) under applied pressures in the range of $10\text{-}60\pm 5$ kPa, and an equation fitting the blank data curve was used to calculate the blank volume change for each pressure in the membrane deformation tests. The deformation of the support layer was assumed negligible under the test pressure, and therefore the difference between ΔV and the calculated volume change in the blank test was used as the volume change of the membrane:

$$\Delta V_{membrane} = \Delta V - \Delta V_{blank} \quad (5.12)$$

where $\Delta V_{membrane}$ is the volume change of the membrane.

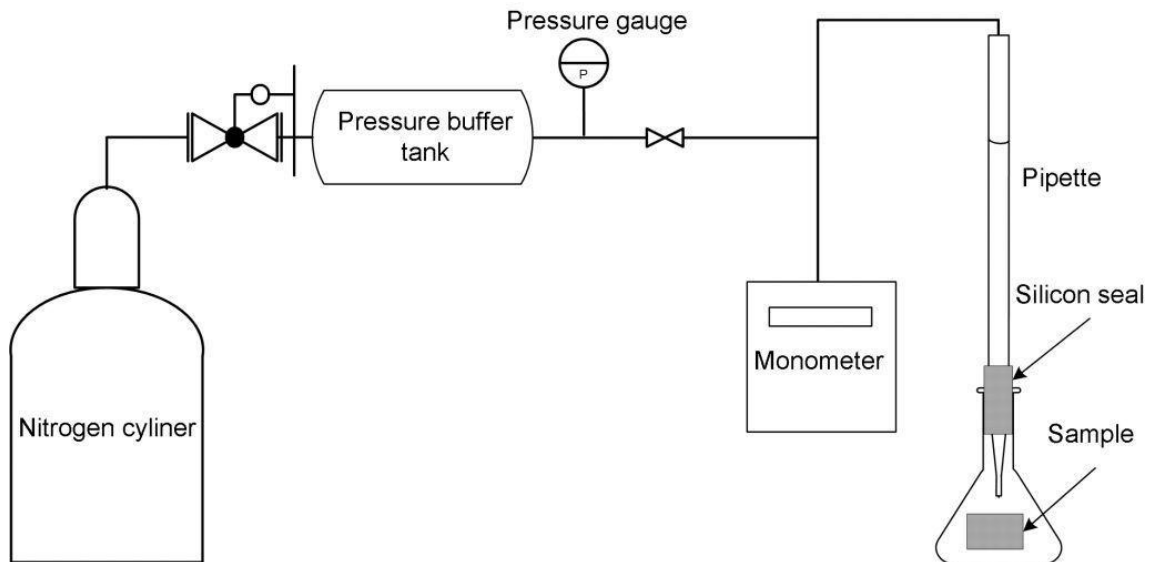


Fig. 5.3 Schematic of membrane deformation measure measurement

The blank volume change at different pressures is shown in Fig. 5.4. Although these tests were done on different days before the membrane compression tests, the blank volume change was similar for any given pressure and therefore, it is applicable to use the fitted equation shown in Fig. 5.4 to calculate ΔV_{blank} for different pressures.

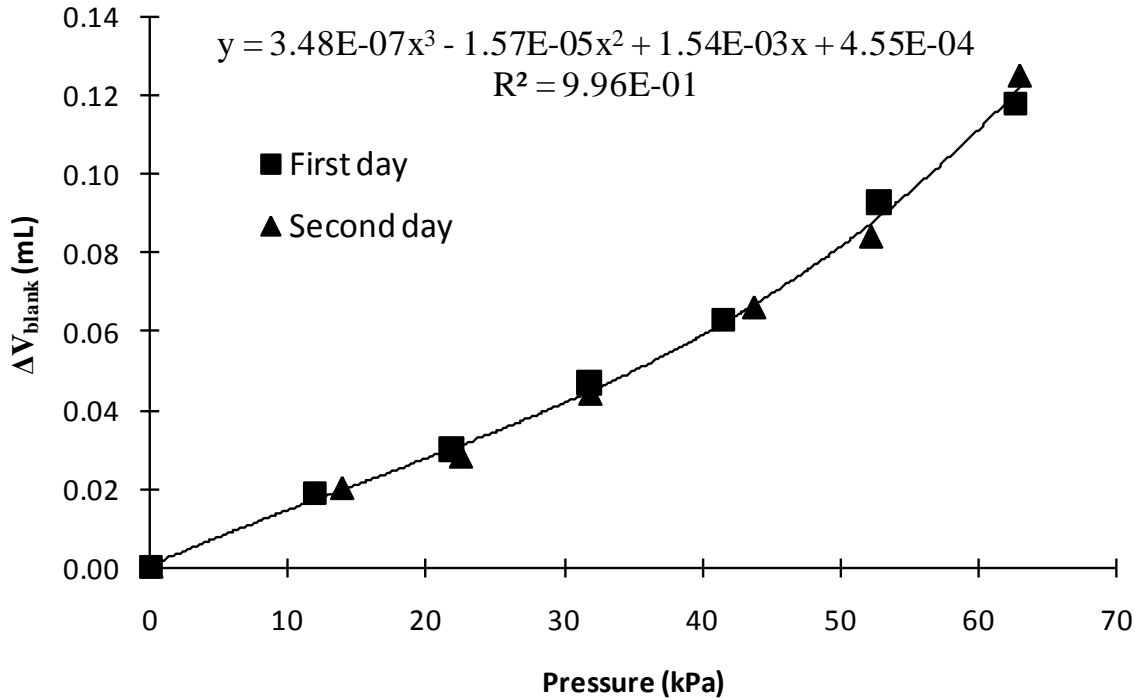


Fig. 5.4 Volume change under different pressures in blank experiment

5.3.3 DCMD experiments

A schematic diagram of a flat sheet DCMD process for the PTFE membrane is shown in Fig. 5.5. This flow chart is similar to the one shown in Fig. 3.5, except for the two pressure control valves that were placed at the outlets of both streams and were used to control the pressures in both streams. Additionally, four pressure detecting ports were installed at the inlets and outlets of hot and cold streams. All experiments were conducted with identical pressures and velocities of the feed and permeate streams by adjusting the valves. To reach the targeted pressure, the pressure control valves on both sides were adjusted simultaneously, and a maximum difference between the both streams was controlled to less than 2 kPa at any time in this procedure, to avoid air escaping from the pores due to unbalanced pressure.

The influence of pressure variation on flux at different velocities was studied. The selected stream velocities were 0.079, 0.097 and 0.115 m/s (420, 520 and 620±10 mL/min), and the cold and hot inlet temperatures were set at 20 and 60°C.

The effect of pressure variation on flux at different hot inlet temperatures was also investigated. The selected hot inlet temperatures were 50, 60 (the same experiment as

the above study conducted at 0.097 m/s) and $70\pm 2^\circ\text{C}$. The cold inlet temperature was set at $20\pm 1^\circ\text{C}$, and the cold and hot stream velocities were set at 0.097 m/s.

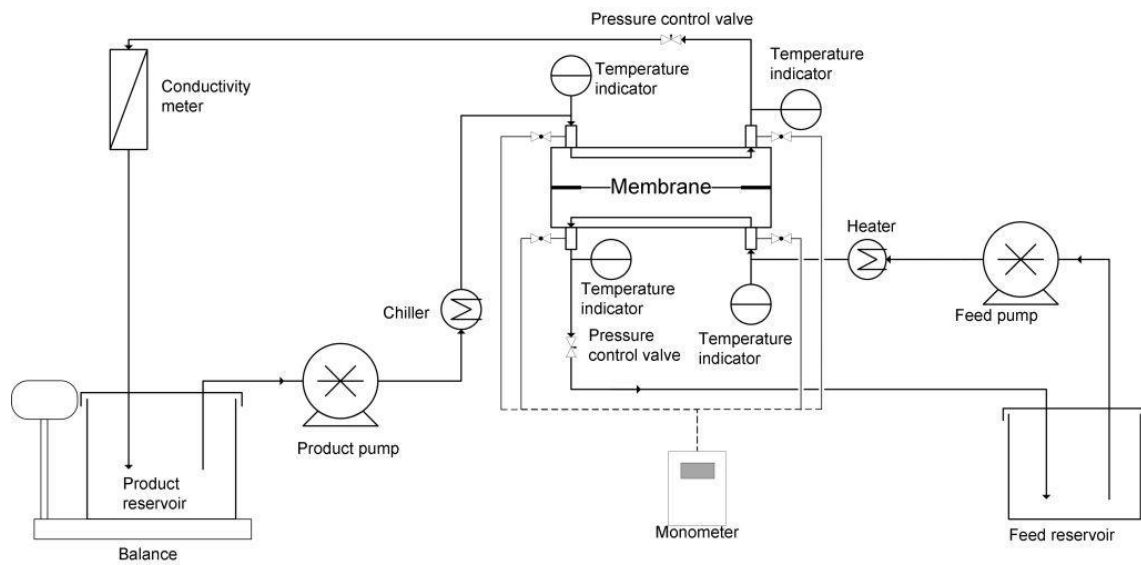


Fig. 5.5 Schematic diagrams of the employed DCMD process

The study was divided into five experimental series. Five pressures were tested in each experimental series, which were in the ranges of 0-10, 10-20, 20-30, 30-40, and 40-50 kPa. For each series, a new membrane with an area of 169 cm^2 ($13\times 13\text{ cm}$) was used. Before the experimental data were collected, the new membrane was conditioned with the pressure control valves fully opened for 3 h at stream velocities of 0.097 m/s and hot and cold inlet temperatures of 60 and 20°C . In the experiment, the pressures (inlet and outlet) were recorded every half and/or one hour with the digital monometer (645, TPI), and the mean value was used as the pressure applied on the membrane in the calculation. The recorded pressure variation of each detecting port was less than $\pm 3\text{ kPa}$ during each experiment. Under each applied pressure, the flux was measured over the experimental period of 2.5-4 h and the variation of flux over this period was within $\pm 5\%$.

Table 5.2 Data of the tubular hollow fibre module

Length (mm)	Inner diameter (mm)	Hollow fibre number
200	6.63	12

Five similar series of experiments were also conducted with a hollow fibre module for

comparison with the flat sheet membrane. The properties of the fibre are the same as those listed in Table 4.4. Data of the hollow fibre module is listed in Table 5.2.

5.4 Results and discussion

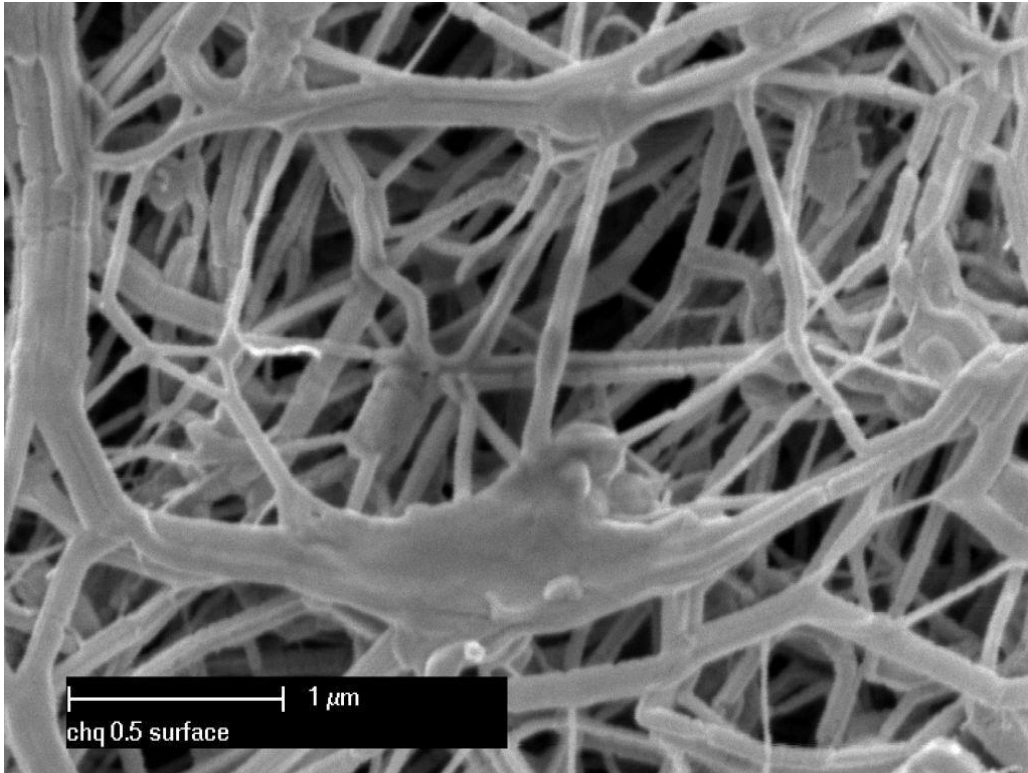
5.4.1 Analytical results and discussion

Table 5.3 lists the measured PTFE and hollow fibre membrane properties. The measured pore size of the PTFE membrane was similar to the nominal pore size provided by the manufacturer (0.5 μm). From this table, the calculated tortuosity (t) was 1.10, which is similar to the reported data [75, 130]. Since the hollow fibre membrane was only used for comparison purposes, it was not characterised by the gas permeation test.

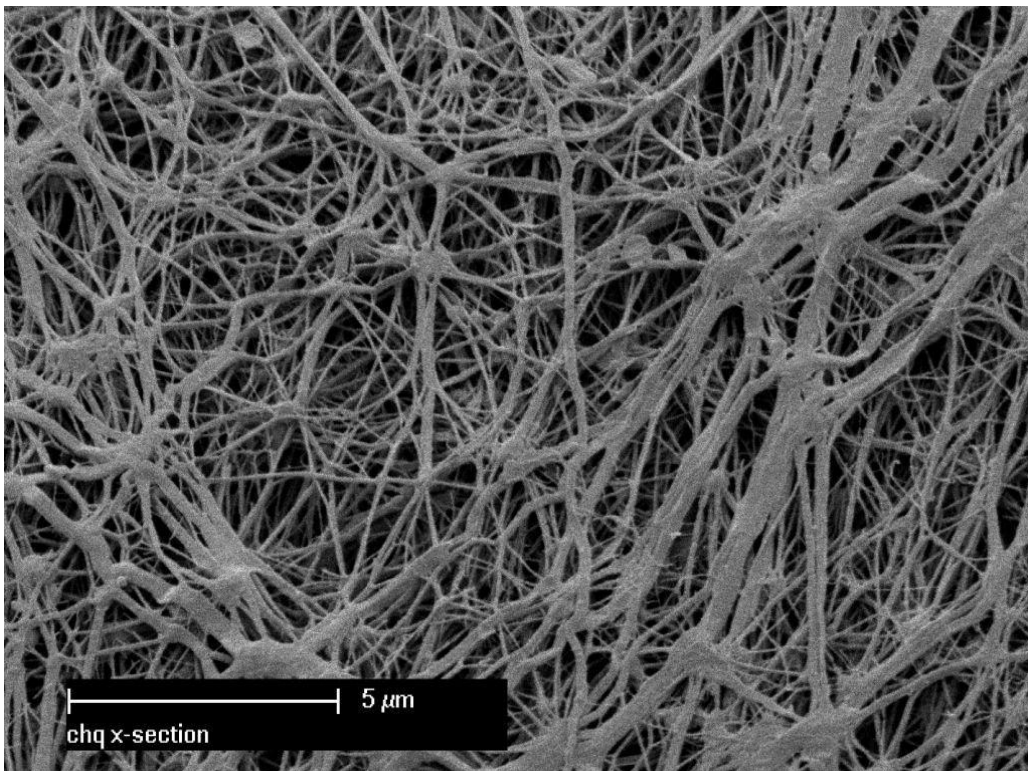
Table 5.3 Properties of membrane

Membrane	d (μm)	ε (%)	b (μm)	ρ_{PTFE} (kg/m^3)	ρ_{scrim} (kg/m^3)	ε/bt (m^{-1})
Flat sheet	0.45 \pm 0.05	94 \pm 0.5	36 \pm 1	2.29	0.88	24,000 \pm 7,000
Hollow fibre	0.33	85	0.67	2.01	/	/

Images of the PTFE active layer are shown in Figs. 5.6a and 5.6b. The PTFE active layer has a networked structure, in which fine fibrils were connected to each other at nodes and all the pores are interconnected. The SEM images of the hollow fibre are shown in Fig. 4.7.



a. Surface of PTFE active layer



b. Cross section of PTFE active layer

Fig. 5.6 Images for membrane structures

5.4.2 Deformation results and discussion

5.4.2.1 Thickness measurement of active layer under different pressures

The two PTFE membrane samples used in the volume change experiments were different in size, so the absolute volume changes of these samples were not directly comparable. It was assumed that the pressure was applied evenly on the membrane surface and that the scrim layer was not compressible. It was also assumed that the active layer was only compressible in the cross sectional direction (normal to the surface), which is reasonable given that this is the largest surface area and hence contributes the most to the deformation. Thus, changes in the active layer thickness for the two membrane samples should be identical under the same pressure. As only the active layer is compressible, $\Delta V_{membrane}$ is equal to the volume change of the active layer (ΔV_{PTFE}). Therefore,

$$\Delta b = \frac{\Delta V_{PTFE}}{A} \quad (5.13)$$

where Δb is the thickness change of the active layer, and ΔV_{PTFE} is the volume change of the active layer.

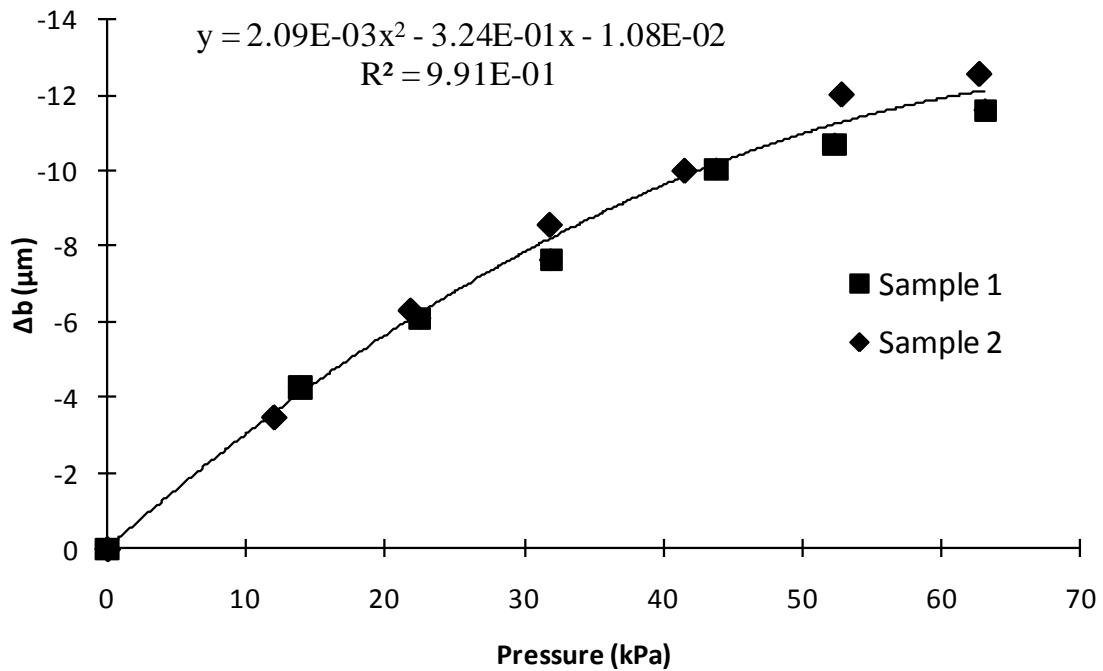


Fig. 5.7 Thickness change under different pressures for the PTFE membranes

Fig. 5.7 shows that the values of Δb from different membranes were similar across the pressure range. This also validated the methods used in measuring the membrane thickness changes since the two set of data were from two membranes of different sizes. A fitted polynomial curve presented in this figure was used to calculate Δb for different pressures in modelling calculations.

5.4.2.2 Comparison of compressibility of PTFE and hollow fibre membrane

The volume change ratio of the PTFE membrane and hollow fibre membrane under pressure are shown in Fig. 5.8.

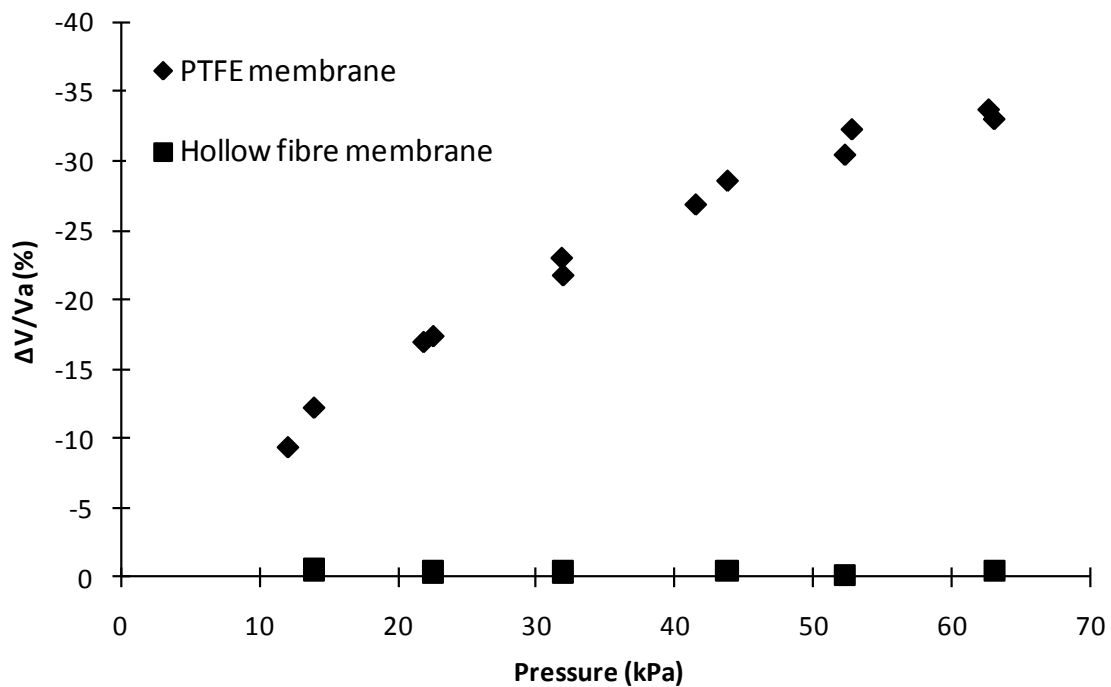


Fig. 5.8 Ratio of volume change to total active layer volume under pressure

Fig. 5.8 shows that as the applied pressure was increased from 12 kPa to 63 kPa, the volume reduction increased from 10 to 34% for the PTFE active layer, and volume change of the hollow fibre membrane was not detectable. Therefore, the PTFE membrane and the hollow fibre membrane can be considered as compressible and incompressible membranes respectively over the pressure range considered.

According to the force balance analysis of the compressible and incompressible membranes, the air pressure in the pores of the hollow fibre membrane does not change as the applied pressure was increases from 0-63 kPa, while the air pressure in the PTFE

membrane pore increases as the pressure applied on its surface is raised.

5.4.2.3 Calculation of pressure in the pores

Eq. (5.3) shows that the pressure in the pores of a compressible membrane will not equal the pressure applied on the membrane surface, due to the extra support force (F_s) from the active layer material (PTFE). However, since the volume of the active layer material will not be compressed under the test pressures, the membrane volume change ($\Delta V_{membrane}$ or ΔV_{PTFE}) is from the compression of air in the membrane pores. Therefore, $\Delta V_{membrane}$ or ΔV_{PTFE} is caused by and equals the air volume change. Because the air in the pores can be assumed as an ideal gas in this low pressure range, the air pressure in the pores (P_{pore}) can be estimated from the measured $\Delta V_{membrane}$ and the ideal gas law [147]. Fig. 5.9 shows the relationship between the applied pressure and calculated pressure in the pores. From this figure, it was found that the pressure in the pores was approximately 94% of the applied pressure on the membrane surface over the investigated pressure range.

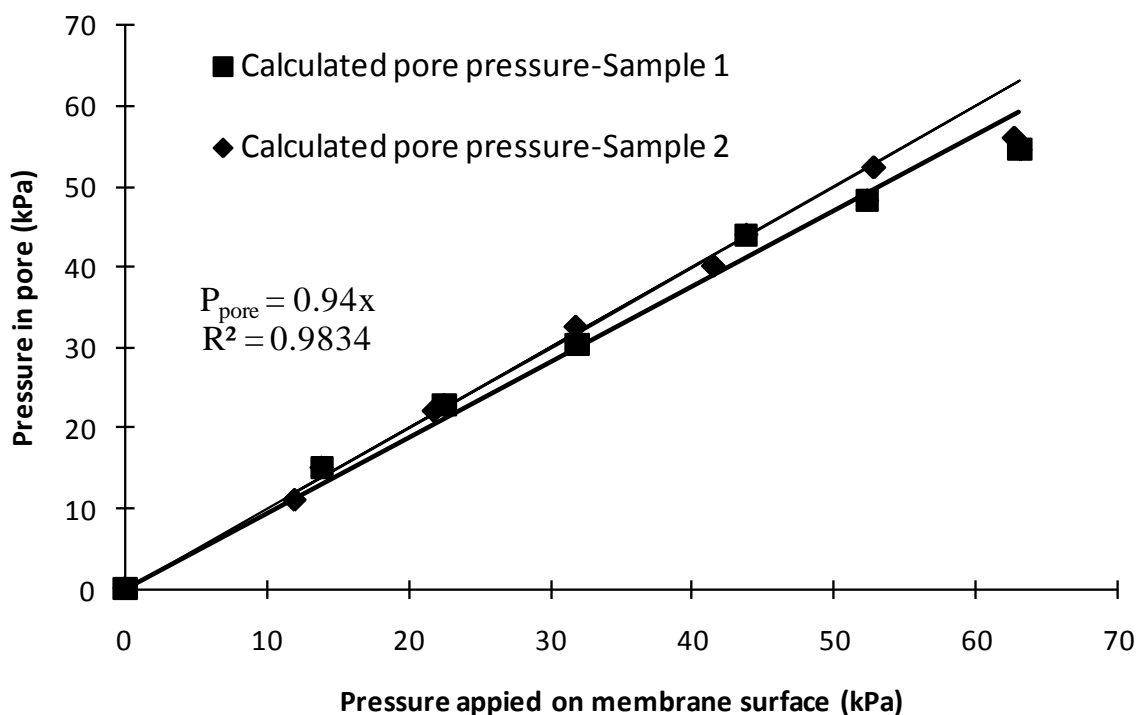


Fig. 5.9 Applied pressure vs calculated pressure in the pore of PTFE membrane

5.4.2.4 Estimation of pressure influence on membrane properties

As the active layer was compressed under higher pressure, the porosity (ε) of the active layer is reduced. The membrane porosity can be calculated from:

$$\varepsilon = \frac{N \frac{\pi d^2}{4} b t}{V_m} = N \frac{\pi d^2 t}{4A} \quad (5.14)$$

where N is the nominal pore number.

Therefore, based on Eq. (5.14), $d^2 t$ is reduced at higher pressure, as the tortuosity is assumed not to reduce under higher pressure, the pore diameter will become smaller because the void volume in the active layer is decreased, while the incompressible solid material retains its volume.

According to Eqs. (5.10) and (5.14),

$$b_p = \frac{V_s}{A(1-\varepsilon_p)} \text{ and } d_p = \sqrt{\frac{4A\varepsilon_p}{N\pi t_p}}$$

As shown in Eqs. (3.4), (4.11) and (4.15), membrane gas permeability can be determined from

$$\frac{d_p \varepsilon_p}{b_p t_p} = \frac{d_p \varepsilon_p (1-\varepsilon_p) A}{V_s t_p} = C_0 \frac{\varepsilon_p^{1.5} (1-\varepsilon_p)}{t_p^{1.5}} \quad (5.15)$$

where d_p , b_p , t_p and ε_p are pore size, membrane thickness, tortuosity and porosity under pressure P , V_s is the volume of PTFE material in the active layer which will not change under different pressures, and C_0 is a constant for a given membrane.

In Fig. 5.10, $\varepsilon_p^{1.5} (1-\varepsilon_p)$ shows an inverse trend with the porosity of the employed PTFE membrane in the tested pressure rang. However, it is difficult to estimate the tortuosity change as the membrane was compressed. Two assumptions exist in the literature: the first is that the tortuosity (t_p) will not change with pressure and as a result, the change of gas permeability with pressure can be expressed by

$$\frac{d_p \varepsilon_p}{b_p t_p} = C_0' \varepsilon_p^{1.5} (1 - \varepsilon_p) \quad (5.16)$$

which increases with increasing pressure (the porosity decreases with pressure).

Therefore, in the tested pressure range, the compaction of the membrane will increase the gas phase diffusion through the membrane.

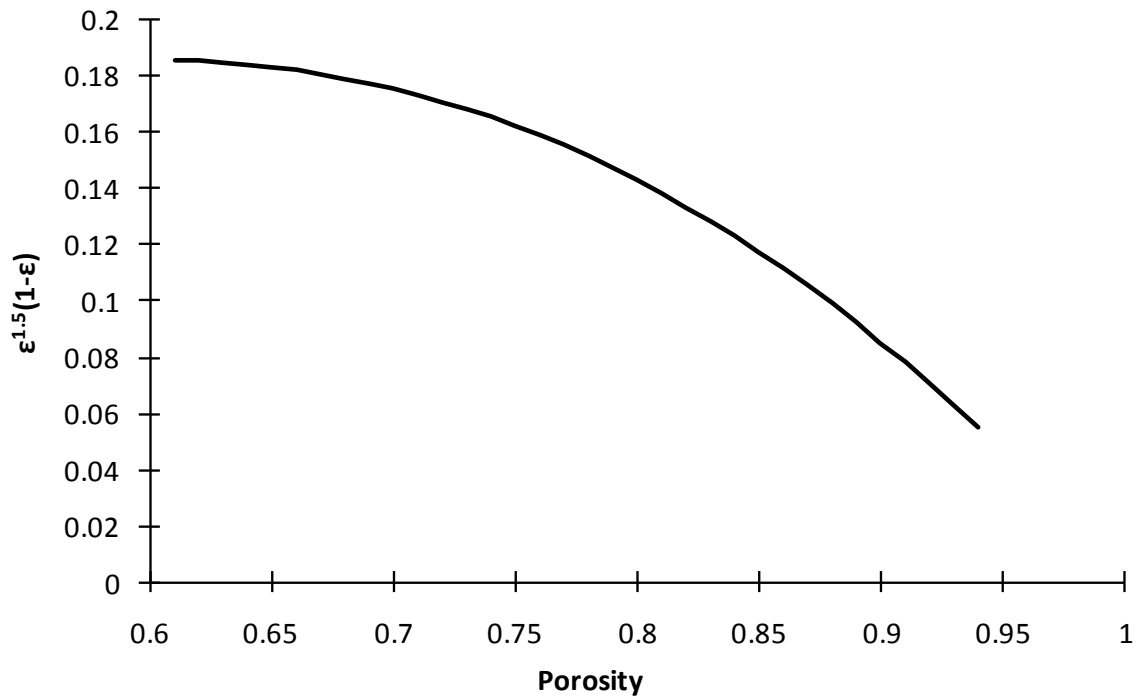


Fig. 5.10 $\epsilon_p^{1.5}(1-\epsilon_p)$ vs porosity variation

The second assumption is that the gas diffusion path length ($b_p t_p$) will not change with membrane deformation, and applying this assumption to Eq. (5.15) leads to

$$\frac{d_p \epsilon_p}{b_p t_p} = C_0' \frac{\epsilon_p^{1.5}}{(1-\epsilon_p)^{0.5}} \quad (5.17)$$

This equation predicts that the compaction of the membrane will cause a decrease of gas phase diffusion.

It can be speculated, based on the interconnected and networked structure shown in Fig. 5.6a and 5.6b that as the membrane is pressurised, the nodes and fibrils will move in the direction normal to the membrane surface and overlap like two nets. This geometry suggests that the nominal pore channel will be shortened and the tortuosity will not vary significantly. Therefore, the first assumption can describe the behaviour of compressed PTFE membrane more accurately than that of the second assumption in this study. The first assumption is also supported by the estimated tortuosity of 1.10, which indicates that the pore is aligned almost perpendicularly to the membrane surface. Hence, the

permeability of the compressed membrane will increase as shown in Fig. 5.10, due to the shortened mass transfer path. Furthermore, an increase of gas permeability through a more compact membrane used for membrane distillation was also observed by Lawson, K.W., etc. [68, 148], from which it also can be deduced that the percentage increment of tortuosity is less than the percentage increase of $\varepsilon_p^{1.5}(1-\varepsilon_p)$ as the membrane was compressed. Therefore, the mass transfer resistance of the membrane will decrease as the membrane is compressed in the pressure range investigated here.

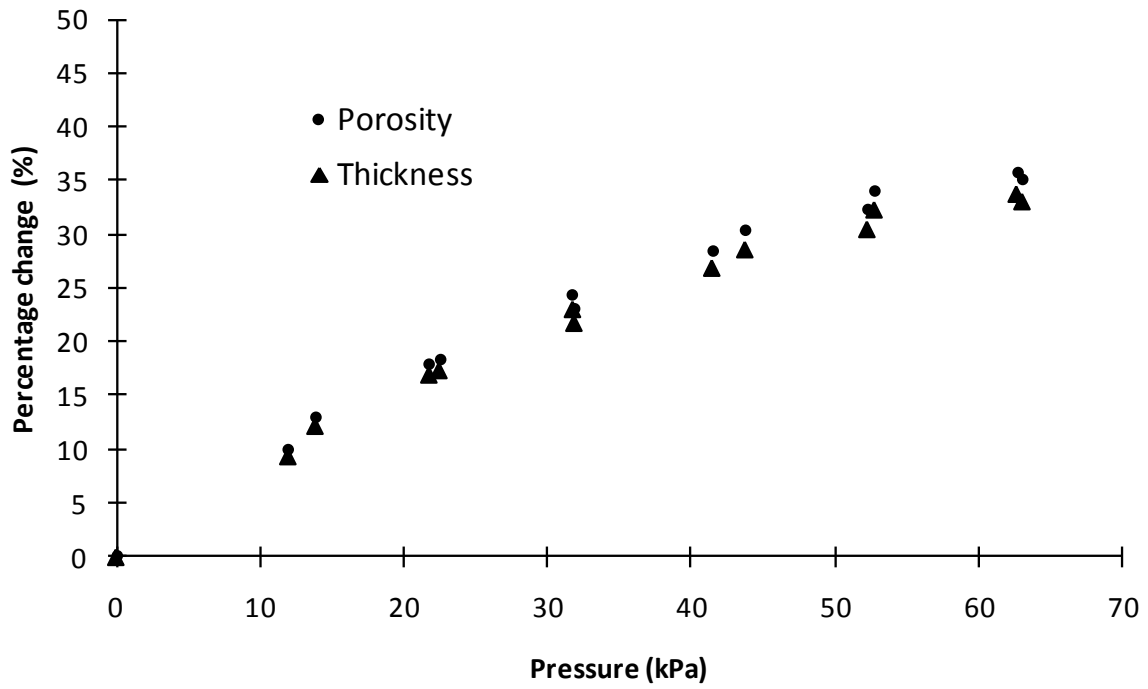
However, membrane distillation is also a thermal process, and the thermal resistance of the membrane is related to the vapour flux. Based on Eq. (2.4) for the calculation of thermal conductivity, the membrane thermal resistance can be expressed as

$$R_p = \frac{b_p}{\lambda_p} = \frac{b_p}{\lambda_{air}\varepsilon_p + \lambda_{solid}(1-\varepsilon_p)} \quad (5.18)$$

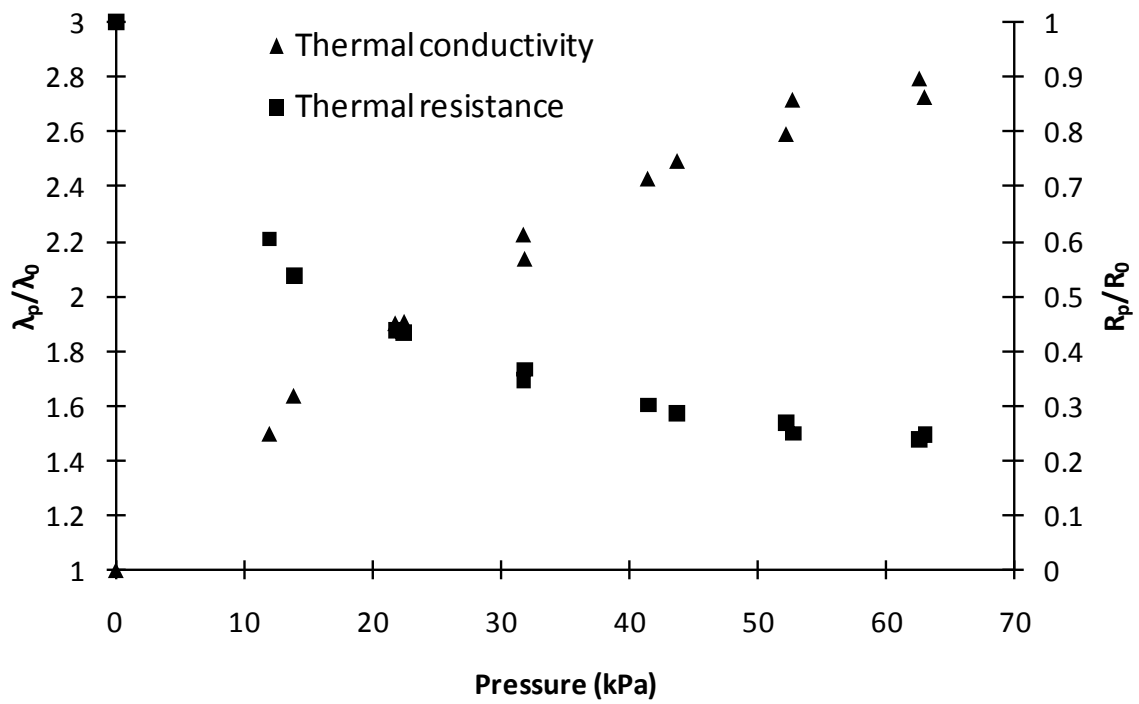
where R_p and λ_p are the thermal resistance and thermal conductivity of the membrane under pressure P .

As shown in Fig. 5.11a, the membrane thickness and porosity were reduced by 34% and 36% as the pressure increased from 0 to 63 kPa. Accordingly in Fig. 5.11b, λ_p calculated from the reported thermal conductivity values of air ($\lambda_{air}=0.026 \text{ Wm}^{-1}\text{K}^{-1}$) and PTFE ($\lambda_{PTFE}=0.25 \text{ Wm}^{-1}\text{K}^{-1}$) [3] increased 1.8 times from its initial value (λ_0), and R_p reduced to less than a quarter of the initial value (R_0).

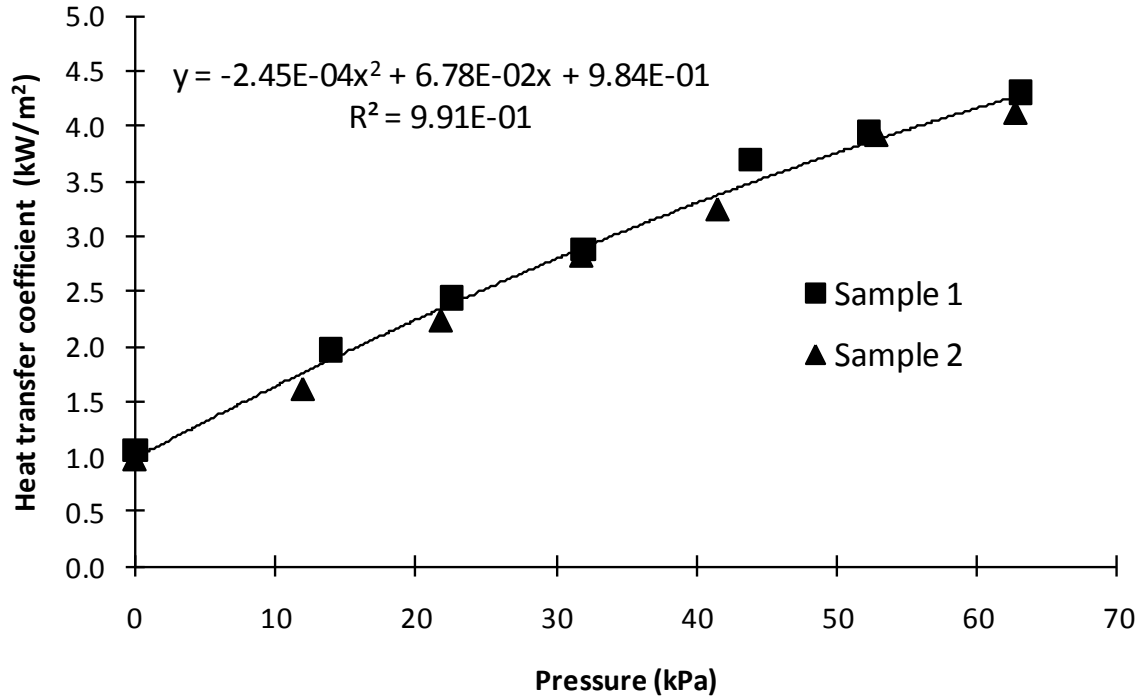
The heat transfer coefficient (λ/b) in Fig. 5.11c increased from 1.1 to 4.3 kW/m². Therefore, the sensible heat loss at 63 kPa is four times of that at 0 kPa for the same temperature difference across the membrane. As the input total heat energy is identical at the same inlet temperatures and flowrate, less thermal energy will be utilised for water evaporation under higher applied pressure because of the reduced resistance to sensible heat transfer.



a. Changes of porosity and thickness



b. Changes of thermal conductivity and resistance



c. Heat transfer coefficient changes under different pressures

Fig. 5.11 Thermal properties changes under pressure

From the analysis of a pressurised membrane, it can be concluded that the shortened mass transfer path with little change in tortuosity inclines to increase the flux due to the shorten diffusion path, but the increased pressure within the pore and the increased membrane thermal conductivity tend to reduce permeate flux by increasing the mass transfer resistance and/or reducing the energy efficiency.

5.4.2.5 Estimation of mean membrane mass transfer coefficient ($C_{membrane}$)

To assess the influence of pressure more accurately, the mean membrane mass transfer coefficient was estimated through the experimental data and the energy balance on the hot side as shown in

$$JH_{latent}A = \dot{m}C_p\Delta T_f - \lambda\Delta T_{interface}A/b, \text{ or}$$

$$\Delta T_{interface} = (JH_{latent}A - \dot{m}C_p\Delta T_f) / (\frac{\lambda A}{b}) \quad (5.19)$$

where ΔT_f is the temperature change between the inlet and the outlet on the hot side, $\Delta T_{interface}$ is the mean pore interface temperature difference between the hot side and

cold side, \dot{m} is the feed mass flowrate, and C_p is the specific heat capacity. $\dot{m}C_p\Delta T_f$ is the total heat loss of the feed, $\lambda A\Delta T_{interface}/b$ is the sensible heat loss, and JAH_{latent} is the evaporation heat. In this equation, JAH_{latent} and $\dot{m}C_p\Delta T_f$ can be calculated based on experimental results, and λ/b can be calculated based on the equation in Fig. 5.11c, so the $\Delta T_{interface}$ can be calculated. The mean temperature polarisation coefficient can be calculated from [5, 142],

$$\tau = \frac{\Delta T_{interface}}{\Delta T_{p,f}} \quad (5.20)$$

where τ is the mean temperature polarisation coefficient, and $\Delta T_{p,f}$ is the mean temperature difference between the hot and cold flows, which can be obtained from the experimental results. Since $\alpha_f(T_f - T_1) = \alpha_p(T_2 - T_p)$ and the convective heat transfer coefficients (α_f, α_p) on both sides will be similar because both sides are at the identical hot and cold stream velocities and the average temperature difference between both sides is not great ($\sim 20 \pm 5^\circ\text{C}$), it can be derived,

$$T_p + T_f \cong T_1 + T_2, \text{ and}$$

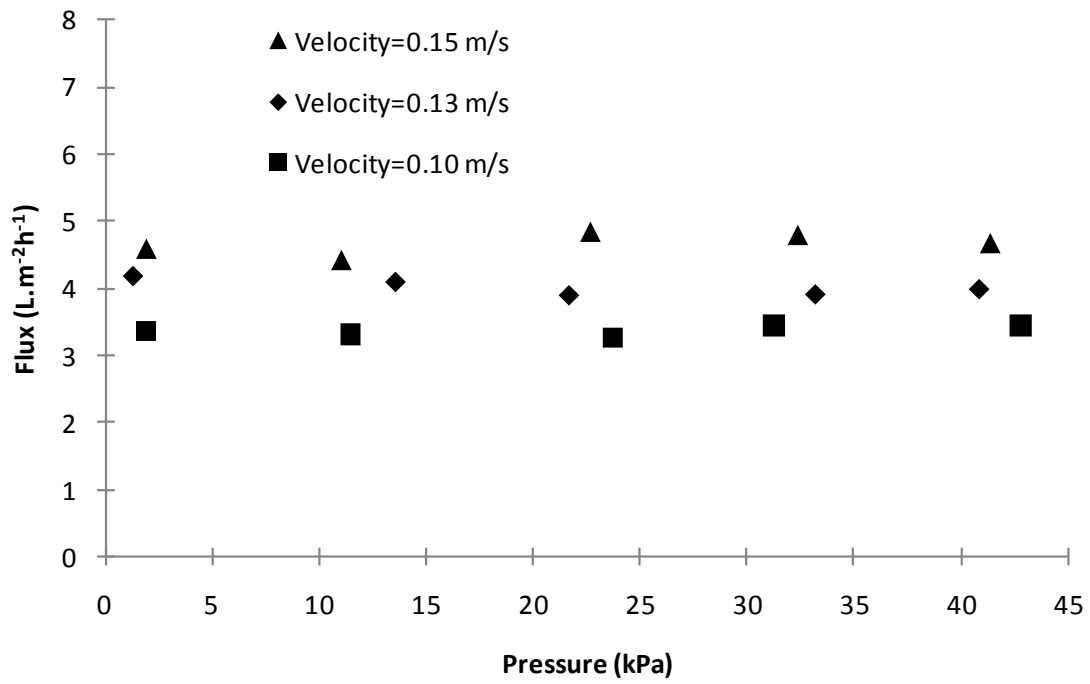
$$T_1 \cong \frac{T_p + T_f + \Delta T_{interface}}{2}, T_2 \cong \frac{T_p + T_f - \Delta T_{interface}}{2} \quad (5.21)$$

Using results from Eq. (5.21) and the Antoine equation, the mean interface vapour pressures and the interface vapour difference between the hot side and cold side can be calculated, from which the mean membrane mass coefficient can be calculated using Eq. (2.19).

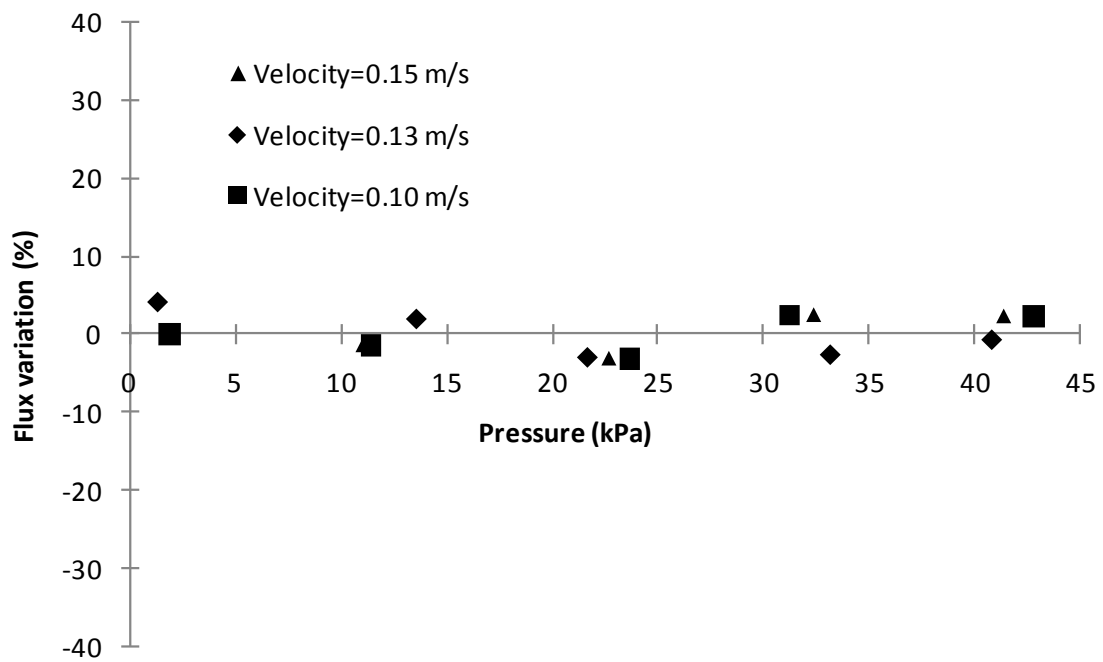
5.4.3 DCMD experimental results and discussion

5.4.3.1 Experimental results for incompressible hollow fibre membrane

Fig. 5.12 shows the relationship between the flux and applied pressure for the hollow fibre membrane at different stream velocities. The experiments were tested at three different feed velocities at identical hot inlet temperatures ($T_{fi}=60^\circ\text{C}$) and cold inlet temperatures ($T_{pi}=20^\circ\text{C}$). These figures show that there was no clear increase or decrease in flux with changes in applied pressure at the same velocity (Fig. 5.12a), and that the variation was $\pm 4\%$ around the mean value (Fig. 5.12b).



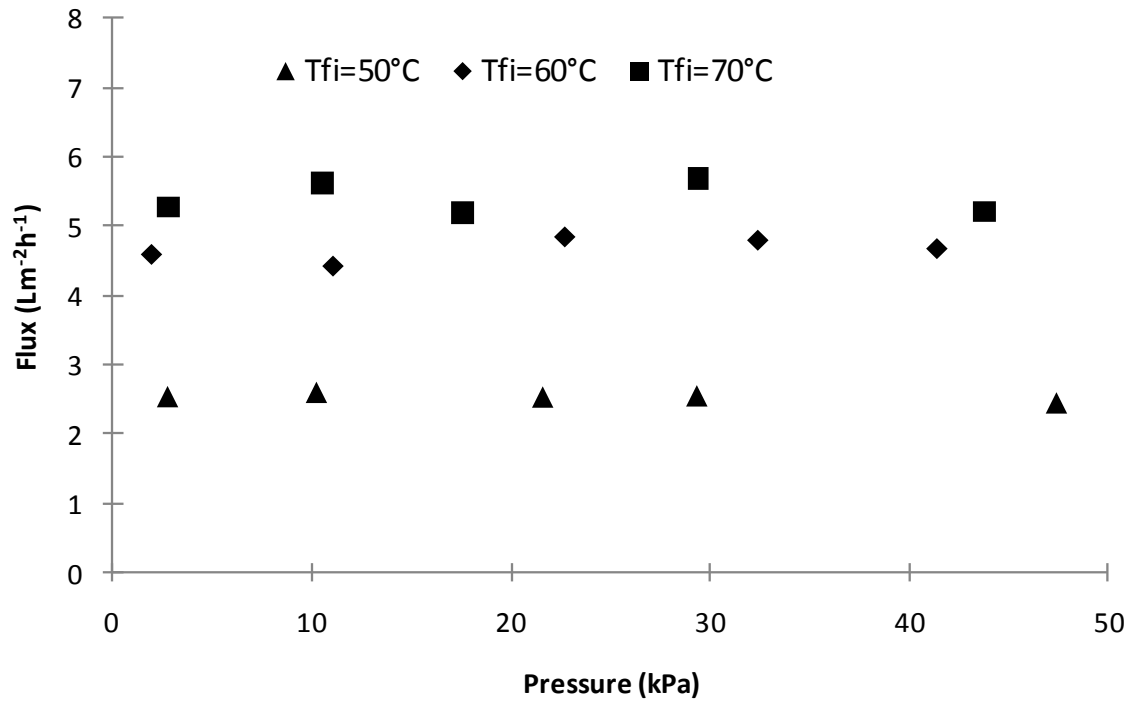
a. Flux vs pressure at different velocities



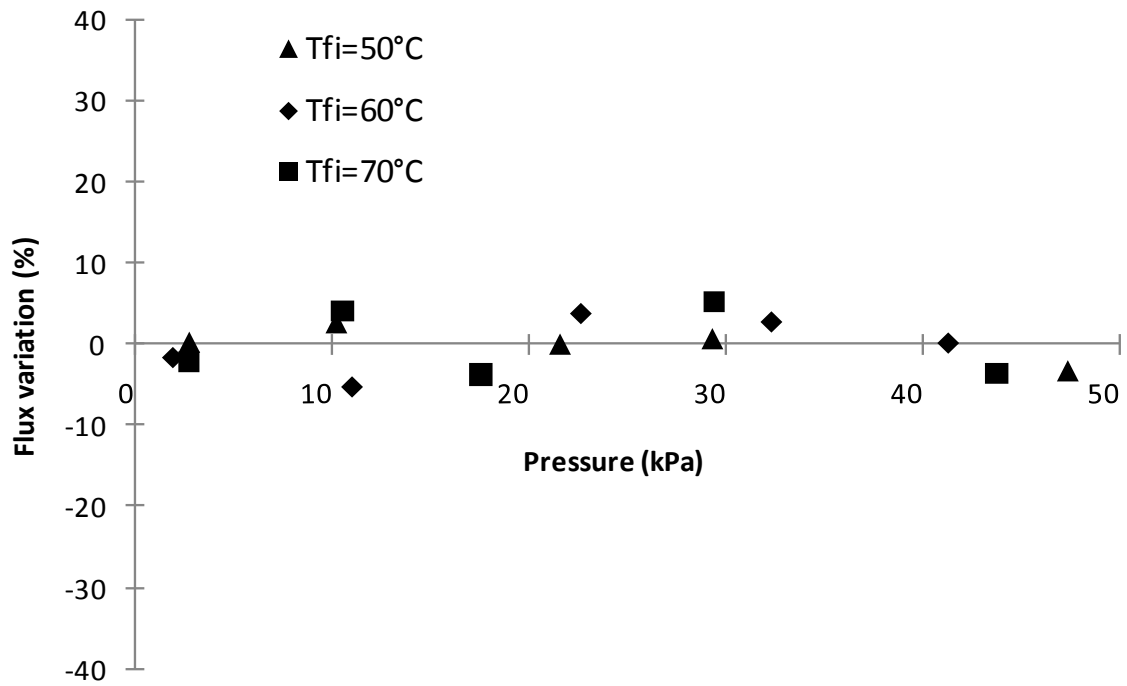
b. Variation of flux with pressures at different velocities

Fig. 5.12 Hollow fibre flux vs applied pressure at different velocities

$$(T_{fi}=60^{\circ}\text{C}, T_{pi}=20^{\circ}\text{C})$$



a. Flux vs pressure at different feed inlet temperatures



b. Variation of flux with pressures at different feed inlet temperatures

Fig. 5.13 Hollow fibre flux vs applied pressure at different feed inlet temperatures

(Stream velocity=0.16 m/s)

Similar to the results shown in Fig. 5.12, the flux variation with varied pressures at different temperatures shown in Fig. 5.13b was $\pm 5\%$ around the mean value which falls within the range of the experimental error.

The independence of flux for the hollow fibre membrane to the applied pressure stems from its incompressible nature, which results in no change of the air pressure in the pores and membrane properties such as thermal conductivity. These results also agreed with the theory in **Chapter 4**, that the pressure within the pore will not change if the positive stream pressure is applied on an incompressible membrane in DCMD.

5.4.3.2 Compressible PTFE membrane experimental results and discussion

5.4.3.2.1 Effect of applied pressure on compressible membrane at different velocities

Fig. 5.14 shows the relationship between the pressure and the flux at the same inlet temperatures and different velocities. The flux at higher velocity is greater than that at lower velocity under the same pressure. Eq. (5.15) suggests that the membrane permeability does not decrease [148] as the membrane is compacted, and therefore it is the combination of an increase in pore pressure and reduction in thermal resistance of the membrane that causes the flux decrease. From the slopes of the curves shown in this figure, it also can be found that the flux decreased faster at a lower stream velocity than that at higher velocity, due to the greater increment of sensible heat loss at low velocity. For example, sensible heat loss of the feed from the inlet to outlet can be described as,

$$\dot{Q}_{sensible} = \int_0^L \frac{\lambda}{b} (T_1 - T_2) W dx \quad (5.22)$$

where $\dot{Q}_{sensible}$ is the sensible heat loss.

For estimation purposes, the interfacial temperature difference ($T_1 - T_2$) across the membrane can be substituted with an average value ($\Delta T_{interface}$), so

$$\dot{Q}_{sensible} = \frac{\lambda}{b} \Delta T_{interface} WL \quad (5.23)$$

Therefore, the increase in sensible heat loss for compacted membranes can be described as,

$$\Delta\dot{Q}_{sensible} = WL \left(\frac{\lambda_p}{b_p} \Delta T_{interface,p} - \frac{\lambda}{b} \Delta T_{interface} \right) \quad (5.24)$$

For simplification, it can be assumed $\Delta T_{interface} \approx \Delta T_{interface,p}$ when the membrane compression is very small, so

$$\Delta\dot{Q}_{sensible} = LW \Delta T_{interface,p} \left(\frac{\lambda_p}{b_p} - \frac{\lambda_{membrane}}{b} \right) \quad (5.25)$$

Therefore, the temperature change due to sensible heat loss after the feed mass passed the membrane can be described as:

$$\Delta T_{f,conduction} = \frac{LW}{\dot{m}c_p} \Delta T_{interface,p} \left(\frac{\lambda_p}{b_p} - \frac{\lambda_{membrane}}{b} \right) = \frac{C'}{v} \left(\frac{\lambda_p}{b_p} - \frac{\lambda_{membrane}}{b} \right),$$

in which:

$$\dot{m} = \rho v h W, \text{ and } C' = \frac{L \Delta T_{interface,p}}{c_p \rho h}$$

$$\Delta T_{f,conduction} = \frac{C'}{v} \Delta \alpha_{conduction} \quad (5.26)$$

where h is the height of the channel, and $\Delta \alpha_{conduction}$ is the change of the membrane heat conduction coefficient under pressure.

Based on Eq. (5.26), as the membrane becomes more compact, there is a greater temperature gradient with $\Delta \alpha_{conduction}$ at lower velocity, which leads to a faster decrease of flux as shown in Fig. 5.14.

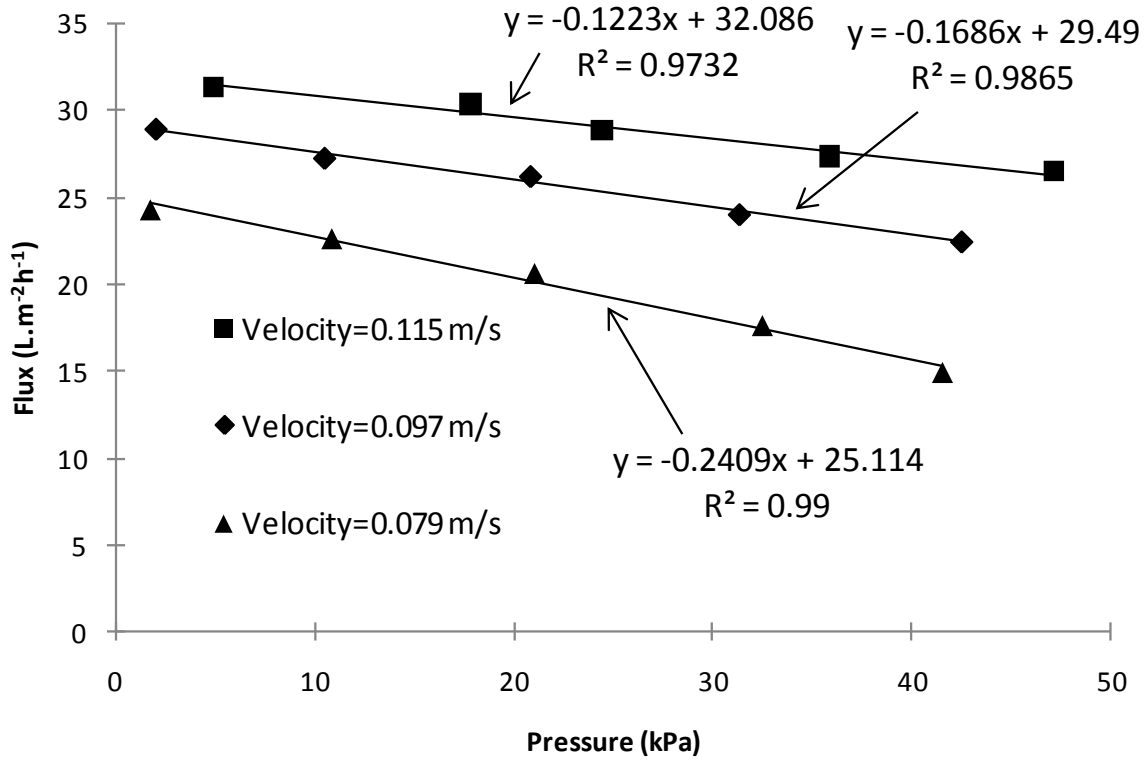
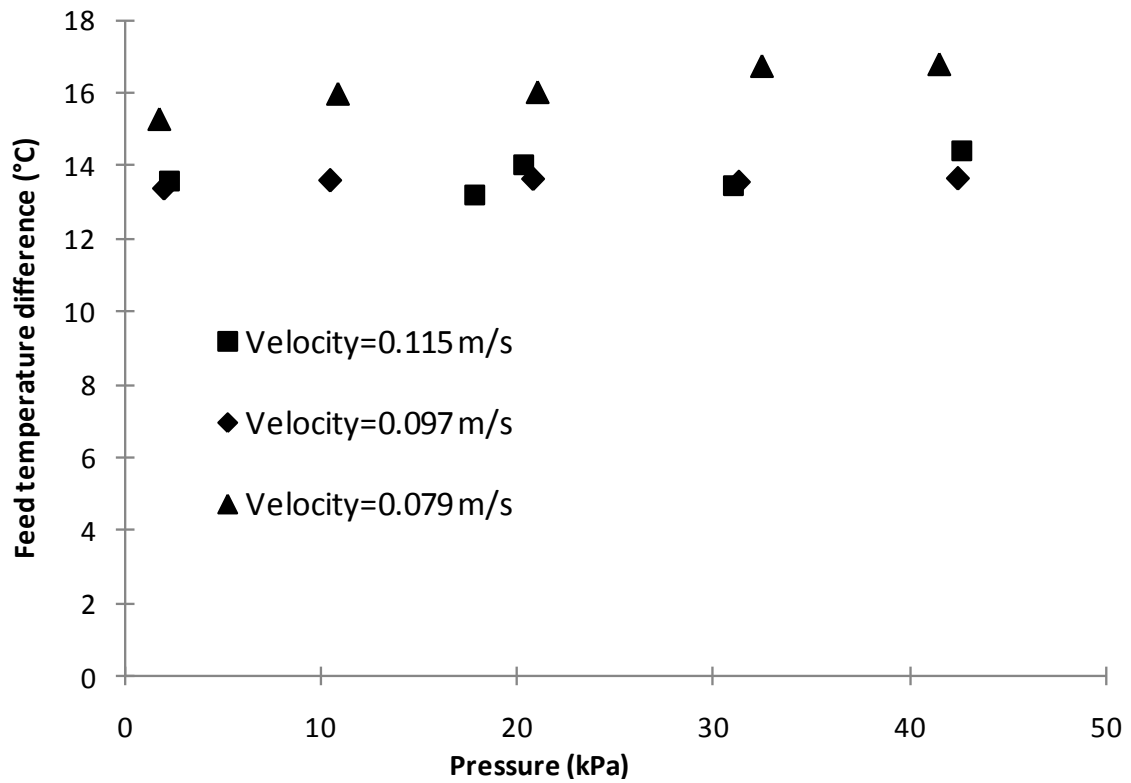


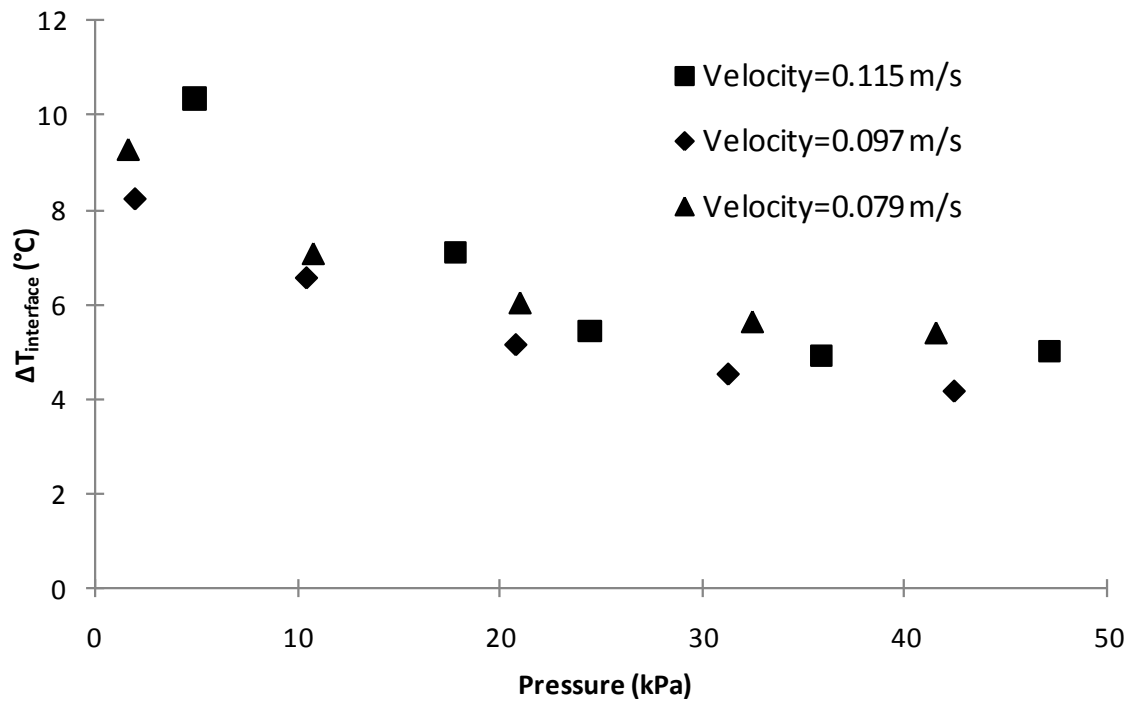
Fig. 5.14 Flat sheet PTFE flux vs applied pressure

$$(T_{fi}=60^{\circ}\text{C}, T_{pi}=20^{\circ}\text{C})$$

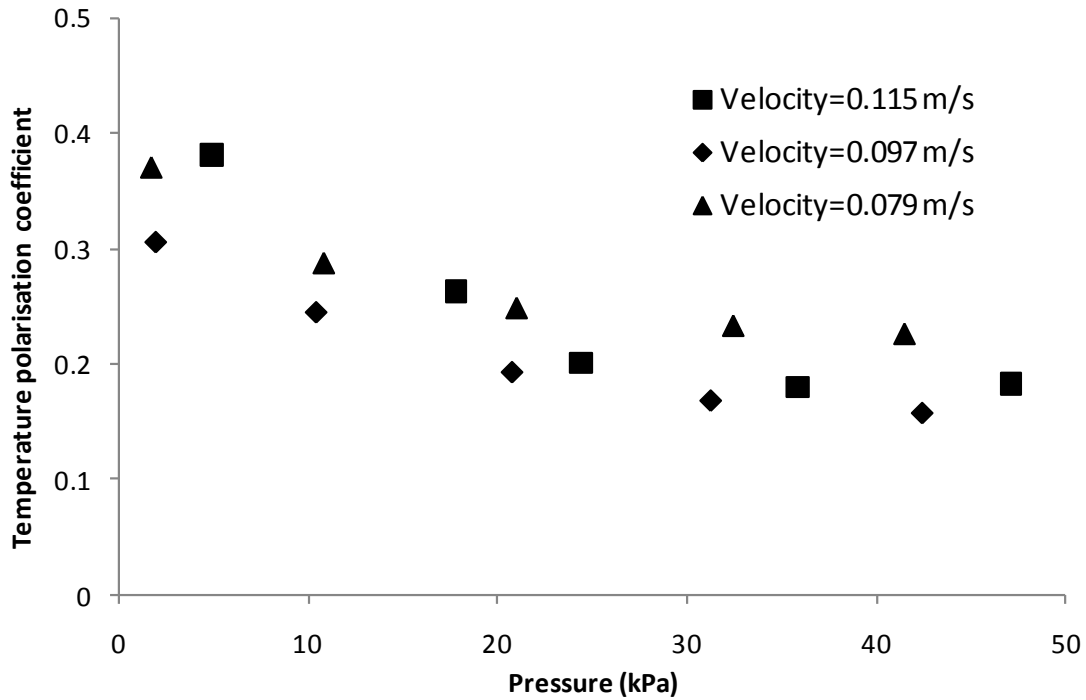
In Fig. 5.15a, the temperature difference between the feed inlet and outlet has a minor increasing trend (from 15.3 to 16.8 at 0.079 m/s, from 13.4 to 13.6°C at 0.097 m/s and from 13.4 to 14.4°C at 0.115 m/s) as the pressure is increased at constant velocity. Because the flux decreased as pressure increased, the heat used for evaporation (JAH_{latent}) was reduced. Therefore, the increment of the sensible heat loss ($\lambda A \Delta T_{interface}/b$) is almost equivalent to the reduction of evaporation heat (JAH_{latent}), because of the reduced membrane thermal resistance.



a. ΔT_f under different pressure



b. $\Delta T_{interface}$ under different pressure



c. Temperature polarisation coefficient under different pressures

Fig. 5.15 Changes of thermal conditions under different pressures ($T_{fi}=60^{\circ}\text{C}$, $T_{pi}=20^{\circ}\text{C}$)

$$(T_{fi}=60^{\circ}\text{C}, T_{pi}=20^{\circ}\text{C})$$

Fig. 5.15b shows the mean $\Delta T_{interface}$ calculated from Eq. (5.19) based on the fitting equation for the heat transfer coefficient in Fig. 5.11c. $\Delta T_{interface}$ shows a declining trend with increased pressure, and reaches a plateau when the pressure is greater than 30 kPa. Furthermore, in Fig. 5.15c, the mean temperature polarisation coefficient shows a similar trend to that of $\Delta T_{interface}$, so the pressure increase also causes an increase in the temperature polarisation.

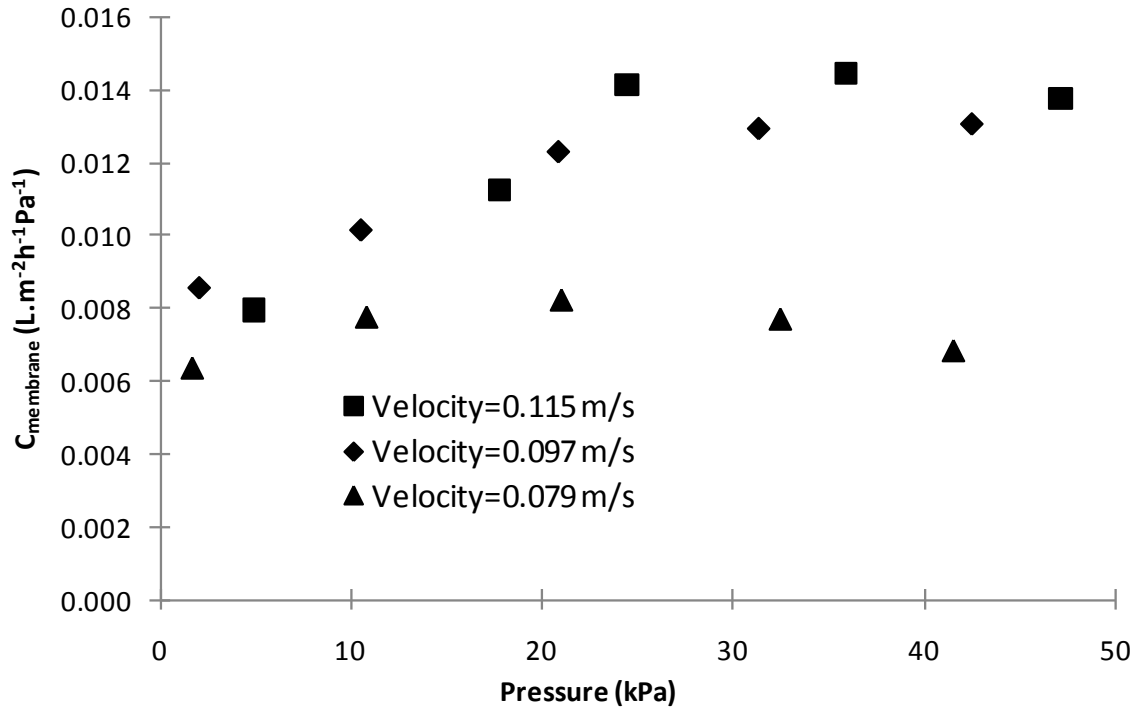


Fig. 5.16 Mean membrane mass transfer coefficient under different pressures

The estimated mean mass transfer coefficients of the three membranes are shown in Fig. 5.16 and based on Eqs. (4.11), (4.12) and (4.15), the membrane mass transfer coefficient can also be expressed as

$$C_{membrane} = 7.81 \times \frac{\varepsilon}{bt} \frac{dMT^{1.072}}{5.685\sqrt{2\pi RMT+4dR(P_{pore}-P_A)}} \quad (5.27)$$

From this figure, it can be found that the membranes used at velocities of 0.097 and 0.115 m/s had similar membrane mass transfer coefficients under different pressures, but the membrane used for 0.079 m/s shows a much lower $C_{membrane}$ than the other two over all pressure ranges, which maybe due to the difference of membrane sample (there are great variation found of different membrane sample seen in Table 5.2 and Fig. 5.2). According to Eq. (5.27), the membrane mass transfer coefficient can be considered as independent of process parameters in DCMD, so the $\Delta T_{interface}$ and temperature polarisation coefficient calculated based on the results at the velocities of 0.115 m/s and 0.097 m/s are comparable under the same conditions. In Figs. 5.15b and 5.15c, less polarisation and higher $\Delta T_{interface}$ are found at higher velocity, but the difference is approaching zero at higher pressure.

In Fig. 5.16, as the pressure is increased, the mass transfer coefficients calculated using

the interfacial temperature (Eq. (5.21)) showed an increasing trend in the lower pressure range, and appeared to reach a plateau in the range of 30-40 kPa. This phenomenon may be caused by a combination of parameter changes at high pressure, and also supports the assumption that the tortuosity remains almost constant. As according to Eq. (5.27), the membrane mass transfer coefficient is a function of membrane properties ($\epsilon d/bt$, d), temperatures (T) in the pores and total pressure in the pores (P_{pore}). By substituting Eq. (5.15) into Eq. (5.27), it can be derived,

$$C_{membrane} = C_0 \frac{\epsilon_p^{1.5}(1-\epsilon_p)}{t_p^{1.5}} \frac{MT^{1.072}}{5.685\sqrt{2\pi RMT} + 4dR(P_{pore} - P_A)} \quad (5.28)$$

When the pressure is increased, the pore temperature remains almost constant according to Eq. (5.21) and the conclusions from Fig. 5.15, the increased $\epsilon_p^{1.5}(1-\epsilon_p)$ and the decreased pore size (discussed in Section 5.4.2.4) tend to increase $C_{membrane}$, but the increased pore pressure acts to decrease $C_{membrane}$. Therefore, it is the different rates of change of these parameters with increasing pressure that cause a reduction in the rate of $C_{membrane}$ increase. This is demonstrated by the flatter curve in Fig. 5.10 at lower porosities (higher pressures) indicating that the rate of increase of $d\epsilon/bt$ as evaluated by $\epsilon_p^{1.5}(1-\epsilon_p)$ is reduced at higher pressures. Additionally, the rate of decrease in pore size is also reduced at higher pressures, as demonstrated by Eq. (5.14) and Fig. 5.11a (porosity and thickness plateaued at higher pressures). The pore pressure, however, which leads to a decrease in $C_{membrane}$, increased linearly with the applied pressure on the membrane (shown in Fig. 5.9) for the range of pressures tested. For example, as the applied absolute pressure increased from 121 to 131 kPa (gauge pressure 20 to 30 kPa), the porosity decreased from approximately 0.79 to 0.73, so there was an 8.3% increment of pore absolute pressure, a 14.3% increase of $d\epsilon/bt$, and a 3.9% reduction of pore size (Eq. (5.14), assuming tortuosities do not change). However, when the pressure was increased from 30 to 40 kPa, porosity decreased from 0.73 to 0.68 and there was a 6% increment of pore pressure, a 5.8% increment of $d\epsilon/bt$ and a 3.5% reduction of pore size. As a result, $C_{membrane}$ remained almost constant for pressures above 30 kPa as shown in Fig. 5.16.

5.4.3.2.2 Effect of applied pressure on compressible membranes at different temperatures

Fig. 5.17 shows the flux variation with the applied pressures for different temperatures,

and demonstrates that the flux was greater at higher temperature for any given pressure. The slopes of the fitting curves (Fig. 5.17) demonstrate that the flux is more strongly dependent upon the applied pressure at higher temperature, which resulted from the exponential relationship of vapour pressure and temperature (the same value of temperature decrease will cause greater vapour pressure reduction at higher temperature as shown in Fig. 4.14).

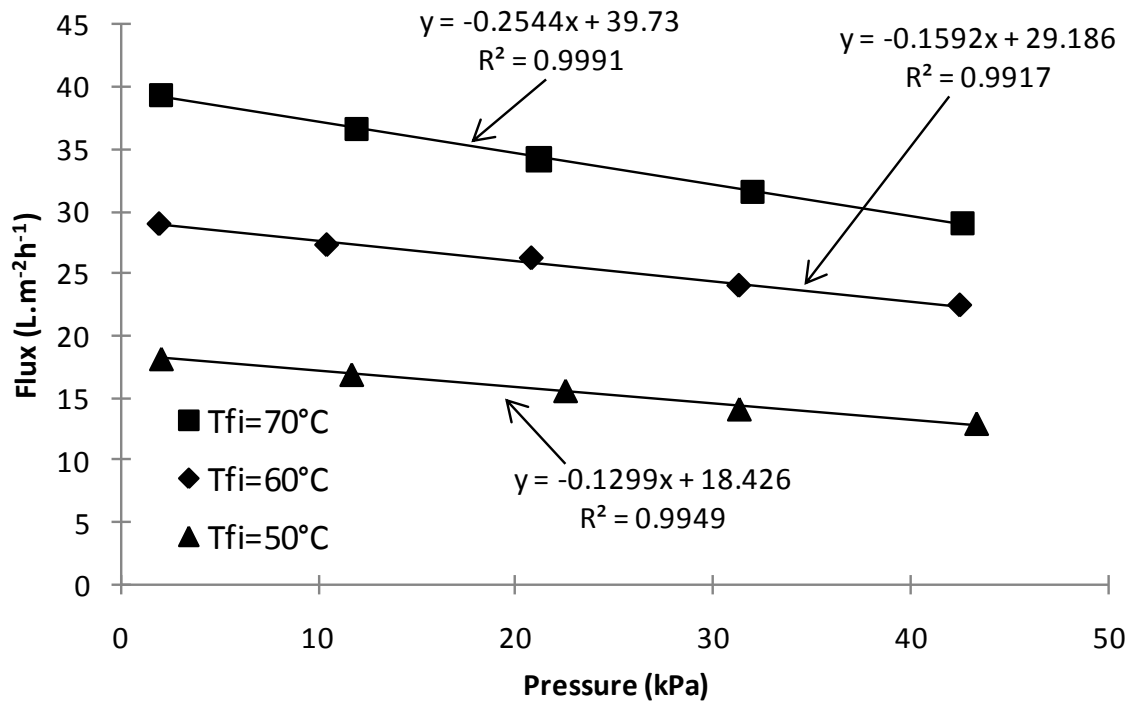
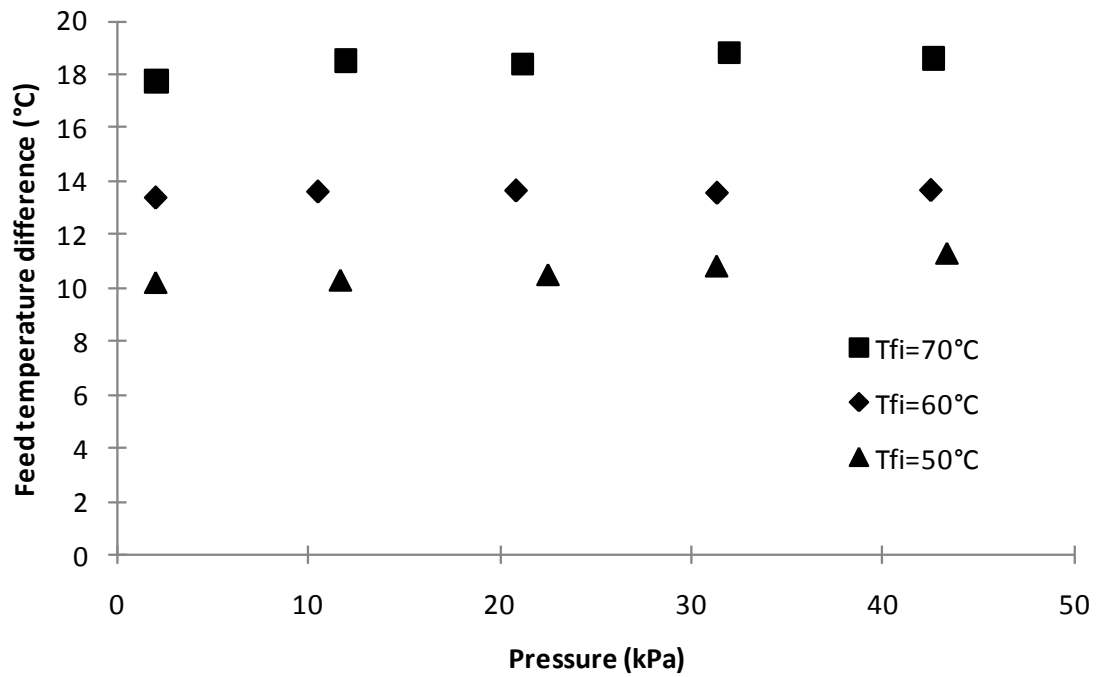


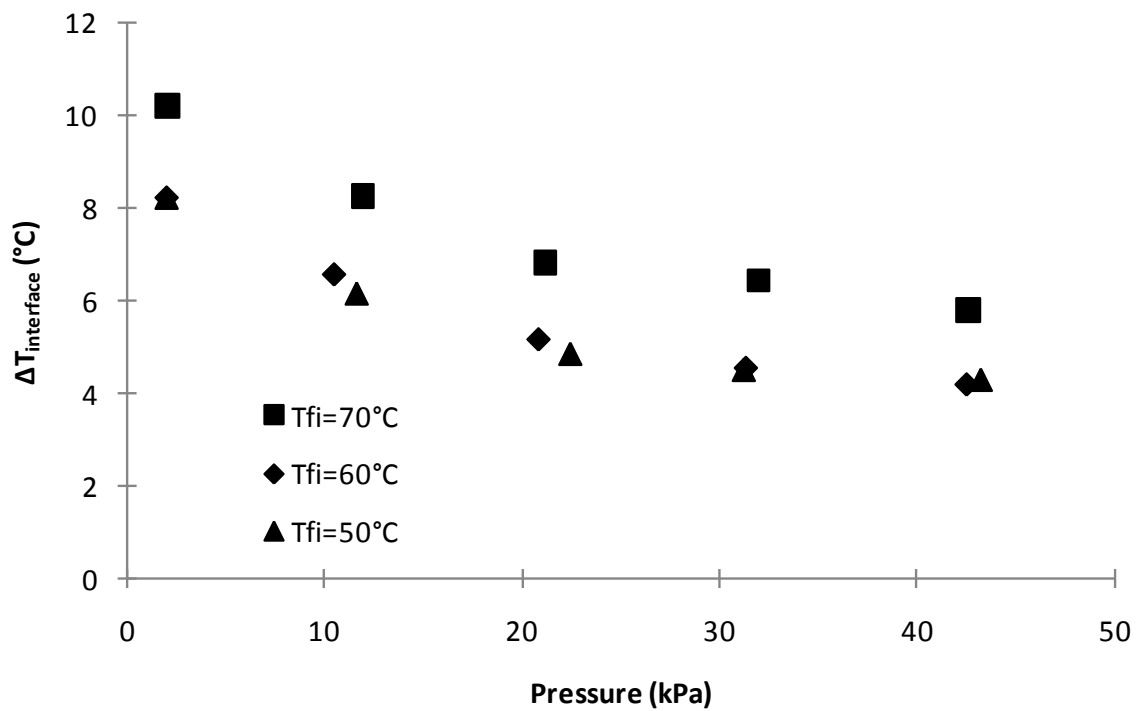
Fig. 5.17 Flux changed with varied pressures at different temperatures

(Velocity=0.097 m/s)

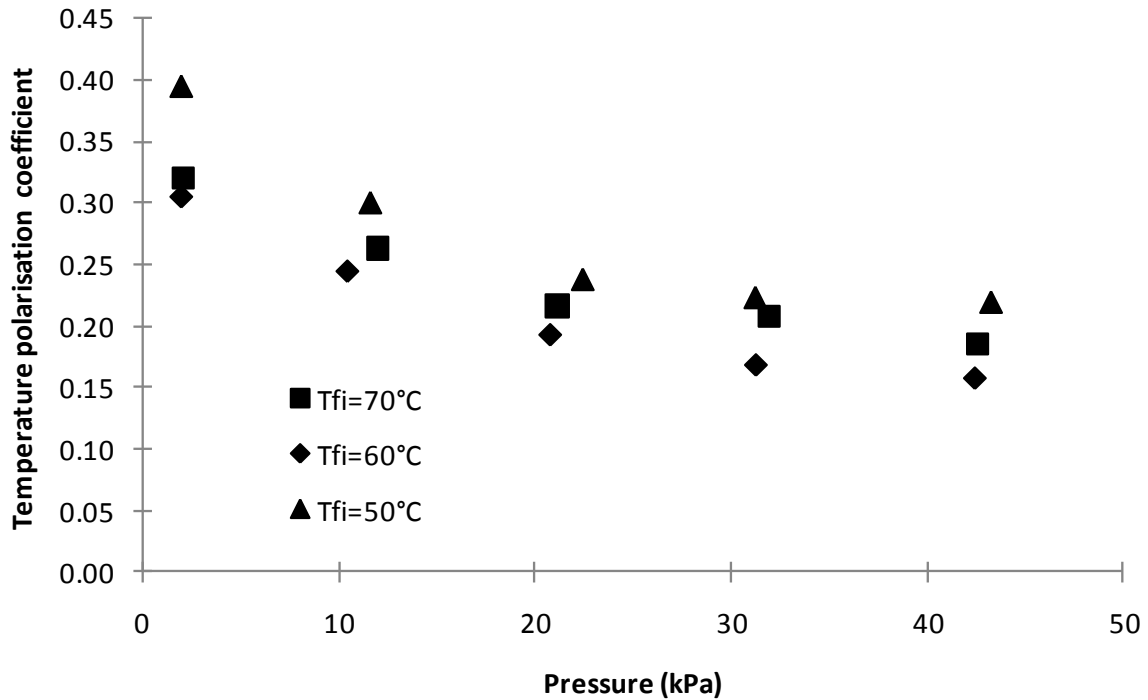
In Figs 5.18 and 5.19, the trends in the variation of thermal conditions and $C_{membrane}$ with pressure for different temperatures are similar to those for different velocities. In Fig. 5.19, the $C_{membrane}$ values at 70°C and 50°C were the same, but $C_{membrane}$ value at 60°C was higher than the other two over the entire range of tested pressures, which maybe due to the difference between membrane samples.



a. ΔT_f under different pressure



b. $\Delta T_{interface}$ under different pressures



c. Temperature polarisation coefficient under different pressures

Fig. 5.18 Changes of thermal conditions under different pressures

(Velocity=0.097 m/s)

By comparing the curves of membranes with the same $C_{membrane}$ values used at 70°C and 50°C in Fig. 5.18c, a slightly smaller temperature polarisation coefficient was observed for higher temperatures across the pressure range, which agrees with the findings from **Chapter 3**. The difference between the temperature polarisation coefficients for the two temperatures is reduced at higher pressure, while the difference in $\Delta T_{interface}$ (Fig. 5.18b) of different temperatures does not change greatly. A similar effect of pressure on temperature polarisation coefficients was also observed for different velocities at higher pressures. However, from Figs. 5.14 and 5.17, it can be seen that the pressure increase enhanced the flux difference at different stream velocities and reduced the flux difference at different feed inlet temperatures.

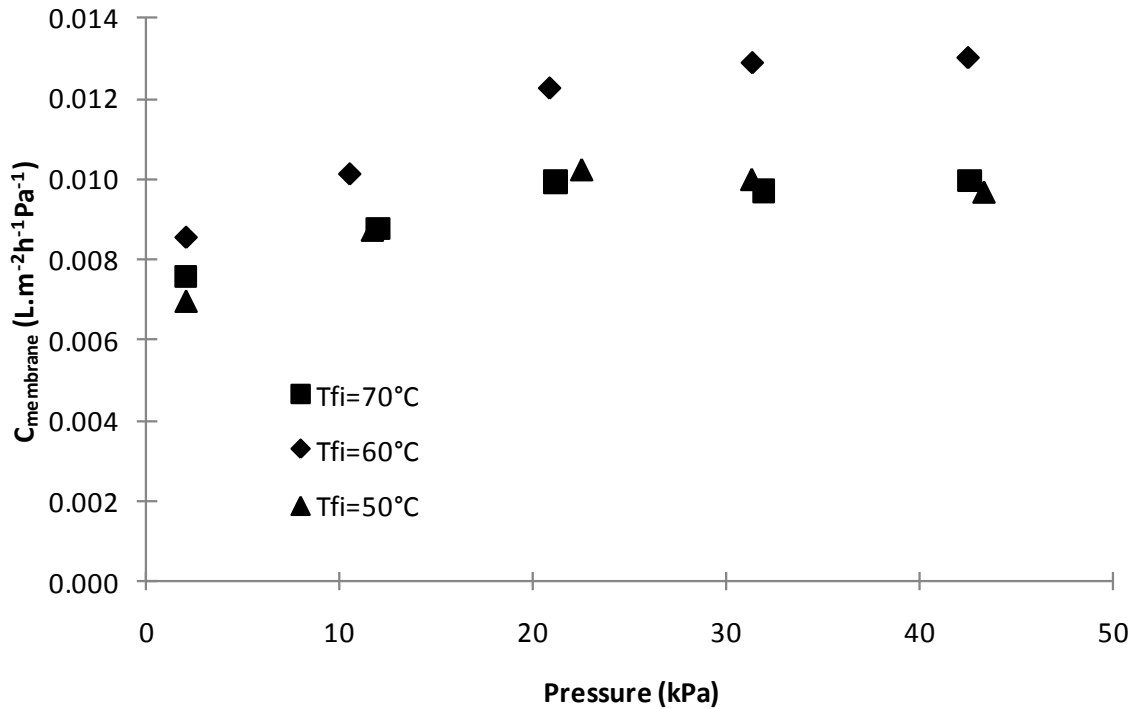


Fig. 5.19 Mean membrane mass transfer coefficient under different pressures (Velocity=0.097 m/s)

5.5 Summary

An incompressible hollow fibre membrane and a compressible PTFE membrane were employed to study the influence of applied pressure on membrane performance in DCMD for several temperatures and velocities.

From the experimental results, it was found that membranes with incompressible or rigid structure produce more stable flux than that of compressible membrane under different pressure. Therefore, it is recommended for manufacturers that membranes with rigid structure will be more suitable for MD scale-up, due to the more predictable flux than that of membranes with compressible structures. It is also recommended for process designers that it is better to reduce membrane length in the flow direction to avoid greater pressure drops along the membrane, if the compressible membrane is the choice for design.

Chapter 6 Mathematical models for direct contact membrane distillation

6.1 Simple model developed based on the global mass transfer coefficient

6.1.1 Introduction

The previous MD modelling has mainly focused on the overall mass transfer and heat transfer processes related to membrane properties, i.e. the porosity, pore size, etc. [27, 74, 90, 114], which are important for membrane design but are less so for process design. Although a model based on engineering measurable parameters is very important for scaling-up MD, there are very few articles in literature focused on this, and the previous process models reported only include the dependence of flux on membrane length of the hollow fibre membranes [149], but did not include that phenomena for flat sheet membranes. Therefore, the aim of this chapter was to develop mathematical models suitable for process design and scale up that incorporate the effect of membrane length, and to experimentally verify the model.

In direct contact membrane distillation, mass transfer (evaporation) is coupled with heat transfer. Therefore, a complex relation between the heat and mass transferred through the membrane should be solved to predict the flux from inlet feed temperatures or membranes of different sizes. From the experimental results (Fig. 4.10b), it was found that the calculated global mass transfer coefficient did not vary greatly when the hydrodynamic conditions (turbulence or boundary layer conditions) were constant, but did vary greatly with different stream velocities (Fig. 4.9b). Based on this finding, a simple model was developed to predict flux from different temperatures and membrane sizes using the global mass transfer coefficient obtained experimentally at the same stream velocity, instead of calculating a local mass transfer coefficient. This model provides a simple tool to estimate the flux of a large sheet membrane based on results from small module test results, and can provide an approximate reference point for designing a pilot module and process. From this model, the temperature profile along the membrane at a given stream velocity can also be described. Furthermore, it can be

used as a technique for comparing the performance of membranes (as shown in **Chapter 3**).

6.1.2 Simulation and experiment

6.1.2.1 Theoretical analysis of one-dimension model for DCMD

For a given DCMD system, it can be expected that the flux (J) depends on many parameters and a general relationship can be written as

$$J = f(A, T_f, T_p, \dot{m}_f, \dot{m}_p, C_{membrane}, U) \quad (6.1)$$

Here, \dot{m}_p and \dot{m}_f are the mass flow rates for the cold side and hot side. .

Additionally, the following assumptions were made to further simplify the model:

1. no heat loss through the module wall to the atmosphere; this is supported by a calculated heat loss through the wall of less than 3 W, which is less than 1% of the heat loss from the feed, and no difference in flux or energy efficiency for experiments with and without thermal insulation,
2. specific heat of evaporation and condensation does not change with concentration, based on the finding of R.G. Lunnon [150],
3. with a given membrane at a given flowrate, both C_{global} and U are constant,
4. there is no temperature gradient across the membrane perpendicular to the flow direction (i.e. the width direction of the module),
5. in balancing the mass transfer, the mass of the permeate crossing the membrane can be neglected, based on the experimental finding that the maximum single pass recovery is 1.1-4% in this study, and
6. in balancing the heat transfer, the sensible heat carried by the permeate can be neglected, because there is normally less than 3% of the total sensible thermal energy carried by the vapour transferred to the cold side. For example, based on the experimental data of this study and calculations in **Chapter 5**, the temperature difference between the hot interface and the cold bulk stream is about 14°C, so the temperature rising due to the sensible heat on the cold side is less than 0.17-0.3°C (based on the maximum 1.1-2% single recovery), which is about 1.7-3% of the total heat transferred through vaporisation and heat

conduction.

According to these assumptions and Eq. (2.19), the flux can be expressed as:

$$J = C_{global}(P_{Tf} - P_{Tp}) \quad (6.2)$$

where C_{global} includes the mass transfer phenomena in the membrane and the boundary layer.

Fig. 6.1 shows a heat and mass transfer element of a co-current DCMD in a flat sheet module. In this element, the thermal energy change in the hot side can be described as

$$C_{p,f}\dot{m}_f(T_{f,i+1} - T_{f,i}) = -(JH_{latent}dA + U(T_f - T_p)dA) \quad (6.3)$$

where $T_{f,i}$ and $T_{f,i+1}$ are temperatures at the i^{th} and $(i+1)^{th}$ points, and $C_{p,f}$ is the specific heat of feed.

Because $dA = Wdx$, where W is the membrane width, the relation between the temperature change and stream displacement can be expressed as,

$$dT_f = -\frac{W(J_i H_{latent} + U(T_{f,i} - T_{p,i}))}{C_{p,f}\dot{m}_f} dx \quad (6.4)$$

Therefore, the feed temperature change after the feed stream passes each element can be described as,

$$\Delta T_{f,i} = -\frac{C_{global}\left[EXP\left(23.1964 - \frac{3816.44}{T_{f,i} + 227.02}\right) - EXP\left(23.1964 - \frac{3816.44}{T_{p,i} + 227.02}\right)\right]H_{latent} + U(T_{f,i} - T_{p,i})}{C_{p,f}\dot{m}_f} W \Delta x \quad (6.5)$$

Because C_{global} and U are assumed to be constants, the temperature of the feed stream at $(i+1)^{th}$ can be calculated by

$$T_{f,i+1} = T_{f,i} - \Delta T_{f,i} \quad (6.6)$$

Similarly, the permeate temperature can be calculated by

$$T_{p,i+1} = T_{p,i} - \frac{\dot{m}_f}{\dot{m}_p} \Delta T_{f,i} \quad (6.7)$$

Thus, the flux at $(i+1)^{th}$ can be calculated as:

$$J_{i+1} = C_{global}(P_{Tf,i+1} - P_{Tp,i+1}) \quad (6.8)$$

From which the total flux of the membrane can be calculated as

$$J = \frac{\sum_{i=0}^N J_i W \Delta x}{A} = \frac{\sum_{i=0}^N J_i \Delta x}{L} \quad (6.9)$$

The above equations can be solved numerically. For co-current flow, the numerical procedure is shown in Fig. 6.2. For counter-current flows, an iteration process is required and the process is shown in Fig. 6.3.

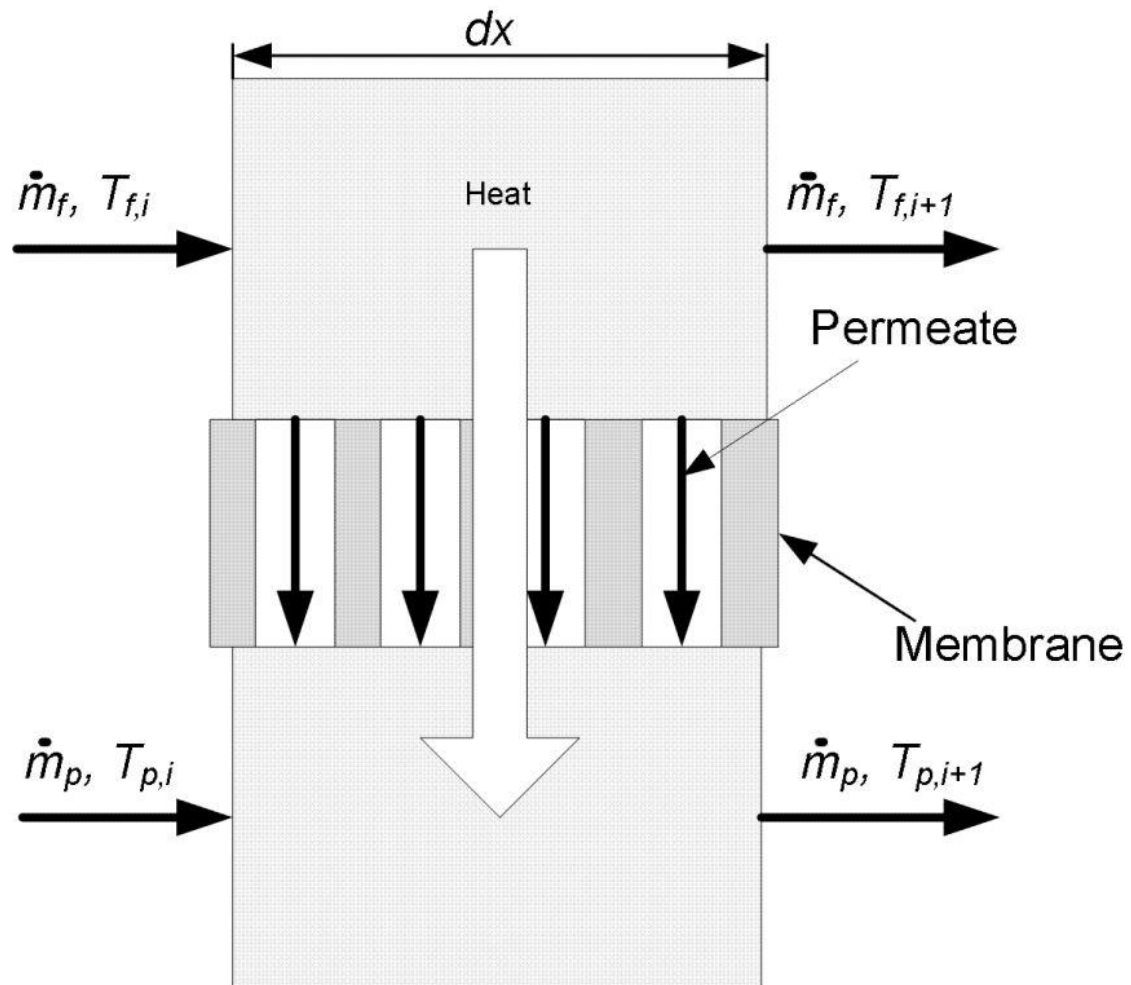


Fig. 6.1 Heat and mass transfer element of a co-current DCMD

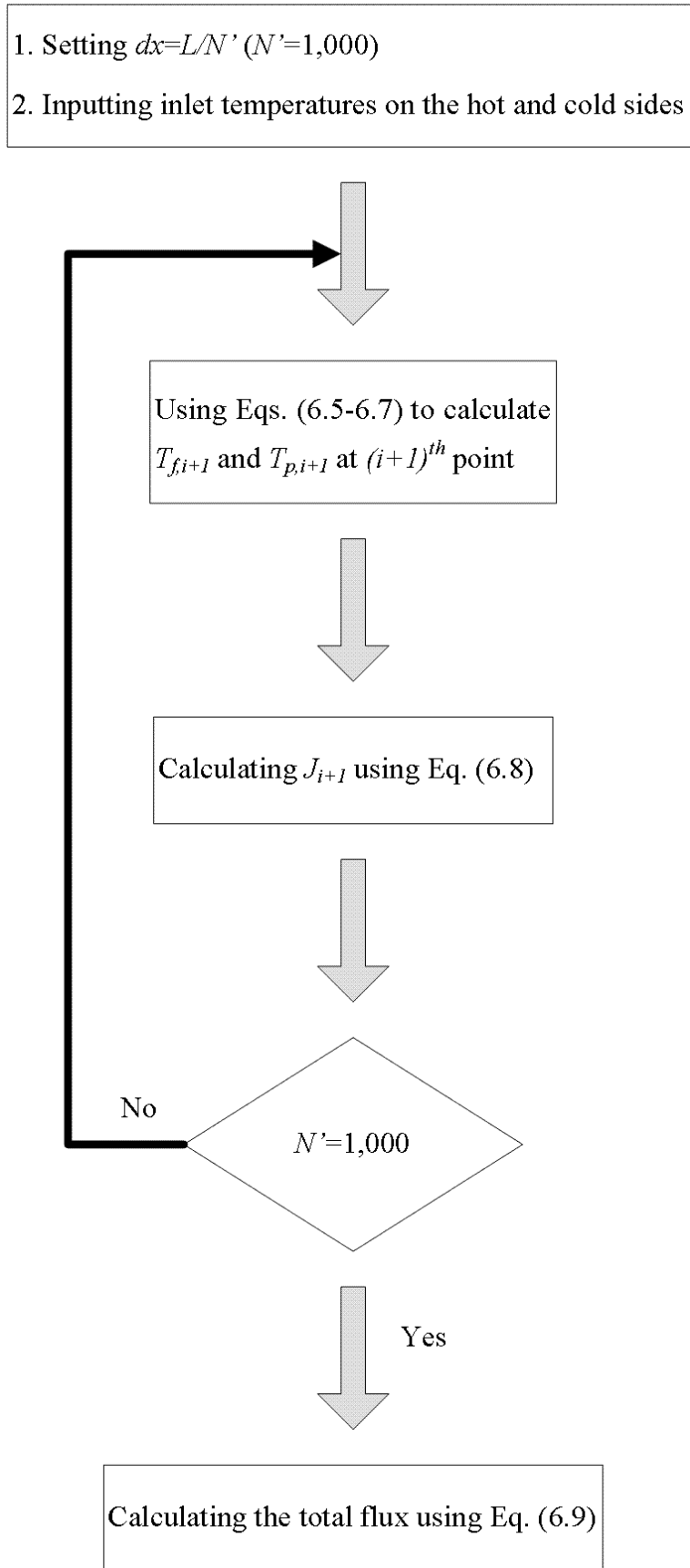


Fig. 6.2 Schematic diagram for numerical flux calculation of co-current flow

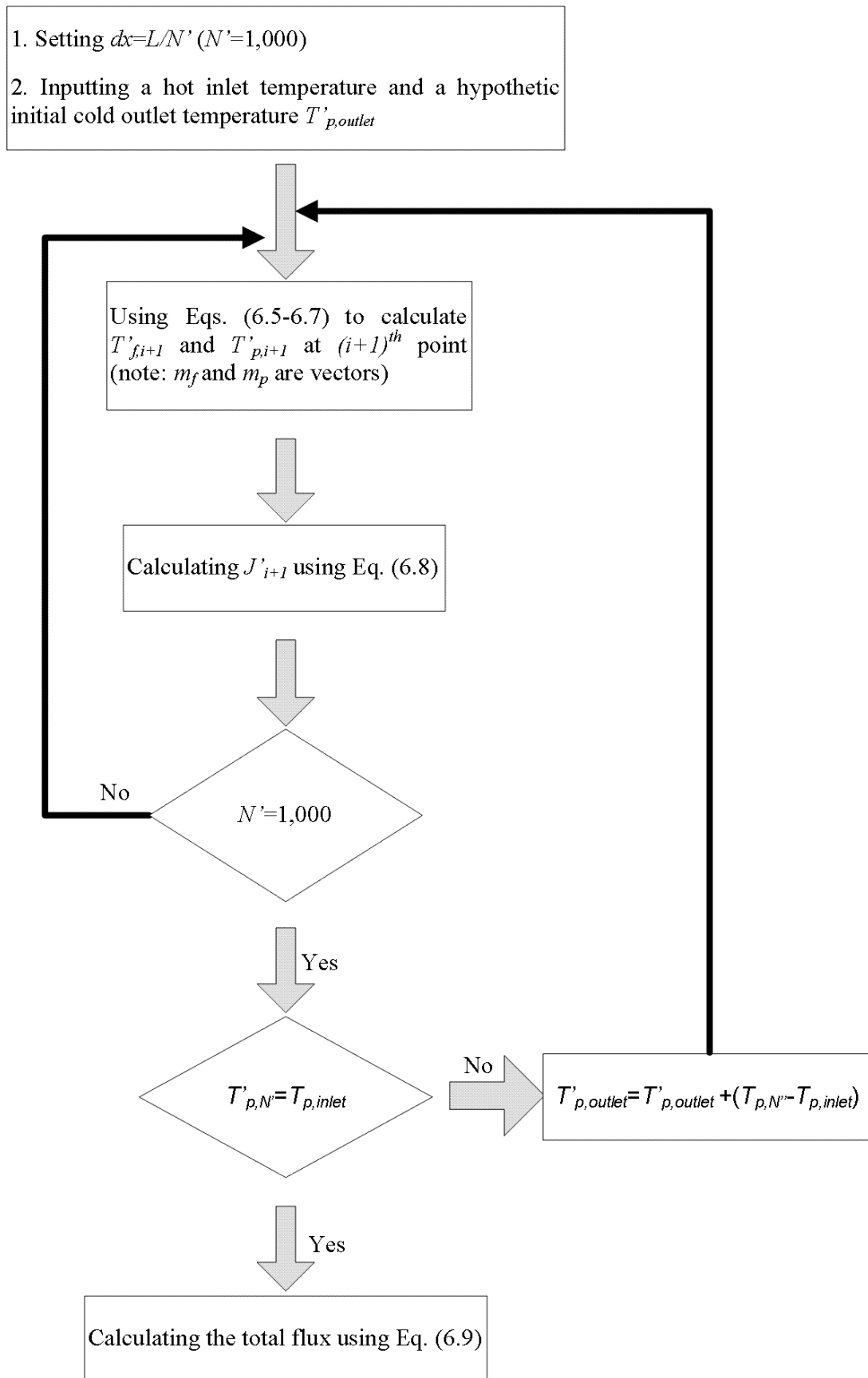


Fig. 6.3 Schematic diagram for numerical flux calculation of counter-current flow

6.1.3 Experimental apparatus and procedure

A schematic diagram of the DCMD process employed in this study is shown in Fig. 3.4. The feed and permeate were set to identical flowrate and varied in range of 300-800±20 mL/min (0.20-0.53 m/s). The cold inlet temperature was held constant at 20±2°C and the hot inlet temperature was varied in the range of 40-80±2°C. The feed solution was made by dissolving 10 grams of sodium chloride in 1 litre of deionised water. Deionised water was used on the permeate side as coolant.

An Osmonic module with effective flow channel length of 0.136 m and a Perspex module with flow channel that varied in the range of 0.07-0.13 m were used in the tests. Two kinds of membranes were tested in this study. The membrane used for the Osmonics module had a nonwoven fabric support layer, nominal pore size of 1 µm, contact angle of 126°±5 and an effective area of 0.0136 m²; the membrane used for the Perspex module has a scrim support layer, pore size of 0.5 µm, contact angle of 140°±5 and the effective area varied in the range of 0.0091-0.0169 m².

Each experiment lasted at least 3 h and the mean flux is reported here. The variation of the experimental flux around the mean value was in the range of ±5%. The global heat transfer coefficients and mass transfer coefficients used in modelling at different velocities were calculated from the experimental results using Eqs. (6.2) and (6.3). Both counter-current and co-current setups were tested and modelled.

6.1.4 Results and discussion

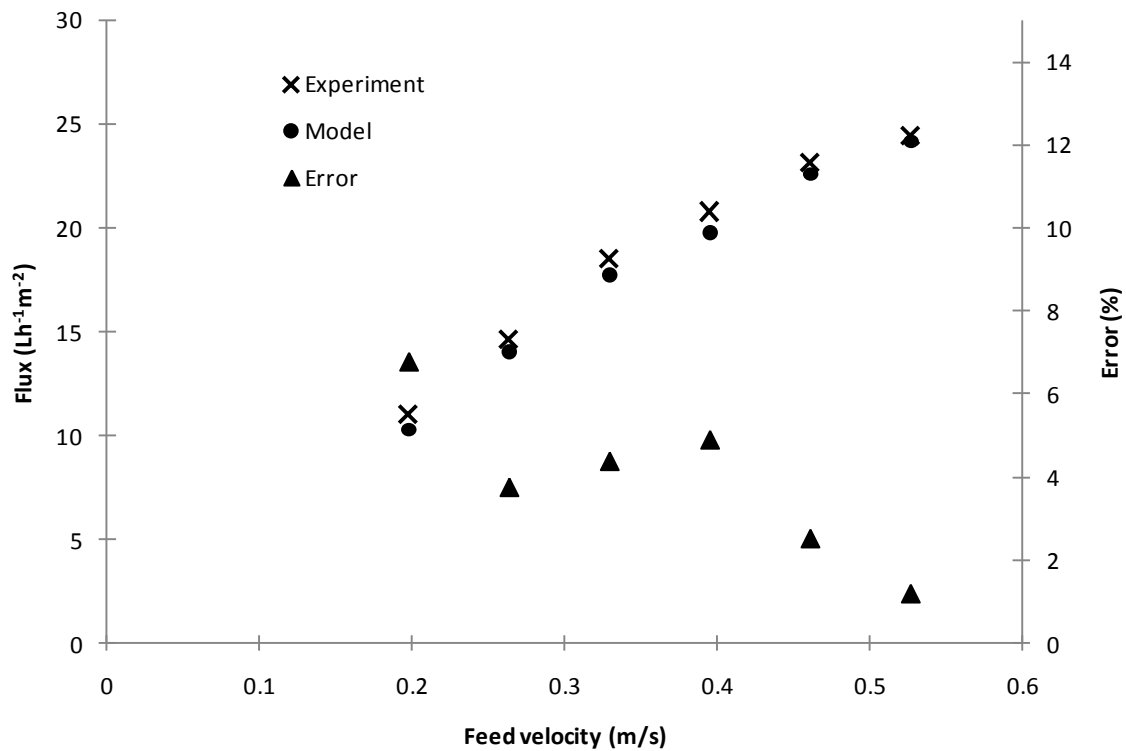
6.1.4.1 Verification of the modelling results

6.1.4.1.1 Validating the use of the mean global mass and heat transfer coefficients in flux prediction

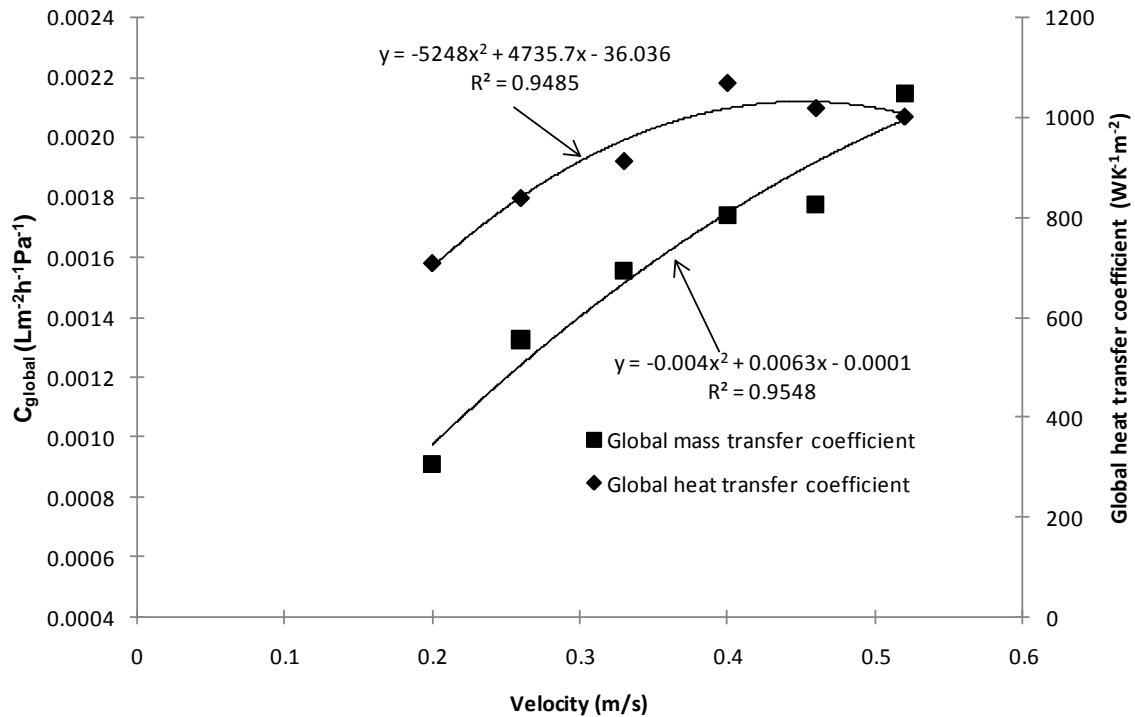
From Eqs (2.19), and (6.1)-(6.3), it can be found that the mean global mass transfer coefficient includes both the mass transfer phenomena in the boundary layer and across the membrane. Although the mass transfer phenomenon across the membrane will only change with the properties of membrane, the boundary layer will be affected dramatically by the turbulence promoter (spacer) and stream velocities. Therefore, the mean global mass transfer coefficient will be also affected, if different membranes,

spacers or/and stream velocities are employed. In DCMD, the variations of the membrane length and temperature will have minor influences on the boundary layer conditions. Hence, if all the factors affecting the boundary conditions are preset, the calculated global mass and heat transfer coefficients from Eqs. (6.2) and (6.3) can theoretically be used to predict the flux under this preset condition.

In the model, the local flux of each element was calculated from the mean mass and heat transfer coefficients based on the fitting equations in Fig. 6.4b, and the total flux from the modelling was calculated by summing up flux of all elements. However, due to the variation of the temperature profiles along the membrane, the real local mass transfer coefficient (function of mean pore temperature) and heat transfer coefficient (function of fluid viscosity) are different in each element. Therefore, it is necessary to validate if using mean values of the global mass and heat transfer coefficients instead of the local values will lead to unacceptable errors.



a. Comparison between experimental and modelling results at different velocities for counter-current



b. Fitting equations of mean global mass and heat transfer coefficients for modelling

Fig. 6.4 Validation of mean global mass and heat transfer coefficients with velocity

(Osmonics Module, 1 μm membrane with nonwoven fabric support)

Fig. 6.4a shows the experimental and predicted results and the errors between them, which were obtained from a PTFE membrane with a pore size of 1 μm using the Osmonics module. The counter-current mode experiments were carried out at different flowrates, and the mean mass and heat transfer coefficients at each flow rate were calculated and used for the model. A maximum error of less than 7% can be found between the predicted and experimental results, which is comparable with the experimental variation ($\pm 5\%$). Thus, the mean global mass and heat transfer coefficients were acceptable for predicting the flux at a given flowrate.

6.1.4.1.2 Verification of the model at different temperatures

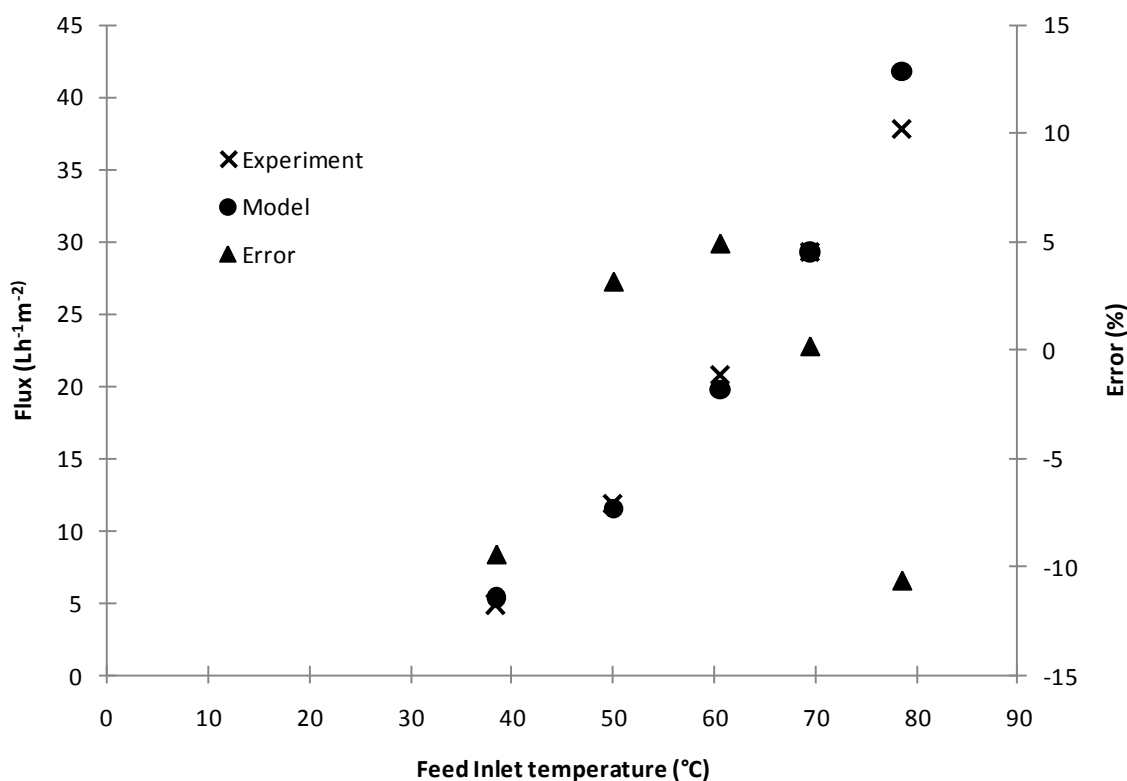


Fig. 6.5 Comparison between experimental and modelling results at different temperatures for counter-current setup

(Osmonics module, 1 μ m membrane with nonwoven fabric support)

To verify the model, the mean global heat and mass transfer coefficients derived from the experimental data shown in Fig. 6.4 were used to predict the flux at different temperatures. In Fig. 6.5, the predicted and experimentally derived flux results from a counter-current DCMD are shown. The experiments were conducted at different hot inlet temperatures (40-80°C) and a fixed velocity of 0.4 m/s (600 mL/min), and the mean global heat and mass transfer coefficients used in the model were calculated from the experiment carried out at feed inlet temperature of 60°C at 0.4 m/s. Although the errors became larger as the feed inlet temperature is further from 60°C, the largest absolute errors were still about 10% and appeared at 40°C and 80°C respectively. Therefore, there is reasonable agreement between the model and experimental results, as the mean mass and heat transfer coefficients derived from one temperature are used in this model to predict the flux at different temperature for a given velocity (ie. similar

hydrodynamic conditions).

However, variations in the flowrate will produce different turbulence regimes and are expected to significantly alter the mean global mass and heat transfer coefficients. Therefore, it is necessary to experimentally build a database of the mean global mass and heat transfer coefficients at different velocities, from which the mean global mass and heat transfer coefficients can be selected or calculated from the polynomial curve of the data for prediction of the flux at different temperatures at a given velocity as shown in Fig. 6.4b.

6.1.4.1.3 Verification the model with different membrane lengths

The model was also verified with different membrane length. In these experiments, the Perspex module and a membrane with pore size of 0.5 μm and scrim support layer were used. Both co- and counter-current setups were tested, and, a new piece of membrane was used for each membrane length test. The mean mass and heat transfer coefficients used in the model were the same for predicting the co- and counter-current flux, which were the mean values from all the experiments at given velocities.

Figs. 6.6 and 6.7 show the experimental and modelling results from both co- and counter-current setups. Although the same kind of membrane was used in the experiment, greater flux was found from the shorter membrane. Therefore, the length of the membrane affects the flux from the membrane at given inlet temperatures and stream velocities, because the shorter membrane will lead to higher mean temperature difference across the membrane due to the reduced residence time for heat and mass transfers. As a result, it is not appropriate to assess performance of MD membranes by flux even under conditions of identical inlet temperature and velocity, if not including the membrane dimension.

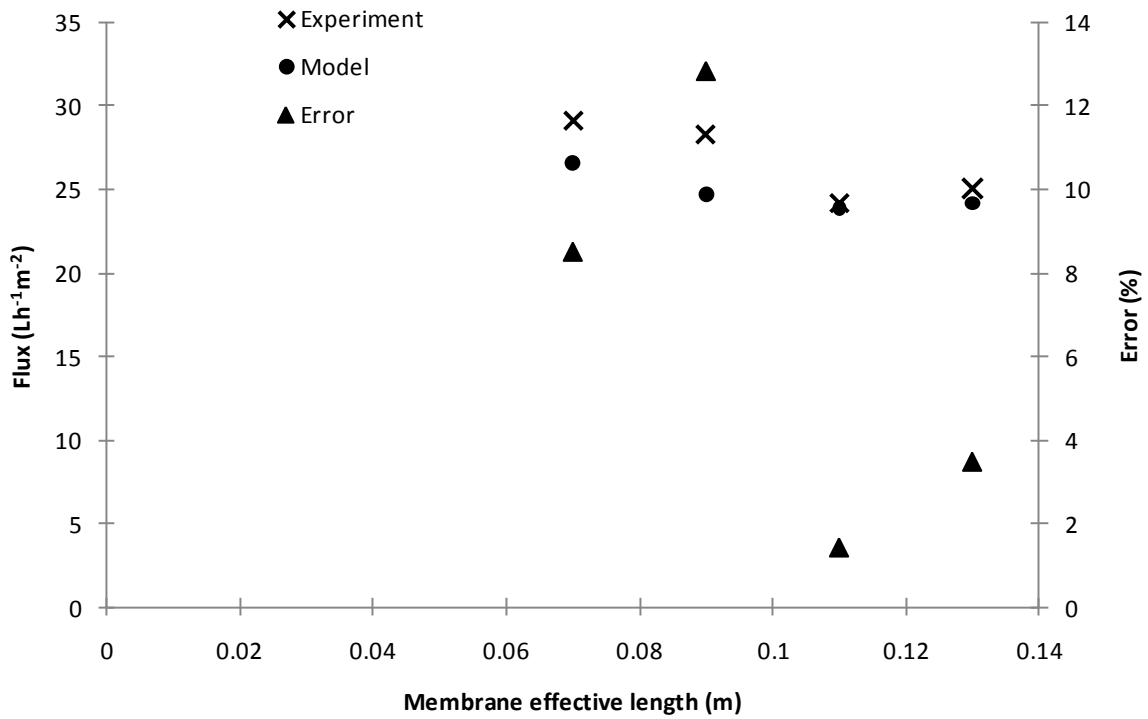


Fig. 6.6 Comparison between experimental and modelling results for different membrane lengths in counter-current setup

(Perspex module, 0.5 μ m membrane with scrim support)

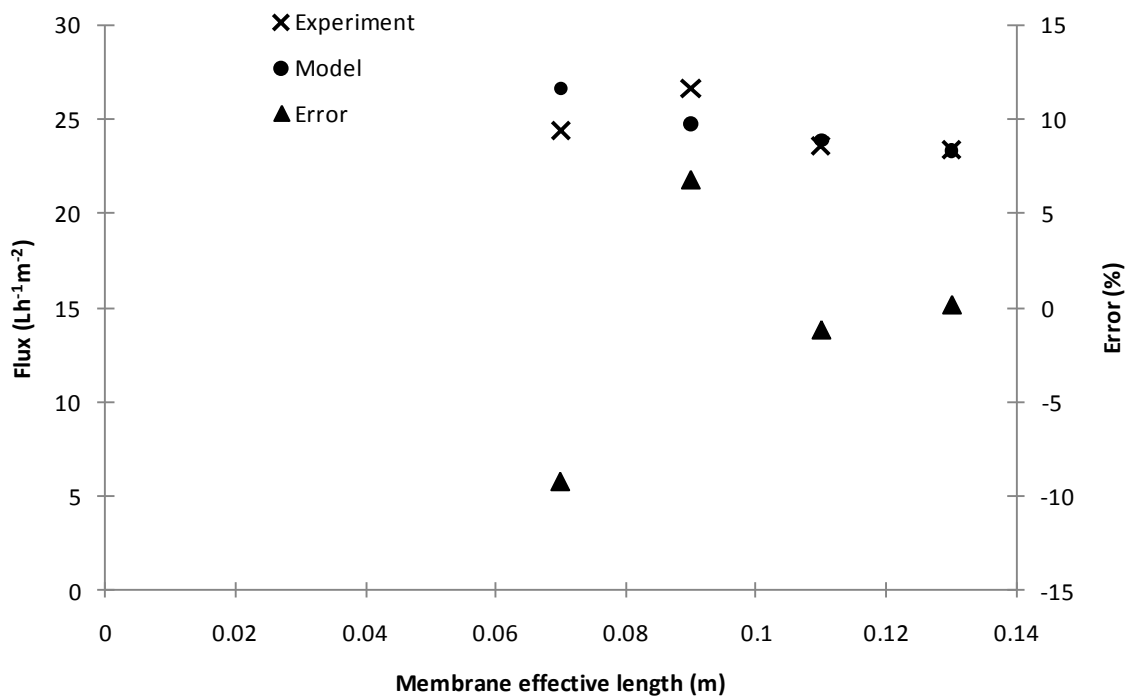


Fig. 6.7 Comparison between experimental and modelling results for different membrane lengths in co-current setup

(Perspex module, 0.5 μ m membrane with scrim support)

The maximum absolute error between the modelling and experimental results in counter-current setup was 13% from a membrane with a length of 0.09 m; while for the co-current setup, the largest absolute error was 9% from a membrane with a length of 0.07 m.

6.1.4.2 Mathematical modelling of temperature profile in direct contact membrane distillation

From the different verifications of the model with different membranes, temperatures and membrane lengths, the maximum error was less than 13%. This provides some confidence that the temperature profiles and flux predicted from the model will be accurate at a given velocity, and the modelling results are based on the global heat and mass transfer coefficients in Fig. 6.4b.

6.1.4.2.1 Prediction of temperature profile of co-and counter-current DCMD

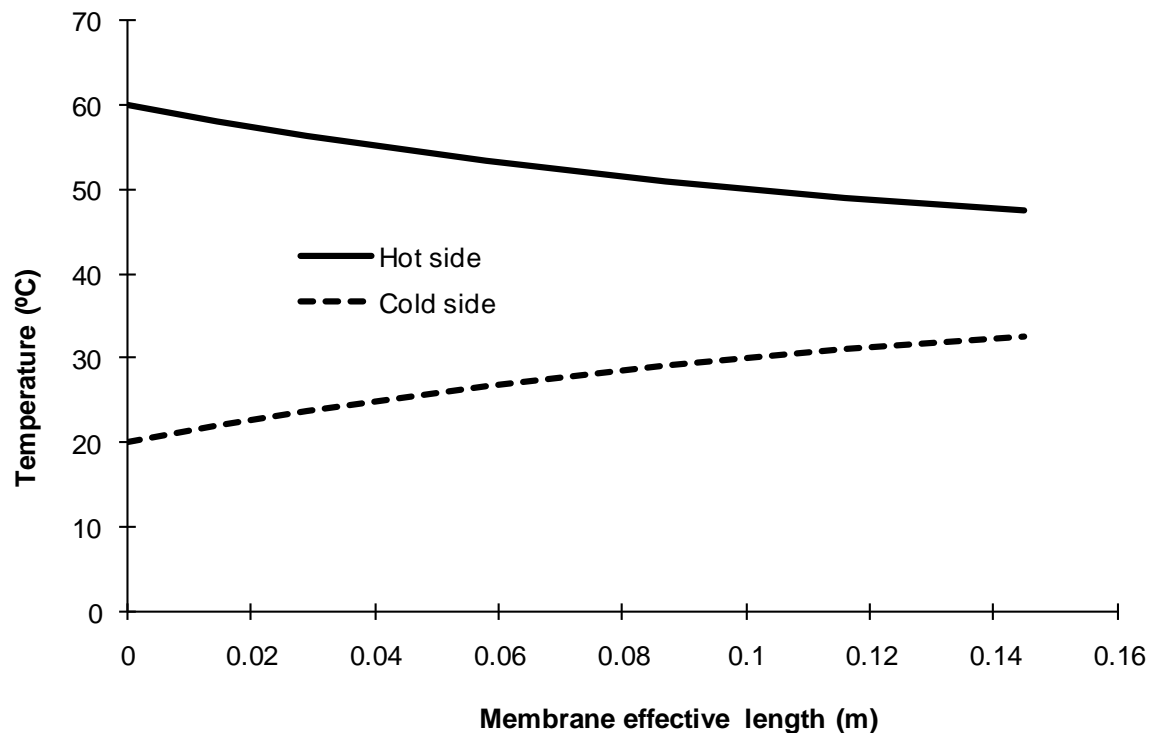


Fig. 6.8 Temperature distributions along the membrane for co-current flow

(Feed velocity=0.40 m/s, feed inlet temperature=60°C, cold inlet temperature=20°C)

Figs. 6.8 and 6.9 show the predictions of the temperature profiles of co- and counter-current DCMD along the stream flow direction. In the co-current setup, the local

temperatures on both sides of the membrane approach each other at positions further from the inlet (origin), while for counter-current flow the temperature profiles on both sides are parallel to each other if their flowrates are identical. From the difference of the temperature profile, it can be speculated that the flux of co-current mode will decrease faster than the counter-current mode along the feed flow direction, due to reduced temperature difference.

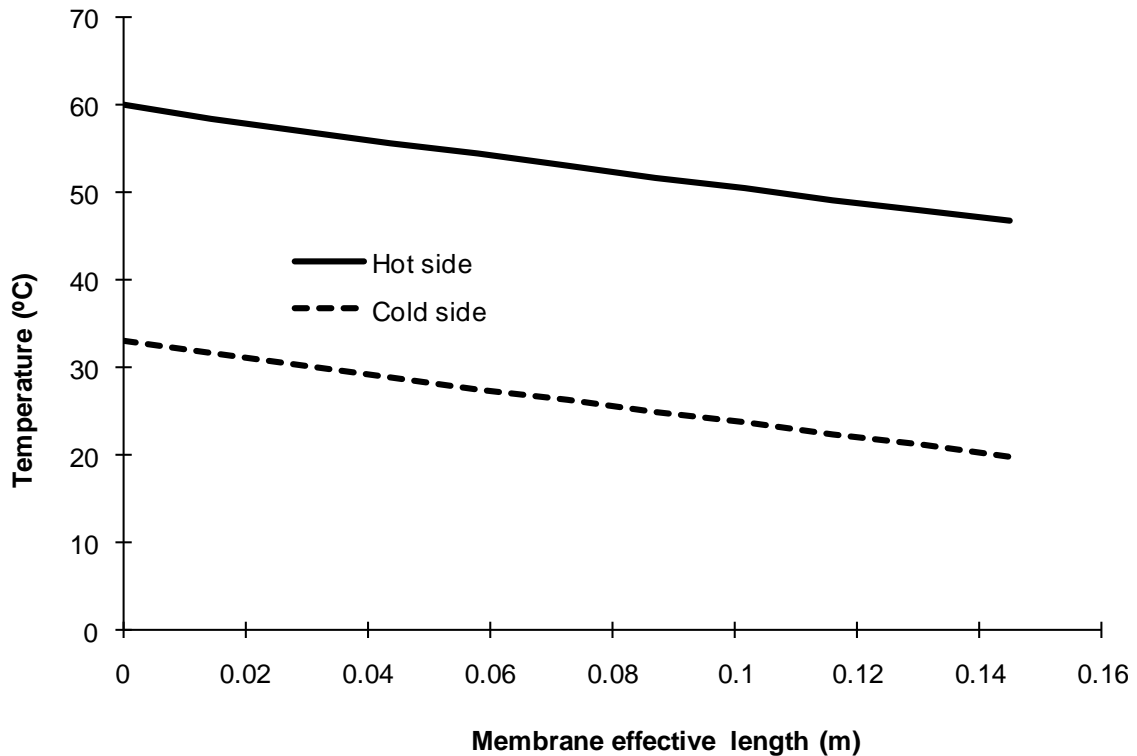


Fig. 6.9 Temperature profile along the membrane for counter-current flow

(Feed velocity=0.40 m/s, feed inlet temperature=60°C, cold inlet temperature=20°C)

6.1.4.2.2 Prediction of temperature difference at difference velocities based on fitting equations in Fig. 6.4b

When the experimental conditions were applied into the model at different velocities, there was $\pm 0.4^{\circ}\text{C}$ error between the predicted and experimental temperature difference across the membrane, which shows an acceptable agreement. Fig. 6.10 shows the predicted mean temperature difference across the membrane at different velocities using the mass and heat transfer coefficients calculated from the built database. From this figure, it was found that the temperature difference increased as the stream velocity becomes higher. Hence, the flux increment with increased flowrate results from both

increased global mass transfer coefficients and higher temperature difference.

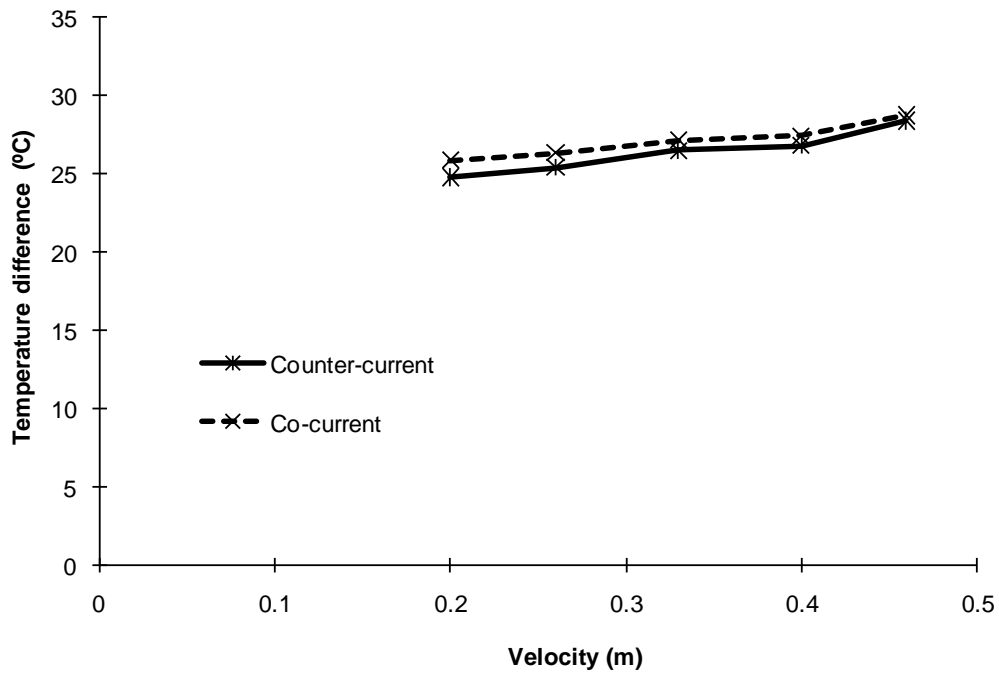


Fig. 6.10 Average temperature difference across the membranes at different velocities (Membrane length=0.145 m, feed inlet temperature=60°C, cold inlet temperature=20°C)

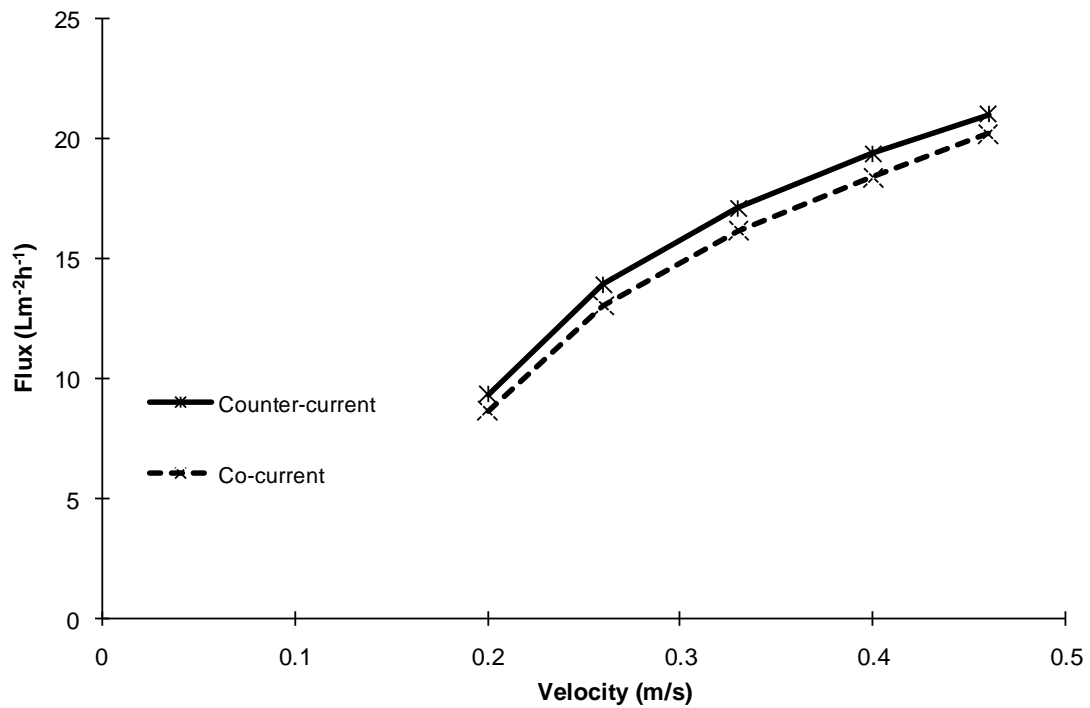


Fig. 6.11 Flux at different velocities

(Membrane length=0.145 m, feed inlet temperature=60°C, cold inlet temperature=20°C)

In Fig. 6.10, it also can be found that the temperature difference of the co-current setup is slightly higher than that of counter-current setup. A similar phenomenon was also found in the experimental results for different membrane lengths (0.5 μm membrane with scrim support) tested at the same velocity. However, a higher flux was found in counter-current DCMD compared to that of co-current DCMD as shown in Fig. 6.11. This may be caused by the different temperature distributions along the membrane between co- and counter-current DCMD. Because the real driving force for the flux is vapour pressure difference not the temperature difference, the streams with the larger temperature difference may have less vapour pressure difference. For example, streams with 10°C temperature difference respectively at 45°C and 35°C have a vapour pressure difference of 4,000 Pa, and streams with 5°C difference respectively at 60°C and 55°C have a vapour pressure difference of 4,200 Pa.

6.1.4.2.3 Prediction of flux changes of co-and counter-current DCMD in flow direction at different feed velocities

Figs. 6.12 and 6.13 show the flux changes along the membrane length at different velocities. The total flux difference reduced from 4.6 to 2.3 $\text{Lm}^{-2}\text{h}^{-1}$ and from 4.7 to 2.3 $\text{Lm}^{-2}\text{h}^{-1}$ respectively in co- and counter-current DCMD, as the velocity increased by an increment of approximately 0.065 m/s. A similar trend of permeate flux with increasing feed flow rates has been reported previously [34, 131], and this provides further support for the reliability of the model predictions. Furthermore, the figures also show that the difference in flux at various velocities becomes less as longer membranes are used. Hence, the feed velocity will have a less effect on flux as larger membranes are employed.

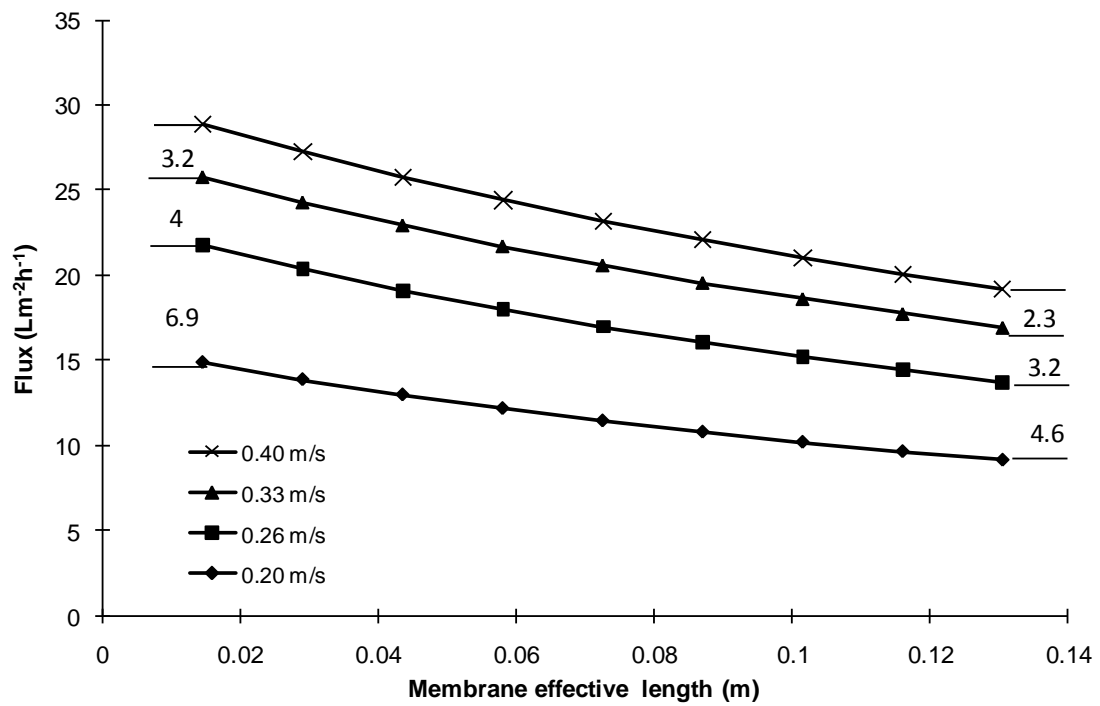


Fig. 6.12 Flux changes of co-current DCMD in flow direction at different velocities

(Feed inlet temperature=60°C, cold inlet temperature=20°C)

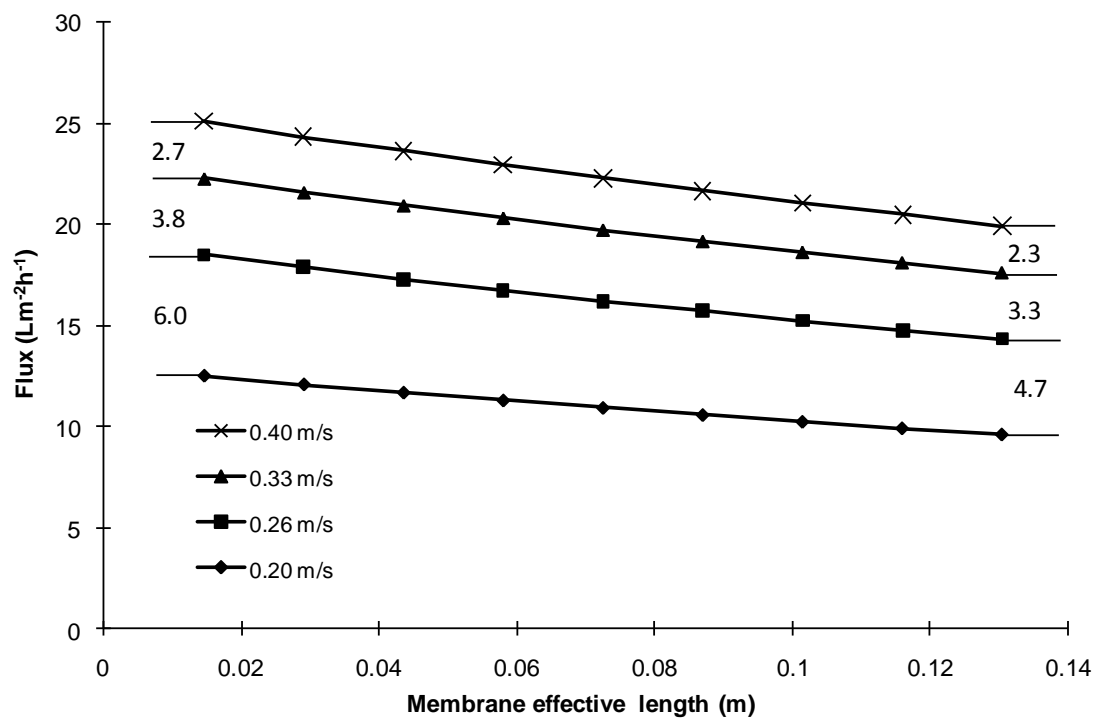


Fig. 6.13 Flux changes of counter-current DCMD in flow direction at different velocities

(Feed inlet temperature=60°C, cold inlet temperature=20°C)

6.2 Mathematic model of DCMD based on membrane properties and hydrodynamic and thermal conditions of streams

6.2.1 Introduction

In section 6.1, a simple model was developed based on the global mass transfer coefficient which was assumed constant at the same flow conditions, and it is a simple tool to roughly predicting flux of a scaled-up module based on a small scale test. However, the global mass transfer coefficient employed in this model includes both the mass transfer phenomena across the membrane and boundary layer, so the simple model is not applicable for predicting the flux from the same kind of membrane employed under different hydrodynamic conditions, i.e. at different flowrates or in a module with different flow channel structure. Furthermore, the thermal energy used for evaporation is also assessed with this model based on the different hydrodynamic and thermal conditions, for the purpose of optimising the operational parameters.

In the previous **Chapters**, based on the Knudsen number calculated from the mean pore size, it was concluded that the Knudsen-molecular diffusion transition mechanism dominates the mass transfer across the porous membrane. This conclusion was also verified by Phattaranawik et al. when the pore size distribution of the polymeric membrane was considered [85, 90] for MD membranes. Therefore, according to Eqs. (4.12) and (4.13), the total mass transfer through the membrane can be expressed as [151],

$$J = 7.81 \times \frac{\varepsilon}{bt} \frac{dMT^{1.072}}{5.685\sqrt{2\pi RMT} + 4dR(P_{pore} - P_A)} (P_{T1} - P_{T2}) \quad (6.10)$$

The actual driving force (interface temperature difference across the membrane) is less than bulk temperature difference between the hot and cold streams due to boundary layer effects. This phenomenon can be assessed by the temperature polarization coefficient [5], τ .

6.2.2 Theoretical analyses of the heat transfer and mass transfer

The parameters identified in Eq. (6.10) can be estimated by:

1. M and R are constant,
2. based on the finding in **Chapter 5**, P_{pore} , d and ε/bt are constants if the membrane is incompressible, or can be considered as constant if a very low pressure (0-3 kPa in this study) is applied on a compressible membrane,
3. T can be calculated by

$$T = \frac{T_1 + T_2}{2} \quad (6.11)$$

4. P_{T1} and P_{T2} are functions of T_1 and T_2 and can be calculated from the Antoine Equation (Eq (6.7)).

Since ε/bt and d are measurable by the gas permeation test mentioned in **Chapter 3**, there are only two unknown variables in this equation, which are T_1 and T_2 . Therefore, if the interfacial temperature gradients on both sides of the membrane can be calculated, the flux can be determined.

Based on Fig. 6.1, assuming the channel width is 1, the differential equations of feed and permeate interfacial temperatures distributed along the membrane can be written as,

$$\frac{dT_f}{dx} = -\frac{\alpha_f}{\dot{m}_f C_{p,f}} (T_f - T_1) \quad (6.12)$$

$$\frac{dT_p}{dx} = \frac{\alpha_p}{\dot{m}_p C_{p,p}} (T_2 - T_p) \quad (6.13)$$

Therefore, the temperature gradient can be obtained by numerically solving Eqs. (6.12) and (6.13).

6.2.3 Experiment and simulation

6.2.3.1 Membrane and module characterisation

The employed membrane materials were provided by Changqi Co. Ltd, the same as those employed in **Chapter 5**.

6.2.3.1.1 Thermal conduction coefficient (λ/b) measurement

In the experiment, plastic shims (0.8 mm polypropylene sheet) were placed both sides of the membrane to reduce the active area of the membrane (see section 6.2.3.3) and make the membrane length less than 0.13 m. Therefore, for shorter membranes (less

than 0.13 m), the cold and hot streams will have heat exchange through the shims before contacting the membrane. To reduce the error, it was necessary to measure the thermal conduction coefficient of these shims so as to calculate the sensible heat loss through them. Thus, a sample configured as the structure in the MD module was made, which was composed of two shims and one membrane sandwiched between them. A heat conduction apparatus (HT1-A, Armfield) was employed to measure the thermal conduction coefficient of this sample. The readings were recorded after both upstream and downstream temperatures were stabilised for 1 h. The measured results of two different round pieces ($\varnothing=25$ mm) are shown in Table 6.1, and the mean value is used in the model.

Table 6.1 Heat conduction measurement of the shim samples

Sample	Area (m ²)	Run	Heat transfer coefficient (Wm ⁻² K ⁻¹)	Upstream temperature (°C)	Downstream temperature (°C)	Input power (W)
1	0.00049	1	315.5	59.8	21.7	5.9
		2	318.6	60.8	21.8	6.1
2	0.00049	1	299.6	63.0	22.2	6.0
		2	305.3	63.0	22.3	6.1

Because the membrane will be compacted after being installed into the heat conduction apparatus, the thermal conductivity of the membrane was calculated from the Eq. (2.4), using reported thermal conductivity values for air ($\lambda_{air}=0.026$ Wm⁻¹K⁻¹) and PTFE ($\lambda=0.25$ Wm⁻¹K⁻¹) [3].

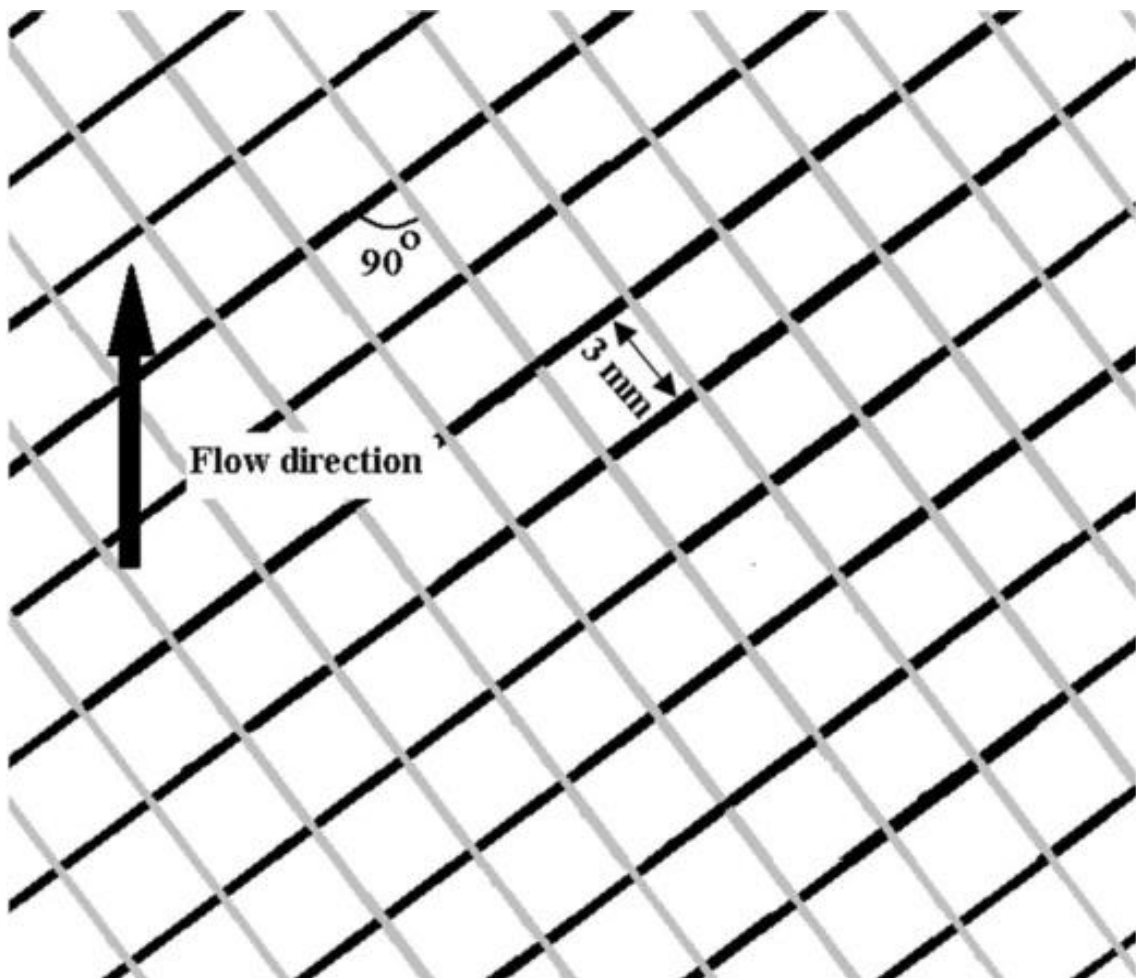
6.2.3.1.2 Spacer and module

The dimensions of the module and spacer are listed in Table 6.2 and shown in Fig. 6.14. The spacer was used to support the membrane and it also acted as a turbulence promoter. Fig. 6.14a shows its structure and position relative to the flow direction. The spacer porosity was measured experimentally and calculated using [48],

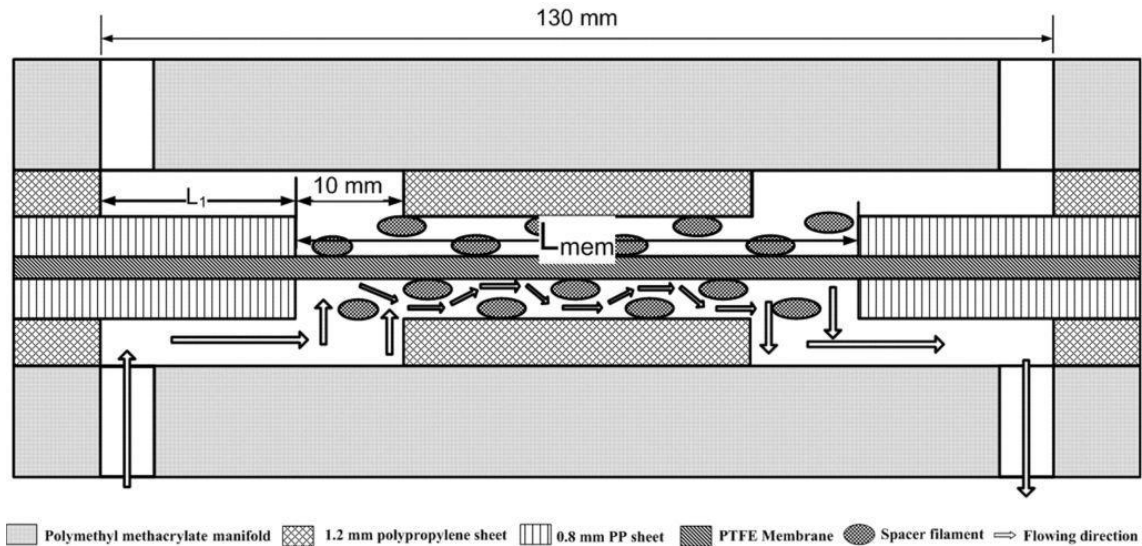
$$\varepsilon_{spacer} = \frac{V_{filament}}{V_{spacer}} \quad (6.14)$$

Table 6.2 Dimension of module and spacer

Flow channel (mm)			Spacer (mm)		
length (L)	width (W)	depth	filament diameter (d_f)	thickness (h_{sp})	mesh size (l_m)
130	130	0.8	0.4	0.8	3



a. Spacer structure and stream direction



b. Module structure and stream through the channel

L_{mem} is the membrane length, and L_1 is the length of the plastic shim

(Two 0.8 mm PP sheets and membrane sandwiched between them)

Fig. 6.14 Dimensions of the module and spacer

where $V_{filament}$ is the volume of spacer filament and V_{spacer} is the total spacer volume. The filament volume was measured by soaking a $130 \times 130 \times 0.8 \text{ mm}^3$ spacer sample into water within a burette that had an accuracy of $\pm 0.02 \text{ mL}$ and measuring the volume change.

6.2.3.2 Experimental process

A schematic diagram of the DCMD process is shown in Fig. 3.4. The velocities of the feed and permeate streams were varied from 0.055 to 0.151 m/s (300-800 mL/min), and the feed and permeate streams were maintained at identical velocity in all experiments. The flowrate was calibrated using a volumetric cylinder and the accuracy was $\pm 10 \text{ mL/min}$. The inlet temperatures of permeate and feed were $20 \pm 2^\circ\text{C}$ and $30\text{-}70 \pm 2^\circ\text{C}$ respectively. The brine feed was prepared by dissolving 50 g NaCl in 5 L water (10 gL^{-1}). All flux results presented were measured over a period of 2.5 to 4 hours and variation in flux over this time was $\pm 5\%$. The membrane length was varied in the range of 50-130 mm by using two 0.8 mm thick polypropylene sheets to cover both sides of the membrane. A larger module with an active membrane size of $200 \times 733 \text{ mm}$ was also used to verify the model and the length of this module was considered similar in size to

DCMD modules that would be used in pilot plant studies. Both co- and counter-current DCMD were tested by switching the hot feed inlet and outlet.

6.2.3.3 Modelling heat and mass transfer

Assumptions made to simplify the model is the same as the assumptions for the simple model in Part I, except the 3rd assumption is substituted by

- with a given membrane, the properties of the membrane, such as thickness, porosity, pore size, and tortuosity are constant, because the maximum pressure applied on the membrane was less than 3 kPa,

In comparison with the assumptions in the simple model based on the global mass transfer coefficient, this model is not confined by experimental acquisition of the global mass transfer coefficient and heat transfer coefficient at different stream velocities. Therefore, if the conditions (e.g. dimensions and spacers) of the channel and membrane properties are given, this model is able to predict the flux under different conditions, such as temperatures, membrane length, and flowrate.

Because temperature varies as the hot and cold streams flow along the DCMD module, water properties (viscosity, saturated vapour pressure) need to be calculated at each point along the membrane length to account for the change in temperature. Therefore, a local Nusselt number (Nu) was used for calculation of the convective heat transfer coefficient, rather than an average Nusselt number as used in [82]. Furthermore, the variation in the heat transfer through the polypropylene shim along the membrane length L_l (Fig. 6.14b) was also included in the calculations when the membrane length was less than 130 mm in the module.

For spacer filled flow channels, the local Reynolds number at point A can be computed by Eq. (2.8) [77, 152], in which d_h , the hydraulic diameter in a spacer filled channel and is calculated by:

$$d_h = \frac{4.0\varepsilon_{spacer}d_f h_{sp}}{2d_f + 4(1-\varepsilon_{spacer})h_{sp}} \quad (6.15)$$

For the spacer filled channel, although the Re is less than 300, the model predictions better fit the experimental data when the stream was assumed to be fully developed turbulent flow in the calculation of the Nu ,

$$Nu = 0.029K_s Re^{0.8} Pr^{0.33} \quad (6.16)$$

K_s is the spacer factor from [77, 82],

$$K_s = \beta \left(\frac{d_f}{h_s} \right)^{-0.039} f(\varepsilon_{spacer}) f(\phi) \quad (6.17)$$

In this work, K_s is expressed by

$$K_s = 1.904 \left(\frac{d_f}{h_s} \right)^{-0.039} \varepsilon_{spacer}^{0.75} \left(\sin \frac{\phi}{2} \right)^{0.086} \quad (6.18)$$

where β is a coefficient, and ϕ is the angle between filaments shown in Fig. 6.14a.

Therefore, the convective heat transfer coefficient, α_f and α_p on feed and permeate side of the membrane can be calculated from,

$$\alpha_f = \frac{Nu \cdot k}{d_h} \quad (6.19)$$

where k is the thermal conductivity of the water.

6.2.3.4 Numerical solution

The differential equations were discretized using a first order forward Euler method and solved numerically [14]. This numerical solution was implemented both into MATLAB and Excel files using Visual Basic.

The DCMD flow channel in the module was divided into small identical elements Δx , and for the j^{th} point, the differential Eqs. (6.12) and (6.13) can be transformed to [76]:

$$\Delta T_{f,j} = T_{f,j+1} - T_{f,j} = -\frac{\alpha_{f,j}}{\dot{m}_f c_{p,f}} (T_{f,j} - T_{1,j}) \Delta x \quad (6.20)$$

$$\Delta T_{p,j} = T_{p,j+1} - T_{p,j} = \frac{\alpha_{p,j}}{\dot{m}_p c_{p,p}} (T_{2,j} - T_{p,j}) \Delta x \quad (6.21)$$

The overall heat transferred through the membrane at this point can be written as

$$\Delta Q_j = \alpha_{f,j} (T_{f,j} - T_{1,j}) \Delta x = \left(J_j H_{latent} + \frac{\lambda}{b} (T_{1,j} - T_{2,j}) \right) \Delta x = \alpha_{p,j} (T_{2,j} - T_{p,j}) \Delta x \quad (6.22)$$

and

$$\Delta Q_j = U (T_{f,j} - T_{p,j}) \quad (6.23)$$

where U can be expressed as

$$\frac{1}{U} = \frac{1}{\alpha_{p,j}} + \frac{1}{\alpha_{f,j}} + \frac{1}{\alpha_{membrane,j}} \quad (6.24)$$

in which

$$\alpha_{membrane,j} = \frac{\lambda}{b} + \frac{J_j H_{latent}}{T_{1,j} - T_{2,j}} \quad (6.25)$$

For co-current DCMD, the location of the cold and hot stream inlets was taken as $x=0$ and that of the outlets was taken as $x=L$. A marching method was used starting from $x=0$ where boundary conditions are given and marched to $x=L$. The convergence of the solution was checked by comparing results (outlet temperatures $T_{f,N}$ and $T_{p,N}$, and total mass transfer) for different N' (number of small elements used in the calculations). The differences between the predicted results from $N'=1,000$ and $10,000$ were less than 0.01%, which indicates the convergence of the numerical solutions for element numbers greater than 1000. Results from $N'=10,000$ are presented. In Fig. 6.15, the flow chart shows the procedures to calculate the interface temperatures in the flow direction.

For counter-current flows, $x=0$ was taken at the inlet of the hot feed and the mass flowrate on the cold permeate side was taken as a negative value. The solution procedure was similar to that for the co-current flow, except that the temperature of the cold permeate stream at $x=0$ (the outlet of the cold permeate) is not known a priori. An iterative method was used to solve the differential-algebraic Eqs. (6.20)-(6.25). For each iteration, a cold permeate temperature $T_{p,o}$ at $x=0$ was estimated and the solution progressed from $x=0$ to $x=L$. The predicted $T_{p,N}$ was then compared with the inlet temperature of the cold permeate at $x=L$, which is a specified boundary condition for the differential Eqs. If the relative error between the predicted $T_{p,N}$ and the given boundary condition $T_{p,i}$ was larger than 10^{-7} , a new $T_{p,o}$ was estimated and the progressive calculations were repeated. As for co-current flows, the differences between the predicted results (exit temperatures and flux) for $N'=1,000$ and $N'=10,000$ was less than 0.01%, and only results from $N'=10,000$ are presented. In Fig. 6.16, the flow chart shows the procedures to calculate the interface temperatures in the feed stream direction.

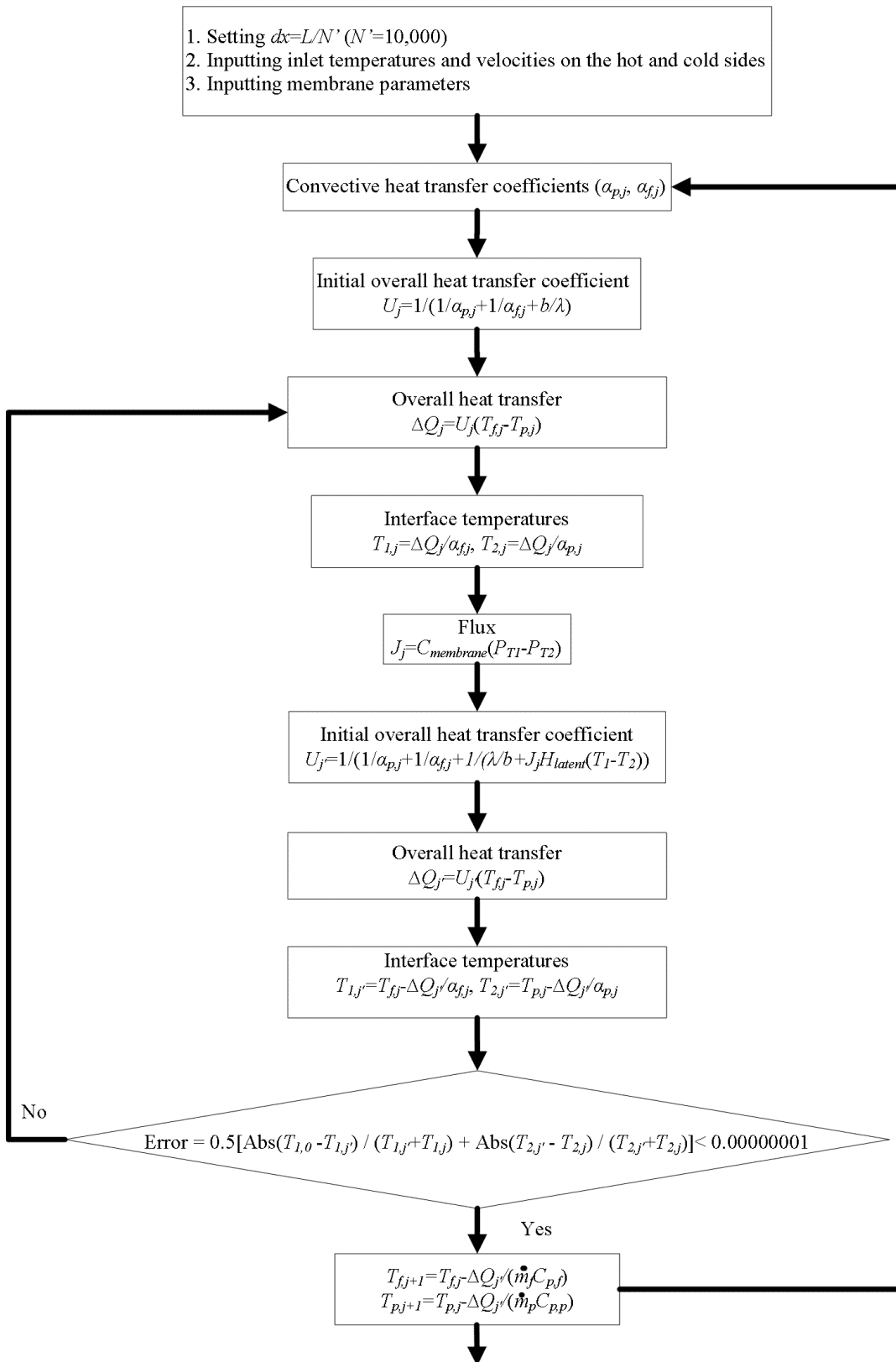


Fig. 6.15 Flow chart for co-current DCMD modelling

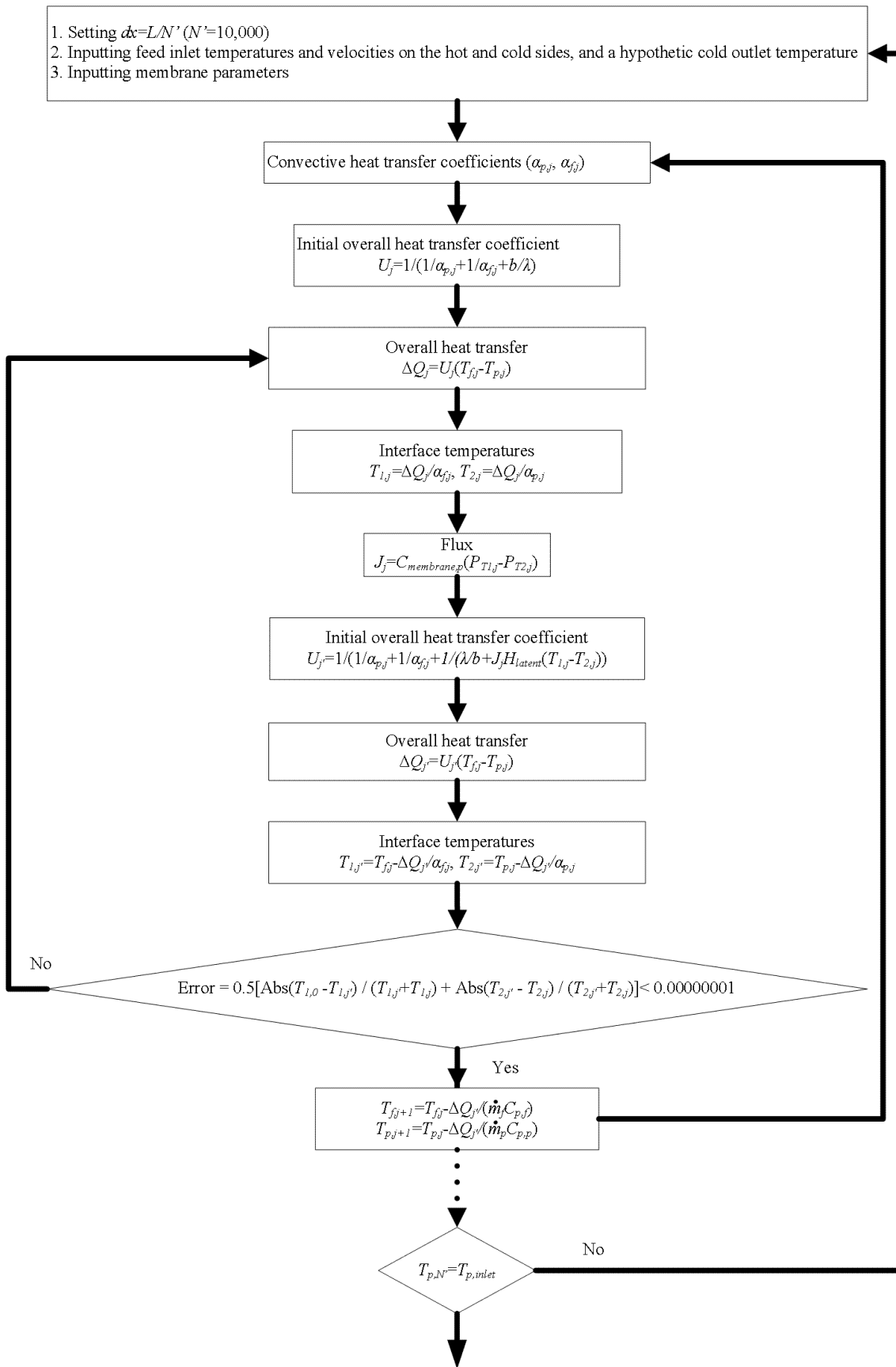


Fig. 6.16 Flow chart for counter-current DCMD modelling

6.2.4 Results and discussion

6.2.4.1 Analytical results and discussion

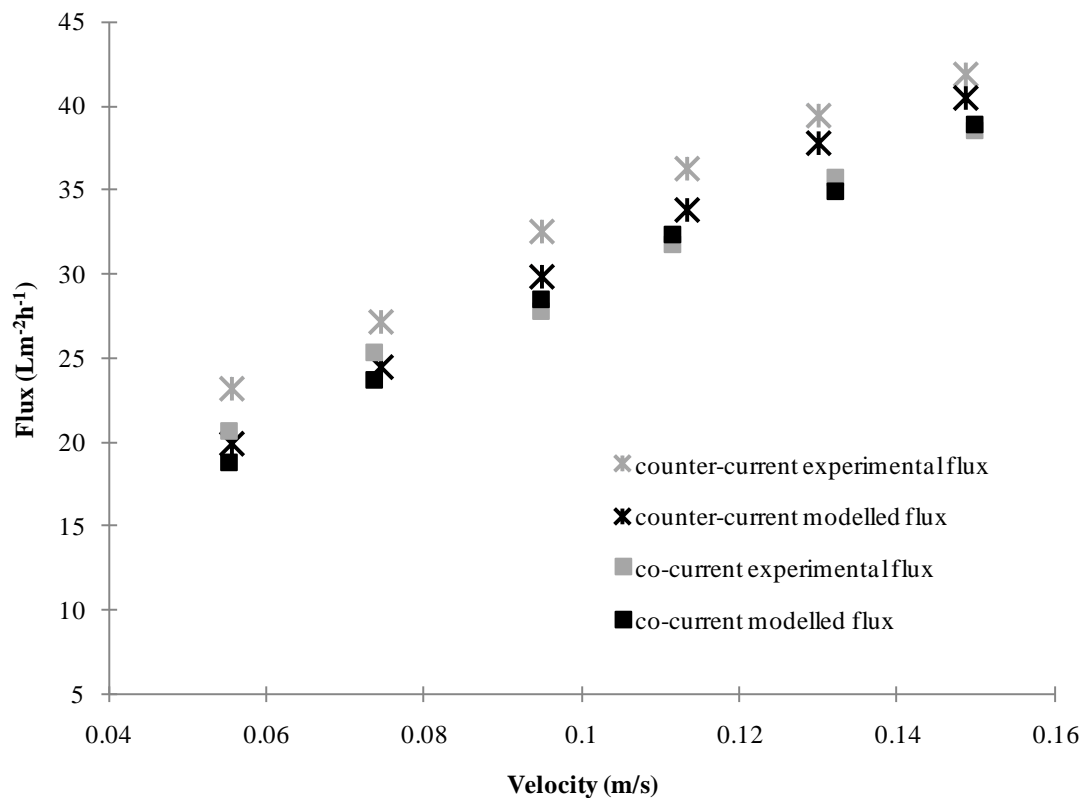
Table 6.3 Thermal conductivity of the membrane and the plastic shim

Membrane	Polypropylene shim
λ/b	λ/b
(WK ⁻¹ m ⁻²)	(WK ⁻¹ m ⁻²)
1095±60	309±10

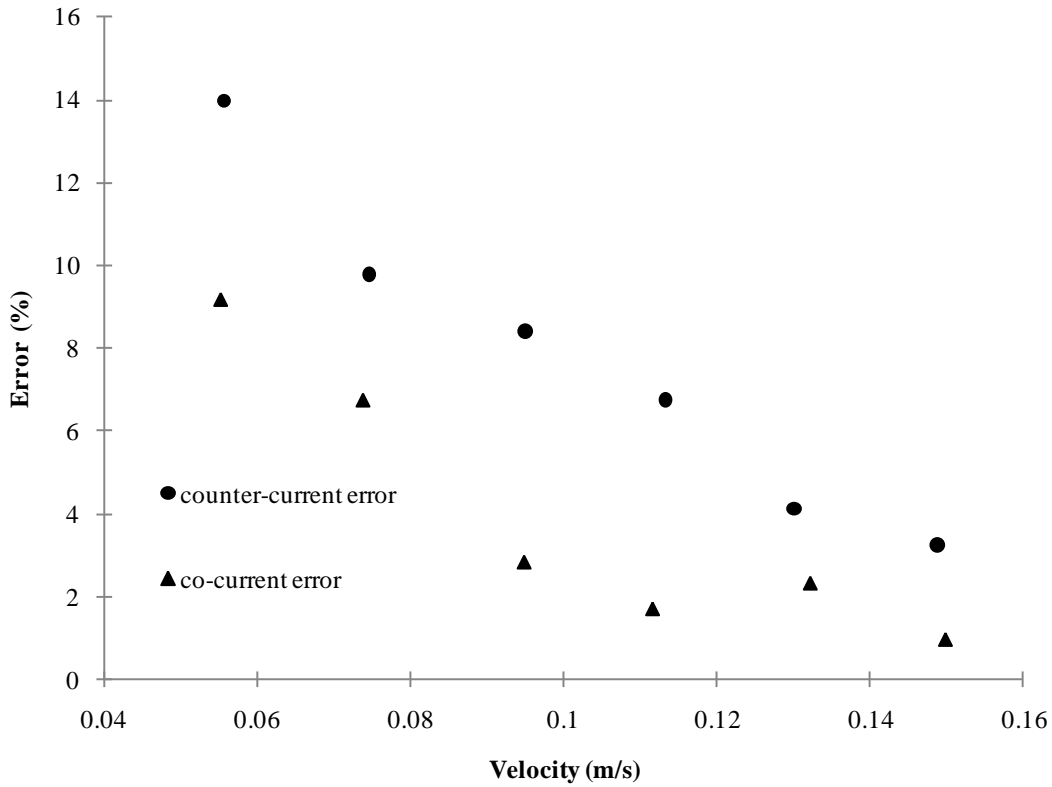
Table 6.3 lists the calculated membrane thermal conductivity based on the data in Table 5.3 and measured thermal conductivity of the polypropylene shim.

6.2.4.2 Modelling and experimental results

6.2.4.2.1 Verification of model



a. Experimental and predicted flux results



b. Error between experimental and predicted results

Fig. 6.17 Model verified at different velocities

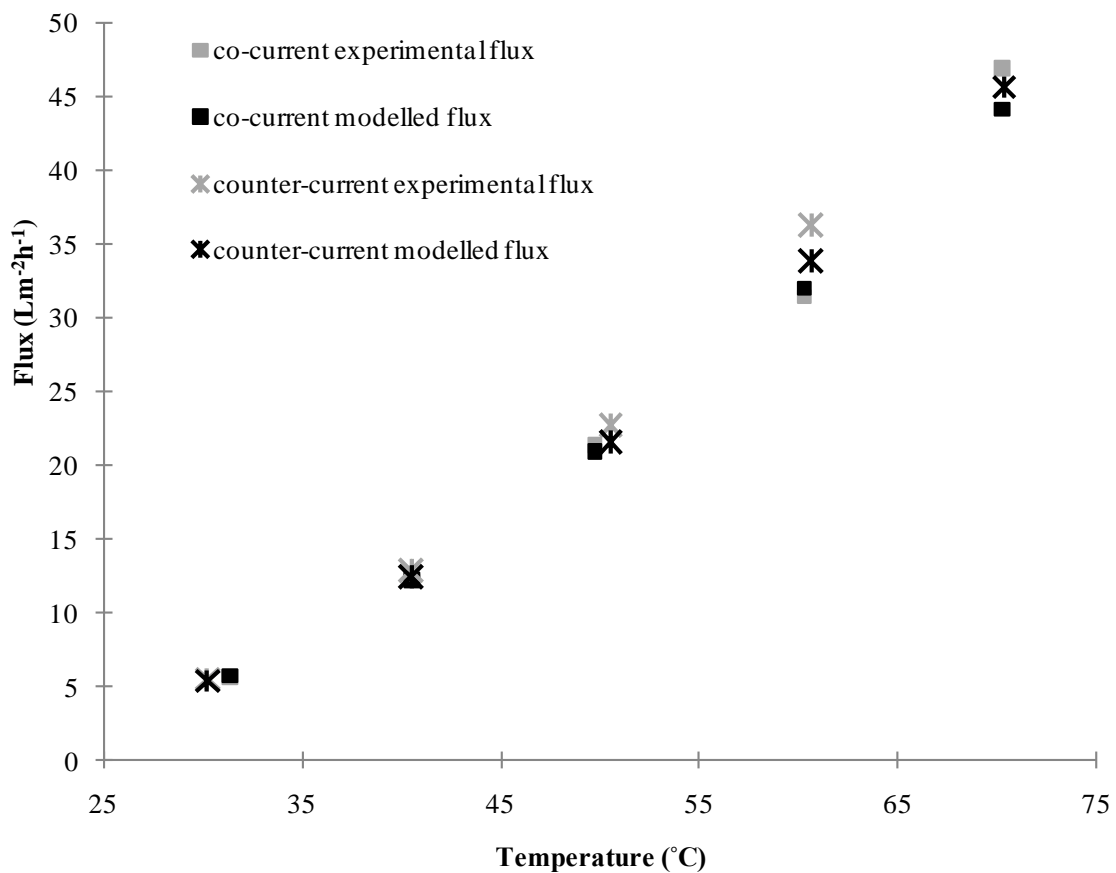
$$(T_{fi}=60^{\circ}\text{C}, T_{pi}=20^{\circ}\text{C} \text{ and } L_{mem}=130 \text{ mm})$$

The model was verified over various velocity and temperature conditions. The consistency of the experimental results was assessed by repeating experiments under the same condition (temperature difference $\pm 1^{\circ}\text{C}$, and flowrate difference $\pm 10 \text{ mL/min}$), except for the experiment results from the large module due to limitations of membrane material. If the variation of the experimental global mass transfer coefficients in the repeating experiment were greater than $\pm 3\text{-}5\%$, a third run was performed to confirm the experimental result. Experimental results presented in each figure in Section 6.2.4.2 are from the same piece of membrane, except for Fig. 6.22 in which for each length a different membrane piece is used.

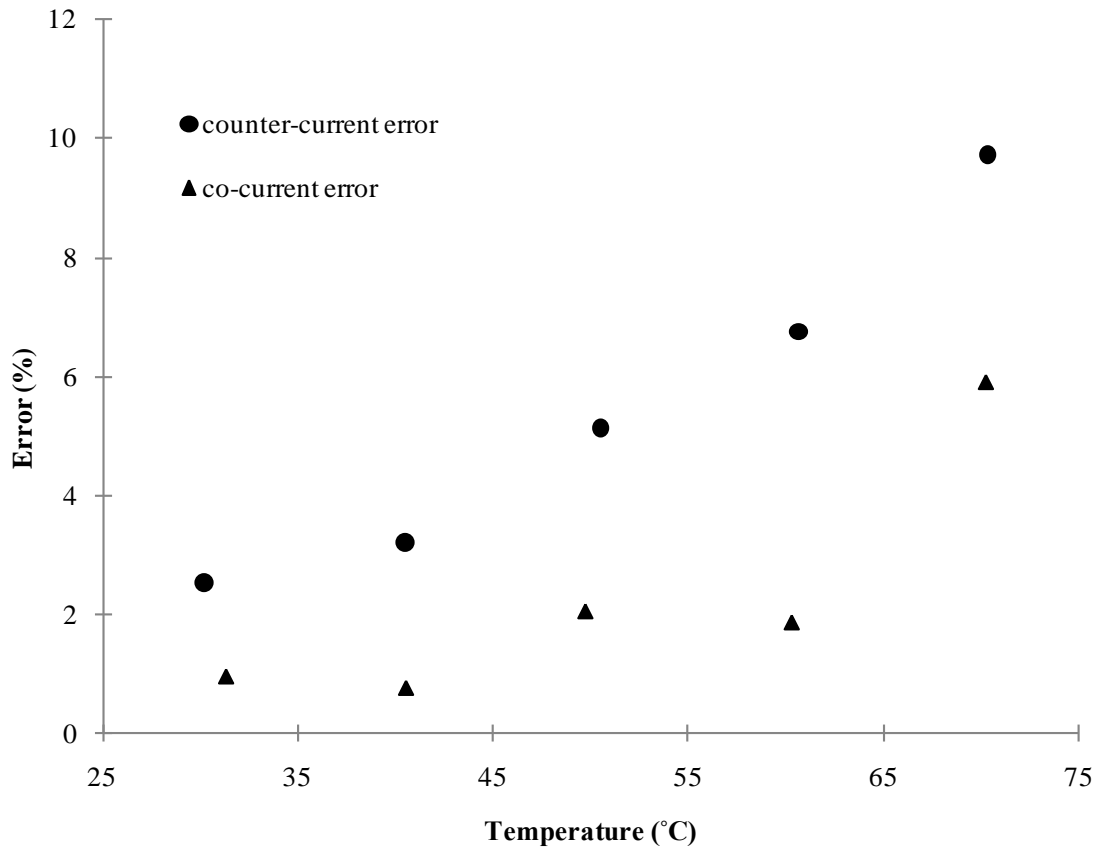
The results of the model verified at different velocity are shown in Fig. 6.17. With increasing velocities, both curves of the experimental and predicted fluxes in Fig. 6.7a shows increasing trends, but both error curves in Fig. 6.17b between the model predictions and the experimental results shows greater accuracy of the model at higher

velocities. The modelling errors are in the range of 0.4-13.9%, and the maximum percentage errors are 13.9% (counter-current) and 9.2% (co-current) at the lowest velocity ($0.056 \text{ m}\cdot\text{s}^{-1}$).

The verification results of the model at different temperatures are shown in Fig. 6.18. With the rising temperature, both experimental and modelling flux curves in Fig. 6.18a showed exponential increases, and the error curves in Fig. 6.18b between the model predictions and the experimental results also showed exponential increases. However, the errors are still in the range of 0.8-9.7%. The maximum percentage errors of 5.9% (co-current) and 9.7% (counter-current) occur at the highest temperature (70°C).



a. Experimental and predicted flux results



b. Error between experimental and predicted results

Fig. 6.18 Model verified at different temperatures

$$(v_f=v_p=0.11 \text{ m/s}, L_{mem} = 130 \text{ mm})$$

In Figs. 6.17b and 6.18b, the errors of the model are not distributed randomly around the experimental results and increased as the velocities decreased or the temperature increased. It also can be found from the analysis of experimental results that the single pass recovery defined in Eq. (6.26) is higher at lower velocity or higher feed inlet temperature. The relationship between the recovery and temperatures and velocity is shown in Fig. 6.19.

$$Recovery = \frac{JA}{\dot{m}_f} \tag{6.26}$$

where A is the membrane effective area.

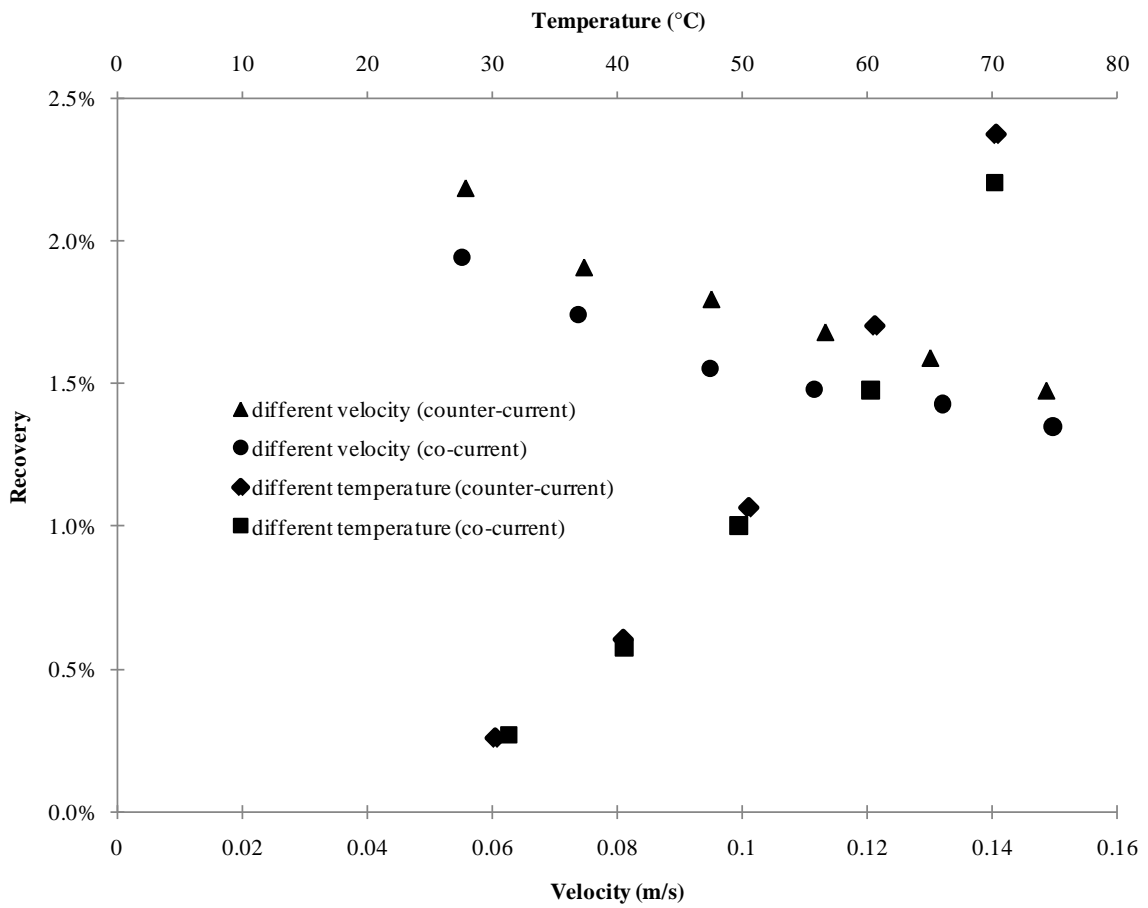


Fig. 6.19 Relationship between the recovery and temperatures and velocity

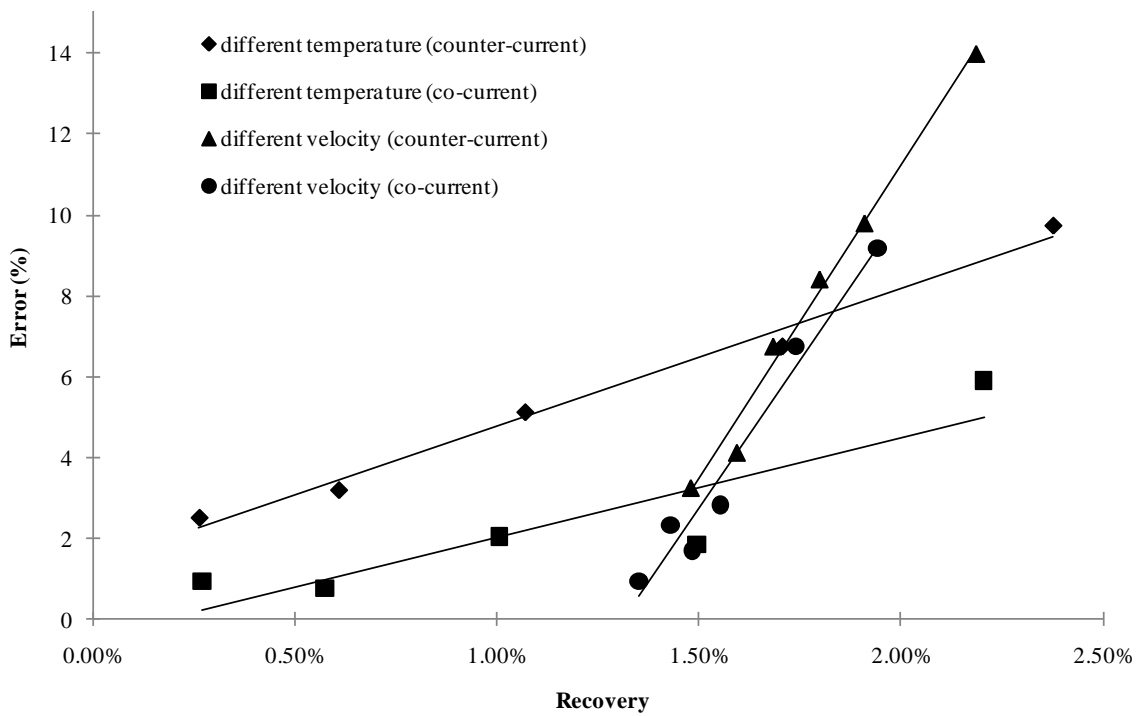


Fig. 6.20 Relationship between single pass recovery and modelling error

Therefore, the systematic error may arise from the assumptions that the influence of mass flux on the mass flowrate can be neglected, as well as the sensible heat carried by the permeate. In Fig. 6.20, the relationship between the modelling error and single pass recovery is shown. From this chart, it is observed that the error increased approximately linearly with single pass recovery.

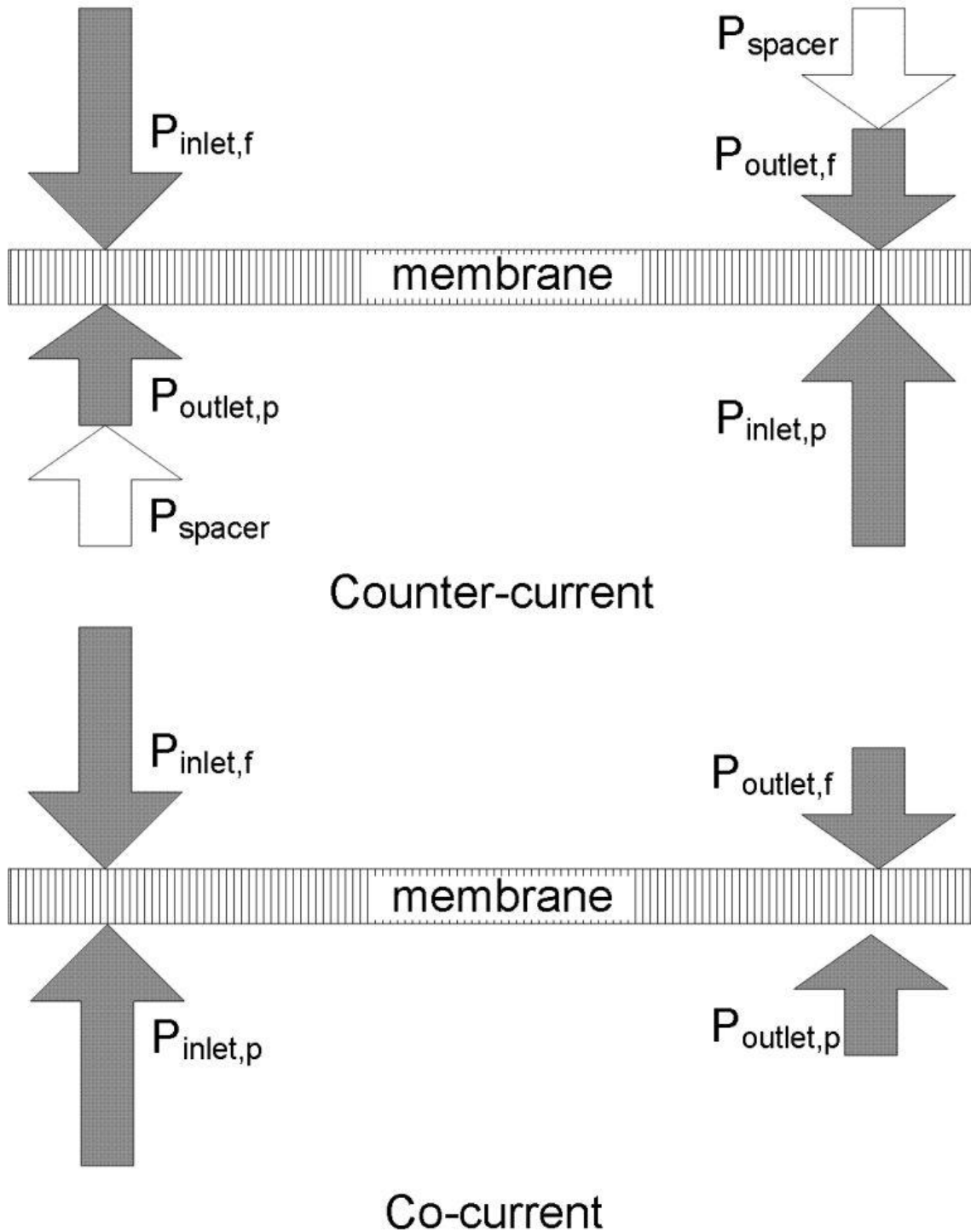
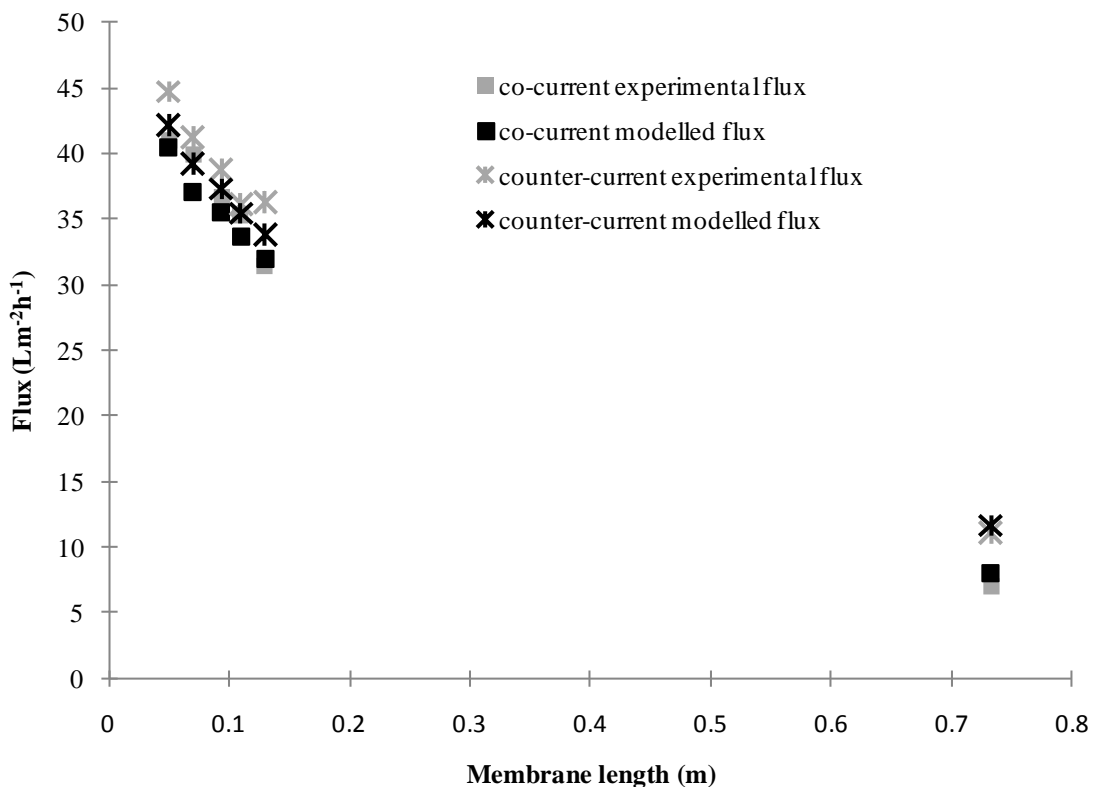
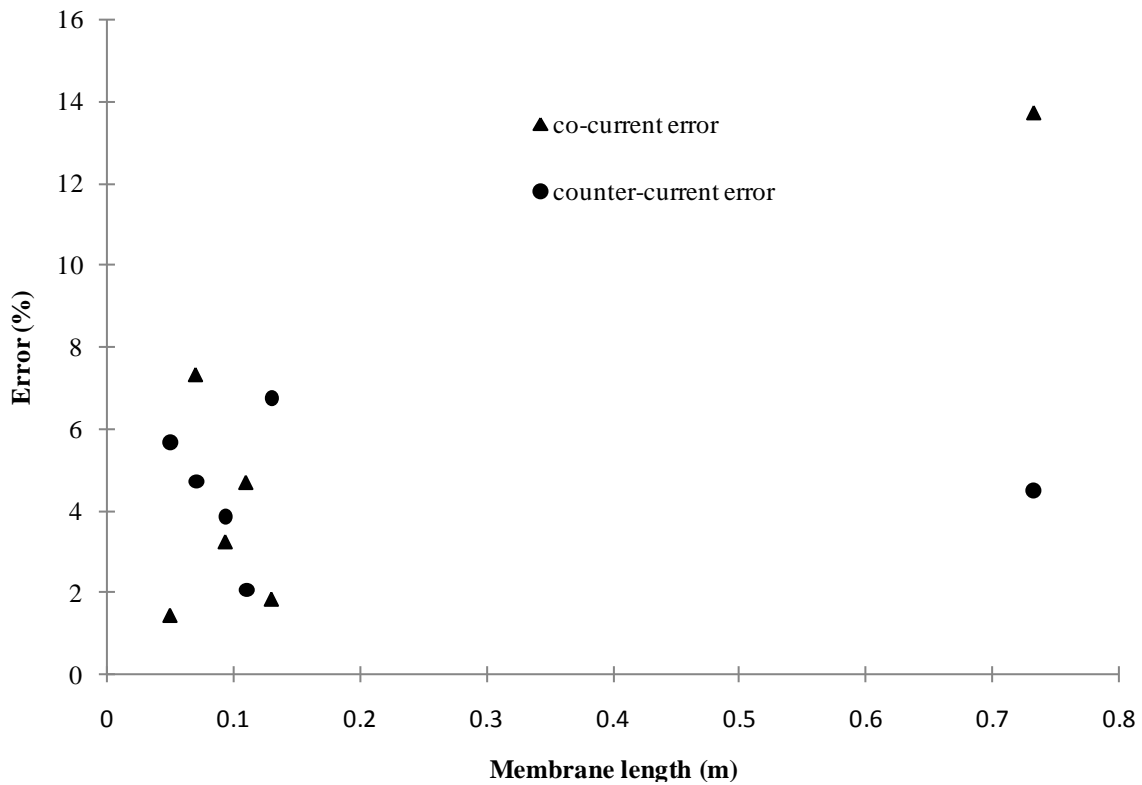


Fig. 6.21 Pressure analysis in counter- and co-current DCMD

Additionally, the predicted results have less error in co-current mode than counter-current mode at the same recovery at different temperatures, which suggests that the programmed counter-current model is more sensitive to mass flow changes in both cold and hot streams. The difference of predicted error between different modes may be caused by the differences in compaction of the membrane. In the assumptions, the properties of the membrane is assumed constant as the pressure applied on the membrane is low (<3 kPa). As mentioned in **Chapter 5**, the deformation of the membrane will cause the change of membrane permeability and conductivity. In the experiments, the measured inlet pressures of both counter- and co-current modes are approximately same at the same velocity. From the pressure schematic in Fig. 6.21, it can be observed that there is greater mean pressure applied on the membrane in the counter-current mode than that of the co-current mode. Thus, compared with the co-current mode, the membrane properties in counter-current mode will have greater difference from the measured membrane properties. As a result, a greater error is found in the counter-current modelling result.



a. Experimental and predicted flux results



b. Error between experimental and predicted results

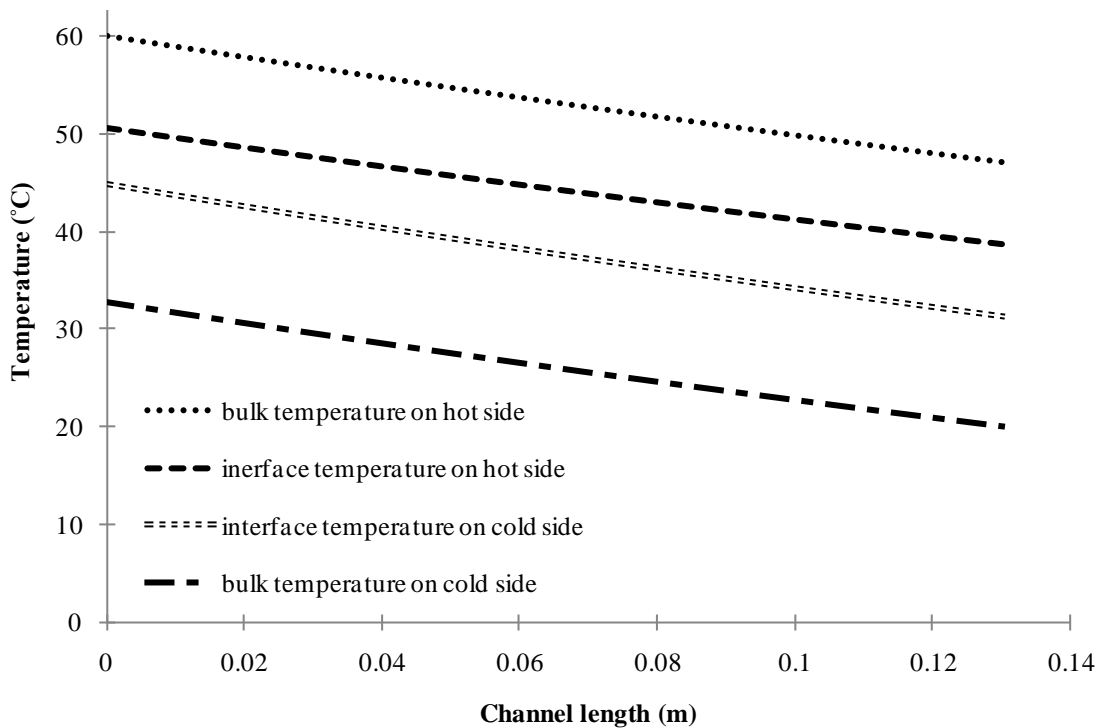
Fig. 6.22 Accuracy assessment with varied membrane lengths

$$(T_{fi}=60^{\circ}\text{C}, T_{pi}=20^{\circ}\text{C}, v_f=v_p=0.11 \text{ m/s})$$

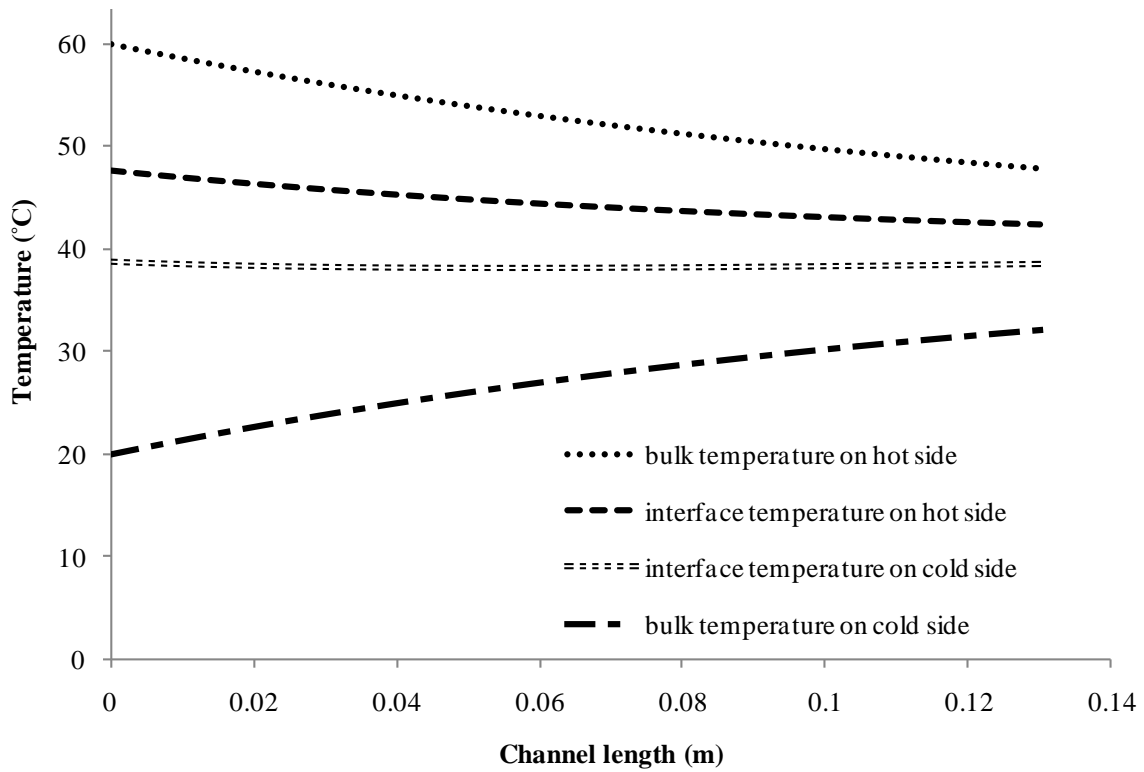
Because the flux in DCMD varies with the membrane length as discussed in section 6.1, the model was also assessed with various membrane lengths. In Fig. 6.22, results from modelling and experiments are presented. In Fig. 6.22a, the flux decreases from 44.7 to 11.1 $\text{Lm}^{-2}\text{h}^{-1}$ (counter-current) and from 41.1 to 7 $\text{Lm}^{-2}\text{h}^{-1}$ (co-current), as the membrane length is increased from 50 mm to 733 mm at the same inlet temperatures and velocity. It can be speculated that the longer membrane will have greater recovery at the same stream velocities and inlet temperatures, because of the longer residence time of the stream. However, the errors (Fig. 6.22b) between the predicted and experimental results are randomly distributed in the range of 1.5-13.7%, although the greatest error is still seen when the longest or the second longest membrane is used (maximum errors are 6.7% with a membrane length of 0.13 m in counter-current mode and 13.7% with a membrane length of 0.73 m in co-current mode). The phenomenon may be caused by the property variation of the employed membrane, because the presented results are from eleven different membrane pieces in different lengths.

6.2.4.2.2 Application of model in analysis and discussion of co- and counter-current DCMD

From the verification of the model under different conditions, there are only two predicted results with errors greater than 10%, which are 13.7% with a membrane length of 733 mm when the model is verified with different membrane lengths in a co-current DCMD, and 13.9% at a velocity of 0.056 m/s in a counter-current DCMD when the model is assessed at different velocities. Considering the $\pm 5\%$ experimental variation and conventional process design factor of chemical design of 10-25% [153-155], the systematic error caused by the assumption in the model is still acceptable. Therefore, the model is applicable in general for predicting the temperature distribution along the membrane and the degree of temperature polarisation.



a. Modelled temperature distribution in counter-current DCMD



b. Modelled temperature distribution in co-current DCMD

Fig. 6.23 Modelled temperature distribution in counter- and co-current DCMD

$$(L_{mem}=130 \text{ mm}, T_{pi}=20^\circ\text{C}, T_{fi}=60^\circ\text{C}, v_f=v_p=0.11 \text{ m/s})$$

Fig. 6.23 shows an example of the temperature distribution estimated in counter- and co-current DCMD for a membrane length of 130 mm, permeate inlet temperature of 20°C, brine inlet temperature of 60°C and feed and permeate velocities of 0.11 m/s. In counter-current DCMD, the cold interface/bulk temperature is almost parallel to the hot interface/bulk temperature because of the identical velocities on both sides of the membrane, while in co-current mode they begin to converge as the streams flow from the inlet to the outlet. Furthermore, at the same location, it was found that the temperature difference between the bulk flow and membrane interface on cold side is greater than that on hot side, due to lower turbulence arising from the greater liquid viscosity at lower temperatures.

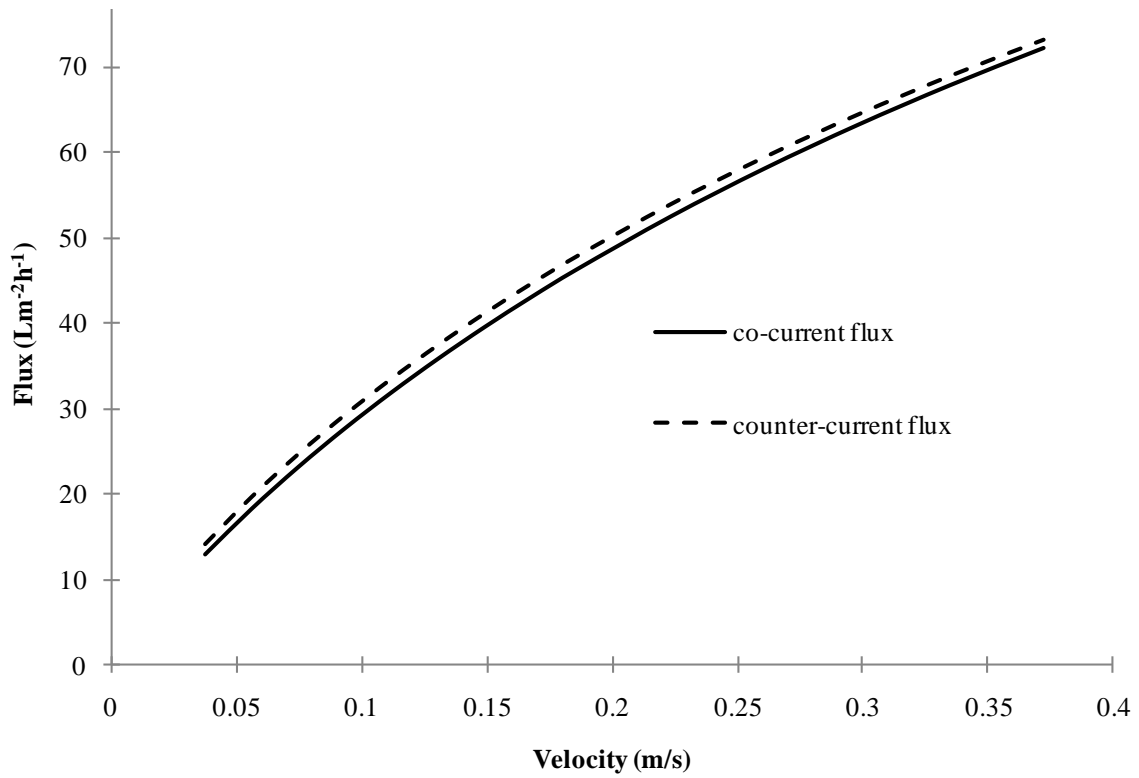
By comparing Fig. 6.23a and 6.23b, it can be found that the temperature polarisation was almost constant for the counter-current mode, but decreases as the hot and cold streams travel further from the inlets in co-current DCMD. Additionally, in a region ($0 \leq x \leq 0.02 \text{ m}$) where there is the highest vapour pressure difference across the

membrane, the temperature polarisation in co-current DCMD is higher than the counter-current mode, but in a region ($0.11 \leq x \leq 0.13$ m) where there is the lowest vapour pressure difference across the membrane, the temperature polarisation in the co-current DCMD is lower than the counter-current mode. Because the mass transfer and the heat transfer rates are respectively exponential and linear functions of the interface temperatures, there is a higher percentage of heat used for mass transfer at higher interface temperatures and a higher percentage of heat used for heat transfer at lower interface temperatures when the temperature difference is the same. Therefore, compared to counter-current DCMD, co-current mode in the region with the highest vapour pressure difference has lower percentage of thermal energy utilised for evaporation, while in the region with the lowest vapour pressure difference there is higher thermal energy loss through conduction, because of the temperature polarisation distribution. Thus, the flux difference between the co-current and counter-current modes is mainly caused by temperature polarisation distribution along the membrane.

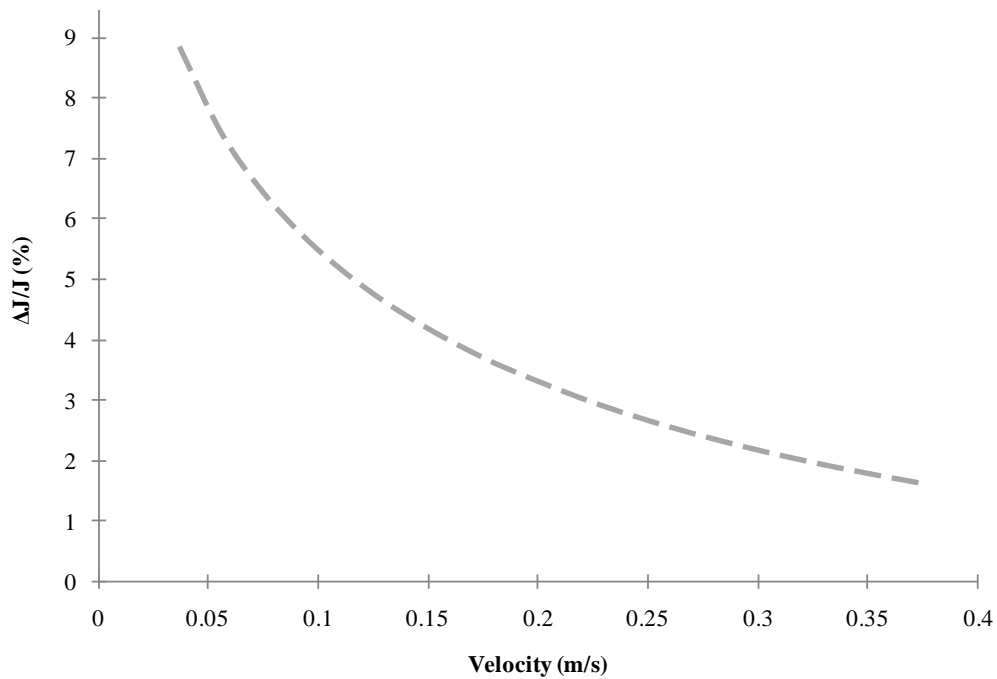
In Fig. 6.24a, the predicted fluxes from both co- and counter-current DCMD at different velocities (0.037-0.37 m/s) are presented. The curve slopes of co- and counter-current processes become smaller at a higher velocity, and flux difference between co- and counter-current DCMD defined in Eq. (6.27) also becomes smaller (shown in Fig. 6.24b).

$$\frac{\Delta J}{J} = \frac{J_{counter} - J}{J} \quad (6.27)$$

where $J_{counter}$ and J are fluxes of counter-current and the co-current modes, and ΔJ is the difference between them. As the stream velocity increases to 0.37 m/s, the predicted flux difference is only 1.6%, so there is not great flux difference between these modes if high stream velocities are used.



a. Predicted counter- and co-current flux as a function of stream velocity



b. Flux difference

Fig. 6.24 Percentage flux difference between counter current and co-current modes

$$(L_{mem}=130 \text{ mm}, T_{pi}=20^\circ\text{C}, T_{fi}=60^\circ\text{C})$$

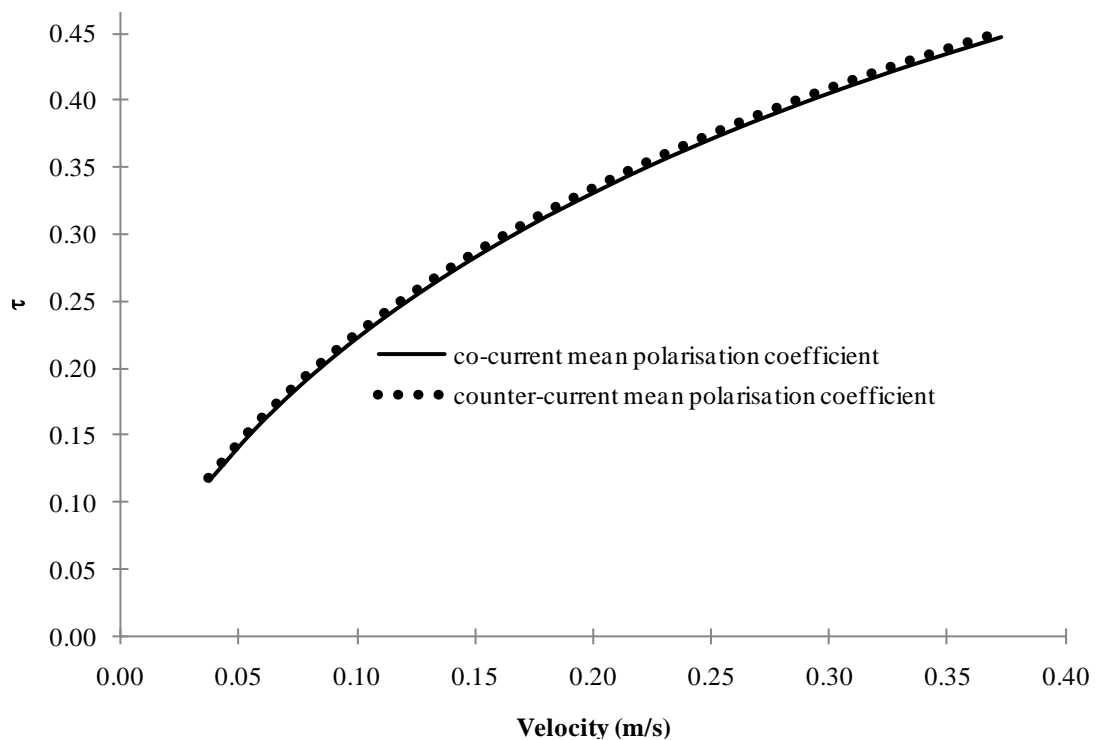
The temperature polarisation coefficient (τ) changed with velocity and the polarisation coefficient difference ($\Delta\tau/\tau$) defined in Eq. (6.28) are shown in Fig. 6.25.

$$\frac{\Delta\tau}{\tau} = \frac{\tau_{counter} - \tau}{\tau} \quad (6.28)$$

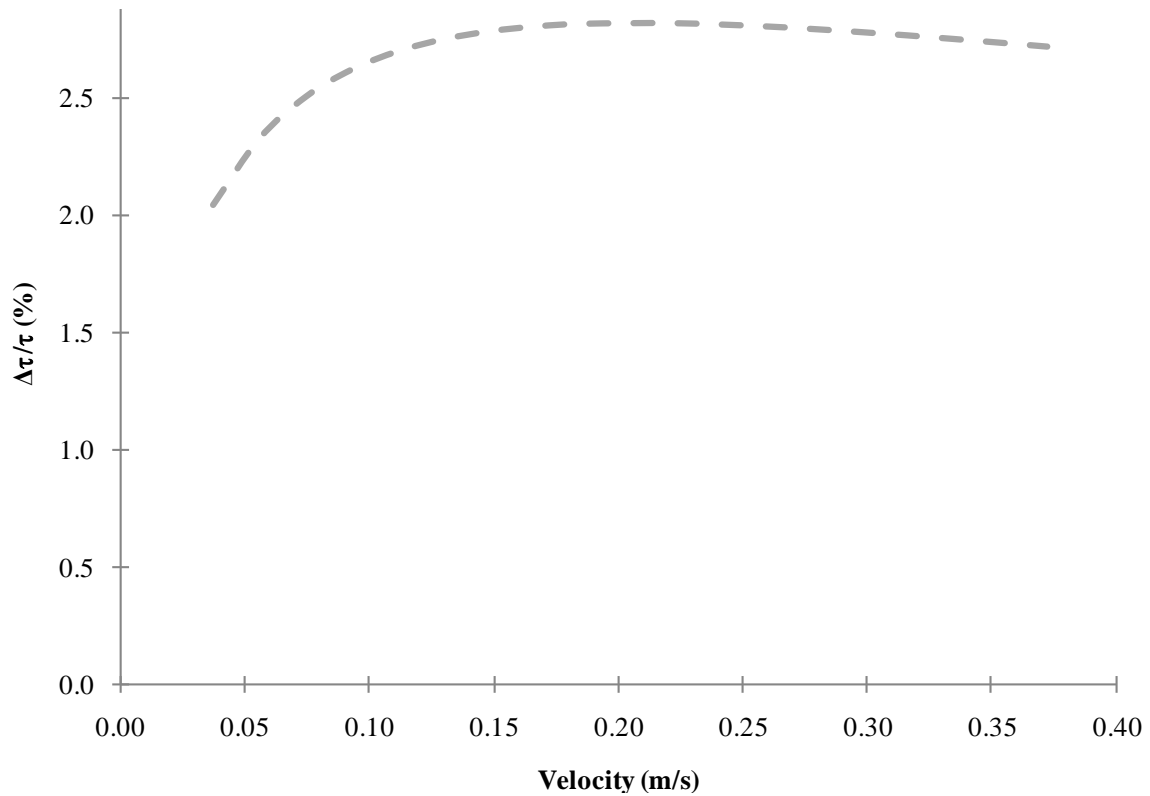
where $\tau_{counter}$ and τ are temperature polarisations of counter-current and the co-current modes, and $\Delta\tau$ is the difference between them.

The temperature polarisation coefficients (Fig. 6.25a) increase with stream velocity because of enhanced convective heat transfer at higher turbulence and reduced boundary layer effects. The temperature polarisation coefficient difference increases initially with velocity and reaches a plateau when the velocity is greater than 0.15 m/s, as the influence of increased velocity on reducing boundary layer effect is low in this region.

As the velocity increases, the flux difference shown in Fig. 6.24b reduces from 8.8% to 1.6%, but τ differences (Fig. 6.25b) increase only from 2% to 2.6%. Therefore, the counter-current DCMD can produce more flux (Fig. 6.24a) and has a higher temperature polarisation coefficient (Fig. 6.25a) than those of co-current DCMD at the same inlet temperatures and velocities, although the differences are relatively small (<10%).



a. Predicted counter- and co-current τ



b. τ difference

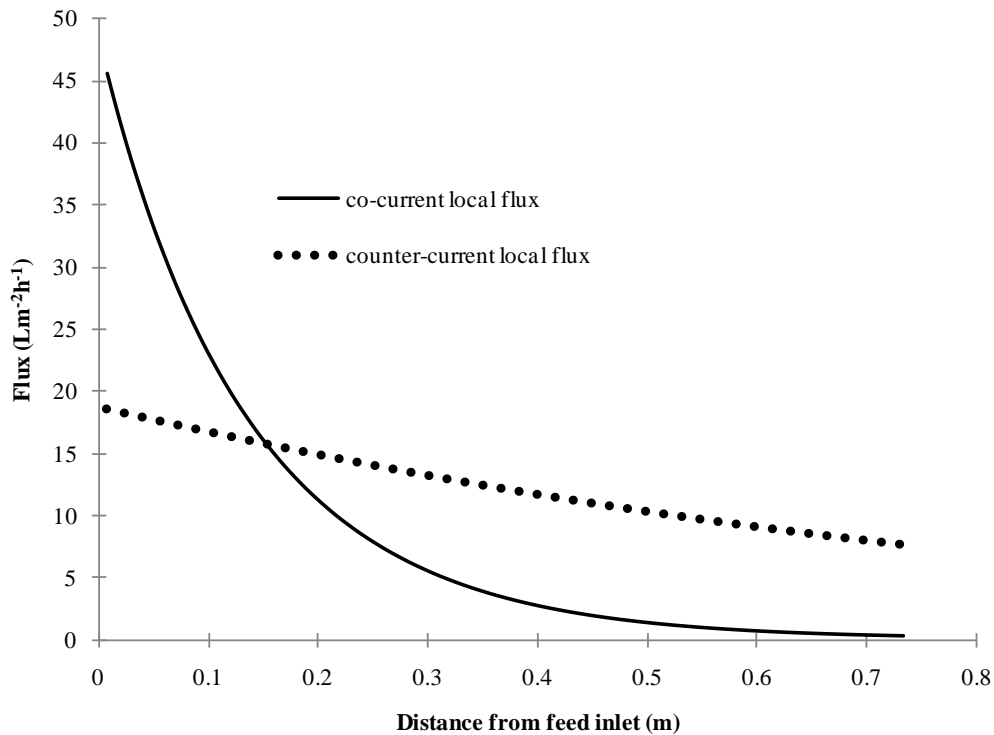
Fig. 6.25 Temperature polarisation coefficient vs feed velocity

$$(L_{mem}=130 \text{ mm}, T_{pi}=20^\circ\text{C}, T_{fi}=60^\circ\text{C})$$

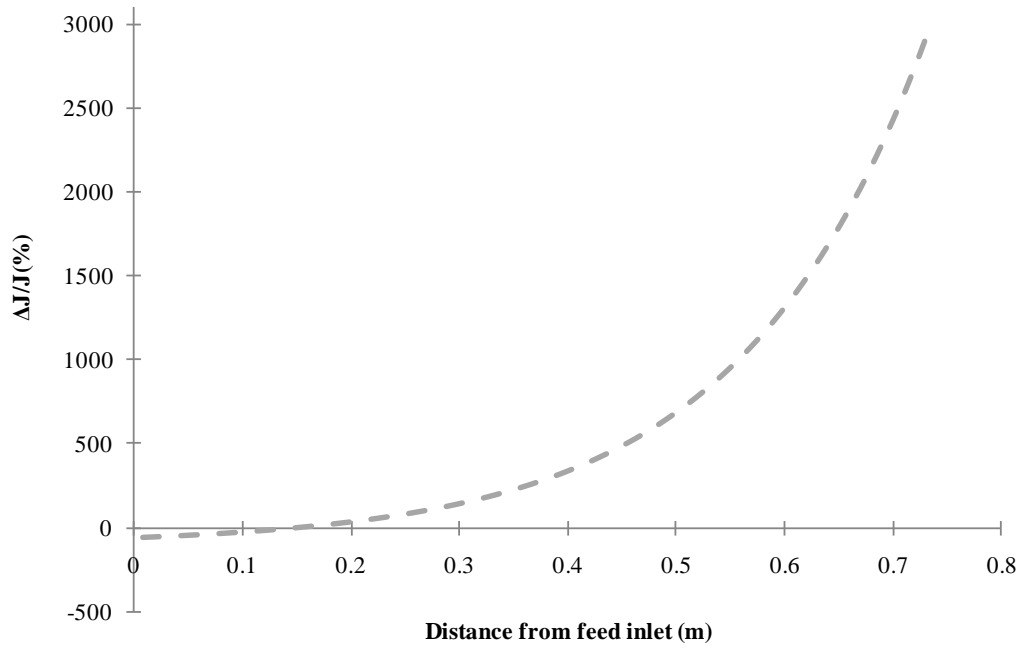
It also can be found from the modelling results that the counter-current DCMD will have much better performance than co-current DCMD at lower stream velocity, and the performance difference is reduced at higher velocities. Furthermore, it is also observed that the slope of the temperature polarisation coefficient curve (Fig. 6.25a) is lower than that of the flux curve (Fig. 6.24a). Therefore, the flux increase with velocity arises from both the change of τ and the greater temperature differences along the membrane that results from higher velocities [48] (ie. greater heat flow through the system).

The profile of the local fluxes and their differences of both DCMD modes are presented in Fig. 6.26. Here, a membrane in our small pilot module ($0.73 \times 0.13 \text{ m}^2$) is modelled. It is observed that the local flux (Fig. 6.26a) reduces for distances further from the feed inlet. In co-current DCMD, most of the co-current permeate is produced from the first quarter of the membrane, and the local flux dramatically reduces by 99.4% (from 45.6 to $0.28 \text{ Lm}^{-2}\text{h}^{-1}$) from the feed inlet to the feed outlet. However, for counter-current

DCMD the local flux reduces almost linearly with distance from the feed inlet, and a local flux reduction of 57.3% (from 18.6 to 8.0 $\text{Lm}^{-2}\text{h}^{-1}$) was found from the feed inlet to the feed outlet. The local flux difference (Fig. 6.26b) between co- and counter-current modes increases almost exponentially with the distance from the feed inlet. Although local flux in the counter-current DCMD is lower than that of the co-current mode when the distance is less 0.14 m, this does not suggest that the co-current DCMD will have a higher flux than that of counter-current DCMD when a short membrane is employed, because the local flux profile varies with the membrane length in counter-current DCMD. As shown in Fig. 6.22a, the counter-current DCMD will have the higher flux when a shorter membrane is used.



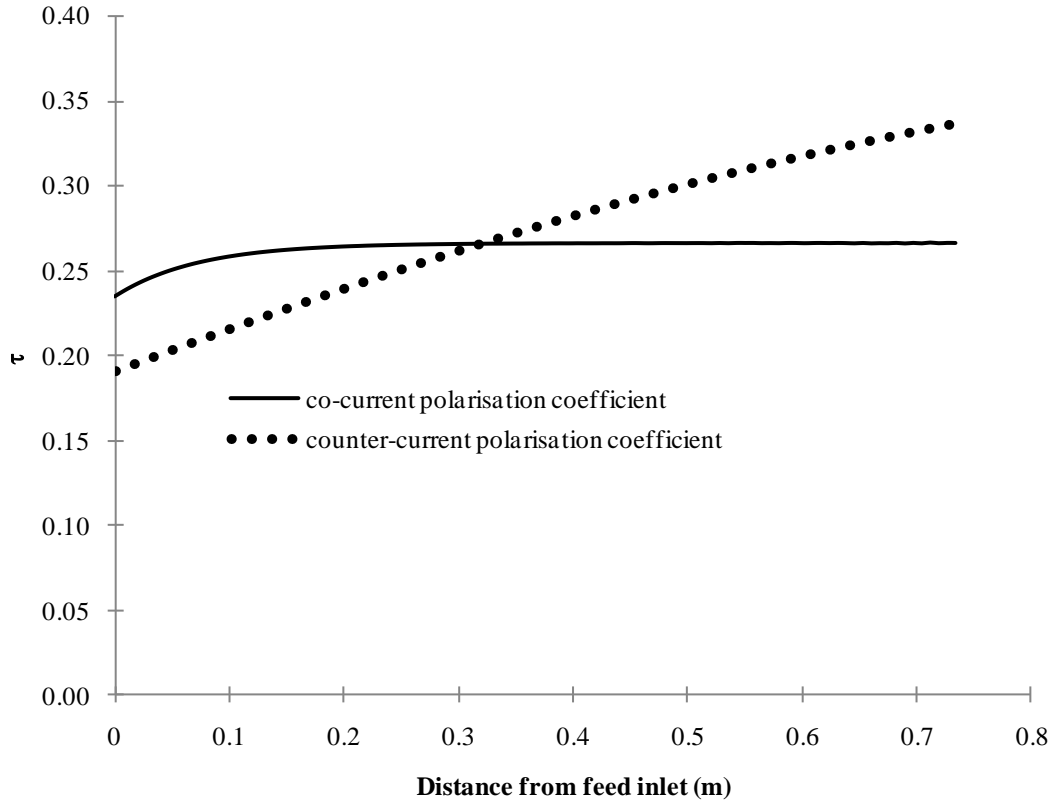
a. Predicted counter- and co-current flux



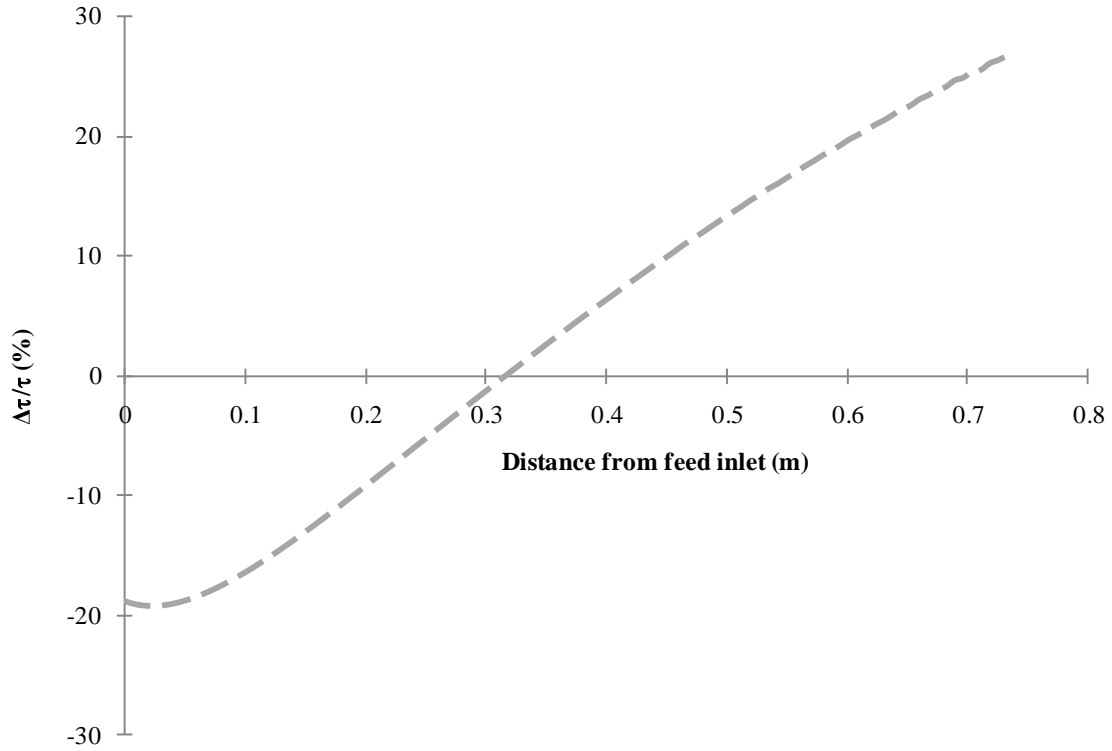
b. Flux difference

Fig. 6.26 Local flux distribution vs membrane length

($L_{\text{mem}}=733$ mm, $T_{\text{pi}}=20^\circ\text{C}$, $T_{\text{fi}}=60^\circ\text{C}$, $v_f=v_p=0.11$ m/s)



a. Predicted counter- and co-current τ



b. τ difference

Fig. 6.27 Local temperature polarisation coefficient distribution vs membrane length

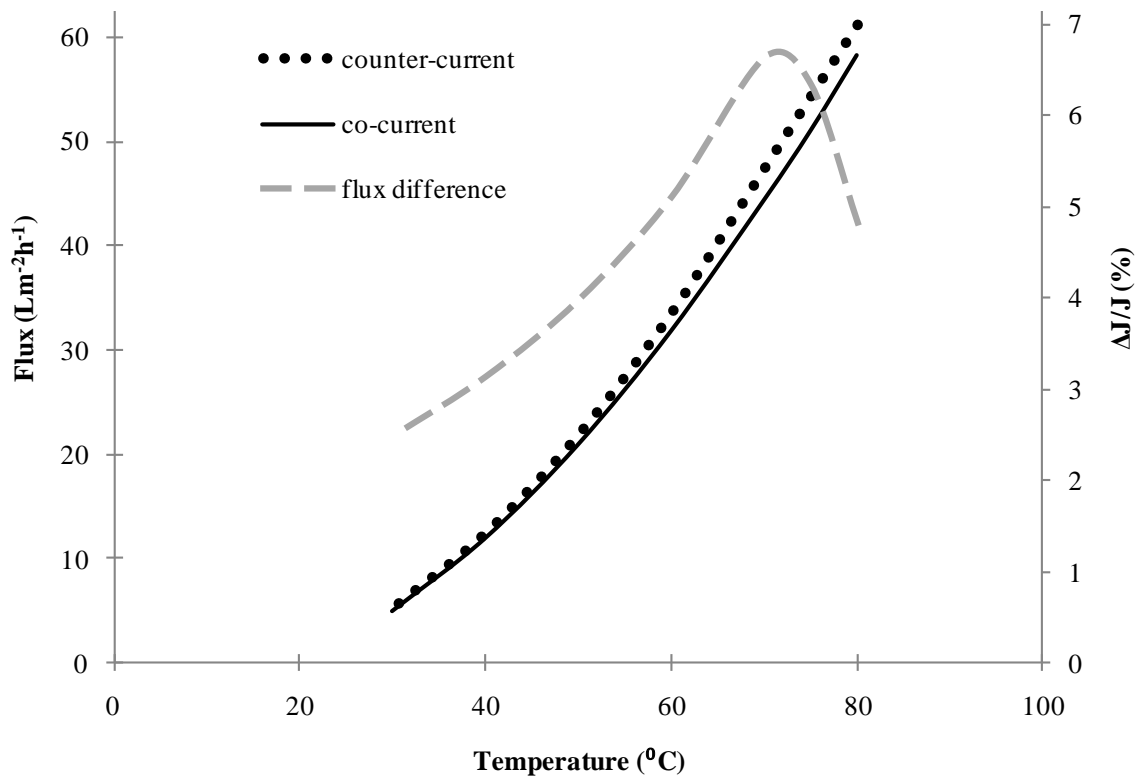
$$(L_{mem}=733 \text{ mm}, T_{pi}=20^\circ\text{C}, T_{fi}=60^\circ\text{C}, v_f=v_p=0.11 \text{ m/s})$$

The temperature polarisation coefficients and their difference along the membrane are presented in Fig. 6.27. The temperature polarisation coefficient (Fig. 6.27a) shows the reverse trend to the flux, which increases linearly with the distance in the counter-current DCMD, and increases initially and reaches a plateau at the distance of 0.2 m in the co-current DCMD.

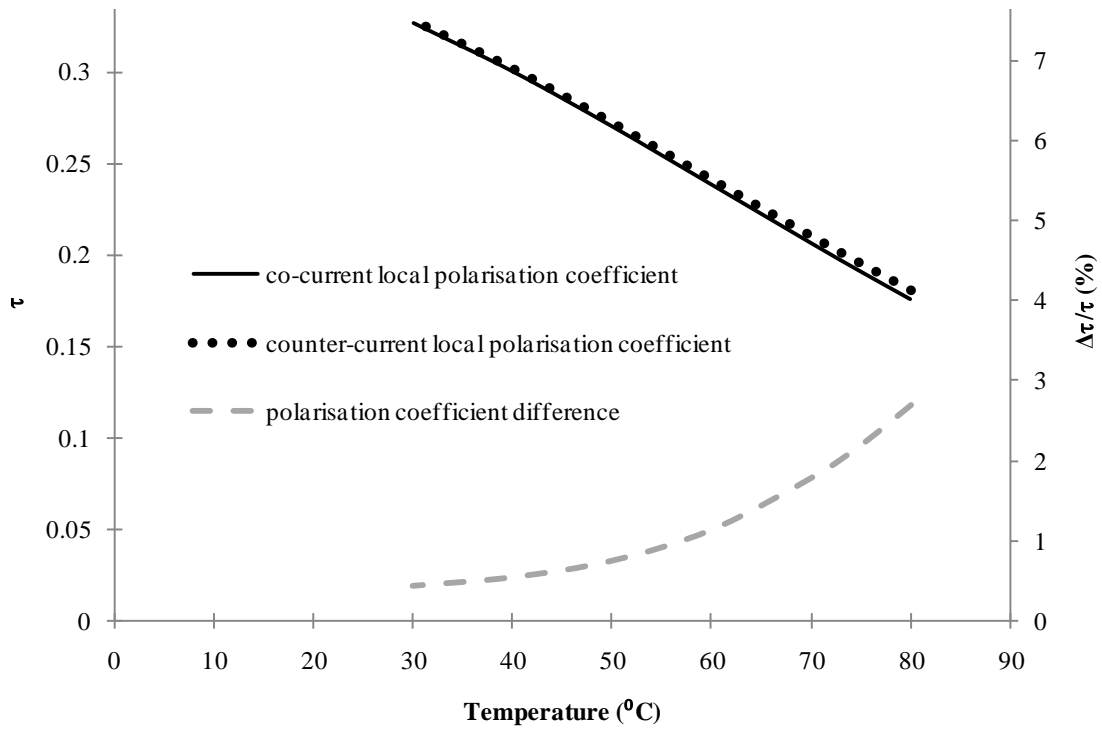
Therefore, the flux of the co-current mode is more sensitive to the membrane length (seen in Fig. 6.22a, the flux of the counter-current mode is 59% higher than that of co-current mode, when a 733 cm membrane was used), so the counter-current DCMD is a better choice for scale-up purpose when a longer membrane is considered. In comparison with a long and narrow membrane, a wide and short membrane with the same area will have higher flux at the same steam linear velocity and inlet temperatures, and higher velocity to reduce scaling at the same pressure drop (limited by LEP) on the membrane. Therefore, a short and wide membrane is suggested to be used rather than a

long and narrow membrane in design.

The predicted results at different temperatures (30-80°C) are shown in Fig. 6.28. This figure shows that although greater temperature is able to boost the flux production almost exponentially (Fig. 6.28a), the temperature polarisation coefficients (Fig. 6.28b) are nearly halved from 30 ($\tau=0.33$) to 80°C ($\tau=0.18$). The counter-current DCMD is predicted to produce more flux in the modelled temperature range and to have a higher temperature polarisation coefficient than those of co-current DCMD under the same conditions. However, the flux difference is reduced after it reaches the peak at 70°C, because of a combination of the local temperature polarisation and heat conduction losses (Fig. 6.28a).



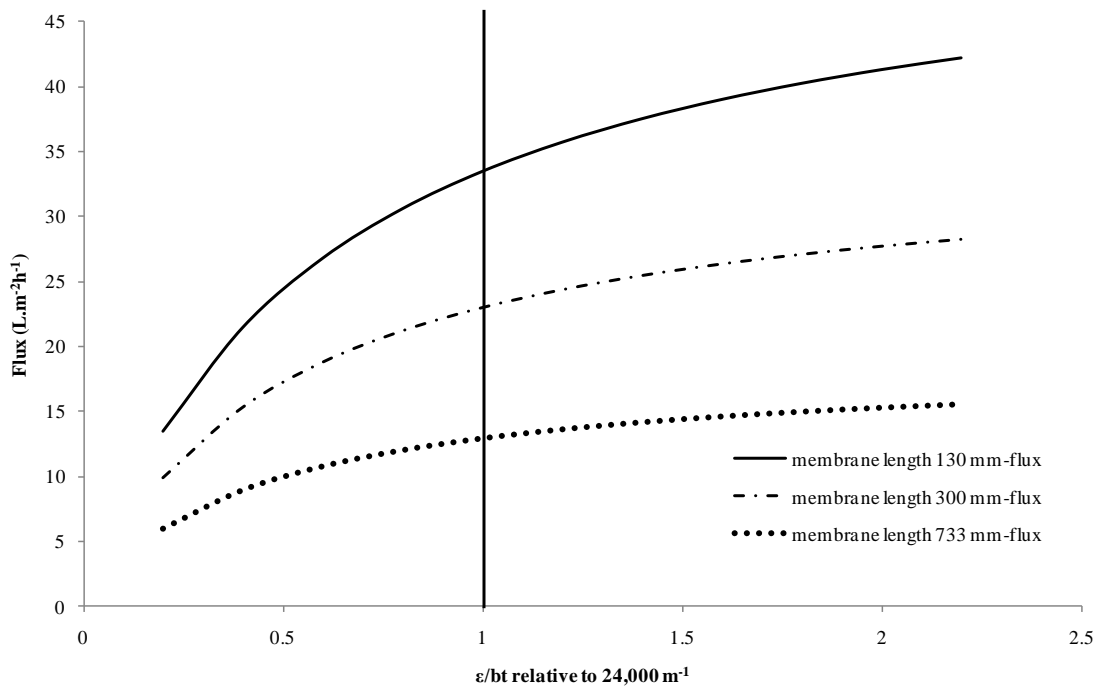
a. Flux vs temperature



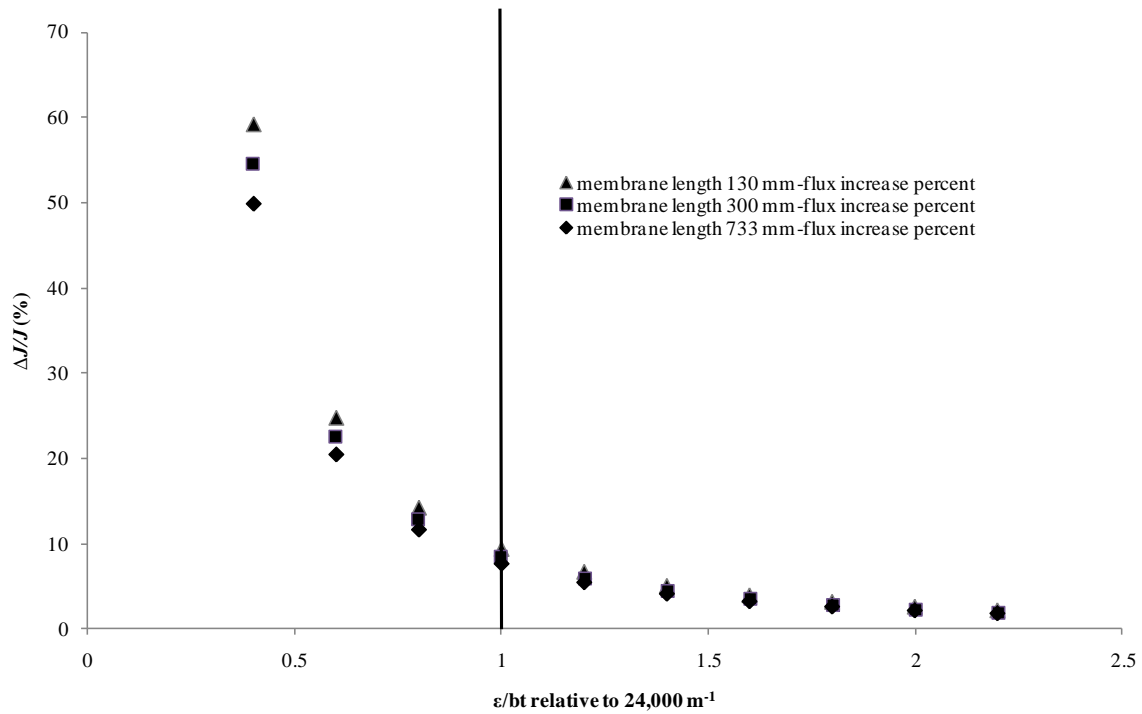
b. Temperature polarisation coefficient vs temperature

Fig. 6.28 Flux and temperature polarisation affected by temperature

($L_{mem}=130$ mm, $v_f=v_p=0.11$ m/s)



a. Flux vs membrane characteristic



b. Flux difference vs membrane characteristic

Fig. 6.29 Influence of membrane characteristics on flux

($T_{pi}=20^{\circ}\text{C}$, $T_{fi}=60^{\circ}\text{C}$, $v_f=v_p=0.11 \text{ m/s}$, counter-current)

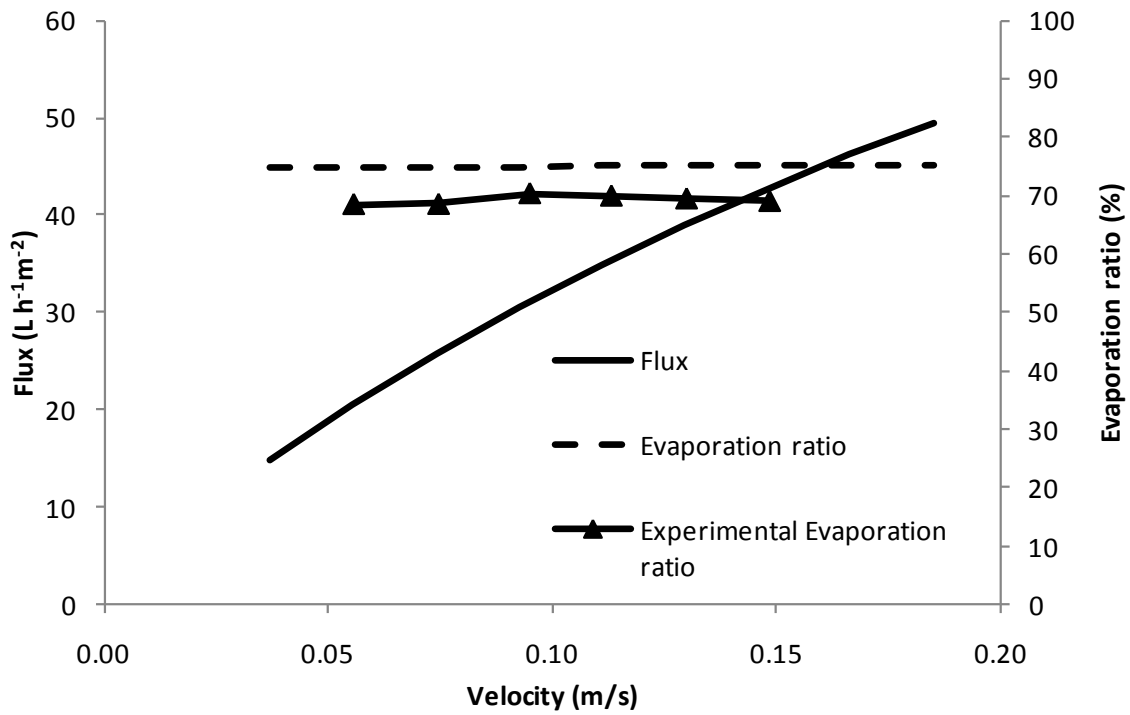
The relationship between the flux increment and the relative membrane mass transfer property (ϵ/bt) is presented in Fig. 6.29 for three different membrane lengths. The mass transfer property of the PTFE membrane employed in this study is used as a reference value. From these curves, it was found that the flux (Fig. 6.29a) increases with an improved membrane mass transfer value (higher ϵ/bt), but the percentage increment (Fig. 6.28b) decreases from more than 50% to below 5% as the relative value of ϵ/bt increases from 0.2 to 1.4 in the increments of 0.2. Fig. 6.29b also demonstrates that the contribution of improved membrane mass transfer properties to flux becomes less as longer membranes are considered. Therefore, the optimisation of the membrane properties (ϵ/bt) will contribute less to flux increases for long membranes, based on this membrane and modelling conditions ($T_{pi}=20^{\circ}\text{C}$, $T_{fi}=60^{\circ}\text{C}$, $v_f=v_p=0.11 \text{ m/s}$, counter-current).

The characteristics of the PTFE membrane used in this study had a porosity of 94%, thickness about $37 \mu\text{m}$ and tortuosity 1.1 ± 0.1 [75, 130]. Porosity can only increase by 6%

(ie. 94-100%) and tortuosity by 10%. These improvements will ideally increase ε/bt by 17%. Therefore, the biggest improvements in ε/bt might come from decreases in membrane thickness. However, previous results suggest [48, 97] that a practical membrane thickness should be no less than 30 μm , due to mechanical strength and salt rejection deterioration. Hence, the greatest practical improvement in ε/bt is less than 45%, and Fig. 6.29b shows that the resultant flux increase is only 12% equivalent to the effect of increasing the stream velocity from 0.11 to 0.13 m/s at hot and cold inlet temperature of 60°C and 20°C. This suggests that efforts to improve the membrane characteristics for flux improvement are unlikely to have a significant impact on DCMD performance if long membrane modules are constructed.

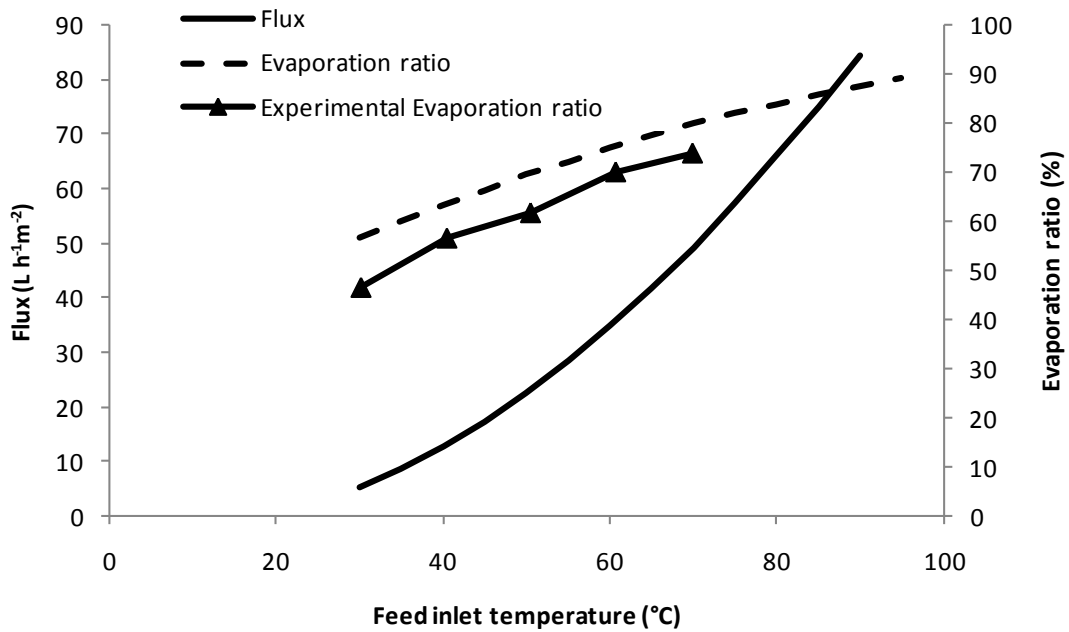
6.2.4.2.3 Single-pass evaporation ratio variation with process parameters

The evaporation ratio defined in Eq. (3.12) shows the percentage of energy used for driving permeate across the membrane, and it is important for optimising the process parameters to increase the energy efficiency. Therefore, the validated model was used to predict the evaporation ratio in counter-current mode under different conditions, which are shown in Fig. 6.30. The modelled results were also verified experimentally shown in Figs. 6.30a and 6.30b. The positive absolute errors (~5%) are also caused by neglecting the permeate flow and sensible heat carried by the permeate flow, which lead to a higher predicted hot outlet temperature and a lower predicted cold outlet temperature than those of the experimental results. As a result, the evaporation ratio is overestimated by the model. However, the modelled results show the same trend as the experimental results.



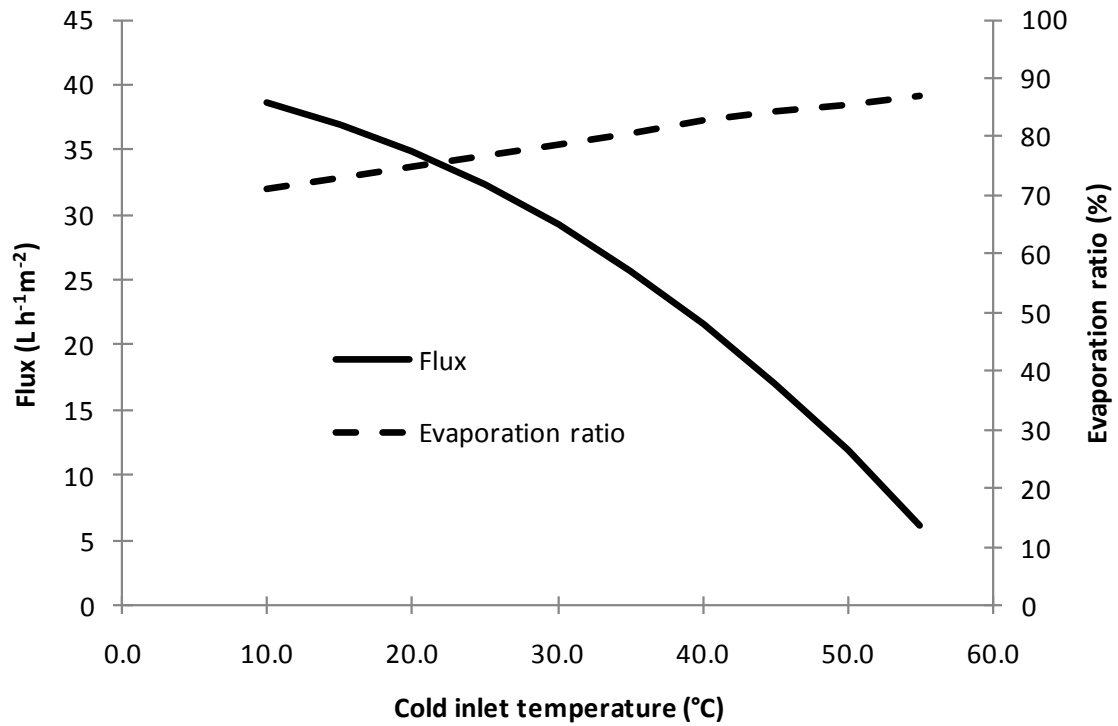
a. Evaporation ratio and flux at different stream velocities

(Hot inlet temperature=60°C, cold inlet temperature=20°C, identical stream velocities)



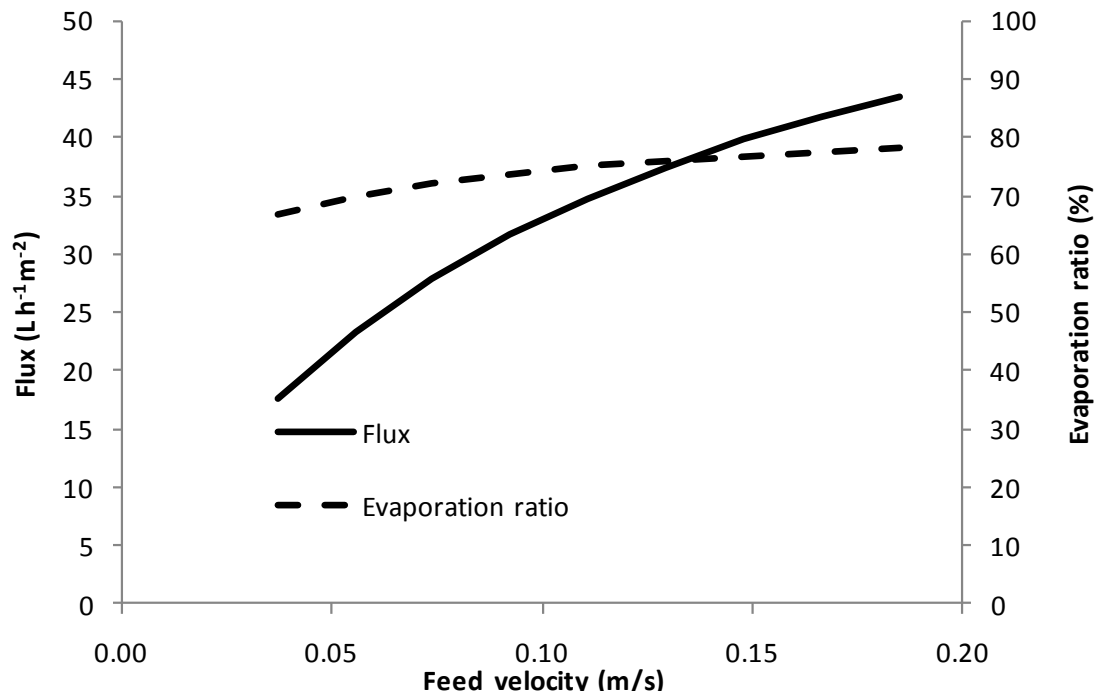
b. Evaporation ratio and flux at different feed inlet temperatures

(Both stream velocities=0.11 m/s, cold inlet temperature=20°C)



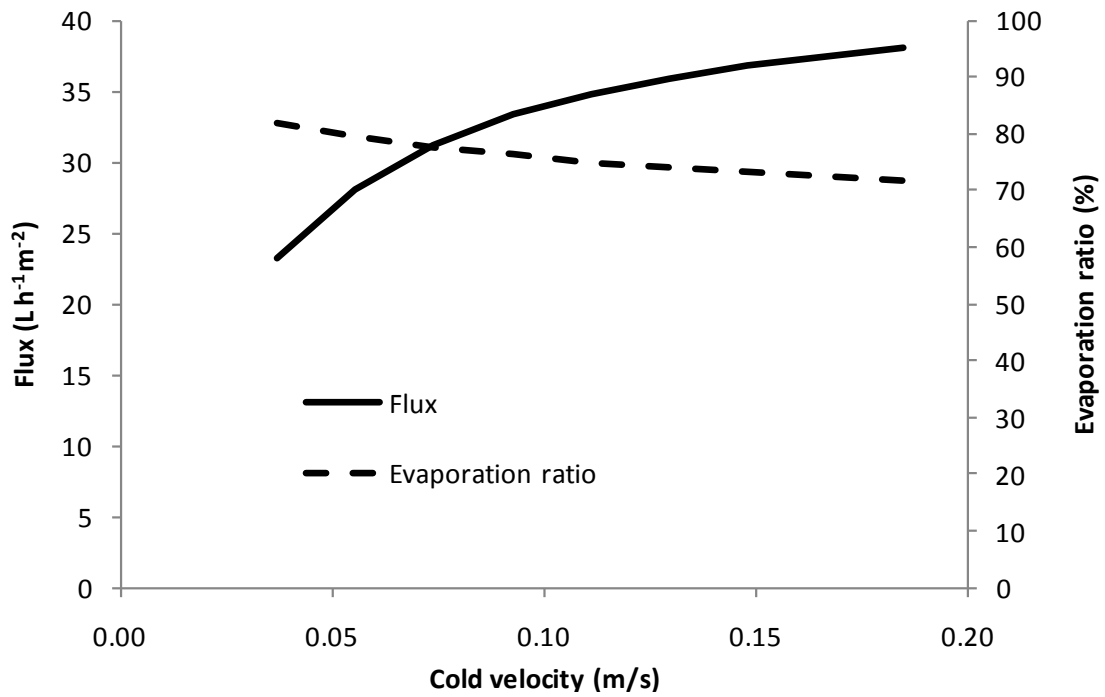
c. Evaporation ratio and flux at different permeate inlet temperatures

(Both stream velocities=0.11 m/s, feed inlet temperature=60°C)



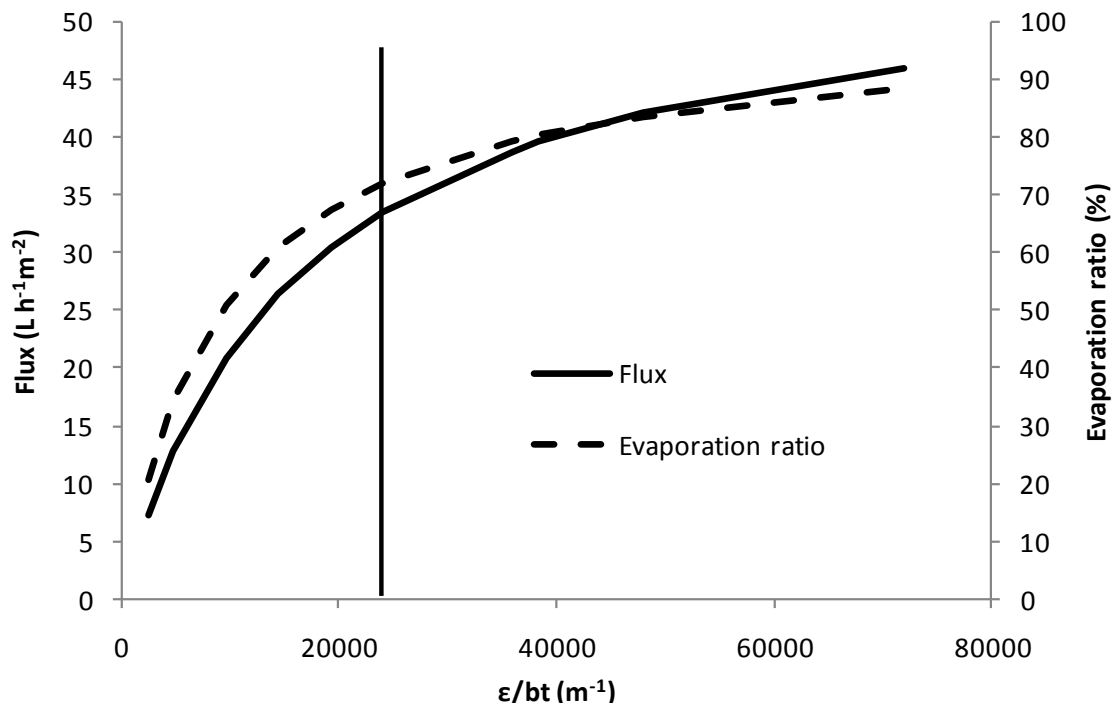
d. Evaporation ratio and flux at different feed stream velocities

(Cold velocity=0.11 m/s, hot inlet temperature=60°C, cold inlet temperature=20°C)



e. Evaporation ratio and flux at different cold stream velocities

(Hot velocity=0.11 m/s, hot inlet temperature=60°C, cold inlet temperature=20°C)



e. Evaporation ratio and flux at membrane properties (ϵ/bt)

(Hot velocity=0.11 m/s, hot inlet temperature=60°C, cold inlet temperature=20°C)

Fig. 6.30 Evaporation ratio and flux at different process conditions
(Membrane length=0.13 m)

From Figs. 6.30 and 6.31, it can be found that:

- Higher feed inlet temperature can improve both the evaporation ratio and flux,
- Increasing velocities of both sides simultaneously will not change the evaporation ratio, but will increase the flux,
- Increasing the permeate temperature can increase the evaporation ratio, but dramatically reduce the flux,
- Increasing the feed stream velocity (keep permeate velocity constant) can greatly increase the flux and slightly increase the evaporation ratio,
- Increasing the permeate stream velocity (keeping feed velocity constant) can greatly increase the flux, but slightly decrease the evaporation ratio,
- Improving membrane properties (ε/bt) will increase both the flux and evaporation ratio almost linearly for $\varepsilon/bt < 24,000 \text{ m}^{-1}$, while the increase in rate becomes much smaller for $\varepsilon/bt > 24,000 \text{ m}^{-1}$,
- Increasing the membrane length will not change greatly the evaporation ratio (about 2.7% absolute value reduction as the membrane length increased by 31 times), but will reduce the flux, and
- The modelling results suggest high feed velocity and high feed inlet temperature will improve both flux and evaporation ratio, and a shorter membrane will improve the flux but not change the evaporation ratio.

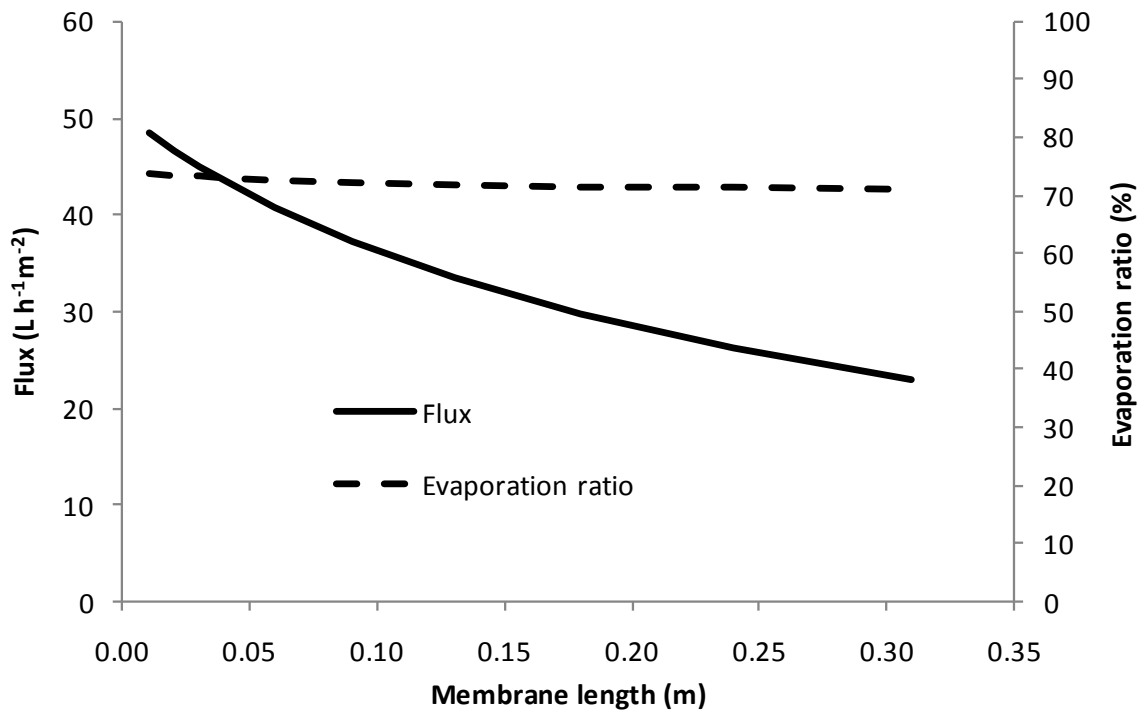


Fig. 6.31 Evaporation ratio and flux varied with membrane length

(Both stream velocities=0.11 m/s, hot inlet temperature=60°C, cold inlet temperature=20°C)

6.3 Summaries for both models

Both simple and complex mathematical models were developed for the DCMD process based on heat and mass balances. Both models showed agreement with experimental results with errors of less than 14%, which is applicable in engineering design if the margin factor (10-25%) and experimental reproducibility ($\pm 5\%$) are considered.

The basis of the simple model is the experimental findings that the mean global heat and mass transfer coefficients only change slightly with variations of some parameters that will not affect the thermal boundary layer greatly, e.g. temperature variation (40-80°C) and length difference of membrane. If a database of global mass and heat transfer coefficients against the velocity is available under given boundary layer conditions, the simple model can be used to predict the flux at different temperatures and membrane lengths. However, the defined boundary layer conditions will also be affected greatly by the characteristics of the module flow channel structure, e.g. the presence of the turbulence promoter (spacer) or the dimension of the flow channel cross section, so the

variations of these characteristics of the flow channel will cause invalidation of such a database at the same stream velocity. Therefore, the model is strictly limited in the prediction of flux under similar boundary layer conditions that the global mass and heat transfer coefficients are acquired. Although the simple model is limited by the boundary layer conditions, the simple model provides a convenient means in the pilot module design if the conditions of the flow channels are preset, because the database of the global mass and heat transfer coefficients against the velocity can be simply obtained from a small module with the same flow channel characteristics. Therefore, this model does not require complex characterisation of the membrane and flow channel, which require special analytical facilities and time consuming calculations.

The complex mathematical model was developed based on the characterisations of the membrane and flow channel. For characterised membranes and flow channels, it can be used to predict flux at different velocities, membrane lengths, and different temperatures. Although this model is versatile in flux prediction under different boundary layer conditions, characterisation of the membrane and flow channel are required before predicting the flux of a pilot design. Compared to the simple model, this complex model has the advantage of being able to optimise module design and process parameters.

The predictions from both models showed:

- The temperature profiles on both the hot and cold sides approach each other in co-current DCMD, but are parallel to each other in counter-current DCMD, when the flowrates on both sides are identical,
- The co-current DCMD showed a greater temperature difference than that of counter-current DCMD under identical inlet conditions, but the counter-current DCMD still produced higher flux than that of the co-current DCMD. The findings suggest that counter-current configurations should be adopted in commercial applications when long membranes are considered, because of the dramatic decrease in flux in co-current DCMD when larger modules are used.
- MD flux is affected by the length of the membrane, and a short and wide membrane is suggested to be used rather than a long and narrow membrane in design for higher average flux, and
- The modelling results showed that the feed velocity will have less influence on the flux for longer membranes.

The employment of the complex model also indicated:

- For spacer filled channels, use of the Nusselt number calculated from turbulent flow leads to a better fit of the experimental results compared to Nusselt numbers calculated from laminar flow,
- Under the same hydraulic flows, higher feed temperature lead to lower temperature polarisation coefficients because the greater heat flux leads to an increased rate of heat and mass flux through the membrane and hence, a greater temperature gradient in the bulk flow.
- Stream velocity is a key factor in DCMD, especially at higher temperatures (70-80°C), because the temperature polarisation coefficient becomes lower as the temperature rises.
- A co-current model and a counter-current model were used to predict flux and temperature coefficients under different conditions. The counter-current model predicted a higher temperature polarisation coefficient than that of the co-current model under the same inlet conditions, which agrees with the experimental findings.
- Optimisation of the membrane structure (increases in ε/bt) is able to increase DCMD flux, but the increases in flux arising from further improvements in ε/bt is unlikely for longer DCMD membrane (>0.7 m). Furthermore, the increased rate of evaporation ratio is reduced greatly for $\varepsilon/bt > 24,000 \text{ m}^{-1}$.
- This work also identifies that characterisation of the mass transfer characteristics of MD membranes is best achieved by reporting ε/bt values, as this term relates to the fundamental characteristics of the membrane. This term can also be used to predict DCMD performance under a range of conditions, while mass transfer co-efficient is a function of pore pressure and the hydraulic conditions of the stream, and flux is dependent on a range of process conditions.
- From the modelling results, it suggests high feed velocity and high feed inlet temperature, which will improve both the flux and evaporation ratio.

Based on the modelling results, there are a few findings need to be addressed:

- For the module design, a short and wide flow channel will be ideal for DCMD, because high velocity can be used due to the less resistance in the flow direction,

- Raising velocities of both sides simultaneously can increase the flux, but can not enhance the evaporation ratio,
- If it is possible, increasing hot temperature is better than decreasing the same degree of cold temperature, which will raise both flux and evaporation ratio.

Based on the research results for PTFE membranes, a further improvement of membrane property will only give minor increases of flux and evaporation ratio.

Chapter 7 Conclusions and Recommendations

The objectives for this thesis were to develop an understanding of:

1. the structure and material properties of membranes suitable for membrane distillation,
2. how mass transfer is affected by the membrane structure of hollow fibre membranes,
3. the influence of system pressure on flux for compressible and incompressible membranes, and
4. to develop a process model for scaling-up of membrane distillation modules and for process design.

For the first objective, membranes with different pore sizes, support layers, and active layers were studied, and these membranes were characterised by the tests of LEP, gas permeation, SEM, and porosity. The performances of these membranes in DCMD were tested under different inlet temperatures and stream velocities, and the membranes were assessed by global mass transfer coefficients and energy efficiency (evaporation ratio). The use of the mass transfer coefficients removes the temperature dependence of the flux measurements, and so provides a means to study polarisation effects and to better identify membrane performance by removing the effect of some of the process variables.

The experimental results showed that the performances of three new PTFE membranes supported with scrims show greater potential for use in desalination processes than do the traditional microfiltration membranes. The new PTFE membranes achieved a significantly higher flux and had better energy efficiency than the MF membranes under the same conditions.

The contact angles of the new PTFE membranes were in the range of 140-160°, which are 1.5 times that of employed micro-filtration PVDF membrane and 1.25 times that of micro-filtration PTFE membrane. Similarly, the LEP of the new membranes were 2 times that of the MF membranes, so the new MD membranes can be used at higher operating pressures without the risk of wetting.

The new membranes also show good salt rejection even under critical conditions. In

comparison with the 96% salt rejection rate of PVDF membrane, all PTFE membranes achieved nearly 100% salt rejection rate at a feed velocity of 0.36 m/s and ≤ 20 kPa. Additionally, all PTFE membranes had global mass transfer coefficients higher than or similar to that of MF membranes under the same conditions.

The more open support layers of the new membranes have less mass transfer resistance than the nonwoven fabric support layer, and subsequently greater flux and energy efficiency. Fluxes of up to $46 \text{ Lm}^{-2}\text{h}^{-1}$ were obtained at 80°C in this objective.

For the second objective, an asymmetric hollow fibre membrane was studied. The LEP of the hollow fibre membrane was characterised by the surface tension effect, thicknesses of the skin and principle layer was estimated through SEM imaging, and the pores size and porosity were measured by BET. The performance of this membrane in DCMD was assessed based on the variation of temperatures, flow velocities, stream configuration, and the degree of cold side vacuum pressure in the hollow fibre module. Flux was calculated based on the outside surface area of the hollow fibre membrane, irrespective of the direction of permeate transport as the skin layer was the rate determining mass transfer layer. Global mass transfer coefficients were calculated to evaluate the performance of the process under different conditions.

The membrane showed different performances when the hot feed passed through different sides (lumen and shell sides) of the membrane. In this study, the highest flux was $19.2 \text{ L.m}^{-2}\text{h}^{-1}$, when the feed flowed through the shell side with a velocity of 0.4 m/s and the inlet temperatures on the cold side and hot side were 20°C and 86°C respectively (without vacuum pressure on the permeate side). The variation in performance can be attributed to the asymmetric structure of the membrane, and the exponential relationship of vapour pressure to temperature.

The experimental results showed that the mass transfer coefficient at high velocities remained approximately constant as the hot feed temperature increased from 30 to 86°C .

Negative gauge pressure on the cold side boosted the flux by reducing the pressure within the pores and thereby increasing the rate of mass transfer through the pores. However, the rate of increase in flux reduced at higher vacuum pressures indicating that there is a diminishing return for flux at higher negative pressures beyond -12 kPa (feed velocity > 0.22 m/s), due to the skin layer effect. A non-compressible hollow fibre would

be advantageous for high flux hollow fibre MD, as it would enable a negative pressure to be employed in the permeate stream on the lumen side.

The results show salt rejections higher than 99% can be achieved even at very high volume feed velocities, due to the large inner diameter of the hollow fibre membrane.

The third objective is focused on the compressibility of PTFE MD membranes, and an incompressible hollow fibre membrane was used for comparison purposes. The pore size and ε/bt of the membrane were determined by gas permeation, and a wetting method was used to measure the mean thickness, porosity of the active layer, and the density of the active layer material. The deformation of the membrane with pressure was also determined experimentally. The influence of applied pressure on membrane performance in DCMD was studied at different temperatures and velocities.

The incompressible and compressible membranes were characterised under different pressures, and relationships between the pressure and the porosity, thickness and thermal resistance of the membrane were presented and used for analysis of the experimental results. A great reduction of membrane thermal resistance was found as the pressure increased for the compressible PTFE membrane.

The flux from the incompressible membrane did not change with applied pressure variations across the entire pressure range considered, and this was attributed to changes in pressure not influencing the pore pressure nor the membrane thickness or pore structure.

For the compressible membrane, the mean membrane mass transfer coefficient and the temperature difference between the membrane interfaces were calculated based on the mass and heat balances and fitting curves from membrane characterisation experiments. Although an optimum mean membrane mass transfer coefficient was found at a pressure of 25 kPa, it was found that the flux decreased with an increased pressure for all experiments due to the increased thermal conductivity of the membrane.

At the same feed inlet temperature, the rate of flux decrease is greater at lower velocity as the pressure increased. The comparison of two membranes with similar mass transfer coefficients showed that there are higher temperature polarisation coefficients and greater membrane interface temperature difference at higher velocity, but their

differences become smaller and approach zero as the pressure becomes higher.

At the same stream velocities, the increased pressure had less effect on the flux at a lower temperature. The results show that there are smaller temperature polarisation coefficients and greater $\Delta T_{interface}$ at higher temperature. Although with increasing pressure, the difference of temperature polarisation coefficients between the experiments at different temperatures becomes smaller, the difference of $\Delta T_{interface}$ between the experiments at different temperatures is not changed greatly.

It also suggests that the process parameters will have less influence on the membrane flux as the membrane becomes more compact.

Two models based on heat and mass balances were programmed for the fourth objective.

Both simple and complex mathematical models were developed for the DCMD process. Both models showed agreement with experimental results, as errors of less than 14% were obtained, making them applicable in engineering design if the margin factor (10-25%) and experimental reproducibility ($\pm 5\%$) are considered.

The basis of the simple model is the experimental findings that the mean global heat and mass transfer coefficients only change slightly with variations of some parameters that will not affect the thermal boundary layer greatly, e.g. temperature variation (40-80°C) and length difference of membrane. If a database of global mass and heat transfer coefficients against the velocity is available under given boundary layer conditions, the simple model can be used to predict the flux at different temperatures and membrane lengths. However, the defined boundary layer conditions will also be affected greatly by the characteristics of the module flow channel structure, e.g. the presence of the turbulence promoter (spacer) or the dimension of the flow channel cross section, so the variations of these characteristics of the flow channel will cause invalidation of the existing database at the same stream velocity. Therefore, the model is strictly limited in the prediction of flux under similar boundary layer conditions to those that the global mass and heat transfer coefficients are acquired. Although the simple model is limited by the boundary layer conditions, the simple model provides a convenient means for pilot module design if the conditions of the flow channels are preset, because the database of the global mass and heat transfer coefficients against the velocity can be simply obtained from a small module with the same flow channel characteristics.

Therefore, this model does not require complex characterisation of the membrane and flow channel, which require special analytical facilities and time consuming calculations.

The complex mathematical model was developed based on the characterisations of the membrane and flow channel. For characterised membrane and flow channel, it can be used to predict flux at different velocities, membrane lengths, and different temperatures. Although this model is versatile in flux prediction under different boundary layer conditions, characterisations of the membrane and flow channel are required before predicting the flux of a pilot design. Compared to the simple model, this complex model has the advantage of being able to optimise module design and process parameters.

The predictions from both models showed

- The temperature profiles on both the hot and cold sides approach each other in co-current DCMD, but are parallel to each other in counter-current DCMD, when the flowrates on both sides are identical,
- The co-current DCMD showed a greater temperature difference than that of counter-current DCMD under identical inlet conditions, but the counter-current DCMD still produced higher flux than that of the co-current DCMD. The findings suggest that counter-current configurations should be adopted in commercial applications when longer membranes are considered, because of the dramatic decrease in flux in co-current DCMD when larger modules are used.
- MD flux is affected by the length of the membrane, and a short and wide membrane is suggested to be used for high flux applications rather than a long and narrow membrane design, and
- The modelling results showed that the feed velocity will have less influence on flux for longer membranes.

The employment of the complex model showed that:

- For spacer filled channels, the model had a better fit to the experimental results when the local Nusselt number was calculated from turbulent flow models rather than laminar flow models.
- Under the same hydraulic flows, higher feed temperature lead to lower

temperature polarisation coefficients because the greater heat flux leads to an increased rate of heat and mass flux through the membrane and hence, a greater temperature gradient in bulk flow.

- Stream velocity is a key factor in DCMD, especially at a higher temperatures (70-80°C), because of the lower temperature polarisation coefficient.
- A co-current model and a counter-current model were used to predict flux and temperature coefficients under different conditions. The counter-current model predicted a higher temperature polarisation coefficient than that of the co-current model under the same inlet conditions, which agrees with the experimental findings.
- Optimisation of the membrane structure (increases in ε/bt) is able to increase DCMD flux, but the increases in flux arising from further improvements in ε/bt is unlikely for long DCMD membrane (>0.7 m). Furthermore, the rate of increase of evaporation ratio is reduced greatly for $\varepsilon/bt > 24,000 \text{ m}^{-1}$.
- This work also identifies that characterisation of the mass transfer characteristics of MD membranes is best achieved by reporting ε/bt values, as this term relates to the fundamental characteristics of the membrane. This term can also be used to predict DCMD performance under a range of conditions, while mass transfer co-efficient is a function of pore pressure and feed stream hydraulic conditions, and flux is dependent on a range of process conditions, and
- The modelling results suggests high feed velocity and high feed inlet temperature will improve both flux and evaporation ratio.

The comprehensive findings and recommendations from this research are:

- Besides porosity, membrane thickness and hydrophobicity of the MD membrane, structured support layer and rigid active layer are also significant parameters when fabricating the membrane,
- As the temperature polarisation can cause dramatic flux decline, high velocity is important for DCMD processes, especially at high temperature where the polarisation is more pronounced. Therefore, if a compressible membrane is used for scale-up, it is better to design a module short in the stream flow direction but wide in the direction transverse to the stream flow, which will reduce membrane deformation and wetting risk at high stream velocity (high pressure expected),

- Placing the hot feed on the higher mass transfer resistance side (if existing) of the membrane and reducing pressure on the permeate side can produce more flux under the same operation conditions.
- Counter-current DCMD configuration has higher energy efficiency and flux under all modelling conditions in this study, so it is not recommended to use co-current configuration in DCMD design, and
- Based on this study of existing flat sheet membranes, adjusting process parameters seems to be more effective than improving the membrane properties.

Chapter 8 Future research directions

The research has focused on an experimental study of membrane performance in DCMD, and theoretical modelling of the DCMD process.

In the future work, the application of membrane distillation will be addressed based on its distinctive features. For example, it may be coupled with the power plant, cooling tower, etc., it also can be coupled with solar panels to produce freshwater from groundwater or water contaminated by non-volatile pollutants, such as heavy metal, fluoride, etc., or can be combined with reverse osmosis processes to improve the recovery of RO plants. All these possibilities need further research to prove the feasibility of MD for these applications.

Membrane distillation is an energy intensive process. Therefore, it is important to improve the energy efficiency or recovery. In my previous work, the single pass energy efficiency was considered, so the latent heat loss was not considered. Therefore, the recover of latent heat should be addressed in future work.

Although the PTFE membranes show excellent performance in DCMD, the compressibility of the active layer leads to some unpredictability of the flux, due to the unknown pressure drop in the module. The relationship between deformation of the membrane and applied pressure needs further researched based on the porosity, pore size, membrane thickness, and support layer in the future, particularly over longer time frames and higher temperatures.

Two mathematic models were designed, but they are still limited by some assumptions and conditions, such as neglecting the permeate flow. More work should be done to reduce these limitations, and make the model more accurate over a wider range of operating conditions.

The presented study has not considered the fouling and wetting issues that may arise over longer periods or from the treatment of water of different quality. Some fouling issues have been found in this study, which need to be examined in future work.

Effect of compression over longer periods of time, particularly at high temperatures where softening of the membrane materials will occur and where the strain may relax

leading to non-elastic deformation.

Nomenclature

a	exponent of r
A	membrane area
A_{cross}	cross sectional area of empty channel
A_{skin}	cumulative pore surface area in pore size ranges of the skin layer
$A_{\dot{m}}$	membrane area that the feed mass \dot{m} is contacted with
α_f, α_p	heat transfer coefficient on hot side and cold side
$\Delta\alpha_{conduction}$	change of the membrane heat conduction coefficient
B	geometric factor
b	membrane thickness
$C_{membrane}$	mass transfer coefficient
C_{global}	global mass transfer coefficient
C_f	feed bulk concentration
$C_{solution}$	concentration of NaCl
$C_{p,f}, C_{p,p}$	specific heat of feed and permeate
C_l	feed concentration at liquid-vapour interface
d_h	hydraulic diameter
ε	membrane porosity
$\varepsilon_{surface}$	surface porosity
ε_{spacer}	spacer porosity

F	surface tension
F_s	force from the membrane material
σ_w, σ_a	collision diameters for water vapour and air
h_{sp}	spacer's thickness
H	water protrusion height
H_{latent}	latent heat of water vaporisation
J	vapour flux
k_B	Boltzman constant
l	the mean free path of the transferred gas molecule
λ	thermal conductivity of membrane
λ_{air}	air thermal conductivity
λ_{solid}	solid thermal conductivity
\dot{m}_f, \dot{m}_p	mass flow rates of feed and permeate streams
m_{total}	mass of membrane with the support layer
$m_{support}$	mass of support layer
N	nominal pore number
N'	element number in modelling
σ	collision cross-section
P_{pore}	gas phase pressure in pores
$P_{process}$	pressure of the process liquid
P_{T1}, P_{T2}	vapour pressure at T1 and T2

P_{fi}, P_{fo}	vapour pressures at inlet and outlet temperatures of the hot side
P_{pi}, P_{po}	vapour pressures at inlet and outlet temperatures of cold side
ΔP_{gas}	pressure difference across the membrane
ρ	material density
Q_1, Q_2	total heat transfer
Q_f	feed mass flowrate
$\dot{Q}_{sensible}$	sensible heat loss
ϕ	angle between filaments
r_{max}	the largest pore size of membrane
d, r	pore diameter and radius of membrane
θ	contact angle between the solution and the membrane surface
t	pore tortuosity
τ	temperature polarisation coefficient
T_p, T_f	permeate and feed bulk temperatures
T_{fi}, T_{fo}	feed inlet and outlet temperatures
T_1, T_2	feed and permeate temperatures at liquid-vapour interface
U	global heat transfer coefficient
v	stream velocity
$V_{membrane}$	membrane volume
V_{PTFE}	active layer volume
$V_{support}$	support layer volume

V_{air}	air volume
\bar{v}	gas' mean molecular speed
γ_l	surface tension of the solution
γ_0	pure water surface tension at 25°C

Reference

- [1] P. K. Weyl, Recovery of demineralized water from saline waters, U. S. A, (1967).
- [2] M. E. Findley, Vaporization through Porous Membranes, *Ind. Eng. Chem. Proc. Des. Dev.* 6(1967) 226-230.
- [3] A. M. Alklaibi, N. Lior, Membrane-distillation desalination: Status and potential, *Desalination*. 171(2005) 111-131.
- [4] W. T. Hanbury, T. Hodgkiess, Membrane distillation - an assessment, *Desalination*. 56(1985) 287-297.
- [5] R. W. Schofield, A. G. Fane, C. J. D. Fell, Heat and mass transfer in membrane distillation, *Journal of Membrane Science*. 33(1987) 299-313.
- [6] L. Carlsson, The new generation in sea water desalination SU membrane distillation system, *Desalination*. 45(1983) 221-222.
- [7] S. I. Andersson, N. Kjellander, B. Rodesj, Design and field tests of a new membrane distillation desalination process, *Desalination*. 56(1985) 345-354.
- [8] T. J. v. G. Klaus Schneider, Membrandestillation, *Chemie Ingenieur Technik*. 56(1984) 514-521.
- [9] S. Al-Obaidani, E. Curcio, F. Macedonio, G. Di Profio, H. Al-Hinai, E. Drioli, Potential of membrane distillation in seawater desalination: Thermal efficiency, sensitivity study and cost estimation, *Journal of Membrane Science*. 323(2008) 85-98.
- [10] M. Tomaszewska, Membrane Distillation-Examples of Applications in Technology and Environmental Protection, *Environmental Studies*. 9(2000) 27-36.
- [11] K. Smolders, A. C. M. Franken, Terminology for Membrane Distillation, *Desalination*. 72(1989) 249-262.
- [12] J. Walton, H. Lu, C. Turner, S. Solis, H. Hein, Solar and waste heat desalination by membrane distillation College of Engineering University of Texas at El Paso, El Paso, 2004
- [13] F. Banat, N. Jwaied, M. Rommel, J. Koschikowski, M. Wiegand, Performance evaluation of the "large SMADES" autonomous desalination solar-driven membrane distillation plant in Aqaba, Jordan, *Desalination*. 217(2007) 17-28.
- [14] A. G. Fane, R. W. Schofield, C. J. D. Fell, The efficient use of energy in membrane distillation, *Desalination*. 64(1987) 231-243.
- [15] S. Kubota, K. Ohta, I. Hayano, M. Hirai, K. Kikuchi, Y. Murayama, Experiments on seawater desalination by membrane distillation, *Desalination*. 69(1988) 19-26.
- [16] J. H. Hanemaaijer, J. van Medevoort, A. E. Jansen, C. Dotremont, E. van Sonsbeek, T. Yuan, L. De Ryck, Memstill membrane distillation - a future desalination technology, *Desalination*. 199(2006) 175-176.
- [17] C. Fritzmann, J. Löwenberg, T. Wintgens, T. Melin, State-of-the-art of reverse osmosis desalination, *Desalination*. 216(2007) 1-76.
- [18] M. S. El-Bourawi, Z. Ding, R. Ma, M. Khayet, A framework for better understanding membrane distillation separation process, *Journal of Membrane Science*. 285(2006) 4-29.
- [19] Operation and Evaluation of Memstill Pilot Plant. 2008 [cited 2010 03/09].
- [20] M. Khayet, Membranes and theoretical modeling of membrane distillation: A review, *Advances in Colloid and Interface Science*. 164(2011) 56-88.
- [21] L. Martinez-Diez, F. J. Florido-Diaz, Theoretical and experimental studies on desalination using membrane distillation, *Desalination*. 139(2001) 373-379.
- [22] K. W. Lawson, D. R. Lloyd, Membrane distillation, *Journal of Membrane Science*. 124(1997) 1-25.
- [23] L. Martinez-Diez, F. J. Florido-Diaz, M. I. Vazquez-Gonzalez, Study of evaporation efficiency in membrane distillation, *Desalination*. 126(1999) 193-198.
- [24] J. Phattaranawik, R. Jiraratananon, Direct contact membrane distillation: effect of mass transfer on heat transfer, *Journal of Membrane Science*. 188(2001) 137-143.
- [25] V. Calabro, B. L. Jiao, E. Drioli, Theoretical and Experimental Study on Membrane Distillation in the Concentration of Orange Juice, *Industrial & Engineering Chemistry Research*. 33(1994) 1803-1808.
- [26] K. W. Lawson, D. R. Lloyd, Membrane distillation. I. Module design and performance evaluation using vacuum membrane distillation, *Journal of Membrane Science*. 120(1996) 111-121.
- [27] A. S. Jossen, R. Wimmerstedt, A. C. Harrysson, Membrane distillation - a theoretical study of evaporation through microporous membranes, *Desalination*. 56(1985) 237-249.
- [28] S. Bandini, C. Gostoli, G. C. Sarti, Separation efficiency in vacuum membrane distillation, *Journal of Membrane Science*. 73(1992) 217-229.
- [29] G. C. Sarti, C. Gostoli, S. Bandini, Extraction of organic components from aqueous streams by vacuum membrane distillation, *Journal of Membrane Science*. 80(1993) 21-33.

- [30] C. A. Rivier, M. C. Garcia-Payo, I. W. Marison, U. von Stockar, Separation of binary mixtures by thermostatic sweeping gas membrane distillation: I. Theory and simulations, *Journal of Membrane Science*. 201(2002) 1-16.
- [31] L. Basini, G. D'Angelo, M. Gobbi, G. C. Sarti, C. Gostoli, A desalination process through sweeping gas membrane distillation, *Desalination*. 64(1987) 245-257.
- [32] M. Khayet, P. Godino, J. I. Mengual, Theory and experiments on sweeping gas membrane distillation, *Journal of Membrane Science*. 165(2000) 261-272.
- [33] M. Khayet, P. Godino, J. I. Mengual, Nature of flow on sweeping gas membrane distillation, *Journal of Membrane Science*. 170(2000) 243-255.
- [34] M. C. Garcia-Payo, C. A. Rivier, I. W. Marison, U. von Stockar, Separation of binary mixtures by thermostatic sweeping gas membrane distillation: II. Experimental results with aqueous formic acid solutions, *Journal of Membrane Science*. 198(2002) 197-210.
- [35] Z. Lei, B. Chen, Z. Ding, Membrane distillation, in: Z. Lei, B. Chen, Z. Ding (Z. Lei, B. Chen, Z. Dings), *Special Distillation Processes*, Elsevier Science, Amsterdam, 2005, pp. 241-319.
- [36] M. N. Chernyshov, G. W. Meindersma, A. B. de Haan, Comparison of spacers for temperature polarization reduction in air gap membrane distillation, *Desalination*. 183(2005) 363-374.
- [37] G. W. Meindersma, C. M. Guijt, A. B. de Haan, Desalination and water recycling by air gap membrane distillation, *Desalination*. 187(2006) 291-301.
- [38] M. C. García-Payo, M. A. Izquierdo-Gil, C. Fernández-Pineda, Air gap membrane distillation of aqueous alcohol solutions, *Journal of Membrane Science*. 169(2000) 61-80.
- [39] R. Chouikh, S. Bouguecha, M. Dhahbi, Modelling of a modified air gap distillation membrane for the desalination of seawater, *Desalination*. 181(2005) 257-265.
- [40] G. L. Liu, C. Zhu, C. S. Cheung, C. W. Leung, Theoretical and experimental studies on air gap membrane distillation, *Heat and Mass Transfer*. 34(1998) 329-335.
- [41] E. Curcio, E. Drioli, *Membrane Distillation and Related Operations: A Review*, Separation and Purification Reviews. 34(2005) 35 - 86.
- [42] E. Drioli, V. Calabrd, Y. Wu, Microporous membranes in membrane distillation, *Pure & Appl. Chem*. 58(1986) 6.
- [43] M. Khayet, T. Matsuura, J. I. Mengual, M. Qtaishat, Design of novel direct contact membrane distillation membranes, *Desalination*. 192(2006) 105-111.
- [44] A. Criscuoli, M. C. Carnevale, E. Drioli, Evaluation of energy requirements in membrane distillation, *Chemical Engineering and Processing: Process Intensification*. 47(2008) 1098-1105.
- [45] L. Peña, M. Paz Godino, J. I. Mengual, A method to evaluate the net membrane distillation coefficient, *Journal of Membrane Science*. 143(1998) 219-233.
- [46] M. Khayet, T. Matsuura, Application of surface modifying macromolecules for the preparation of membranes for membrane distillation, *Desalination*. 158(2003) 51-56.
- [47] B. Jiao, A. Cassano, E. Drioli, Recent advances on membrane processes for the concentration of fruit juices: a review, *Journal of Food Engineering*. 63(2004) 303-324.
- [48] J. Zhang, N. Dow, M. Duke, E. Ostarcevic, J.-D. Li, S. Gray, Identification of material and physical features of membrane distillation membranes for high performance desalination, *Journal of Membrane Science*. 349(2010) 295-303.
- [49] L. F. Dumée, K. Sears, J. Schütz, N. Finn, C. Huynh, S. Hawkins, M. Duke, S. Gray, Characterization and evaluation of carbon nanotube Bucky-Paper membranes for direct contact membrane distillation, *Journal of Membrane Science*. 351(2010) 36-43.
- [50] J. Zhang, J.-D. Li, M. Duke, Z. Xie, S. Gray, Performance of asymmetric hollow fibre membranes in membrane distillation under various configurations and vacuum enhancement, *Journal of Membrane Science*. 362(2010) 517-528.
- [51] M. Mulder, *Basic Principles of Membrane Technology*. 2nd edn ed., Kluwer, Dordrecht, 1996.
- [52] D. R. Lloyd, K. E. Kinzer, H. S. Tseng, Microporous membrane formation via thermally induced phase separation. I. Solid-liquid phase separation, *Journal of Membrane Science*. 52(1990) 239-261.
- [53] M. Tomaszewska, Preparation and properties of flat-sheet membranes from poly(vinylidene fluoride) for membrane distillation, *Desalination*. 104(1996) 1-11.
- [54] J. Huang, Y.-C. Wang, C.-L. Li, K.-R. Lee, S.-C. Fan, T.-T. Wu, J.-Y. Lai, Dehydration of water-alcohol mixtures by pervaporation and vapor permeation through surface resintering expanded poly(tetrafluoroethylene) membranes, *European Polymer Journal*. 38(2002) 179-186.
- [55] N. A. Zubir, A. F. Ismail, Effect of sintering temperature on the morphology and mechanical properties of PTFE membranes as a base substrate for proton exchange membrane, *Songklanakarinn Journal of Science and Technology*. 24(2002) 823-831.
- [56] J. Huang, J. Zhang, X. Hao, Y. Guo, Study of a new novel process for preparing and co-stretching PTFE membrane and its properties, *European Polymer Journal*. 40(2004) 667-671.

- [57] H. Strathmann, K. Kock, P. Amar, R. W. Baker, The formation mechanism of asymmetric membranes, *Desalination*. 16(1975) 179-203.
- [58] M. Khayet, T. Matsuura, Preparation and Characterization of Polyvinylidene Fluoride Membranes for Membrane Distillation, *Industrial & Engineering Chemistry Research*. 40(2001) 5710-5718.
- [59] M. M. Teoh, T.-S. Chung, Membrane distillation with hydrophobic macrovoid-free PVDF-PTFE hollow fiber membranes, *Separation and Purification Technology*. 66(2009) 229-236.
- [60] N. N. Li, G. A. Fane, W. S. W. Ho, T. Matsuura, eds. *Advanced Membrane Technology and Applications*. John Wiley & Sons, Inc.: Hoboken, New Jersey.
- [61] L. Song, B. Li, K. K. Sirkar, J. L. Gilron, Direct Contact Membrane Distillation-Based Desalination: Novel Membranes, Devices, Larger-Scale Studies, and a Model, *Ind. Eng. Chem. Res.* 46(2007) 2307-2323.
- [62] M. Gryta, M. Tomaszewska, A. W. Morawski, A Capillary Module for Membrane Distillation Process, *Chemical Papers*. 54(2000) 370-374
- [63] S. Bonyadi, T. S. Chung, Flux enhancement in membrane distillation by fabrication of dual layer hydrophilic-hydrophobic hollow fiber membranes, *Journal of Membrane Science*. 306(2007) 134-146.
- [64] L.-H. Cheng, P.-C. Wu, J. Chen, Modeling and optimization of hollow fiber DCMD module for desalination, *Journal of Membrane Science*. 318(2008) 154-166.
- [65] S. Bonyadi, T.-S. Chung, Highly porous and macrovoid-free PVDF hollow fiber membranes for membrane distillation by a solvent-dope solution co-extrusion approach, *Journal of Membrane Science*. 331(2009) 66-74.
- [66] S. Bonyadi, T. S. Chung, R. Rajagopalan, A novel approach to fabricate macrovoid-free and highly permeable PVDF hollow fiber membranes for membrane distillation, *AIChE Journal*. 55(2009) 828-833.
- [67] J. Zhang, J.-D. Li, M. Duke, Z. Xie, S. Gray, Performance of asymmetric hollow fibre membranes in membrane distillation under various configurations and vacuum enhancement, *Journal of Membrane Science*. In Press, Accepted Manuscript(2010).
- [68] M. Gryta, Long-term performance of membrane distillation process, *Journal of Membrane Science*. 265(2005) 153-159.
- [69] S. I. Andersson, N. Kjellander, B. Rodesjö, Design and field tests of a new membrane distillation desalination process, *Desalination*. 56(1985) 345-354.
- [70] K. Schneider, W. Hölz, R. Wollbeck, S. Ripperger, Membranes and modules for transmembrane distillation, *Journal of Membrane Science*. 39(1988) 25-42.
- [71] H. Guo, Y. Wyart, J. Perot, F. Nauleau, P. Moulin, Low-pressure membrane integrity tests for drinking water treatment: A review, *Water Research*. 44(2010) 41-57.
- [72] W. T. Johnson, Predicting log removal performance of membrane systems using in-situ integrity testing, *Filtration & Separation*. 35(26-29).
- [73] M. Qtaishat, T. Matsuura, B. Kruczek, M. Khayet, Heat and mass transfer analysis in direct contact membrane distillation, *Desalination*. 219(2008) 272-292.
- [74] J. Phattaranawik, R. Jiraratananon, A. G. Fane, Heat transport and membrane distillation coefficients in direct contact membrane distillation, *Journal of Membrane Science*. 212(2003) 177-193.
- [75] R. W. Schofield, A. G. Fane, C. J. D. Fell, Gas and vapour transport through microporous membranes. II. Membrane distillation, *Journal of Membrane Science*. 53(1990) 173-185.
- [76] M. Gryta, M. Tomaszewska, Heat transport in the membrane distillation process, *Journal of Membrane Science*. 144(1998) 211-222.
- [77] J. Phattaranawik, R. Jiraratananon, A. G. Fane, C. Halim, Mass flux enhancement using spacer filled channels in direct contact membrane distillation, *Journal of Membrane Science*. 187(2001) 193-201.
- [78] L. Martinez-Diez, M. I. Vazquez-Gonzalez, F. J. Florido-Diaz, Study of membrane distillation using channel spacers, *Journal of Membrane Science*. 144(1998) 45-56.
- [79] Y. Yao, ed. *Principle of Chemical Engineering*. 1st ed. 1992, Tianjin Science Technology Press: Tianjin. 225.
- [80] A. R. Da Costa, A. G. Fane, D. E. Wiley, Spacer characterization and pressure drop modelling in spacer-filled channels for ultrafiltration, *Journal of Membrane Science*. 87(1994) 79-98.
- [81] J. Schwinge, D. E. Wiley, A. G. Fane, R. Guenther, Characterization of a zigzag spacer for ultrafiltration, *Journal of Membrane Science*. 172(2000) 19-31.
- [82] J. Phattaranawik, R. Jiraratananon, A. G. Fane, Effects of net-type spacers on heat and mass transfer in direct contact membrane distillation and comparison with ultrafiltration studies, *Journal of Membrane Science*. 217(2003) 193-206.
- [83] A. R. Da Costa, A. G. Fane, C. J. D. Fell, A. C. M. Franken, Optimal channel spacer design for ultrafiltration, *Journal of Membrane Science*. 62(1991) 275-291.
- [84] G. Schock, A. Miquel, Mass transfer and pressure loss in spiral wound modules, *Desalination*. 64(1987) 339-352.

- [85] Z. Ding, R. Ma, A. G. Fane, A new model for mass transfer in direct contact membrane distillation, *Desalination*. 151(2003) 217-227.
- [86] W. Kast, C. R. Hohenthanner, Mass transfer within the gas-phase of porous media, *International Journal of Heat and Mass Transfer*. 43(2000) 807-823.
- [87] H. Kuhn, H.-D. Forstering, *Principles of Physical Chemistry*, Wiley, New York, 2000.
- [88] R. A. Albert, R. J. Silbey, *Physical Chemistry*. 2nd ed., Wiley, New York.
- [89] E. L. Cussler, *Diffusion: Mass Transfer in Fluid System*. 2nd ed., Cambridge University Press, New York, 1997.
- [90] J. Phattaranawik, R. Jiraratananon, A. G. Fane, Effect of pore size distribution and air flux on mass transport in direct contact membrane distillation, *Journal of Membrane Science*. 215(2003) 75-85.
- [91] R. W. Schofield, A. G. Fane, C. J. D. Fell, Gas and vapour transport through microporous membranes. I. Knudsen-Poiseuille transition, *Journal of Membrane Science*. 53(1990) 159-171.
- [92] E. A. Mason, A. P. Malinauskas, *Gas transport in porous media : the dusty-gas model* Elsevier Scientific Pub. Co, Amsterdam ; New York :, 1983.
- [93] C. Fernandez-Pineda, M. A. Izquierdo-Gil, M. C. Garcia-Payo, Gas permeation and direct contact membrane distillation experiments and their analysis using different models, *Journal of Membrane Science*. 198(2002) 33-49.
- [94] K. Schneider, T. J. van Gassel, Membrandestillation, *Chemie Ingenieur Technik*. 56(1984) 514-521.
- [95] A. F. Mills, *Mass Transfer*, Upper Saddle River, EUA : Prentice-Hall, 2001.
- [96] E. A. Mason, A. P. Malinauskas, R. B. Evans, *Flow and Diffusion of Gases in Porous Media*, *The Journal of Chemical Physics*. 46(1967) 3199-3216.
- [97] N. Dow, J. Zhang, M. Duke, J. Li, S. R. Gray, E. Ostarcevic, *Membrane Distillation of Brine Wastes*, CRC for Water Quality and Treatment 2008
- [98] F. Suárez, S. W. Tyler, A. E. Childress, A theoretical study of a direct contact membrane distillation system coupled to a salt-gradient solar pond for terminal lakes reclamation, *Water Research*. 44(2010) 4601-4615.
- [99] N. Dow, M. Duke, J. Zhang, T. O'Rielly, J.-D. Li, S. Gray, E. Ostarcevic, P. Atherton. Demonstration of solar driven membrane distillation in remote Victoria. in *AWA Ozwater10*. 2010. Brisbane, Queensland, Australia.
- [100] D. W. Gore. Gore-Tex Membrane Distillation. in *Proc. 10th Ann. Con. Water*. 1982. Honolulu, Hawaii.
- [101] N. Kjellander, Design and field tests of a membrane distillation system for seawater desalination, *Desalination*. 61(1987) 237-243.
- [102] M. P. Godino, L. Peña, C. Rincón, J. I. Mengual, Water production from brines by membrane distillation, *Desalination*. 108(1997) 91-97.
- [103] F. A. Banat, J. Simandl, Desalination by Membrane Distillation: A Parametric Study, *Separation Science and Technology*. 33(1998) 201-226.
- [104] F. Macedonio, E. Curcio, E. Drioli, Integrated membrane systems for seawater desalination: energetic and exergetic analysis, economic evaluation, experimental study, *Desalination*. 203(2007) 260-276.
- [105] A. G. Fane, W. University of New South, R. Energy, C. Development, *Solar heated membrane distillation* Energy Research and Development Corporation, Canberra 1992.
- [106] F. Banat, R. Jumah, M. Garaibeh, Exploitation of solar energy collected by solar stills for desalination by membrane distillation, *Renewable Energy*. 25(2002) 293-305.
- [107] E. Drioli, F. Laganà, A. Criscuoli, G. Barbieri, Integrated membrane operations in desalination processes, *Desalination*. 122(1999) 141-145.
- [108] P. P. Zolotarev, V. V. Ugrozov, I. B. Volkina, V. M. Nikulin, Treatment of waste water for removing heavy metals by membrane distillation, *Journal of Hazardous Materials*. 37(1994) 77-82.
- [109] M. Tomaszewska, M. Gryta, A. W. Morawski, Recovery of hydrochloric acid from metal pickling solutions by membrane distillation, *Separation and Purification Technology*. 22-23(2001) 591-600.
- [110] M. Tomaszewska, Concentration of the extraction fluid from sulfuric acid treatment of phosphogypsum by membrane distillation, *Journal of Membrane Science*. 78(1993) 277-282.
- [111] G. Zakrzewska-Trznadel, M. Harasimowicz, A. G. Chmielewski, Concentration of radioactive components in liquid low-level radioactive waste by membrane distillation, *Journal of Membrane Science*. 163(1999) 257-264.
- [112] F. A. Banat, J. Simandl, Removal of benzene traces from contaminated water by vacuum membrane distillation, *Chemical Engineering Science*. 51(1996) 1257-1265.
- [113] M. J. Semmens, R. Qin, A. Zander, Using a Microporous Hollow-Fiber Membrane to Separate VOCs From Water, *Journal AWWA*. 81(1989) 162-167.

- [114] F. Lagana, G. Barbieri, E. Drioli, Direct contact membrane distillation: modelling and concentration experiments, *Journal of Membrane Science*. 166(2000) 1-11.
- [115] S. Nene, S. Kaur, K. Sumod, B. Joshi, K. S. M. S. Raghavarao, Membrane distillation for the concentration of raw cane-sugar syrup and membrane clarified sugarcane juice, *Desalination*. 147(2002) 157-160.
- [116] K. Sakai, T. Koyano, T. Muroi, M. Tamura, Effects of temperature and concentration polarization on water vapour permeability for blood in membrane distillation, *The Chemical Engineering Journal*. 38(1988) B33-B39.
- [117] K. SAKAI, T. MUROI, K. OZAWA, S. TAKESAWA, M. TAMURA, T. NAKANE, Extraction of Solute-Free Water from Blood by Membrane Distillation, *ASAIO Journal*. 32(1986) 397-400.
- [118] A. Capuano, B. Memoli, V. E. Andreucci, A. Criscuoli, E. Drioli, Membrane distillation of human plasma ultrafiltrate and its theoretical applications to haemodialysis techniques, *Int. J. Artif. Organs*. 23(2000) 415-422.
- [119] M. Gryta, A. W. Morawski, M. Tomaszewska, Ethanol production in membrane distillation bioreactor, *Catalysis Today*. 56(2000) 159-165.
- [120] M. Khayet, J. I. Mengual, T. Matsuura, Porous hydrophobic/hydrophilic composite membranes: Application in desalination using direct contact membrane distillation, *Journal of Membrane Science*. 252(2005) 101-113.
- [121] M. Khayet, T. Matsuura, J. I. Mengual, Porous hydrophobic/hydrophilic composite membranes: Estimation of the hydrophobic-layer thickness, *Journal of Membrane Science*. 266(2005) 68-79.
- [122] B. Li, K. K. Sirkar, Novel membrane and device for vacuum membrane distillation-based desalination process, *Journal of Membrane Science*. 257(2005) 60-75.
- [123] M. Gryta, M. Tomaszewska, A. W. Morawski, Membrane distillation with laminar flow, *Separation and Purification Technology*. 11(1997) 93-101.
- [124] N. Sghaier, M. Prat, S. Ben Nasrallah, On the influence of sodium chloride concentration on equilibrium contact angle, *Chemical Engineering Journal*. 122(2006) 47-53.
- [125] R. Tuckermann, Surface tension of aqueous solutions of water-soluble organic and inorganic compounds, *Atmospheric Environment*. 41(2007) 6265-6275.
- [126] S. Srisurichan, R. Jiratananon, A. G. Fane, Mass transfer mechanisms and transport resistances in direct contact membrane distillation process, *Journal of Membrane Science*. 277(2006) 186-194.
- [127] R. Mishra, S. P. Tripathy, D. Sinha, K. K. Dwivedi, S. Ghosh, D. T. Khathing, M. Muller, D. Fink, W. H. Chung, Optical and electrical properties of some electron and proton irradiated polymers, *Nuclear Instruments and Methods in Physics Research Section B: Beam Interactions with Materials and Atoms*. 168(2000) 59-64.
- [128] Y. Luo, Y. Liu, Q. Yu, Influence of glow discharge plasma treatment on vapor-induced response of poly(vinylidene fluoride)-carbon black composite thin films, *Thin Solid Films*. 515(2007) 4016-4023.
- [129] E. Quartarone, A. Carollo, C. Tomasi, F. Belotti, S. Grandi, P. Mustarelli, A. Magistris, Relationships between microstructure and transport properties of proton-conducting porous PVDF membranes, *Journal of Power Sources*. 168(2007) 126-134.
- [130] C.-C. Ho, A. L. Zydney, Measurement of membrane pore interconnectivity, *Journal of Membrane Science*. 170(2000) 101-112.
- [131] M. Matheswaran, T. O. Kwon, J. W. Kim, I. Moon, Factors Affecting Flux and Water Separation Performance in Air Gap Membrane Distillation, *Journal of Industrial and Engineering Chemistry*. 13(2007) 965-970.
- [132] J. Zhang, S. Gray, J.-D. Li, Modelling heat and mass transfer in membrane distillation process, *Chemical Engineering Journal*. 2010) (submitted).
- [133] M. N. Chernyshov, G. W. Meindersma, A. B. de Haan, Modelling temperature and salt concentration distribution in membrane distillation feed channel, *Desalination*. 157(2003) 315-324.
- [134] F. W. Sears, M. W. Zemanski, *University Physics*. 2nd ed., Addison Wesle, 1955.
- [135] G. K. Batchelor, *An introduction in fluid dynamics*. First ed., Cambridge University Press, London, 1970.
- [136] L. Ghasemi-Mobarakeh, D. Semnani, M. Morshed, A novel method for porosity measurement of various surface layers of nanofibers mat using image analysis for tissue engineering applications, *Journal of Applied Polymer Science*. 106(2007) 2536-2542.
- [137] A. Manuel Stephan, D. Teeters, Characterization of PVdF-HFP polymer membranes prepared by phase inversion techniques I. Morphology and charge-discharge studies, *Electrochimica Acta*. 48(2003) 2143-2148.
- [138] T. A. Sergeeva, S. A. Piletsky, E. V. Piletska, O. O. Brovko, L. V. Karabanova, L. M. Sergeeva, A. V. El'skaya, A. P. F. Turner, In Situ Formation of Porous Molecularly Imprinted Polymer Membranes, *Macromolecules*. 36(2003) 7352-7357.

- [139] M. S. Kim, S. J. Lee, J. U. Kang, K. J. Bae, Preparations of Polypropylene Membrane with High Porosity in Supercritical CO₂ and Its Application for PEMFC, *Journal of Industrial and Engineering Chemistry*. 11(2005) 187-193.
- [140] N. Diban, O. C. Voinea, A. Urteaga, I. Ortiz, Vacuum membrane distillation of the main pear aroma compound: Experimental study and mass transfer modeling, *Journal of Membrane Science*. 326(2009) 64-75.
- [141] Z. Wang, Z. Gu, S. Feng, Y. Li, Applications of membrane distillation technology in energy transformation process-basis and prospect, *Chinese Science Bulletin*. 54(2009) 2766-2780.
- [142] L. Martinez-Diez, M. I. Vazquez-Gonzalez, Temperature and concentration polarization in membrane distillation of aqueous salt solutions, *Journal of Membrane Science*. 156(1999) 265-273.
- [143] H. Schlichting, K. Gersten, *Boundary-layer theory* 8th ed., Springer, Berlin ; London, 2000.
- [144] T. Y. Cath, V. D. Adams, A. E. Childress, Experimental study of desalination using direct contact membrane distillation: a new approach to flux enhancement, *Journal of Membrane Science*. 228(2004) 5-16.
- [145] T. Ahmed, M. J. Semmens, M. A. Voss, Oxygen transfer characteristics of hollow-fiber, composite membranes, *Advances in Environmental Research*. 8(2004) 637-646.
- [146] R. C. Reid, J. M. Prausnitz, B. E. Poling, *The properties of gases and liquids*, 1987.
- [147] E. Clapeyron, Mémoire sur la puissance motrice de la chaleur, *Journal de l'École Polytechnique*. XIV(1834) 153-190.
- [148] K. W. Lawson, M. S. Hall, D. R. Lloyd, Compaction of microporous membranes used in membrane distillation. I. Effect on gas permeability, *Journal of Membrane Science*. 101(1995) 99-108.
- [149] S. P. Agashichev, D. V. Falalejev, Modeling temperature polarization phenomena for longitudinal shell-side flow in membrane distillation process, *Desalination*. 108(1997) 99-103.
- [150] R. G. Lunnon, The Latent Heat of Evaporation of Aqueous Salt Solutions, *Proceedings of the Physical Society of London*. 25(1912) 180.
- [151] A. O. IMDAKM, T. MATSUURA, A Monte Carlo simulation model for membrane distillation processes: direct contact (MD), Elsevier, Amsterdam, PAYS-BAS, 2004.
- [152] C. J. Geankoplis, *Transport processes and separation process principles* 4th ed., Prentice Hall Press, Saddle River, 2003.
- [153] G. Towler, R. K. Sinnott, *Chemical engineering design : principles, practice and economics of plant and process design*, Elsevier/Butterworth-Heinemann, Burlington, 2007.
- [154] M. S. Ray, D. W. Johnston, *Chemical engineering design project : a case study approach*, Gordon and Breach, New York 1989.
- [155] T. E. Marlin. Teaching "Operability" in Undergraduate Chemical Engineering Design Education. in ASEE Conference. 2007. Honolulu.

Appendix

I. Simple modelling programs

a. Co-current modelling programme

```
Sub cocurrent()
```

```
Dim increment, interval, full_length, Flux, L As Double
```

```
Dim FLT(1 To 10, 1 To 4) As Double
```

```
Dim K As Integer
```

```
Range("D2").Select  
interval = ActiveCell.Value
```

```
Range("C2").Select  
full_length = ActiveCell.Value
```

```
Worksheets(1).Range("B6:C6").Value = Worksheets(1).Range("A2:B2").Value
```

```
K = 0
```

```
Flux = 0
```

```
Do While K < 10
```

```
'output ten points for plotting
```

```
Range("C3").Select  
L = ActiveCell.Value
```

```
K = K + 1
```

```
L = L * K
```

```
increment = interval
```

```
'calculate temperature at along the length
```

```
Do While increment < full_length / 10
```

```
increment = increment + interval
```

```
Worksheets(1).Range("B6:E6").Value = Worksheets(1).Range("B7:E7").Value
```

```
Range("F7").Select  
Flux = ActiveCell.Value + Flux
```

```
Loop
```

```
FLT(K, 1) = Flux
```

```
FLT(K, 2) = L
```

```
FLT(K, 3) = Worksheets(1).Range("B7").Value
```

```
FLT(K, 4) = Worksheets(1).Range("C7").Value
```

```
increment = 0
```

```
Loop
```

```

Range("F8").Select
ActiveCell = Flux

Worksheets(1).Range("E2:F2").Value = Worksheets(1).Range("B7:C7").Value

Worksheets(1).Range("A10:D10").Value = Array("Permeate", "Length", "Hot Temperature", "Cold
Temperature")

Worksheets(1).Range("A11:D20").Value = FLT

End Sub

```

b. Counter-current modelling programe

```

Sub countercurrent()

Dim increment, interval, full_length, Tci, Tco, Dif, Step_length, Ti_cal, Flux, L, Delta_T, Hv, Width,
Mass_co, Heat_co, P_cold, P_hot, Flow_hot, Flow_cold, T_cold As Double
Dim FLT(1 To 11, 1 To 4) As Double
Dim K, counter As Integer

Range("D2").Select
interval = ActiveCell.Value

increment = 0

counter = 0

Range("I2").Select
Hv = ActiveCell.Value

Range("C2").Select
full_length = ActiveCell.Value

Range("F2").Select
Tci = ActiveCell.Value

Range("P2").Select
Width = ActiveCell.Value

Range("K2").Select
Heat_co = ActiveCell.Value

Range("O2").Select
Mass_co = ActiveCell.Value

Range("C3").Select
Loutput = ActiveCell.Value

Range("G2").Select
Flow_hot = ActiveCell.Value

Range("H2").Select
Flow_cold = ActiveCell.Value

Range("A4").Select

```

```

Step_length = ActiveCell.Value

Range("A2").Select
Ti_cal = ActiveCell.Value

Dif = Ti_cal - Tci

Tco = Ti_cal - 1

Flux = 0

K = 0

'loop to get cold out temperature

'MsgBox (increment)

Do While Dif >= 0

Tco = Tco - Step_length

T_cold = Tco

Range("A2").Select
Ti_cal = ActiveCell.Value

    Do While increment < full_length
'counter = counter + 1
    P_cold = Exp(23.1964 - 3816.44 / (T_cold + 227.02))
    P_hot = Exp(23.1964 - 3816.44 / (Ti_cal + 227.02))

    Delta_T = -interval * Width * (Hv * 1000 * Mass_co * (P_hot - P_cold) + Heat_co * (Ti_cal - T_cold))
/ 4.2 / (Flow_hot / 60)

    Ti_cal = Ti_cal + Delta_T

    T_cold = T_cold + Delta_T / (Flow_cold / Flow_hot)

    increment = increment + interval

    Loop
'MsgBox (counter)

increment = 0

Dif = T_cold - Tci

'MsgBox ("Dif=" & Dif)

Loop

Worksheets(2).Range("B2").Value = Tco

Worksheets(2).Range("E2") = Ti_cal
'loop to get ten values for plotting

T_cold = Tco

L = 0
'MsgBox (T_cold)

```

```
Range("A2").Select
Ti_cal = ActiveCell.Value
```

```
Do While K < 11
```

```
    increment = interval
```

```
    K = K + 1
```

```
    FLT(K, 1) = Flux
```

```
    FLT(K, 2) = L
```

```
    FLT(K, 3) = Ti_cal
```

```
    FLT(K, 4) = T_cold
```

```
    Do While increment < full_length / 10
```

```
        P_cold = Exp(23.1964 - 3816.44 / (T_cold + 227.02))
```

```
        P_hot = Exp(23.1964 - 3816.44 / (Ti_cal + 227.02))
```

```
        Delta_T = -interval * Width * (Hv * 1000 * Mass_co * (P_hot - P_cold) + Heat_co * (Ti_cal - T_cold)) / 4.2 / (Flow_hot / 60)
```

```
        Flux = Mass_co * (P_hot - P_cold) * Width * interval + Flux
```

```
        Ti_cal = Ti_cal + Delta_T
```

```
        T_cold = T_cold + Delta_T / (Flow_cold / Flow_hot)
```

```
        increment = increment + interval
```

```
    Loop
```

```
    L = L + full_length / 10
```

```
    MsgBox (increment)
```

```
    MsgBox (L)
```

```
Loop
```

```
Worksheets(2).Range("A5:D5").Value = Array("Permeate", "Length", "Hot Temperature", "Cold Temperature")
```

```
Worksheets(2).Range("A6:D16").Value = FLT
```

```
End Sub
```

II Complex modelling programs

a. Co-current modelling program

Sub cocurrent()

Dim k_m, K, W, D, delta, Ru, M_H2O, epsilon, dm, m, tau, Patm, L1, epsilon_s, A, df, Error, tht, tct, alpha_s, m1, Pmem, Ppore, mass_coeff, rho_h, Ph_sat, Pc_sat, Tmeant, theta, dh, L, hsp, mh, Vh, Vc, beta, h_fg0, Lmem, lm, conductivity, Qh, Qc, x1, dx, th, tc, tfw, tpw, m_total, flux, N1, U As Double

Dim N, I, B, J, Nline As Integer

Dim FLT(1 To 10000, 1 To 6) As Double

Dim x(1 To 10000), thw(1 To 10000), tcw(1 To 10000), tf(1 To 10000), tp(1 To 10000), F(1 To 10001) As Double

Lmem = Worksheets(1).Range("D2").Value

L = Worksheets(1).Range("C2").Value

L1 = (L - Lmem) / 2

W = Worksheets(1).Range("E2").Value

N = Worksheets(1).Range("A4").Value

Pmem = Worksheets(1).Range("H2").Value

Qh = Worksheets(1).Range("F2").Value

Qc = Worksheets(1).Range("G2").Value

mh = Qh / (1000# * 60)

mc = Qc / (1000# * 60)

'Pressure in pore

Ppore = Worksheets(1).Range("D4").Value

'membrane thickness

delta = 0.0001

'membrane pore size

dm = 0.000000456

'membrane conductivity

k_m = Worksheets(1).Range("A6").Value

'conductivity of membrane + plastic sheets (two layers)

conductivity = 309#

'parameter of spacer

df = 0.0004

hsp = 0.0008

theta = 3.1415 / 2

lm = 0.003

epsilon_s = 0.86

'channel depth

D = 0.0008

'inlet temperature

Th_in = Worksheets(1).Range("A2").Value

Tc_in = Worksheets(1).Range("B2").Value

'mass flowrate

'Molar mass

M_H2O = 18

Rv = 0.462

Ru = 8134#

'parameter of spacer filament

Svsp = 4# / df

dh = 4# * epsilon_s / (2 / hsp + (1 - epsilon_s) * Svsp)

'Define increment

$$dx = L / (N - 1)$$

$$x1 = 0\#$$

$$N1 = (L - 2 * L1) * N / L$$

$$Patm = 104325 \text{ 'in Pa}$$

$$\text{Worksheets(1).Range("A10:B10").Value} = \text{Worksheets(1).Range("A2:B2").Value}$$

$$th_i = \text{Worksheets(1).Range("A2").Value}$$

$$tc_i = \text{Worksheets(1).Range("B2").Value}$$

$$th = th_i$$

$$tc = tc_i$$

$$B = 1$$

$$\text{beta} = 1\#$$

$$m_total = 0\#$$

$$x(1) = 0$$

$$tf(1) = th_i$$

$$tp(1) = tc_i$$

$$Tmean = (tc + th) / 2$$

'feed properties

$$\rho_h = 1002.6 - 0.2177 * th - 0.0020099 * th^2 + 0.0000011897 * th^3$$

$$\text{vis}_h = \text{Exp}(-6.3933 - 0.026299 * th + 0.000097341 * th^2 - 0.00000013986 * th^3)$$

$$\text{cp}_h = 1000 * \text{Exp}(1.4423 - 0.00084025 * th + 0.0000141 * th^2 - 0.000000073846 * th^3 + 0.00000000014856 * th^4)$$

$$k_h = 0.56611 + 0.002048 * th - 0.000010205 * th^2 + 0.000000011897 * th^3$$

'permeate properties

$$\rho_c = 1002.6 - 0.2177 * tc - 0.0020099 * tc^2 + 0.0000011897 * tc^3$$

$$\text{vis}_c = \text{Exp}(-6.3933 - 0.026299 * tc + 0.000097341 * tc^2 - 0.00000013986 * tc^3)$$

$$\text{cp}_c = 1000 * \text{Exp}(1.4423 - 0.00084025 * tc + 0.0000141 * tc^2 - 0.000000073846 * tc^3 + 0.00000000014856 * tc^4)$$

$$k_c = 0.56611 + 0.002048 * tc - 0.000010205 * tc^2 + 0.000000011897 * tc^3$$

'velocities of hot and cold water;

$$Vh = mh / (\rho_h * W * D * \text{epsilon}_s)$$

$$Vc = \text{Abs}(mc) / (\rho_c * W * D * \text{epsilon}_s)$$

If $x1 < L1$ Then

$$Re_h = Qh / (60 * 0.13 * 0.0012) * (x1 + dx) * \rho_h / \text{vis}_h$$

$$Pr_h = \text{cp}_h * \text{vis}_h / k_h$$

$$Re_c = Qc / (60 * 0.13 * 0.0012) * (x1 + dx) * \rho_c / \text{vis}_c$$

$$Pr_c = \text{cp}_h * \text{vis}_c / k_c$$

$$Nu_h = 0.332 * Re_h^{0.5} * Pr_h^{0.33}$$

$$Nu_c = 0.332 * Re_c^{0.5} * Pr_c^{0.33}$$

$$h_h = \text{beta} * Nu_h * k_h / (x1 + dx)$$

$$h_c = \text{beta} * Nu_c * k_c / (x1 + dx)$$

$$U = 1\# / (1 / h_h + 1 / \text{conductivity} + 1 / h_c)$$

$$dQdx = U * (th - tc)$$

$$tfw = th - dQdx / h_h$$

$$tpw = tc + dQdx / h_c$$

$$m = 0\#$$

ElseIf $L1 \leq x1$ And $x1 \leq L - L1$ Then

$$Re_h = Vh * dh * \rho_h / \text{vis}_h$$

$$Pr_h = \text{cp}_h * \text{vis}_h / k_h$$

$$Re_c = Vc * dh * \rho_c / \text{vis}_c$$

$$Pr_c = \text{cp}_c * \text{vis}_c / k_c$$

```

alpha_s = 1.904 * (df / D) ^ (-0.039) * epsilon_s ^ 0.75 * (Sin(theta / 2)) ^ 0.086
Nu_h = 0.029 * alpha_s * Re_h ^ 0.8 * Pr_h ^ 0.33
Nu_c = 0.029 * alpha_s * Re_c ^ 0.8 * Pr_c ^ 0.33
h_h = beta * Nu_h * k_h / dh
h_c = beta * Nu_c * k_c / dh
U = 1 / (1 / h_h + 1 / k_m + 1 / h_c)
dQdx = U * (th - tc)
tfw = th - dQdx / h_h
tpw = tc + dQdx / h_c

Error = 1#

Do While Error > 0.00000001

tht = tfw
tct = tpw

Ph_sat = 1000# * Exp(-0.4702 + 0.06991 * tfw - 0.0002249 * tfw ^ 2 + 0.0000003563 * tfw ^ 3)
Pc_sat = 1000# * Exp(-0.4702 + 0.06991 * tpw - 0.0002249 * tpw ^ 2 + 0.0000003563 * tpw ^ 3)

Tmeant = Tmean + 273.15

Dv = 0.0003939 * Tmeant ^ 1.5
cp_v = 1000 * (1.8653 + 0.0010881 * Tmean - 0.0000044902 * Tmean ^ 2 + 0.00000011083 * Tmean
^ 3)

Pmean_sat = 1000 * Exp(-0.4702 + 0.06991 * Tmean - 0.0002249 * Tmean ^ 2 + 0.0000003563 *
Tmean ^ 3)

hfg = 1000 * (1989.416 * ((373.92 - tfw) / (273.15 + 373.92)) ^ (1 / 3) + 11178.46 * ((373.92 - tfw) /
(273.15 + 373.92)) ^ 0.79 + 26923.69 * ((373.92 - tfw) / (273.15 + 373.92)) ^ (1 - 1 / 8 + 1 / 3) + (-
28989.29 * ((373.92 - tfw) / (273.15 + 373.92)) + -19797.04 * ((373.92 - tfw) / (273.15 + 373.92)) ^ 2 +
28403.32 * ((373.92 - tfw) / (273.15 + 373.92)) ^ 3 + -30382.31 * ((373.92 - tfw) / (273.15 + 373.92)) ^ 4
+ 15210.38 * ((373.92 - tfw) / (273.15 + 373.92)) ^ 5)

mass_coeff = (M_H2O / (Ru * Tmeant)) * ((Ppore - Pmean_sat) / Dv + 0.75 * (2 * 3.1416 * M_H2O /
(Ru * Tmeant)) ^ 0.5 / dm) ^ (-1) * Pmem

m = mass_coeff * (Ph_sat - Pc_sat)
A = m * 3600
U = 1 / (1 / h_h + 1 / (k_m + m * hfg / (tfw - tpw)) + 1 / h_c)
dQdx = U * (th - tc)
tfw = th - dQdx / h_h
tpw = tc + dQdx / h_c
Tmean = 0.5 * (tfw + tpw)
Error = 0.5 * (Abs(tht - tfw) / (tht + tfw) + Abs(tct - tpw) / (tct + tpw))
Loop

Elseif x1 > (L - L1) Then
Re_h = Qh / (60 * 0.13 * 0.0012) * (x1 - L + L1 + dx) * rho_h / vis_h
Pr_h = cp_h * vis_h / k_h
Re_c = Qc / (60 * 0.13 * 0.0012) * (x1 - L + L1 + dx) * rho_c * epsilon_s * 0.667 / vis_c
Pr_c = cp_h * vis_c / k_c
Nu_h = 0.332 * Re_h ^ 0.5 * Pr_h ^ 0.33
Nu_c = 0.332 * Re_c ^ 0.5 * Pr_c ^ 0.33
h_h = beta * Nu_h * k_h / (x1 - L + L1 + dx)
h_c = beta * Nu_c * k_c / (x1 - L + L1 + dx)
U = 1# / (1 / h_h + 1 / conductivity + 1 / h_c)

```

```

dQdx = U * (th - tc)
tfw = th - dQdx / h_h
tpw = tc + dQdx / h_c
m = 0#
End If

```

```

thw(1) = tfw
tcw(1) = tpw
F(1) = m * 3600
m_total = m_total + m

```

```

For I = 2 To N

```

```

x(I) = x1 + dx
th = tf(I - 1) - dx * W * dQdx / (mh * cp_h)
tc = tp(I - 1) + dx * W * dQdx / (mc * cp_c)
tf(I) = th
tp(I) = tc
Tmean = (tc + th) / 2

```

```

'feed properties

```

```

rho_h = 1002.6 - 0.2177 * th - 0.0020099 * th ^ 2 + 0.0000011897 * th ^ 3
vis_h = Exp(-6.3933 - 0.026299 * th + 0.000097341 * th ^ 2 - 0.00000013986 * th ^ 3)
cp_h = 1000 * Exp(1.4423 - 0.00084025 * th + 0.0000141 * th ^ 2 - 0.000000073846 * th ^ 3 +
0.00000000014856 * th ^ 4)
k_h = 0.56611 + 0.002048 * th - 0.000010205 * th ^ 2 + 0.000000011897 * th ^ 3

```

```

'permeate properties

```

```

rho_c = 1002.6 - 0.2177 * tc - 0.0020099 * tc ^ 2 + 0.0000011897 * tc ^ 3
vis_c = Exp(-6.3933 - 0.026299 * tc + 0.000097341 * tc ^ 2 - 0.00000013986 * tc ^ 3)
cp_c = 1000 * Exp(1.4423 - 0.00084025 * tc + 0.0000141 * tc ^ 2 - 0.000000073846 * tc ^ 3 +
0.00000000014856 * tc ^ 4)
k_c = 0.56611 + 0.002048 * tc - 0.000010205 * tc ^ 2 + 0.000000011897 * tc ^ 3

```

```

'velocities of hot and cold water;

```

```

Vh = mh / (rho_h * W * D * epsilon_s)
Vc = Abs(mc) / (rho_c * W * D * epsilon_s)

```

```

If x1 < L1 Then

```

```

Re_h = Qh / (60 * 0.13 * 0.0012) * (x1 + dx) * rho_h / vis_h
Pr_h = cp_h * vis_h / k_h
Re_c = Qc / (60 * 0.13 * 0.0012) * (x1 + dx) * rho_c / vis_c
Pr_c = cp_c * vis_c / k_c
Nu_h = 0.332 * Re_h ^ 0.5 * Pr_h ^ 0.33
Nu_c = 0.332 * Re_c ^ 0.5 * Pr_c ^ 0.33
h_h = beta * Nu_h * k_h / (x1 + dx)
h_c = beta * Nu_c * k_c / (x1 + dx)
U = 1# / (1 / h_h + 1 / conductivity + 1 / h_c)
dQdx = U * (th - tc)
tfw = th - dQdx / h_h
tpw = tc + dQdx / h_c
m = 0#
A = m
End If

```

```

If L1 <= x1 And x1 <= (L - L1) Then

```

```

Re_h = Vh * dh * rho_h / vis_h
Pr_h = cp_h * vis_h / k_h
Re_c = Vc * dh * rho_c / vis_c
Pr_c = cp_c * vis_c / k_c

```

```

alpha_s = 1.904 * (df / D) ^ (-0.039) * epsilon_s ^ 0.75 * (Sin(theta / 2)) ^ 0.086
Nu_h = 0.029 * alpha_s * Re_h ^ 0.8 * Pr_h ^ 0.33
Nu_c = 0.029 * alpha_s * Re_c ^ 0.8 * Pr_c ^ 0.33
h_h = beta * Nu_h * k_h / dh
h_c = beta * Nu_c * k_c / dh
U = 1 / (1 / h_h + 1 / k_m + 1 / h_c)
dQdx = U * (th - tc)
tfw = th - dQdx / h_h
tpw = tc + dQdx / h_c

Error = 1#

Do While Error > 0.00000001

tht = tfw
tct = tpw

Ph_sat = 1000# * Exp(-0.4702 + 0.06991 * tfw - 0.0002249 * tfw ^ 2 + 0.0000003563 * tfw ^ 3)
Pc_sat = 1000# * Exp(-0.4702 + 0.06991 * tpw - 0.0002249 * tpw ^ 2 + 0.0000003563 * tpw ^ 3)

Tmeant = Tmean + 273.15

Dv = 0.0003939 * Tmeant ^ 1.5
cp_v = 1000 * (1.8653 + 0.0010881 * Tmean - 0.0000044902 * Tmean ^ 2 + 0.00000011083 * Tmean
^ 3)

Pmean_sat = 1000 * Exp(-0.4702 + 0.06991 * Tmean - 0.0002249 * Tmean ^ 2 + 0.0000003563 *
Tmean ^ 3)

hfg = 1000 * (1989.416 * ((373.92 - tfw) / (273.15 + 373.92)) ^ (1 / 3) + 11178.46 * ((373.92 - tfw) /
(273.15 + 373.92)) ^ 0.79 + 26923.69 * ((373.92 - tfw) / (273.15 + 373.92)) ^ (1 - 1 / 8 + 1 / 3) + (-
28989.29 * ((373.92 - tfw) / (273.15 + 373.92)) + -19797.04 * ((373.92 - tfw) / (273.15 + 373.92)) ^ 2 +
28403.32 * ((373.92 - tfw) / (273.15 + 373.92)) ^ 3 + -30382.31 * ((373.92 - tfw) / (273.15 + 373.92)) ^ 4
+ 15210.38 * ((373.92 - tfw) / (273.15 + 373.92)) ^ 5)
mass_coeff = (M_H2O / (Ru * Tmeant)) * ((Ppore - Pmean_sat) / Dv + 0.75 * (2 * 3.1416 * M_H2O /
(Ru * Tmeant)) ^ 0.5 / dm) ^ (-1) * Pmem

m = mass_coeff * (Ph_sat - Pc_sat)
A = m * 3600
U = 1 / (1 / h_h + 1 / (k_m + m * hfg / (tfw - tpw)) + 1 / h_c)
dQdx = U * (th - tc)
tfw = th - dQdx / h_h
tpw = tc + dQdx / h_c
Tmean = 0.5 * (tfw + tpw)
Error = 0.5 * (Abs(tht - tfw) / (tht + tfw) + Abs(tct - tpw) / (tct + tpw))
Loop

End If

If x1 > (L - L1) Then
Re_h = Qh / (60 * 0.13 * 0.0012) * (x1 - L + L1 + dx) * rho_h / vis_h
Pr_h = cp_h * vis_h / k_h
Re_c = Qc / (60 * 0.13 * 0.0012) * (x1 - L + L1 + dx) * rho_c * epsilon_s * 0.667 / vis_c
Pr_c = cp_h * vis_c / k_c
Nu_h = 0.332 * Re_h ^ 0.5 * Pr_h ^ 0.33
Nu_c = 0.332 * Re_c ^ 0.5 * Pr_c ^ 0.33
h_h = beta * Nu_h * k_h / (x1 - L + L1 + dx)
h_c = beta * Nu_c * k_c / (x1 - L + L1 + dx)
U = 1# / (1 / h_h + 1 / conductivity + 1 / h_c)
dQdx = U * (th - tc)

```

```

tfw = th - dQdx / h_h
tpw = tc + dQdx / h_c
m = 0#

```

End If

```

thw(I) = tfw
tcw(I) = tpw
m_total = m_total + m

```

```

x1 = x1 + dx
F(I) = A

```

Next I

J = 0

I = 1

Nline = Worksheets(1).Range("E4").Value

Do While I <= N

FLT(B, 1) = tf(I)

FLT(B, 2) = tp(I)

FLT(B, 3) = thw(I)

FLT(B, 4) = tcw(I)

FLT(B, 5) = x(I)

FLT(B, 6) = F(I)

B = B + 1

I = I * J + N / Nline

J = 1

Loop

flux = m_total * 3600 / N1

Worksheets(1).Range("A8:F8").Value = Array("feed bulk temperature", "permeate bulk temperature", "feed interface temperature", "permeate interface temperature", "channel length", "permeate")

Worksheets(1).Range("A9:F2010").Value = FLT

Worksheets(1).Range("G9").Value = flux

End Sub

b. Counter-current modelling program

Sub countercurrent()

Dim k_m, K, W, D, delta, Ru, M_H2O, epsilon, dm, m, tau, Patm, L1, A, L, Pmem, epsilon_s, df, Ppore, Error, x1, tht, tct, alpha_s, mass_coeff, rho_h, texit, Ph_sat, Pc_sat, Tmeant, theta, dh, hsp, mh, Vh, Vc, beta, h_fg0, Lmem, lm, conductivity, Qh, Qc, dx, th, tc, tfw, tpw, m_total, flux, N1, U As Double

Dim N, I, B, J, counter, Nline As Integer

Dim FLT(1 To 1000, 1 To 6) As Double

Dim x(1 To 100000), thw(1 To 100000), tcw(1 To 100000), tf(1 To 100000), tp(1 To 100000), F(1 To 100000) As Double

Lmem = Worksheets(2).Range("D2").Value

I = 1

L = Worksheets(2).Range("C2").Value

L1 = (L - Lmem) / 2

W = Worksheets(2).Range("E2").Value

N = Worksheets(2).Range("A4").Value

Pmem = Worksheets(2).Range("H2").Value

```

'inlet temperature
'mass flowrate
Qh = Worksheets(2).Range("F2").Value
Qc = Worksheets(2).Range("G2").Value
mh = Qh / (1000# * 60)
mc = Qc / (1000# * 60)
Ppore = Worksheets(2).Range("D4").Value
'membrane thickness
delta = 0.0001
'membrane pore size
dm = 0.000000456
'membrane conductivity
k_m = Worksheets(2).Range("A6").Value
'conductivity of membrane + plastic sheets (two layers)
conductivity = 309#

'parameter of spacer
df = 0.0004
hsp = 0.0008
theta = 3.1416 / 2
lm = 0.003
epsilon_s = 0.86
'channel depth
D = 0.0008

'Molar mass
M_H2O = 18
Rv = 0.462
Ru = 8134#

'parameter of spacer filament
Svsp = 4# / df
dh = 4# * epsilon_s / (2 / hsp + (1 - epsilon_s) * Svsp)
'Define increment
dx = L / (N - 1)
x1 = 0#
N1 = (L - 2 * L1) * N / L
Patm = 104325 'in Pa

th_i = Worksheets(2).Range("A2").Value
tc_i = Worksheets(2).Range("B2").Value
textit = (th_i + tc_i) / 2
B = 1
beta = 1#

Error = 1#

counter = 0

Do While Error > 0.00001

m_total = 0#
th = th_i
tc = textit
x1 = 0
x(1) = 0
tf(1) = th
tp(1) = textit
Tmean = (tc + th) / 2

```

```

'feed properties
rho_h = 1002.6 - 0.2177 * th - 0.0020099 * th ^ 2 + 0.0000011897 * th ^ 3
vis_h = Exp(-6.3933 - 0.026299 * th + 0.000097341 * th ^ 2 - 0.00000013986 * th ^ 3)
cp_h = 1000 * Exp(1.4423 - 0.00084025 * th + 0.0000141 * th ^ 2 - 0.000000073846 * th ^ 3 +
0.00000000014856 * th ^ 4)
k_h = 0.56611 + 0.002048 * th - 0.000010205 * th ^ 2 + 0.000000011897 * th ^ 3
'permeate properties
rho_c = 1002.6 - 0.2177 * tc - 0.0020099 * tc ^ 2 + 0.0000011897 * tc ^ 3
vis_c = Exp(-6.3933 - 0.026299 * tc + 0.000097341 * tc ^ 2 - 0.00000013986 * tc ^ 3)
cp_c = 1000 * Exp(1.4423 - 0.00084025 * tc + 0.0000141 * tc ^ 2 - 0.000000073846 * tc ^ 3 +
0.00000000014856 * tc ^ 4)
k_c = 0.56611 + 0.002048 * tc - 0.000010205 * tc ^ 2 + 0.000000011897 * tc ^ 3
'velocities of hot and cold water;
Vh = mh / (rho_h * W * D * epsilon_s)
Vc = Abs(mc) / (rho_c * W * D * epsilon_s)

If x1 < L1 Then
Re_h = Qh / (60 * 0.13 * 0.0012) * (x1 + dx) * rho_h / vis_h
Pr_h = cp_h * vis_h / k_h
Re_c = Qc / (60 * 0.13 * 0.0012) * (x1 + dx) * rho_c / vis_c
Pr_c = cp_c * vis_c / k_c
Nu_h = 0.332 * Re_h ^ 0.5 * Pr_h ^ 0.33
Nu_c = 0.332 * Re_c ^ 0.5 * Pr_c ^ 0.33
h_h = beta * Nu_h * k_h / (x1 + dx)
h_c = beta * Nu_c * k_c / (x1 + dx)
U = 1# / (1 / h_h + 1 / conductivity + 1 / h_c)
dQdx = U * (th - tc)
tfw = th - dQdx / h_h
tpw = tc + dQdx / h_c
m = 0#

Elseif L1 <= x1 And x1 <= L - L1 Then

Re_h = Vh * dh * rho_h / vis_h
Pr_h = cp_h * vis_h / k_h
Re_c = Vc * dh * rho_c / vis_c
Pr_c = cp_c * vis_c / k_c
alpha_s = 1.904 * (df / D) ^ (-0.039) * epsilon_s ^ 0.75 * (Sin(theta / 2)) ^ 0.086
Nu_h = 0.029 * alpha_s * Re_h ^ 0.8 * Pr_h ^ 0.33
Nu_c = 0.029 * alpha_s * Re_c ^ 0.8 * Pr_c ^ 0.33
h_h = beta * Nu_h * k_h / dh
h_c = beta * Nu_c * k_c / dh
U = 1 / (1 / h_h + 1 / k_m + 1 / h_c)
dQdx = U * (th - tc)
tfw = th - dQdx / h_h
tpw = tc + dQdx / h_c

Error = 1#

Do While Error > 0.0001

tht = tfw
tct = tpw

Ph_sat = 1000# * Exp(-0.4702 + 0.06991 * tfw - 0.0002249 * tfw ^ 2 + 0.0000003563 * tfw ^ 3)
Pc_sat = 1000# * Exp(-0.4702 + 0.06991 * tpw - 0.0002249 * tpw ^ 2 + 0.0000003563 * tpw ^ 3)

Tmeant = Tmean + 273.15

```

$$Dv = 0.0003939 * Tmeant ^ 1.5$$

$$cp_v = 1000 * (1.8653 + 0.0010881 * Tmean - 0.0000044902 * Tmean ^ 2 + 0.00000011083 * Tmean ^ 3)$$

$$Pmean_sat = 1000 * \text{Exp}(-0.4702 + 0.06991 * Tmean - 0.0002249 * Tmean ^ 2 + 0.0000003563 * Tmean ^ 3)$$

$$hfg = 1000 * (1989.416 * ((373.92 - tfw) / (273.15 + 373.92)) ^ (1 / 3) + 11178.46 * ((373.92 - tfw) / (273.15 + 373.92)) ^ 0.79 + 26923.69 * ((373.92 - tfw) / (273.15 + 373.92)) ^ (1 - 1 / 8 + 1 / 3) + (-28989.29 * ((373.92 - tfw) / (273.15 + 373.92)) + -19797.04 * ((373.92 - tfw) / (273.15 + 373.92)) ^ 2 + 28403.32 * ((373.92 - tfw) / (273.15 + 373.92)) ^ 3 + -30382.31 * ((373.92 - tfw) / (273.15 + 373.92)) ^ 4 + 15210.38 * ((373.92 - tfw) / (273.15 + 373.92)) ^ 5)$$

$$\text{mass_coeff} = (M_H2O / (Ru * Tmeant)) * ((Ppore - Pmean_sat) / Dv + 0.75 * (2 * 3.1416 * M_H2O / (Ru * Tmeant)) ^ 0.5 / dm) ^ (-1) * Pmem$$

$$m = \text{mass_coeff} * (Ph_sat - Pc_sat)$$

$$A = m * 3600$$

$$U = 1 / (1 / h_h + 1 / (k_m + m * hfg / (tfw - tpw)) + 1 / h_c)$$

$$dQdx = U * (th - tc)$$

$$tfw = th - dQdx / h_h$$

$$tpw = tc + dQdx / h_c$$

$$Tmean = 0.5 * (tfw + tpw)$$

$$\text{Error} = 0.5 * (\text{Abs}(tht - tfw) / (tht + tfw) + \text{Abs}(tct - tpw) / (tct + tpw))$$

Loop

```

ElseIf x1 > L - L1 Then
Re_h = Qh / (60 * 0.13 * 0.0012) * (x1 - L + L1 + dx) * rho_h / vis_h
Pr_h = cp_h * vis_h / k_h
Re_c = Qc / (60 * 0.13 * 0.0012) * (x1 - L + L1 + dx) * rho_c * epsilon_s * 0.667 / vis_c
Pr_c = cp_h * vis_c / k_c
Nu_h = 0.332 * Re_h ^ 0.5 * Pr_h ^ 0.33
Nu_c = 0.332 * Re_c ^ 0.5 * Pr_c ^ 0.33
h_h = beta * Nu_h * k_h / (x1 - L + L1 + dx)
h_c = beta * Nu_c * k_c / (x1 - L + L1 + dx)
U = 1# / (1 / h_h + 1 / conductivity + 1 / h_c)
dQdx = U * (th - tc)
tfw = th - dQdx / h_h
tpw = tc + dQdx / h_c
m = 0#

```

End If

$$thw(1) = tfw$$

$$tcw(1) = tpw$$

$$m_total = m_total + m$$

$$F(1) = m * 3600$$

```

For I = 2 To N
x(I) = x1 + dx
th = tf(I - 1) - dx * W * dQdx / (mh * cp_h)
tc = tp(I - 1) - dx * W * dQdx / (mc * cp_c)
tf(I) = th
tp(I) = tc
Tmean = (tc + th) / 2

```

'feed properties

```

rho_h = 1002.6 - 0.2177 * th - 0.0020099 * th ^ 2 + 0.0000011897 * th ^ 3
vis_h = Exp(-6.3933 - 0.026299 * th + 0.000097341 * th ^ 2 - 0.00000013986 * th ^ 3)
cp_h = 1000 * Exp(1.4423 - 0.00084025 * th + 0.0000141 * th ^ 2 - 0.000000073846 * th ^ 3 +
0.00000000014856 * th ^ 4)
k_h = 0.56611 + 0.002048 * th - 0.000010205 * th ^ 2 + 0.000000011897 * th ^ 3
'permeate properties
rho_c = 1002.6 - 0.2177 * tc - 0.0020099 * tc ^ 2 + 0.0000011897 * tc ^ 3
vis_c = Exp(-6.3933 - 0.026299 * tc + 0.000097341 * tc ^ 2 - 0.00000013986 * tc ^ 3)
cp_c = 1000 * Exp(1.4423 - 0.00084025 * tc + 0.0000141 * tc ^ 2 - 0.000000073846 * tc ^ 3 +
0.00000000014856 * tc ^ 4)
k_c = 0.56611 + 0.002048 * tc - 0.000010205 * tc ^ 2 + 0.000000011897 * tc ^ 3
'velocities of hot and cold water;
Vh = mh / (rho_h * W * D * epsilon_s)
Vc = Abs(mc) / (rho_c * W * D * epsilon_s)

```

```

tf(I) = th
tp(I) = tc

```

```

If x1 < L1 Then

```

```

Re_h = Qh / (60 * 0.13 * 0.0012) * (x1 + dx) * rho_h / vis_h
Pr_h = cp_h * vis_h / k_h
Re_c = Qc / (60 * 0.13 * 0.0012) * (x1 + dx) * rho_c / vis_c
Pr_c = cp_c * vis_c / k_c
Nu_h = 0.332 * Re_h ^ 0.5 * Pr_h ^ 0.33
Nu_c = 0.332 * Re_c ^ 0.5 * Pr_c ^ 0.33
h_h = beta * Nu_h * k_h / (x1 + dx)
h_c = beta * Nu_c * k_c / (x1 + dx)
U = 1# / (1 / h_h + 1 / conductivity + 1 / h_c)
dQdx = U * (th - tc)
tfw = th - dQdx / h_h
tpw = tc + dQdx / h_c
m = 0#
A = m

```

```

ElseIf L1 <= x1 And x1 <= L - L1 Then

```

```

Re_h = Vh * dh * rho_h / vis_h
Pr_h = cp_h * vis_h / k_h
Re_c = Vc * dh * rho_c / vis_c
Pr_c = cp_c * vis_c / k_c
alpha_s = 1.904 * (df / D) ^ (-0.039) * epsilon_s ^ 0.75 * (Sin(theta / 2)) ^ 0.086
Nu_h = 0.029 * alpha_s * Re_h ^ 0.8 * Pr_h ^ 0.33
Nu_c = 0.029 * alpha_s * Re_c ^ 0.8 * Pr_c ^ 0.33
h_h = beta * Nu_h * k_h / dh
h_c = beta * Nu_c * k_c / dh
U = 1 / (1 / h_h + 1 / k_m + 1 / h_c)
dQdx = U * (th - tc)
tfw = th - dQdx / h_h
tpw = tc + dQdx / h_c

```

```

Error = 1#

```

```

Do While Error > 0.0001

```

```

tht = tfw
tct = tpw

```

```

Ph_sat = 1000# * Exp(-0.4702 + 0.06991 * tfw - 0.0002249 * tfw ^ 2 + 0.0000003563 * tfw ^ 3)
Pc_sat = 1000# * Exp(-0.4702 + 0.06991 * tpw - 0.0002249 * tpw ^ 2 + 0.0000003563 * tpw ^ 3)

```

```

Tmeant = Tmean + 273.15

Dv = 0.0003939 * Tmeant ^ 1.5

Pmean_sat = 1000 * Exp(-0.4702 + 0.06991 * Tmean - 0.0002249 * Tmean ^ 2 + 0.0000003563 *
Tmean ^ 3)

hfg = 1000 * (1989.416 * ((373.92 - tfw) / (273.15 + 373.92)) ^ (1 / 3) + 11178.46 * ((373.92 - tfw) /
(273.15 + 373.92)) ^ 0.79 + 26923.69 * ((373.92 - tfw) / (273.15 + 373.92)) ^ (1 - 1 / 8 + 1 / 3) + (-
28989.29 * ((373.92 - tfw) / (273.15 + 373.92)) + -19797.04 * ((373.92 - tfw) / (273.15 + 373.92)) ^ 2 +
28403.32 * ((373.92 - tfw) / (273.15 + 373.92)) ^ 3 + -30382.31 * ((373.92 - tfw) / (273.15 + 373.92)) ^ 4
+ 15210.38 * ((373.92 - tfw) / (273.15 + 373.92)) ^ 5)

mass_coeff = (M_H2O / (Ru * Tmeant)) * ((Ppore - Pmean_sat) / Dv + 0.75 * (2 * 3.1416 * M_H2O
/ (Ru * Tmeant)) ^ 0.5 / dm) ^ (-1) * Pmem

m = mass_coeff * (Ph_sat - Pc_sat)
A = m * 3600
U = 1 / (1 / h_h + 1 / (k_m + m * hfg / (tfw - tpw)) + 1 / h_c)
dQdx = U * (th - tc)
tfw = th - dQdx / h_h
tpw = tc + dQdx / h_c
Tmean = 0.5 * (tfw + tpw)
Error = 0.5 * (Abs(tht - tfw) / (tht + tfw) + Abs(tct - tpw) / (tct + tpw))

Loop

ElseIf x1 > L - L1 Then
Re_h = Qh / (60 * 0.13 * 0.0012) * (x1 - L + L1 + dx) * rho_h / vis_h
Pr_h = cp_h * vis_h / k_h
Re_c = Qc / (60 * 0.13 * 0.0012) * (x1 - L + L1 + dx) * rho_c * epsilon_s * 0.667 / vis_c
Pr_c = cp_h * vis_c / k_c
Nu_h = 0.332 * Re_h ^ 0.5 * Pr_h ^ 0.33
Nu_c = 0.332 * Re_c ^ 0.5 * Pr_c ^ 0.33
h_h = beta * Nu_h * k_h / (x1 - L + L1 + dx)
h_c = beta * Nu_c * k_c / (x1 - L + L1 + dx)
U = 1# / (1 / h_h + 1 / conductivity + 1 / h_c)
dQdx = U * (th - tc)
tfw = th - dQdx / h_h
tpw = tc + dQdx / h_c
m = 0#
A = m
End If

thw(I) = tfw
tcw(I) = tpw
m_total = m_total + m
x1 = x1 + dx
F(I) = A
Next I

Error = Abs(tp(N) - tc_i)

textit = textit + tc_i - tp(N)

Loop

Worksheets(2).Range("B4").Value = tf(N)
Worksheets(2).Range("C4").Value = tp(1)

```

```

Nline = Worksheets(2).Range("E4").Value

J = 0
I = 1
Do While I <= N
  FLT(B, 1) = x(I)
  FLT(B, 2) = tf(I)
  FLT(B, 3) = tp(I)
  FLT(B, 4) = thw(I)
  FLT(B, 5) = tcw(I)
  FLT(B, 6) = F(I)
  B = B + 1
  I = I * J + N / Nline
  J = 1
Loop
flux = m_total * 3600 / N1
Worksheets(2).Range("A8:F8").Value = Array("channel length", "feed bulk temperature", "permeate bulk
temperature", "feed interface temperature", "permeate interface temperature", "permeate")
Worksheets(2).Range("A9:F1003").Value = FLT
Worksheets(2).Range("G9").Value = flux

End Sub

```